
Optical and X-ray structures in the REXCESS sample of galaxy clusters

John Gerrard Holland



München 2015

Optical and X-ray structures in the REXCESS sample of galaxy clusters

John Gerrard Holland

Dissertation
an der Fakultät für Physik
der Ludwig-Maximilians-Universität
München

vorgelegt von
John Gerrard Holland
aus Rawtenstall, England

München, den 7. Mai 2015

Erstgutachter: Prof. Dr. Hans Böhringer
Zweitgutachter: Prof. Dr. Ortwin Gerhard
Tag der mündlichen Prüfung: 9. Juni 2015

Contents

Contents	v
List of Figures	xi
List of Tables	xvii
Zusammenfassung	xix
Abstract	xxi
1 Introduction: the structure of galaxy clusters	1
1.1 Galaxy clusters and the cosmological context	2
1.1.1 A potted history of key developments in cosmology and galaxy cluster research	2
1.1.2 Current theoretical context – the concordance cosmology	6
1.2 Hot dense ICM	6
1.2.1 Appearance	6
1.2.2 Constituents	7
1.2.3 Heating and cooling	8
1.2.3.1 Adiabatic compression	8
1.2.3.2 Accretion and merger shocks	8
1.2.3.3 Radiative cooling and cool cores	9
1.3 Galaxy population	10
1.3.1 Galaxy types and non-galaxy stellar populations in clusters	10
1.3.1.1 Spiral galaxies	10
1.3.1.2 Elliptical and lenticular galaxies	11
1.3.1.3 Brightest cluster galaxies and cD galaxies	11
1.3.1.4 Intracluster light	11
1.3.2 Observed galaxy distribution	14
1.3.2.1 The cosmic web and cluster environment	14
1.3.2.2 Luminosity function of clusters	14
1.3.2.3 Number counts of field galaxies	15
1.3.2.4 Colour–magnitude relation and the red sequence	16

1.3.2.5	The distribution of red and blue galaxies	18
1.4	Galaxies, ICM and dark matter	19
1.4.1	Collisionless interactions – violent relaxation	19
1.4.2	Galaxy–galaxy interactions	20
1.4.2.1	Harassment	20
1.4.2.2	Dynamical friction and cannibalism	21
1.4.2.3	Tidal disruption and starbursts	21
1.4.3	Galaxy–ICM interactions	21
1.4.3.1	Ram pressure stripping	22
1.4.3.2	Feedback from active galactic nuclei	23
1.5	Mergers, smooth accretion and substructure	23
1.5.1	Identification of pre-, current- and post-merger states, and smooth accretion	24
2	REXCESS: optical and X-ray galaxy cluster observations	27
2.1	REXCESS and <i>XMM-Newton</i>	28
2.1.1	<i>XMM-Newton</i>	28
2.1.2	<i>XMM-Newton</i> backgrounds	29
2.1.3	Survey and observation parameters	29
2.2	Observations using the MPG/ESO 2.2 m telescope Wide Field Imager	30
2.2.1	Telescope and instrument parameters	31
2.2.2	Observation parameters	31
2.2.3	Image point spread function	32
2.2.4	Calibration and artefact correction	33
2.2.5	Stacked images	37
2.3	Object detection and catalogue generation	37
2.3.1	Detection of objects in optical images	37
2.3.2	Object analysis and classification	37
2.3.3	Star-galaxy separation	38
2.3.4	Final catalogue generation	41
2.4	Magnitude and colour calibration	41
2.4.1	Zero points from standard star observations	41
2.4.2	Zero point reference from the APASS all-sky survey	42
2.4.3	Colour calibration by stellar locus regression	42
3	Galaxy distribution structural analysis techniques	45
3.1	Density estimate from a 2D point distribution	46
3.1.1	Simple binned count map	47
3.1.2	Fixed aperture smoothing	50
3.1.3	Voronoi tessellation	51
3.1.4	Adaptive aperture smoothing	52
3.1.5	Summary	53
3.2	Background subtraction	54

3.2.1	Stochastic point removal	54
3.2.2	Membership probability from density estimates	55
3.3	Red sequence	58
3.3.1	Fitting methods	61
3.3.1.1	Iterative clipping methods	61
3.3.1.2	Iterative clipping after collapse along red sequence axis	64
3.3.2	3D appearance	65
4	Optical and X-ray profiles in REXCESS	67
4.1	Introduction	68
4.2	Sample description	70
4.2.1	REXCESS sample	70
4.2.2	X-ray data	70
4.2.3	Optical data	72
4.2.4	Subsamples	72
4.3	Analysis	72
4.3.1	Source detection and classification	72
4.3.2	Magnitude calibration	75
4.3.3	Luminosity function analysis	77
4.3.3.1	Galaxy catalogue completeness from off-target observations	77
4.3.3.2	Initial cluster luminosity function analysis	79
4.3.4	Catalogue contamination by misidentified stars	80
4.3.5	Red sequence selection	81
4.3.6	Radial density model	85
4.3.7	Brightest cluster galaxy properties and positions	85
4.3.8	Radial density profiles	86
4.3.8.1	Count density profile fitting	86
4.3.8.2	Background count density analysis	87
4.3.8.3	Comparison profiles and normalisation	90
4.3.8.4	Stacked profiles	90
4.3.9	Luminosity measurements	95
4.3.9.1	Variation of the cluster luminosity function with radius	95
4.3.9.2	Residual cluster luminosity function in the off-target region	100
4.3.9.3	Total cluster luminosity	100
4.3.9.4	Mass-to-light ratio relation	102
4.4	Discussion	106
4.5	Summary and conclusions	108
5	Optical and X-ray substructure in REXCESS	111
5.1	Introduction	112
5.2	Sample description	114
5.3	Methods	115
5.3.1	Cluster X-ray peak centred coordinate system	115

5.3.2	Smoothed density map generation	117
5.3.2.1	Smoothing algorithm	118
5.3.2.2	Background level estimate	118
5.3.2.3	Overdensity contours	118
5.3.3	Image analysis	119
5.3.3.1	Moments	119
5.3.3.2	Centroiding algorithm	120
5.3.4	Centre shifts	121
5.3.5	Ellipticity and orientation	123
5.4	Results	123
5.4.1	Centre shift parameter	123
5.4.2	Cluster shape analysis	125
5.4.3	Sub-clumps within clusters	127
5.4.3.1	Clump detection and significance measurement	127
5.4.3.2	Normalised clump count	128
5.4.4	Optical morphology and mismatched classifications of disturbance	131
5.4.4.1	Matched: optically- and X-ray-regular	131
5.4.4.2	Matched: optically- and X-ray-disturbed	132
5.4.4.3	Mismatched: optically-disturbed and X-ray-regular	133
5.4.4.4	Mismatched: optically-regular and X-ray-disturbed	134
5.5	Discussion	135
5.6	Conclusions	137
6	Summary of findings and outlook	139
6.1	Summary of findings	139
6.2	Outlook	140
A	X-ray surface brightness maps and optical wide field images	143
B	SEXTRACTOR parameters	173
C	Additional galaxy distribution structural analysis examples	177
C.1	2D point distribution smoothing examples	177
C.2	Additional background subtraction examples	177
D	Additional plots and tables for Chapter 4	183
D.1	Additional figures	183
D.2	Individual cluster radial profiles	188
D.3	Background count density analysis	195
E	Additional plots and tables for Chapter 5	197
E.1	Smoothed density maps	197
	Bibliography	211

Acknowledgments

237

List of Figures

1.1	Distribution of galaxies in the Two-degree Field Galaxy Redshift Survey, including the Sloane Great Wall.	4
1.2	RGB images of spiral, elliptical and S0 galaxies.	12
1.3	RGB images of galaxy cluster centres.	13
1.4	Single and double Schechter luminosity functions.	15
1.5	Galaxy number counts with respect to observed magnitude.	16
1.6	Example fitted red sequences.	18
2.1	WFI@2.2 m bandpasses for the standard <i>UBVRI</i> filter set, showing where the 400 nm spectral break characteristic of elliptical galaxies falls.	31
2.2	Simulated point spread functions for short and long exposures with different telescope sizes and atmospheric conditions.	34
2.3	Examples of image artefacts which may be difficult or impossible to correct during image reduction.	36
2.4	FWHM–magnitude diagram for sources detected in a single R_c band exposure.	39
2.5	FWHM variation across a WFI@2.2 m image, showing the increase in PSF FWHM of unsaturated stars as distance from the image centre increases.	40
2.6	Calibrated star colours and fitted stellar locus from Ziparo et al. (2012), compared with the stellar locus of Covey et al. (2007).	44
3.1	Simulation input density map and the resulting point distribution.	48
3.2	Smoothed density maps based on the point distribution in Figure 3.1b and several different algorithms.	48
3.3	Plots showing the differences between the smoothed density map generated by smoothing a point distribution and the original density map.	49
3.4	Results of a stochastic point removal algorithm when run on a point distribution with a known background density map which varies across the field.	56
3.5	Plot showing the results of a stochastic point removal algorithm when run on the same distribution as in Figure 3.4, but with a uniform background level estimate.	57

3.6	Map showing distribution of points estimated to be members or non-members of a cluster with perfect estimates of the cluster and background density.	59
3.7	Map showing distribution of points estimated to be members or non-members of a cluster with imperfect estimates of the cluster and background density.	60
3.8	Colour–magnitude distribution of cluster galaxies with point sizes proportional to the calculated probability that they belong to the cluster or the background.	63
3.9	Colour–magnitude diagrams for galaxies in clusters based on two different measurement bands.	66
4.1	Examples of masks covering diffraction spikes and intra-telescope reflections due to bright stars.	74
4.2	Images showing the differences between objects classified as point-like or extended using SEXTRACTOR’s object classifier.	75
4.3	Number counts of field galaxies surrounding the clusters in REXCESS.	78
4.4	Stacked luminosity function for all of the clusters in the sample.	80
4.5	Fitted red sequences for each cluster in the sample.	83
4.6	Stacked radial profiles for all the clusters in the sample.	91
4.7	Stacked radial profiles for clusters above and below the median mass in the sample.	92
4.8	Stacked radial profiles for disturbed and regular clusters.	93
4.9	Stacked radial profiles for cool-core and non-cool-core clusters.	94
4.10	The cumulative fraction of red galaxies with increasing radial distance for different cluster subsamples.	97
4.11	Stacked luminosity functions, showing variations with distance from the cluster centre for all of the clusters, as well as for the massive and low mass subsamples.	98
4.12	Stacked luminosity functions, showing variations with distance from the cluster centre for disturbed and regular clusters.	99
4.13	Measurements showing a remnant luminosity function outside the cluster virial radius.	101
4.14	Mass-to-light ratio vs. mass relation fits.	104
5.1	For a point density field, plots showing variations in a centroid cost parameter which can be used for direct detection of stable minima in density fields, and of routes available in the same fields to iterative centroiding methods.	122
5.2	Comparison of the results of running the centre shift algorithm as defined in this work, compared with that of Böhringer et al. (2010).	124

5.3	Measurements of the centre shift parameter calculated for optical point distributions vs. the X-ray centre shift parameter measured by Böhringer et al. (2010) for the same galaxy clusters.	124
5.4	Comparisons between the orientation and ellipticity of galaxy and X-ray emitting gas distributions in clusters.	126
5.5	Normalised clump count versus the X-ray centre shift parameter.	131
A.1	X-ray flux density map of RXC J0006.0–3443.	144
A.2	Optical image of RXC J0006.0–3443.	145
A.3	X-ray flux density map of RXC J0049.4–2931.	146
A.4	Optical image of RXC J0049.4–2931.	147
A.5	X-ray flux density map of RXC J0345.7–4112.	148
A.6	Optical image of RXC J0345.7–4112.	149
A.7	X-ray flux density map of RXC J0547.6–3152.	150
A.8	Optical image of RXC J0547.6–3152.	151
A.9	X-ray flux density map of RXC J0605.8–3518.	152
A.10	Optical image of RXC J0605.8–3518.	153
A.11	X-ray flux density map of RXC J0616.8–4748.	154
A.12	Optical image of RXC J0616.8–4748.	155
A.13	X-ray flux density map of RXC J0645.4–5413.	156
A.14	Optical image of RXC J0645.4–5413.	157
A.15	X-ray flux density map of RXC J0821.8+0112.	158
A.16	Optical image of RXC J0821.8+0112.	159
A.17	X-ray flux density map of RXC J2023.0–2056.	160
A.18	Optical image of RXC J2023.0–2056.	161
A.19	X-ray flux density map of RXC J2048.1–1750.	162
A.20	Optical image of RXC J2048.1–1750.	163
A.21	X-ray flux density map of RXC J2129.8–5048.	164
A.22	Optical image of RXC J2129.8–5048.	165
A.23	X-ray flux density map of RXC J2218.6–3853.	166
A.24	Optical image of RXC J2218.6–3853.	167
A.25	X-ray flux density map of RXC J2234.5–3744.	168
A.26	Optical image of RXC J2234.5–3744.	169
A.27	X-ray flux density map of RXC J2319.6–7313.	170
A.28	Optical image of RXC J2319.6–7313.	171
C.1	Point distribution and smoothing results for a simulated colour–magnitude diagram.	178
C.2	Plots showing the differences between the smoothed density map generated by smoothing a colour–magnitude point distribution and the original density map.	179
C.3	Results of a stochastic point removal algorithm when run on a simulated colour–magnitude diagram, with an ideal model of the background density.	181

C.4	Map showing distribution of points estimated to be members or non-members of a cluster in a colour–magnitude diagram, with perfect estimates of the cluster and background density.	182
D.1	R_c band detection image for RXC J0006.0–3443.	184
D.2	R_c band detection image for RXC J0616.8–4748.	185
D.3	R_c band detection image for RXC J2234.5–3744.	186
D.4	Cluster centre detail of the R_c band detection image for RXC J0006.0–3443.	187
D.5	Individual radial density profiles for RXC J0006.0–3443, RXC J0049.4–2931, RXC J0345.7–4112 and RXC J0547.6–3152.	189
D.6	Individual radial density profiles for RXC J0605.8–3518, RXC J0616.8–4748, RXC J0645.4–5413 and RXC J0821.8+0112.	190
D.7	Individual radial density profiles for RXC J2023.0–2056, RXC J2048.1–1750, RXC J2129.8–5048 and RXC J2218.6–3853.	191
D.8	Individual radial density profiles for RXC J2234.5–3744 and RXC J2319.6–7313.	192
E.1	Maps of sub-clumps detected in and around RXC J0006.0–3443.	200
E.2	Maps of sub-clumps detected in and around RXC J0049.4–2931.	200
E.3	Maps of sub-clumps detected in and around RXC J0345.7–4112.	201
E.4	Maps of sub-clumps detected in and around RXC J0547.6–3152.	201
E.5	Maps of sub-clumps detected in and around RXC J0605.8–3518.	201
E.6	Maps of sub-clumps detected in and around RXC J0616.8–4748.	202
E.7	Maps of sub-clumps detected in and around RXC J0645.4–5413.	202
E.8	Maps of sub-clumps detected in and around RXC J0821.8+0112.	202
E.9	Maps of sub-clumps detected in and around RXC J2023.0–2056.	203
E.10	Maps of sub-clumps detected in and around RXC J2048.1–1750.	203
E.11	Maps of sub-clumps detected in and around RXC J2129.8–5048.	203
E.12	Maps of sub-clumps detected in and around RXC J2218.6–3853.	204
E.13	Maps of sub-clumps detected in and around RXC J2234.5–3744.	204
E.14	Maps of sub-clumps detected in and around RXC J2319.6–7313.	204
E.15	Maps of centroid positions in RXC J0006.0–3443.	205
E.16	Maps of centroid positions in RXC J0049.4–2931.	205
E.17	Maps of centroid positions in RXC J0345.7–4112.	206
E.18	Maps of centroid positions in RXC J0547.6–3152.	206
E.19	Maps of centroid positions in RXC J0605.8–3518.	206
E.20	Maps of centroid positions in RXC J0616.8–4748.	207
E.21	Maps of centroid positions in RXC J0645.4–5413.	207
E.22	Maps of centroid positions in RXC J0821.8+0112.	207
E.23	Maps of centroid positions in RXC J2023.0–2056.	208
E.24	Maps of centroid positions in RXC J2048.1–1750.	208
E.25	Maps of centroid positions in RXC J2129.8–5048.	208
E.26	Maps of centroid positions in RXC J2218.6–3853.	209

E.27 Maps of centroid positions in RXC J2234.5–3744.	209
E.28 Maps of centroid positions in RXC J2319.6–7313.	209

List of Tables

4.1	Basic parameters of the REXCESS clusters.	71
4.2	Details of optical observations.	73
4.3	Magnitude zero points for each set of WFI@2.2 m observations.	76
4.4	Parameters used to convert between WFI@2.2 m native magnitudes and standard magnitude systems.	77
4.5	Results of fitting an empirical function describing field galaxy number counts to the REXCESS observations.	79
4.6	Best fitting Schechter function parameters.	79
4.7	Contamination fraction for each catalogue measured at the bright limit, the faint limit, and the 50% detection limit.	81
4.8	Red sequence parameters transformed in the standard Johnson-Cousins colour–magnitude space.	84
4.9	Concentration parameters for use with Navarro-Frenk-White radial density model for each cluster.	85
4.10	Parameters for each cluster’s BCG.	86
4.11	Best fitting parameters for a Navarro-Frenk-White radial density model for individual clusters.	87
4.12	Comparisons between galaxy distribution background count densities estimated by different methods.	89
4.13	Background count density measurements used for background subtraction in the radial profiles.	89
4.14	Best fit parameters for NFW models fitted to the stacked cluster profiles.	96
4.15	Total R band luminosities.	103
4.16	Best fitting parameters for the mass-to-light ratio vs. mass relation fits.	105
5.1	Key X-ray parameters for the clusters in the sample.	116
5.2	Positions of X-ray surface brightness peaks detected on a 8.2'' smoothing scale.	117
5.3	Residual galaxy counts in each cluster after background subtraction for selected magnitude bands.	119
5.4	Key parameters measured for significant sub-clumps detected in cluster galaxy density maps.	129

5.5	The normalised clump count – the relative size and count of sub-clumps compared with the size of the circularly symmetric component in a galaxy cluster.	130
D.1	NFW fitting results for individual clusters.	193
D.2	Comprehensive background count density measurements.	195
E.1	Significance measures and background subtracted object count for all the clumps found by inspection.	197

Zusammenfassung

Galaxienhaufen sind die größten und massivsten gravitativ gebundenen Objekte im Universum, die Zeit hatten, zu kollabieren und virialisieren. Das Intracluster-Medium (ICM) innerhalb Galaxienhaufen ist ein Plasma, das durch Röntgenstrahlung sichtbar ist. Galaxien in Galaxienhaufen sind durch optische Strahlung zu sehen, sie sind hauptsächlich rot und haben eine niedrige Sternbildungsrate. Neu akkretierte Galaxien können blauere Farben und eine höhere Sternbildungsrate aufweisen und werden durch Interaktion mit dem ICM röter. Wachstum von Galaxienhaufen findet durch sporadisches Verschmelzen mit anderen Galaxienhaufen und Gruppen statt, oder durch gleichmäßige Akkretion von Galaxien aus dem Milieu.

Um die Hauptfrage »ergänzen sich Röntgen- und optische Messungen von Galaxienhaufen, oder zeigen sie dasselbe?« zu beantworten, haben wir eine Studie durchgeführt, bei der die Verteilung von Galaxien und ICM in Galaxienhaufen verglichen wurden. Im Besonderen, haben wir untersucht, ob optische Daten zusätzliche Information wegen der dynamischen Befindlichkeit von einzelnen Galaxienhaufen liefern, die nicht aus Röntgendaten allein hervorgehen können. Surveys in Röntgen und optischer Strahlung sind in den nächsten Jahrzehnten zu erwarten, die Daten von viel weiteren Gebieten des Universums liefern werden. Diese Daten können, mit den Methoden, die wir hier vorlegen, untersucht werden.

Wir benutzten Weitwinkelbeobachtungen des MPG/ESO 2.2 m Telescopes und Röntgenbeobachtungen von *XMM-Newton*, um die Distribution von Galaxien innerhalb Galaxienhaufen mit der Distribution des ICM zu vergleichen. Wir haben gefunden, dass die 1D Radialdistribution der roten Galaxien zu der des ICM zusammenpasst, aber die blauen Galaxien folgen einem flacheren Profil. Mit 2D Abbildungen der Galaxienhaufen, haben wir gefunden dass die roten Galaxien sehr ähnlich verteilt sind, wie das ICM, aber fast jeder Galaxienhaufen hat unvirialisierte rote Subklumpen. Blaue Galaxien andererseits haben zu wenig Zeit zum virialisieren bevor sie rot werden, weil sie ihre sternbildendes Gas innerhalb einer Übergangszeit durch ICM-Staudruckstripping verlieren. Röntgenbeobachtungen sind besser für die Bestimmung des Verschmelzungsverlaufes von Galaxienhaufen, weil sie die Kennzeichen von Verschmelzung für eine kürzere Zeit zeigen. Wir haben mehrere Subklumpen von roten Galaxien entdeckt, die scheinen auf einfallenden Trajektorien in Galaxienhaufen zu sein und noch merkliche Mengen von Röntgenemittierendem Gas zu haben.

Abstract

Galaxy clusters are the largest and most massive gravitationally bound objects in the Universe which have had time to collapse and virialise. The intra cluster medium (ICM) within clusters is a plasma seen in the X-ray band. Galaxies within clusters are visible in the optical band and are primarily red and have low star formation rates. Newly accreted galaxies may have more star formation and bluer colours, but they become red as galaxies interact with the ICM. Growth of clusters occurs by sporadic mergers with other galaxy groups/clusters, or through smooth accretion of galaxies from clusters' surroundings.

In order to answer the key question 'Are X-ray and optical measurements of galaxy clusters complementary, or do they show the same things?' we carried out a study comparing the distribution of galaxies and ICM in galaxy clusters. In particular, we investigated whether optical data gave additional information about the dynamical state of individual clusters which could not be recovered from X-ray data alone. Imaging surveys in optical and X-ray which are expected in the coming decades will provide similar data for much larger regions of the Universe which can be analysed using the techniques we investigated.

We used wide field optical images from the MPG/ESO 2.2 m telescope and X-ray data from *XMM-Newton* to investigate the distribution of galaxies within clusters as compared with the ICM. The 1D radial distribution of the red galaxies was found to match the ICM, but the blue galaxies had a much flatter distribution. Using 2D maps of the clusters, we found that the distribution of red galaxies was similar to that of the ICM, but most clusters also contained red galaxy sub-clumps which were unvirialised. The blue galaxies had insufficient time to virialise as they were stripped of their star forming gas by ram pressure stripping by the ICM within their first crossing of the cluster and became red. X-ray observations are better for determining the recent merger history of galaxy clusters because they retain the signatures of mergers for a shorter period of time. We identified several red clumps of galaxies which appeared to be on infall trajectories into the clusters, and which still retained significant amounts of X-ray emitting gas.

Chapter 1

Introduction: the structure of galaxy clusters

All you really need to know for the moment is that the Universe is a lot more complicated than you might think, even if you start from a position of thinking it's pretty damn complicated in the first place.

Douglas Adams, *The Hitchhiker's Guide to the Galaxy*, 1979

This dissertation is concerned with the interaction of gas and galaxies within galaxy clusters. We focus on the distribution of galaxies of different colours – a proxy for the star formation and history of the galaxy – with respect to the density of the gas which surrounds the galaxies and affects their evolution.

The purpose of this chapter is to outline the formation, evolution and appearance of the components of galaxy clusters, and the interactions the components undergo. In Section §1.1 we describe galaxy clusters' structure and formation in the context of the Λ CDM cosmological model and provide a very brief overview of the history of galaxy cluster research. The dominant baryonic component of galaxy clusters – the hot intracluster plasma – is described in Section §1.2. In Section §1.3 we describe the population of galaxies in clusters, in comparison to galaxies in lower density environments. We outline the key interactions between cold dark matter, gas and galaxies within galaxy clusters in Section §1.4 and these are investigated in more detail in Chapters 4 and 5. The significance of substructures within galaxy clusters is described in Section §1.5. The substructures found in a sample of galaxy clusters are investigated in Chapter 5.

1.1 Galaxy clusters and the cosmological context

1.1.1 A potted history of key developments in cosmology and galaxy cluster research

Messier (1781) and Herschel (1785) observed groups of nebulae in the constellations Coma Berenices and Virgo which were noticeably denser than the overall *field* distribution of galaxies on the sky. These groups are now known as the Coma and Virgo galaxy clusters. The first detailed study of a galaxy cluster was carried out by Wolf (1906) who noted a generally high density of nebulae on plates taken of Perseus, and a particularly high density region containing 148 galaxies within a $60' \times 60'$ region. He described two prominent galaxy types – round with a central concentration (elliptical), and others in the pattern of the Andromeda galaxy (spiral), and that spiral types were more common at larger distances from the cluster centre.

Hubble (1929) showed that the Universe was expanding. This expansion causes the wavelength of light emitted by distant objects to lengthen in transit, so that its energy is reduced and it appears redder – is *redshifted* – when compared to reference sources on Earth. For a reference wavelength λ_0 and wavelength shift $\Delta\lambda$, the redshift is $z = \frac{\Delta\lambda}{\lambda_0}$. Nearby objects with no peculiar (additional) motion relative to the expansion of space have $z \sim 0$, and distant objects have higher z . Due to the finite speed of light, objects at higher z are observed at an earlier time in the history of the Universe. The expansion of the Universe – also called the *Hubble flow* – is isotropic, such that the velocity v at which two arbitrary points at rest with respect to the space-time are moving away from each other is only dependent on their separation x , $v = x H_0$, where H_0 is the Hubble parameter. H_0 takes a range of values around $70 \text{ km s}^{-1} \text{ Mpc}^{-1}$ in the literature [e.g. $(67.0 \pm 1.2, 73.8 \pm 2.4 \text{ and } 74.3 \pm 2.5) \text{ km s}^{-1} \text{ Mpc}^{-1}$ in Planck Collaboration et al. 2014a; Riess et al. 2011 and Freedman et al. 2012 respectively]. H_0 also defines a characteristic timescale, the Hubble time $t_{\text{Hubble}} = \frac{1}{H_0} \sim 1.4 \times 10^{10} \text{ yr}$, approximately the age of the Universe.

Hubble’s work, and its clear demonstration that the Universe was not static, meant that the *cosmological constant* component labelled Λ , which Einstein had included in his theory of gravity to enable the existence of the static Universe he preferred, was not required. Einstein famously referred to his inclusion of Λ as his “greatest blunder.”

A few years later, it became clear that the galaxies within galaxy clusters had very high velocity dispersions relative to the expected dispersion based on the masses of their observed components (Zwicky, 1933; Smith, 1936). Zwicky derived an expected velocity dispersion of 80 km s^{-1} based on the observed stellar mass in the Coma cluster, compared with an observed velocity dispersion in the range $(1500 - 2000) \text{ km s}^{-1}$, implying a total central density $400\times$ larger than that observed in luminous material. He wrote:

Falls sich dies bewahrheiten sollte, würde sich also das überraschende Resultat ergeben, dass dunkle Materie in sehr viel grösserer Dichte vorhanden ist als leuchtende Materie. [If this is verified, it would amount to the surprising result

that dark matter is present in much higher densities than luminous material.]
(Zwicky, 1933)

The observations of the *missing mass* and the expansion of the Universe drove thinking and research in cosmology for the rest of the 20th century.

The first systematic catalogue of galaxy clusters in the 20th century was compiled by Abell (1958) based on photographs from the Palomar Observatory Sky Survey. In this seminal work, he showed evidence that clusters of galaxies themselves tend to cluster – a sign of even larger cosmic structures.

Systematic surveys of galaxies including the Centre for Astrophysics (CfA) Redshift Survey (Davis et al., 1982; Huchra et al., 1983), Two-degree Field (2dF) Galaxy Redshift Survey (Colless et al., 2001; shown in Figure 1.1) and the Sloan Digital Sky Survey (SDSS, York et al., 2000; Einasto et al., 2003; Eisenstein et al., 2011) revealed a web of galaxy clusters, filaments, walls and empty voids, in which galaxy clusters were the most massive virialised objects (in which the object structure is supported against further gravitational collapse by the motions of the particles). These surveys allowed the discovery of much larger structures than galaxy clusters like the CfA2 Great Wall (Geller and Huchra, 1989) and the filaments in the 2dF (Peacock, 2002). They also provided measurements of the clustering of galaxies (the power spectrum of galaxy density fluctuations, Cole et al., 2005; Anderson et al., 2012).

Early experiments in X-ray astronomy (Meekins et al., 1971; Fritz et al., 1971; Gursky et al., 1971) suggested that clusters of galaxies might all be X-ray sources (Cavaliere et al., 1971), and this was confirmed with all-sky X-ray object catalogues from the *Uhuru* satellite (Giacconi et al., 1972). These were the first observations of the hot plasma which is found between galaxies in clusters – the *intra-cluster medium* (ICM). The ratio between gas and stellar mass in clusters varies in the range $\sim 1-5$ from groups to massive clusters (e.g. Giodini et al., 2009), but despite the fact that the total luminous mass measured within clusters rose substantially once this ICM was found, the total baryonic mass in clusters was still too little to account for the missing mass. The distribution of objects' mass (the mass function) is an important property predicted by cosmological models, and the luminosity and temperature of the ICM are related to the total mass of the cluster (e.g. Bahcall and Cen, 1993; Reiprich and Böhringer, 2002; Pratt et al., 2009). Consequently, X-ray observations can be used to measure the mass function and test cosmological models.

The *ROSAT* All Sky Survey (RASS, Voges et al., 1999) was used to produce several important galaxy cluster surveys (Ebeling et al., 1998; Böhringer et al., 2000, 2001a; Cruddace et al., 2002; Böhringer et al., 2013). More recently, *Chandra* and *XMM-Newton* have allowed observations of clusters with higher spatial and spectral resolution, allowing temperature profiles to be measured and leading to better constraints on cluster masses than were possible with earlier measurements. The next generation X-ray survey of galaxy clusters to be performed by the planned *eROSITA* mission is predicted to detect $\sim 9.3 \times 10^4$ clusters which will allow even finer constraints to be placed on cosmological parameters characterised by the cluster mass function (Pillepich et al., 2012).

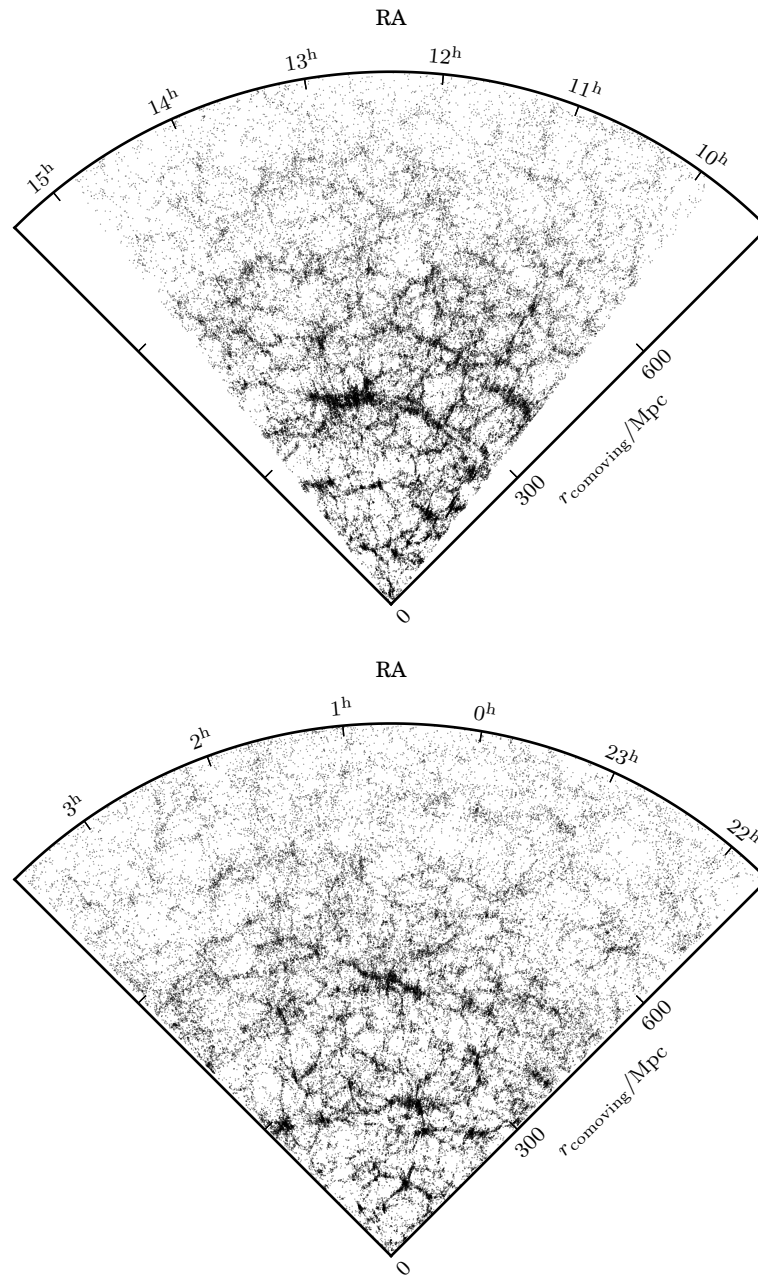


Figure 1.1: Distribution of galaxies in the northern (top) and southern (bottom) fields of the Two-degree Field Galaxy Redshift Survey (Colless et al., 2001), which illustrates the filaments, clusters, voids and superclusters which make up the cosmic web. The Sloan Great Wall is the overdense region shown in the northern panel at comoving distance $r_{\text{comoving}} \sim 310 \text{ Mpc}$.

Following the detection of the leftover radiation from the Big Bang – the *cosmic microwave background* (CMB) (Penzias and Wilson, 1965), a further method to characterise galaxy clusters became available. The CMB has a temperature of $(2.725\,48 \pm 0.000\,57)$ K and is extremely isotropic, but small variations in the temperature due to the primordial quantum fluctuations are observed. The power spectrum of these variations is related to the cosmology, and can be used to characterise the initial conditions of the Universe and its constituents. Sunyaev and Zeldovich (1972) proposed a mechanism by which CMB photons are scattered to higher energies by inverse Compton scattering off thermal electrons in galaxy cluster ICM, leading to additional changes in the temperature of the CMB on small scales. This is known as the Sunyaev-Zel’dovich effect (SZ-effect). In their paper, they refer to observations of the Coma cluster in which the brightness of the CMB in one band was reduced, and they posited that this was due to the up-scattering of photons out of this band and could not be explained by the peculiar motion of the cluster with respect to the expansion of the Universe. The multi-wavelength observations required to confirm the mechanism were published by Birkinshaw et al. (1984). The SZ-effect has since been used for galaxy cluster surveys (e.g. Planck Collaboration et al., 2014b) and carries information about the cluster structure which is complementary to X-ray observations (e.g. Hasler et al., 2012).

The development of affordable computers allowed simulations of cosmic structure formation and comparisons of different cosmological models. These simulations, along with a range of observational studies, produced several remarkable results. Firstly, structures similar to those in the observed Universe could be generated by the hierarchical clustering of collisionless particles with non-relativistic energies which only interact gravitationally – cold dark matter (CDM). Secondly, cosmologies without an additional *dark energy* component, which accelerated expansion and could be parametrised as Einstein’s Λ , were inconsistent with reality (e.g. Gunn and Tinsley, 1975; Bagla et al., 1996). Simulations of CDM clustering and galaxy evolution within the context of an expanding universe with a positive cosmological constant (e.g. Davis et al., 1985; the Millennium simulation Springel et al., 2005; the Illustris simulation, Vogelsberger et al., 2014a) have been successful in recreating many of the observed properties of the Universe. The first direct observational evidence of the resulting accelerating expansion from surveys of distant supernovae – the smoking gun of dark energy – was published at the close of the 20th century (Riess et al., 1998; Perlmutter et al., 1999). Direct evidence of the existence of CDM was published in the early 21st century (Clowe et al., 2006), solving – to some extent – the missing mass problem. Work is ongoing to understand both dark energy and dark matter.

1.1.2 Current theoretical context – the concordance cosmology

According to the current consensus, the current phase of the Universe’s evolution was very hot, dense and uniform, after which it expanded and cooled.¹ It continues to expand.

(69.11 ± 0.62) % of the mass-energy of the Universe is dark energy (Planck Collaboration, 2015). Since it does not have a significant impact within bound objects, we do not consider it further.

CDM is the major matter constituent and represents (25.9 ± 0.4) % of the mass-energy of the Universe (Planck Collaboration, 2015). The fraction of the total energy budget taken up by the baryons which form the visible Universe of stars, gas and dust is just (4.86 ± 0.07) %, but it is this small fraction which we can study using optical and X-ray telescopes today.

Over-densities of matter compared with the mean density of the Universe – like galaxies, galaxy clusters, filaments and the large scale structure of the cosmos – arose from quantum density fluctuations present at early times, which merged hierarchically, forming ever-larger over-densities (e.g. White and Rees, 1978; White and Frenk, 1991; Kauffmann et al., 1993; Fritsch et al., 1997; Navarro et al., 1997). This *concordance cosmological model* consisting of a cosmological constant, cold dark matter, and a minor baryonic component is represented by the abbreviation Λ CDM. For calculations in this work, we use a flat cosmology with $H_0 = 70 \text{ km s}^{-1} \text{ Mpc}^{-1}$, $\Omega_m = 0.3$ and $\Omega_\Lambda = 0.7$.

The largest of these over-densities which have had time to collapse are large galaxy groups and galaxy clusters. These have sizes of $r_{500} \sim \text{Mpc}$ and masses of $M_{500} \sim (10^{13} - 10^{15}) M_\odot$, where r_{500} is the radius within which the mean density is $500\times$ the mean density of the Universe, and M_{500} is the total mass within that radius. The fractional content of the over-densities – the different particle species they contain – is representative to first order of the Universe as a whole (e.g. White and Frenk, 1991; Evrard, 1997). This means that the gravitational field of galaxy clusters is dominated by their CDM. The dark matter distribution is the stage upon which the dance of gas and galaxies is performed.

1.2 Hot dense ICM

1.2.1 Appearance

The X-ray emission from galaxy clusters is primarily generated in the ICM by thermal Bremsstrahlung due to the acceleration of electrons passing by atomic nuclei. The X-ray emission extends for several Mpc, and ICM are amongst the most luminous objects in the X-ray sky. Typical clusters have X-ray luminosities L_X in the range ($10^{36} - 10^{38}$) W, and up to $L_X = 6 \times 10^{38}$ W in the most luminous galaxy cluster RX J1347.5–1145 (Voges et al., 1999). The overall shape of the X-ray spectrum, in particular the position of the exponential falloff at higher energies, is determined by the temperature of the ICM, T_{ICM} .

¹It is thought that a previous phase of exponential inflation of space-time stretched initially small quantum perturbations onto cosmological scales, sowing the seeds for later large scale structures.

Gas falling into galaxy cluster scale CDM haloes is generally thermalised by accretion shocks and reaches the virial temperature of the halo. Typical temperatures of $T_{\text{ICM}} \sim (2 \times 10^7 - 10^8)$ K are measured for clusters with masses in the range $\sim (10^{14} - 10^{15}) M_{\odot}$, corresponding to X-ray photons with energies in the range $T_{\text{ICM}} k_{\text{B}} \sim (2 - 9)$ keV (Pratt et al., 2009) where k_{B} is the Boltzmann constant. Emission lines from heavy elements are also present in cluster X-ray spectra. The prominent 7 keV iron line can be used to determine the redshift of a cluster. For gas temperatures lower than 2 keV, spectral lines become the dominant source of emission.

During hierarchical collapse of the primordial over-densities, the collisionless CDM forms an approximately spherically symmetric and virialised *halo* which has a shape only dependent on the time of formation (Navarro et al., 1995, 1996). Within this halo's gravitational potential well, the gas is supported against collapse by its internal pressure, and its configuration is approximately in hydrostatic equilibrium. The time required for hydrostatic equilibrium to be reached is approximately the sound crossing time for the cluster,

$$t_{\text{s}} = 6.6 \times 10^8 \text{ yr} \left(\frac{T_{\text{ICM}}}{10^8 \text{ K}} \right)^{-\frac{1}{2}} \left(\frac{D}{1 \text{ Mpc}} \right), \quad (1.1)$$

for D the cluster diameter (eq. 5.54 in Sarazin, 1986).

Perturbations and collisions with other gas clouds can break the hydrostatic equilibrium. If the gas is able to cool, it can collapse further. The same processes potentially occur within the sub-haloes associated with cluster galaxies within the cluster, but on different mass scales, and with different modifying effects due to the ICM. Moderation of cooling by heating from galaxies has also been shown to be very important. These galaxy–ICM interactions are discussed in Section §1.4.3. CDM sub-haloes can dissolve over time as their constituent particles have additional energy imparted and/or are stripped away by tidal forces (e.g. Goerdt et al., 2007), at which point any gas originally bound to the sub-halo is absorbed into the ICM of the absorbing system.

Gas distributions observed in galaxy clusters range from smooth and very symmetrical to elliptical to lumpy and asymmetrical. Due to the longer relaxation times of collisionless CDM haloes which dominate the gravitational potential and therefore the hydrostatic equilibrium configuration, elliptical ICM distributions within post-merger clusters may be long lived. Collisionless relaxation in CDM haloes is discussed in Section §1.4.1.

1.2.2 Constituents

The ICM is the most massive baryonic constituent of clusters. The fraction of the total mass in the cluster held in the ICM f_{gas} ranges between 0.05 – 0.135 for groups and clusters of mass $(10^{13} - 10^{15}) M_{\odot}$ (Pratt et al., 2009), and represents $\sim 1 - 5 \times$ the mass of stars in clusters of mass $(10^{14} - 10^{15}) M_{\odot}$ (Gonzalez et al., 2013). To first order, the constituents of the ICM are representative of the baryonic constituents of the Universe as a whole, but the presence of emission from heavier elements than those present during the primordial episode of nucleosynthesis after the Big Bang shows that the ICM was enriched with the

products of stellar nucleosynthesis after initial accretion.

Heavy elements are produced in stars and injected into the ICM. C and N come from massive and intermediate asymptotic giant branch (AGB) stars and are injected into the ICM in stellar winds; O and Mg are formed in core collapse supernovae and Fe and Ni are generated predominantly by type Ia supernovae of accreting white dwarf stars in binary systems (de Plaa, 2013; Böhringer, 2014). Clusters of galaxies (as opposed to less massive galaxy groups) are massive enough to retain essentially all of these heavy elements (Loewenstein, 2004, and references therein), and therefore the abundance of these elements in the ICM as measured using X-ray spectra can be used to test the models of star formation and evolution.

1.2.3 Heating and cooling

Gas falling into a galaxy cluster CDM halo is heated to the virial temperature of the halo by compression, by accretion shocks and by merger shocks. The specific energy of initially cold gas falling into galaxy clusters naturally leads to a final temperature equal to the virial temperature of the cluster.

1.2.3.1 Adiabatic compression

Gas clouds associated with CDM haloes are compressed by gravity into a hydrostatic equilibrium. In the absence of radiative heating and cooling, an increase in the gravitational field strength due to increasing mass compresses the gas, increasing the temperature and pressure without changing the specific entropy of the gas. Gas packets within the ICM of a cluster which are moving towards the cluster centre at subsonic speeds can undergo the same type of compressional heating.

1.2.3.2 Accretion and merger shocks

For gas packets moving at supersonic speeds with respect to the ICM, thermodynamic shocks are an important heating method. Merger shocks in clusters of galaxies are reviewed in Markevitch and Vikhlinin (2007); Kravtsov and Borgani (2012) and are a candidate source for acceleration of cosmic ray particles.

A shock is a region in which the properties of a thermodynamic fluid undergoes a discontinuous (or nearly discontinuous) change in pressure, temperature or density due to the supersonic relative speed of colliding fluids. In the context of galaxy clusters, shocks frequently occur where an infalling gas cloud collides with the ICM of a cluster.

The mean free paths between Coulomb interactions of electrons and ions in galaxy clusters are typically much shorter ($\sim 1\%$) than the cluster radius (Sarazin, 2008). In addition, evidence of a significant magnetic field in clusters (e.g. Ferretti and Giovannini, 2008), gives particles small gyro-radii so that so it is probably always reasonable to treat the ICM as a fluid (Sarazin, 2008). However, the mean free path of electrons and ions is long compared to the shock region, so the accretion shocks in clusters are collisionless,

even though the gas can be treated as collisional in general. The long mean free path allows electrons accelerated in the shock to carry the energy away from the immediate shock region (McKee, 1974; Sarazin, 2008).

Shocks may be associated with gas infalling from the surroundings of a cluster, or may be due to collision of the ICMs of two merging clusters. Shock fronts in ICM have been detected as sharp, bright X-ray features, for instance in the Bullet Cluster 1E 0657–55.8 (Clowe et al., 2006), A2146 (Russell et al., 2010) and A3376 (Akamatsu et al., 2012). They are also thought to be the source of Mpc scale regions in radio observations – *radio haloes*, for instance in A3376 (Bagchi et al., 2006; reviewed in Feretti et al., 2012).

1.2.3.3 Radiative cooling and cool cores

The high temperatures and densities reached in the ICM in some galaxy cluster centres allow substantial X-ray emission which is sufficiently rapid for gas to cool on timescales shorter than the age of the Universe. Radiative cooling outside of these central regions is typically much slower – the gas there remains hot.

For galaxy clusters, with gas particle energies $k_B T_{\text{ICM}} \gtrsim 2 \text{ keV}$, cooling is primarily through thermal Bremsstrahlung continuum, where the X-ray emissivity ϵ_X is related to the electron number density n_e and temperature by

$$\epsilon_X \propto n_e^2 T_{\text{ICM}}^{\frac{1}{2}}, \quad (1.2)$$

(for a net neutral plasma; Lea et al., 1973; Sarazin, 1986). At lower temperatures, line emission becomes important.

During galaxy cluster formation a region of ICM at the centre of the cluster may cool very efficiently and reach a cooler temperature than the rest of the cluster. These *cool cores* can be disrupted by major mergers early in the lifetime of a cluster, but are less likely to be disrupted by mergers later on (e.g. Burns et al., 2008). (50–70)% of clusters have cool cores at $z \sim 0$ (Chen et al., 2007; Dunn and Fabian, 2008; Hudson et al., 2010; Santos et al., 2010). Various parameters have been used to identify clusters which have cool cores in the literature; for instance: cooling times $t_{\text{cool}} < 0.1 t_{\text{Hubble}}$ or $t_{\text{cool}} < 10^9 \text{ yr}$ (e.g. Pratt et al., 2009); steep temperature gradients (e.g. Burns et al., 2008), or a high mass deposition rate (e.g. Chen et al., 2007). They remain very luminous at lower temperatures because their emissivity is only weakly dependent on T_{ICM} (see Equation (1.2)). The X-ray luminosity is sufficient to allow $(10–1000) M_{\odot} \text{ yr}^{-1}$ of gas to cool within clusters but the expected cold gas clouds due to this cooling have not been detected (e.g. Böhringer et al., 2002; Peterson et al., 2003, and references therein). This is known as the *classic cooling flow problem*, the solution to which – feedback from galaxies – is discussed in Section §1.4.3.2. There are rare counterexamples – McDonald et al. (2012) present an example of a very strong cooling flow and high star formation rate at the centre of a cluster in which the feedback is presumably not fully established.

1.3 Galaxy population

Galaxy clusters' most prominent members, observable using traditional optical telescopes working at (400–800) nm, are the galaxies they contain. These galaxies form within the CDM haloes which accumulate to form galaxy clusters (e.g. White and Frenk, 1991; Bower et al., 2006). Much of the evolution and appearance of galaxies is determined by their stellar populations. In clusters, their interactions with the ICM, other galaxies and the cluster gravitational potential have marked consequences for their shape and their phase-space structure, luminosity and their stellar populations. Each CDM halo may hold an extended gas cloud which feeds star formation within the galaxy, but star formation can only be supported if the gas cooling time within an individual gas halo is shorter than t_{Hubble} (e.g. Silk, 1977; Rees and Ostriker, 1977; van de Voort et al., 2011). In addition, the interstellar gas may be stripped by interactions with the ICM, stopping star formation and turning galaxies from blue to red.

Clusters contain a population of galaxies of which the majority formed and evolved over approximately the same period, in approximately the same environment – they are *coeval*. Mergers and smooth accretion introduce new galaxies – which are not coeval – later in a cluster's history. The coeval population of galaxies has regularities like a relation between their colour and brightness (magnitude) which allow it to be identified and analysed somewhat separately to newer galaxies. There is evidence discussed in Chapter 5 that infalling galaxies are stripped of their gas reservoirs and driven onto the red sequence by interactions with the ICM, but these infalling galaxies form a small proportion of the cluster galaxies overall.

1.3.1 Galaxy types and non-galaxy stellar populations in clusters

In this section, we outline the main galaxy types present in clusters, as well as light from stars unbound to galaxies. The formation of galaxies is complex and has an extensive literature of peer-reviewed articles and textbooks (e.g. Mo et al., 2010).

1.3.1.1 Spiral galaxies

Spiral galaxies are recognisable by their spiral structure when viewed face on, or their thin discs of stars, gas and dust when viewed edge on. They may also have a central bulge dominated by older, redder stars. Spiral galaxies with large amounts of cool gas in their disc or gas halo can support high star formation rates, leading to stellar populations in which a large fraction of the light is produced by young, massive stars with short lifespans. Massive stars are bluer than lower mass stars, so this type of galaxy typically appears bluer than galaxies whose stellar populations are older. Examples of spiral galaxies are shown in Figure 1.2.

1.3.1.2 Elliptical and lenticular galaxies

Elliptical and Lenticular (S0) galaxies have low star formation rates in comparison with spirals, and as a consequence redder colours. These are the most common types of galaxies found in clusters, but are less common in the field (Loveday, 1996). Examples of these galaxies are shown in Figure 1.2.

Elliptical galaxies are so called because of their shape. Simulation suggest that they are formed by mergers of progenitor galaxies (e.g. Barnes, 1989; Taranu et al., 2013).

S0 galaxies are morphologically similar to spiral galaxies in that they contain rotationally supported discs with significant amounts of dust, but have much lower star formation rates than spiral galaxies and no spiral arms.

1.3.1.3 Brightest cluster galaxies and cD galaxies

The brightest galaxy in a cluster (brightest cluster galaxy – BCG) is often, but not always a very large galaxy with an elliptical-like nucleus and extended envelope of stars on Mpc scales (e.g. Morgan et al., 1975) known as a cD galaxy. The total luminosity of the extended envelope is correlated with cluster richness (Oemler, 1976; Schombert, 1986, 1988) and where there is no strong colour gradient between the centre and edge of the envelope (Schombert, 1988). Typically, they have low star formation rates, and can grow by absorbing small galaxies in their surroundings – in a process called *galactic cannibalism*. Their positions usually coincide with the ICM density peak, but may be found off-centre in some clusters (e.g. Matthews et al., 1964; Morgan et al., 1975; Haarsma et al., 2010). Examples of clusters with cD galaxies and other not dominated by a single large galaxy are shown in Figure 1.3.

Simulations suggest that the extended halo of cD galaxies originate at redshifts $z > 1$ and comprise $\gtrsim 90\%$ of stars stripped from progenitor galaxies (e.g. Dubinski, 1998; Cooper et al., 2014). A correlation between BCG central luminosity and cluster mass in clusters without cool cores, which is present even when the BCG is not centred in the cluster potential, was noted by Haarsma et al. (2010). This connection can be interpreted as additional evidence that the stellar density in the BCG is more fundamentally linked to the mergers which formed the cluster and the BCG than later star formation once the cluster had been formed.

1.3.1.4 Intracluster light

A substantial fraction of the light from clusters – perhaps $\sim 10\%$ in some cases (e.g. Zibetti et al., 2005) – comes from stars bound in the cluster potential but not to individual galaxies, known as intracluster light (ICL).

Because the ICL is diffuse, its surface brightness is low and it is difficult to detect and study. Stars in the ICL are thought to result from tidal interactions between galaxies which strip away material – discussed in Section §1.4.2.1. It can be tricky to define the edge of a cD galaxy’s extended halo and the start of the ICL, but this may be possible by finding a change in the surface brightness profile trend (e.g. Patel et al.,

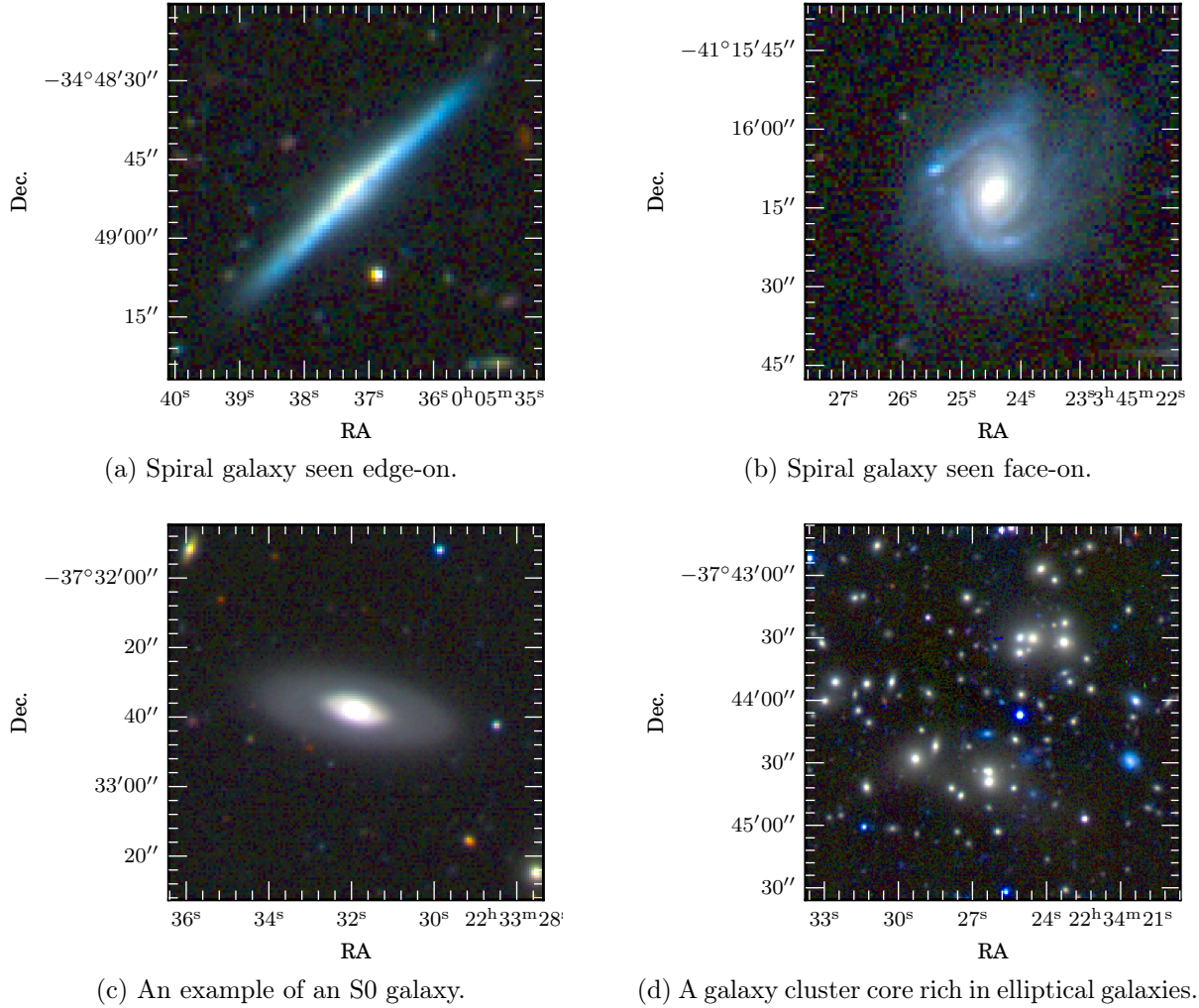
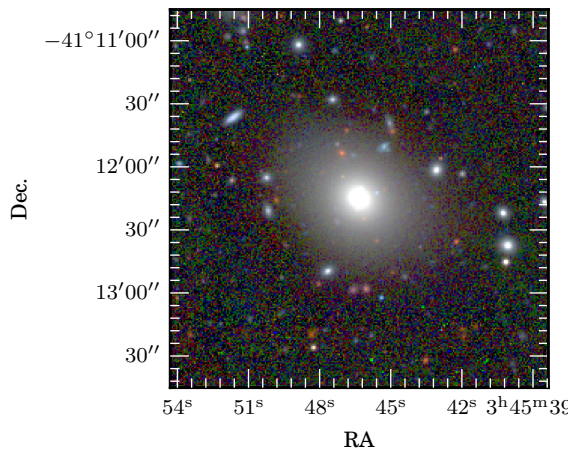
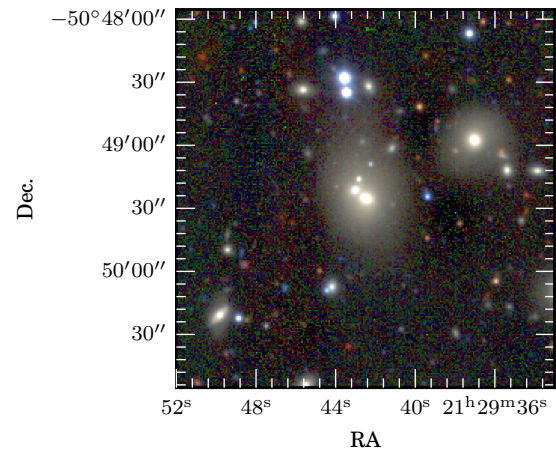


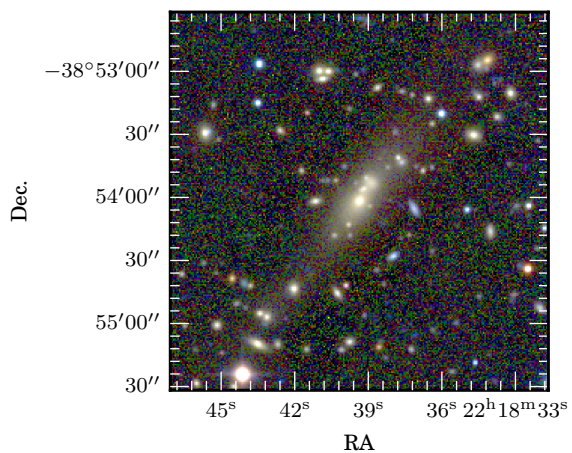
Figure 1.2: Spiral, elliptical and S0 galaxies observed in the REXCESS survey. The images reveal a clear difference in colour between the bluer spirals and redder elliptical/S0 galaxies. The solid black regions are where the brightest stars have been masked using the method described in Section §4.3.1, and the colours have been enhanced. Compositing of *BVR* frames into colour images was carried out using STIFF (Bertin, 2012).



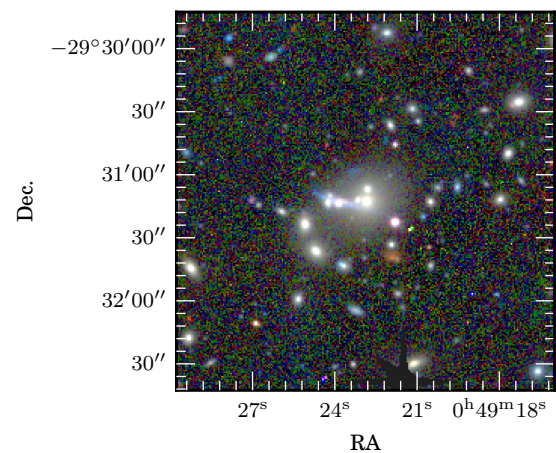
(a) Cluster centre with a single prominent galaxy.



(b) Cluster centre with two bright galaxies.



(c) Elongated BCG.



(d) Cluster centre where the BCG is clearly defined, but there are a number of relatively bright galaxies around it.

Figure 1.3: Images of galaxy cluster centres with and without cD type BCGs observed in the REXCESS survey. The solid black regions are where the brightest stars have been masked using the method described in Section §4.3.1, and the colours have been enhanced.

2006). An example of a cluster centre with a substantial diffuse light component is shown in Figure 1.3b. The ICL does not form a major part of the analyses in Chapter 4 or Chapter 5.

1.3.2 Observed galaxy distribution

1.3.2.1 The cosmic web and cluster environment

Wide field galaxy redshift surveys reveal a *cosmic web* – a network of filaments draped through space, with galaxy clusters and superclusters at the nodes (see Figure 1.1; Stoughton et al. 2002; Zehavi et al. 2011). The largest identifiable structures, like the Sloan Great Wall which has length 4.2×10^8 pc (Gott et al., 2005), or the structure detected by Horváth et al. (2014) traced by gamma-ray bursts in the redshift range $1.6 < z < 2.1$ with length $(2 \times 10^9 - 3 \times 10^9)$ pc, show that the minimum length scales on which the Universe can be considered homogenous and isotropic are at least on the scales of hundreds of Mpc, and possibly more.

Galaxy clusters associated with high density regions of the cosmic web experience more frequent mergers (Chon et al., 2013), which can lead to changes in their ICM distribution and galaxy populations compared to clusters in lower density regions (e.g. Böhringer et al., 2001b; Braglia et al., 2009). The influence of cluster outskirts on the presence of substructure in the ICM is investigated in Chapter 5.

1.3.2.2 Luminosity function of clusters

The distribution of galaxy luminosities – the *galaxy luminosity function* – is redshift dependent, related to the halo mass function (dominated by the CDM hierarchical clustering) and is also dependent on processes which regulate star formation.

The brightness/luminous flux f (with base units W m^{-2}) of a galaxy observed from Earth is related to its intrinsic luminosity L and the *luminosity distance* D_L by

$$f = \frac{L}{4\pi D_L^2}. \quad (1.3)$$

For nearby objects, e.g. stars within the Milky Way, the D_L is well approximated by the physical distance to the object. For objects at cosmological distance the curvature of space, redshift and time dilation must also be taken into account (Hogg, 1999).

By measuring the luminosities of a population of galaxies at a common distance – i.e. those in a galaxy cluster – correcting for the change in brightness of each galaxy due to their different distances in order to investigate the distribution of intrinsic luminosities is not required (e.g. Oemler, 1974).

A common analytic function used to characterise the luminosity function of galaxies is the *Schechter function* (Schechter, 1976) based on the halo mass distribution of Press and Schechter (1974) but including a correction compared to the halo mass distribution

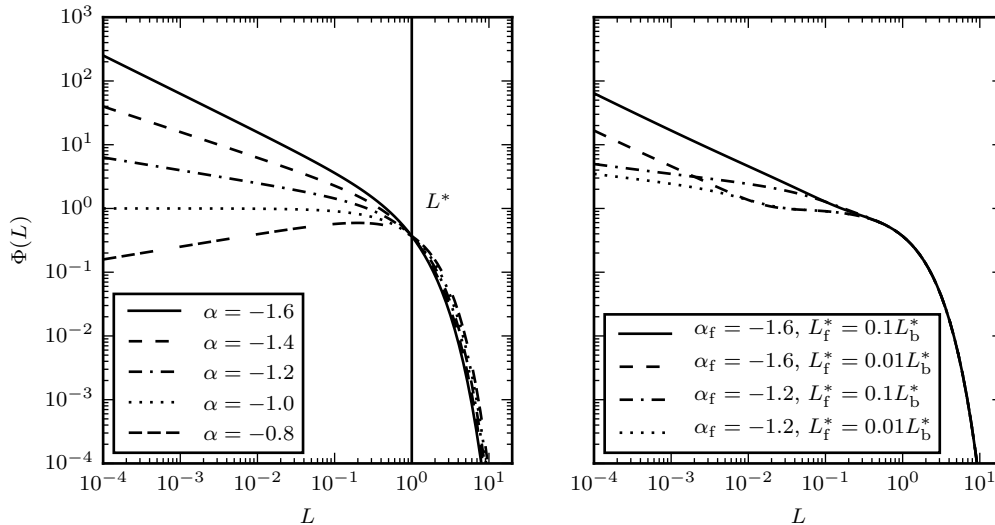


Figure 1.4: Example luminosity functions. The left panel shows single Schechter function models [Equation (1.4)] with a fixed characteristic luminosity $L^* = 1$ and a range of slopes α . The right panel shows double Schechter function models [Equation (1.5)], with a range of L_f^* and α_f where $L_b^* = 1$ and $\alpha_b = -1$ are fixed.

for faint objects. For galaxies of luminosity L , the single Schechter function is

$$\Phi(L) = \phi \left(\frac{L}{L^*} \right)^\alpha \exp \left(\frac{-L}{L^*} \right), \quad (1.4)$$

where L^* is the characteristic *Schechter luminosity* of the exponential fall-off for bright objects, α is the slope for fainter objects, and ϕ is a normalisation. More recently, improvements in image depth and galaxy catalogue completeness for fainter objects – dwarf galaxies – has shown that a second component for fainter magnitudes with an independent slope and characteristic luminosity is required in some cases. The double Schechter function is defined as

$$\Phi_{\text{double}}(L) = \phi \left[\left(\frac{L}{L_b^*} \right)^{\alpha_b} \exp \left(\frac{-L}{L_b^*} \right) + \left(\frac{L_b^*}{L_f^*} \right) \left(\frac{L}{L_f^*} \right)^{\alpha_f} \exp \left(\frac{-L}{L_f^*} \right) \right], \quad (1.5)$$

where L_b^* and L_f^* are characteristic fall-off luminosities for the bright and faint parts of the function, and α_b and α_f are the bright and faint slope parameters (e.g. Popesso et al., 2006). Example luminosity functions with a range of parameters are shown in Figure 1.4.

1.3.2.3 Number counts of field galaxies

The luminosity distribution of field galaxies not obviously associated with clusters or groups can be studied to reveal information about the evolution of the galaxy population

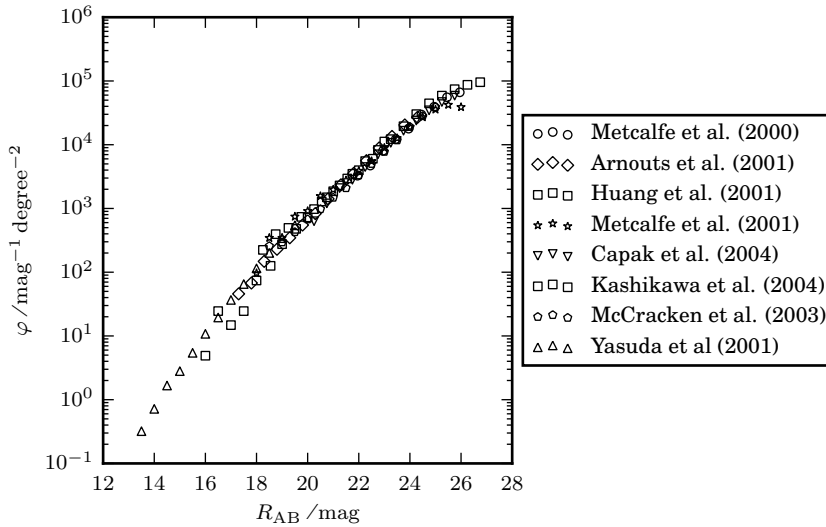


Figure 1.5: Galaxy number counts with respect to observed magnitude. These data were compiled by Metcalfe (2010).

through time. The number density on the sky of galaxies with a particular observed flux arises from the integration of the luminosity function along the line of sight, including the f - L dependence Equation (1.3). This count distribution of galaxies of different brightness is referred to as the galaxy *number counts* distribution. The form of the number counts distribution depends on the cosmology, and on the formation and evolution of galaxies within the cosmic web. The count distribution is variable for different directions on the sky – a phenomenon known as *cosmic variance* – as shown in Figure 1.5, and the variance reduces with increasing survey area. The survey areas of the data shown here are: 4.7 arcmin² (Hubble Deep Fields; Metcalfe et al., 2001; Capak et al., 2004); 49 arcmin² (William Herschel Deep Field; McCracken et al., 2000; Metcalfe et al., 2001); 400 arcmin² (Chandra Deep Field South; Arnouts et al., 2001); 840 arcmin² (Calar Alto Deep Imaging Survey; Huang et al., 2001); 918 arcmin² (Subaru Deep Field; Kashikawa et al., 2004); 1122 arcmin² (VIRMOS 0226-04 deep field; McCracken et al., 2003); and 440 degree² (SDSS Commissioning data; Yasuda et al., 2001). The scatter in this group of measurements is $\sim 2\times$. We use an empirical fit to number counts data in Chapter 4 to quantify the field galaxy distribution within our galaxy cluster observations.

1.3.2.4 Colour–magnitude relation and the red sequence

Elliptical galaxies in galaxy clusters have similar red colours (Butcher and Oemler, 1978a) which vary with the galaxy brightness. It is customary to measure astronomical objects'

observed brightness in magnitudes M , where

$$M_X = -2.5 \log_{10} \left(\frac{f_X}{f_{0X}} \right), \quad (1.6)$$

where X denotes the filter band, and f_{0X} is the flux for a reference object which would be measured using the same filter.² Historically, the zero point f_{0X} was based on the star Vega, but more recently magnitudes normalised against a precisely defined spectral flux density of $3.631 \times 10^{-23} \text{ W Hz}^{-1} \text{ m}^{-2}$ – AB system magnitudes – have become common and practical (the AB magnitude system is specified in Oke and Gunn, 1983). The photometric colour C_{X-Y} is the difference in magnitude measured in two filters X and Y ,

$$C_{X-Y} = M_X - M_Y. \quad (1.7)$$

The colours of elliptical galaxies within clusters become bluer as their magnitudes increase, and scatter tightly around a line in colour–magnitude space. These galaxies form a so-called *red sequence*, which has similar slope and intercept for clusters at approximately the same redshift (e.g. the Coma and Virgo clusters; Bower et al., 1992). Example colour–magnitude plots showing the red sequence are given in Figure 1.6. The observed red sequence shifts in colour space with redshift, due to the red-shifting of the break feature and due to stellar population evolution. This property can be used to detect galaxy clusters as over-densities in colour–magnitude space and to estimate their redshifts (Gladders and Yee, 2000, 2005). The colour–magnitude relation can be detected when the 400 nm spectral break (4000 Å), typical of elliptical galaxy spectra, is bracketed (e.g. Kauffmann et al., 2003) by X and Y .

Two possible primary reasons for the slope of the relation are posited in the literature: stellar population age and metallicity. Old stellar populations have predominantly redder stars with longer lifespans; the blue stars which are initially very bright come to the end of their lives on short time scales and lead to a redder mean colour for the whole population. The lifetime for a high mass $25 M_{\odot}$ star is $\sim 7 \times 10^6$ yr, compared to $\sim 10^{10}$ yr for a $1 M_{\odot}$ star (Pols et al., 1998). However, Worthey (1994) showed that combined spectrum from one stellar population is identical by many measures to a population which is twice as old and has half the amount of heavy elements generated in stars after the primordial nucleosynthesis. The presence of these heavier elements in stellar atmospheres shifts energy from high to low frequencies by absorption and emission at lower frequencies.

In Section §1.4.3 we outline processes which strip cool gas from galaxies on short timescales and quench their star formation, driving blue galaxies onto the red sequence (i.e. changing them from galaxy types with gas reservoirs to those types without). Blue galaxies falling into clusters do not have time to virialise into the cluster potential before they are stripped of the cool gas which fuels star formation and allows the short-lived population of blue stars to be replenished. This effect is investigated in Chapter 4 and

²The human eye has a logarithmic response to light which leads naturally to a logarithmic scale for measuring stellar magnitudes.

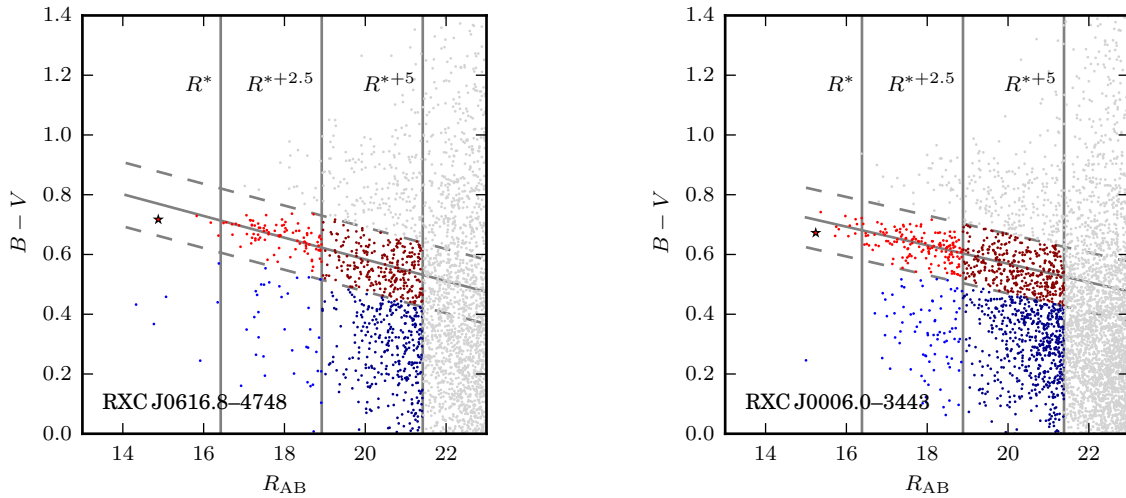


Figure 1.6: Red sequences in the REXCESS sample. The dashed lines show the upper and lower limits of the red sequence. The vertical lines labelled R^* , $R^{*+2.5}$ and R^{*+5} mark R magnitudes corresponding to L^* , $0.1L^*$ and $0.01L^*$ respectively. The star marks the BCG.

exploited in Chapter 5 to detect pre- and post-merger clumps of galaxies falling into clusters.

1.3.2.5 The distribution of red and blue galaxies

There are differences in the way that red vs. blue galaxies are arranged in galaxy clusters and the field. In Chapter 4 these differences are investigated statistically in different types of clusters, and in Chapter 5 these differences are investigated on a cluster-to-cluster basis.

The observation that there is a higher fraction of elliptical galaxies in regions with a high density of galaxies than in lower density environments of the field is known as the *morphology–density relation* (e.g. van den Bergh, 1960; Oemler, 1974; Dressler, 1980). This extends all the way to the densest environments – the centres of compact rich clusters of galaxies or those dominated by cD galaxies, where the red galaxy fraction f_r approaches 1. The *Butcher–Oemler effect* is related, and describes the change in the fraction of blue galaxies in the central (highly dense) regions of galaxy clusters from an appreciable fraction $\frac{1}{3} - \frac{1}{2}$ at intermediate redshifts $z \gtrsim 0.3$ to approximately zero at $z = 0$ (Butcher and Oemler, 1978a,b).

1.4 Galaxies, ICM and dark matter – an interlinked system

Both the population of galaxies within a cluster and the particles which form the dark matter halo have long mean free paths within clusters, so they can be treated as collisionless fluids. In these, the major drivers of relaxation are collisionless effects due to the rapidly changing gravitational potential due to the evolution of the whole system, rather than individual particle–particle or galaxy–galaxy interactions, discussed in Section §1.4.1. The collisionless shocks seen in ICM–ICM interactions of merging clusters are discussed in Section §1.2.3.2.

The most profound and striking changes to galaxy morphology occur during galaxy–galaxy interactions, in which galaxies’ morphologies can be altered very rapidly, outbursts of star formation (starbursts) can occur and galaxies can be completely disrupted. In the cluster environment, the density of galaxies is higher than in the field, such that close-encounters between galaxies in clusters are much more frequent. These are discussed in Section §1.4.2.

Interactions between galaxies and the ICM may be less spectacular, but are continuous and have a huge impact on the formation of stars within galaxies. Thermodynamic and chemical feedback from galaxies into the ICM by stellar winds, supernovae, and astrophysical jets emitted by accreting supermassive black holes which grow in tandem with the stellar bulges of galaxies, makes the evolution of cluster galaxies and ICM a complex interlinked problem. Since the density of gas in clusters is higher than in the Universe in general, the effects of interactions between galaxies and the surrounding gas unbound to the galaxy are stronger in clusters. These are discussed in Section §1.4.3.

1.4.1 Collisionless interactions – violent relaxation

Lynden-Bell (1967) coined the term *violent relaxation* for one mode of collapse in which the gravitational potential due to the whole population of particles acts to redistribute energies, rather than because of pair-wise collisional interactions. During collapse of an initially gravitationally bound approximately uniform density sphere of particles with zero velocity where each particle’s energy is identical to its initial gravitational potential, requires that gravitational potential energy be converted into kinetic energy. As the collection of particles collapses and reaches very high densities in the distribution centre, there exists a rapidly changing anisotropic gravitational potential field with strong gradients, in which individual particles are accelerated and decelerated, not by individual particle–particle interactions but by the field as a whole. Some of the particles attain high energies and end up on trajectories out of the dense central region, leaving a population of particles with lower energies in the centre. The timescale for violent relaxation is approximately equal to the free fall time for the system,

$$t_{\text{free-fall}} \simeq \left(\frac{3\pi}{32G\bar{\rho}} \right)^{\frac{1}{2}} = 4.7 \times 10^9 \text{ yr} \left(\frac{D}{1 \text{ Mpc}} \right)^{\frac{3}{2}} \left(\frac{M}{10^{14} \text{ M}_{\odot}} \right)^{-\frac{1}{2}}, \quad (1.8)$$

which is longer than Equation (1.1) but still much shorter than t_{Hubble} .

Lynden-Bell's statistical mechanical treatment was extended over the following decades using increasingly realistic numerical simulations. Within hierarchical clustering scenarios in an expanding space-time (discussed in White, 1996), the picture is more complicated in that the epoch of formation of a mass distribution has an effect on the final concentration. The seminal paper Navarro et al. (1997) describes a universal density profile found in simulations of hierarchical cold dark matter halo formation – the NFW profile – which depends on formation time and total mass. Direct tests of the NFW profile form can be performed using weak gravitational lensing studies. Gravitational lensing occurs when light passes through a region of curved space-time (due to a nearby massive object) and is deflected. In the weak lensing regime, images of distant galaxies which are a short projected distance from a massive galaxy cluster are elongated, introducing correlations in the observed shear of galaxies which is not seen in field galaxies in general (reviewed in Hoekstra and Jain, 2008). The pattern can be used to reconstruct the projected mass distribution, which in turn can be used in statistical tests of mass profiles. These investigations are ongoing and not yet conclusive. Major advances are expected to be made when the Large Synoptic Survey Telescope (LSST) start to operate within the next decade. Baryonic processes also shape the inner parts of cold dark matter haloes, but these have only recently been included in cosmological simulations (e.g. Vogelsberger et al., 2014b).

1.4.2 Galaxy–galaxy interactions

1.4.2.1 Harassment

Although the mean free path of galaxies in clusters is long enough that dynamical friction is inefficient in virialising their infall energy, close encounters between galaxies in cluster centres are common enough that significant effects due to galaxy–galaxy interactions can be identified.

Tidal forces between extended objects like galaxies are able to increase their internal energy and cause morphological change (Richstone, 1976). Farouki and Shapiro (1981) investigated simulated close encounters of a disk galaxy with the centre of a cD cluster and found that the outer galaxy disk was seriously disrupted whereas the nuclear bulge was essentially unperturbed. Using these data, they infer that any extended gas haloes feeding gas for star formation onto the disk would also be susceptible to disruption. They also noted that if the galaxy were embedded in a stabilising halo which could also be tidally disrupted, this may have profound effects on the evolution of the disk.

More complex simulations (e.g. Moore et al., 1996, 1998) showed that the *harassment* of small spiral galaxies caused them to undergo a transient phase of rapid star formation, before transforming into spheroidal types. The key parameter for survival in this type of environment is the density of the galaxy being disrupted – higher density galaxies are less affected. Tests of the relative importance of the tidal forces arising from the cluster potential as a whole and with the dark matter halo plus a population of galaxies showed

that morphological change was substantially more marked in the case with the galaxy population.

1.4.2.2 Dynamical friction and cannibalism

Within a population of particles interacting gravitationally, the particle–particle interactions lead to the equipartitioning of energy (equal energy per particle) by a process called *dynamical friction*, described by Chandrasekhar (1943b,a,c). This was proposed as a possible process by which bright satellites of cD galaxies could be slowed to speeds below the velocity dispersion of the satellite, and then accreted into the cD (Ostriker and Hausman, 1977), a process known as *cannibalism*. However, the equipartitioning of energy would lead to higher velocity dispersions for lower mass galaxies which are not seen in reality. Dubinski (1998) showed using simulations that dynamical friction has a minor effect over the whole lifetime of a cluster, and that exceptionally large bright galaxies can form naturally during the early stages of cluster evolution through the merger of several massive progenitors.

1.4.2.3 Tidal disruption and starbursts

The tidal effects unleashed by close encounters between galaxies can lead to significant morphological and stellar population changes. Mergers involving spiral galaxies are thought to drive outbursts of star formation – *starbursts* – at low redshift (e.g. Duc et al., 1997, and references therein), by driving gas towards the disc centre where it can fuel star formation Barnes and Hernquist (1998). The galaxy–ICM interactions discussed in Section §1.4.3 make this type of interaction increasingly rare towards the centres of clusters because of the reduction in the available gas. Tidal disruption due to other galaxies (e.g. Merritt, 1983) or due to the cluster potential (e.g. Byrd and Valtonen, 1990; Valluri, 1993) can lead to stars being stripped from a galaxy without disrupting it completely, providing a source for the ICL. Tidal interactions are also required for the dynamical modifications required for conversions from spiral to lenticular galaxy types and may occur in large scale structures like filaments, before galaxies are accreted into clusters (Cortese et al., 2007).

1.4.3 Galaxy–ICM interactions

Modes of gas accretion and cooling in clusters are outlined in Section §1.2.3. These cooling processes provide fuel for the active galactic nuclei described in Section §1.4.3.2. The same processes occur on the scale of individual galaxies which are moving through the ICM, each embedded in its own CDM sub-halo of the cluster (at least until the halo dissolves), but proceed differently due to the different mass scale and cooling times involved. The interaction of the ICM with the gas haloes of individual galaxies makes clusters rather hostile to the retention of individual gas haloes. Whenever galaxy gas haloes are stripped by pressure from the ICM (*ram pressure stripping*) or have low cooling rates because their

entropy is too high (*strangulation*), star formation cannot proceed and blue galaxy types become red (Larson et al., 1980). We investigate the consequential increased fraction of red galaxies towards the centres of massive clusters in Chapter 4.

Material also moves in the other direction. Supernovae and stars inside and outside of galaxies inject material into the interstellar medium (ISM) and potentially the ICM (e.g. Veilleux et al., 2005). These stellar winds are thermodynamically much less important than AGN feedback (Benson et al., 2003; Bower et al., 2006), but they are important in producing the heavy elements which are seen in galaxy cluster spectra (Sarazin, 1986).

In the following sections, we outline the major physical interactions between galaxies and the ICM.

1.4.3.1 Ram pressure stripping

As a galaxy moves through a cluster, the ram pressure due to the relative ICM–galaxy gas halo velocity serves to strip weakly bound gas from the galaxy. In the initial formulation proposed by Gunn and Gott (1972) the galaxy was modelled as a face-on disk moving through a uniform ICM. The ram pressure in this case is $P_{\text{ram}} = \rho_{\text{ICM}} v_{\text{orbital}}^2$ where ρ_{ICM} is the ICM density and v_{orbital} is the velocity of the disc with respect to the ICM. The restoring force per unit area is $P_{\text{restoring}} = 2\pi G S_* S_{\text{gas}}$ where S_{gas} and S_* are the gas and stellar surface densities in the disk respectively. Gas stripping will occur if $P_{\text{ram}} > P_{\text{restoring}}$. The orbital velocity of objects within clusters is dependent on the cluster mass M by $v_{\text{orbital}}^2 \propto M$, so ram pressure stripping is expected to be more rapid in the most massive clusters.

The stripping of gas from spheroidal configurations is different in that more distant gas from the centre is more weakly bound and ablated first (e.g. Gisler, 1976; Sarazin, 1979; McCarthy et al., 2008). McCarthy et al. (2008) investigated a suite of simulations of ram pressure stripping with spheroidal haloes in galaxy clusters and massive groups. The simulations showed that for realistic orbits and gas cloud parameters, $\sim 30\%$ of the original gas halo of a galaxy may remain after $\sim 10^{10}$ yr, rather than the stripping process being complete and instantaneous as is typically assumed (e.g. Cole et al., 1994). They found that a modified ram pressure stripping criterion with a single tuneable parameter gave a good description of the data. Their criterion was $P_{\text{ram}}(t) > \alpha \frac{GM_{\text{gal}}(<r)\rho_{\text{gas}}(r)}{r}$, where α is a tuneable constant parameter of order 1, r is the distance from the galaxy centre, the gas density distribution is ρ_{gas} , the total enclosed galaxy mass within radius r is $M_{\text{gal}}(<r)$, and P_{ram} is dependent on the time t allowing for evolution of the galaxy and cluster gas distribution and for the orbit of the galaxy within the cluster. Only a small fraction of cases with extreme parameters were not well described by the criterion, such as cases where a galaxy has mass 10% the mass of the cluster and an extremely non-radial orbit.

1.4.3.2 Feedback from active galactic nuclei

Clusters have sufficient X-ray luminosity to allow $(10 - 1000) M_{\odot} \text{ yr}^{-1}$ of gas to cool. This cool gas is largely unseen (discussed in Section §1.2.3.3). Galaxies appear to evolve in tandem with supermassive black holes (SMBH) at their centres, which have masses in the range $\sim \frac{1}{1000} \times$ of the mass of the galaxy central bulge (e.g. Häring and Rix, 2004). These SMBH – operating in the kinetic/radio jet mode – are associated with astrophysical jets which can reach \sim Mpc scales and convert up to $\sim 10\%$ of the mass-energy of accreted matter into kinetic energy (Allen et al., 2006), approaching theoretical limits on mass-to-energy conversion efficiency (reviewed in Begelman et al., 1984; Fabian, 2012). These extremely luminous sources at the centres of galaxies are known as active galactic nuclei (AGN). A second mode of energy release from AGN – the radiative/quasar mode – is thought to be important at $z \sim 2 - 3$ when galaxies were gas rich, but is less important at the lower redshifts we consider.

If SMBH accrete even a small fraction of the inflowing gas $< 1\%$, their high mass-to-energy conversion efficiency means that jet power is sufficient to balance the X-ray cooling. The expected sufficiency of AGN feedback is borne out by observations (Böhringer et al., 2002). Since the accretion onto the SMBH is due to gas being accreted from the halo (which is also being heated), this coupling causes a feedback loop which regulates the gas flow, leading to a balance between the AGN heating and radiative cooling (reviewed in Peterson and Fabian, 2006; McNamara and Nulsen, 2007; Cattaneo et al., 2009). In addition to their thermodynamic influence, AGN jets are able to displace matter from the centres of clusters to their edges, including gas enriched with heavy elements (Fabjan et al., 2010; Barai et al., 2011).

Bower et al. (2006) used galaxy formation and evolution simulations to test a scenario in which gas cooling into a galaxy is accreted onto the central SMBH (as proposed by Granato et al., 2004; Croton et al., 2006). The energy emitted from AGN back into galaxy gas haloes keeps the gas entropy high, counteracting cooling, and restricting the replenishment of cool gas for star formation. They found that this naturally causes the break in the galaxy luminosity function shown in Figure 1.4 and provides an explanation for the observed reduction in star formation in massive galaxies after $z = 1$ (Cowie et al., 1996; Juneau et al., 2005).

1.5 Mergers, smooth accretion and substructure

A galaxy cluster has *substructure* in the context of this work if it contains two or more identifiable clumps of galaxies and/or gas. The specification of ‘identifiable’ is not trivial, and is explored in Chapter 5. All galaxy clusters contain several galaxies, which are (sub-)structures in their own right, but the definition we use is trying to address the existence of formerly independent galaxy groups or galaxy clusters which may be bound to – but not yet assimilated into – the larger structure. We define the term *clump* to denote a group of galaxies, possibly with associated gas, regardless of its mass. This encompasses

infalling and merging galaxy groups and clusters, both before and after they lose their gas haloes.

Galaxy clusters observed at low redshift continue to accrete matter, by smooth accretion from their surroundings or along filaments, or during violent mergers where they consume another galaxy group or cluster. Infalling galaxies, groups and clusters are associated with dark matter and gas haloes, and the different ways the gas and galaxies interact with the dark matter, ICM and galaxy distribution of the main cluster lead to complementary observational signals, which are different before and after the merger.

This dissertation is a study of the evidence of this accretion/interaction scenario. In Chapter 4, we show evidence that gas is stripped very rapidly from galaxies on infall trajectories into cluster and that regions with the highest gas densities have either very sparse or entirely absent blue populations. In Chapter 5, we extend this analysis into 2D and demonstrate that there is little resemblance between the distribution of red vs. blue galaxies within clusters, but that independent clumps rich in blue galaxies and sometimes with measurable gas can be seen outside r_{500} . A merger/accretion scenario, coupled with galaxy-ICM interactions which tend to turn blue galaxies red, gives a simple, elegant framework within which these observations make sense.

1.5.1 Identification of pre-, current- and post-merger states, and smooth accretion

There is good evidence from observations of the Bullet cluster that the gas component of infalling clusters is stripped from its dark matter halo very rapidly, whereas the two progenitor total mass distributions determined using gravitational lensing, which are also traced by the galaxy distributions, retain their identities for longer (e.g. Clowe et al., 2006). If we assume that all infalling clumps – not just very massive infalling clusters – retain their spatial identities for longer than their associated gas, we may be able to classify clusters as pre-, current- and post-mergers. It may also be possible to identify regions of enhanced smooth accretion, since these are associated with galaxies not yet stripped of their gas haloes and without a spherically symmetric clump structure. This is our fundamental hypothesis of merger state identification.

If it can be determined if a clump is still associated with a gas cloud, this may be taken as evidence that it has not yet begun to merge. In Chapter 5 we use X-ray observations to try to detect these un-merged gas haloes. In low mass infalling clusters, the virial temperature of the gas may be too low to detect using our observations, however it may still be possible to show that a merging clump contains a significant population of galaxies still forming stars. As discussed in Section §1.4.3, the cool gas which fuels star formation is ablated by ram pressure stripping within clusters, so a high blue galaxy fraction is suggestive of a pre-merger.

Current- and post-merger states are characterised by shocks, disrupted gas distributions and potentially starbursts. A fraction of clusters show evidence of shock regions (discussed in Section §1.2.3.2) due to the interaction of the gas in an infalling clump

interacting with the ICM of the primary cluster. These may be more common than observed but not be visible because of low luminosity or unfavourable orientation. Clusters with asymmetrical gas distributions are more common. As gas relaxes to follow the CDM dominated potential over time (see Section §1.2) this asymmetry reduces. A very disrupted ICM distribution may be taken as evidence of a current merger because the ICM relaxes on relatively short timescales. Additional evidence for this may be available from the ellipticity of the gas distribution – since the gas distribution traces the CDM dominated potential, it may show up as the elliptical shape which would be expected after the injection of momentum along a merger axis.

Collisionless galaxies have longer relaxation times than the collisional ICM (discussed in Section §1.4.1), and therefore identification of cases where the galaxy distribution has an asymmetrical/clumpy appearance whilst the ICM distribution is more relaxed and regular may be taken as evidence of a relatively recent merger. During the galaxy–galaxy interactions which also occur in mergers, tidal forces may cause rapid star formation (starbursts) in cluster galaxies if they already have cool gas haloes which are sufficiently tightly bound not to be stripped away by the ICM (discussed in Section §1.4.2.3; observed by Poggianti et al., 2009; Ma et al., 2010). This type of interaction is expected to be rare at low redshifts because of the rarity of cold gas clouds.

Galaxies undergoing smooth accretion along filaments may retain their gas haloes and increased star formation rates for much longer than those within the ICM. A series of blue galaxies without an obvious clump structure may be observed in this mode of accretion (e.g. Fadda et al., 2008).

Chapter 2

REXCESS: optical and X-ray galaxy cluster observations

It is a capital mistake to theorize before one has data. Insensibly one begins to twist facts to suit theories, instead of theories to suit facts.

Arthur Conan Doyle, *The Adventures of Sherlock Holmes*, 1892

It became clear that systematic surveys of galaxy clusters at a range of z would be required to fulfil their potential for studies of astrophysics and cosmology, and so a concerted effort was made to set up X-ray observing programmes using the X-ray telescopes *XMM-Newton* and *Chandra*, which both launched in 1999.

The *ROSAT* All-Sky Survey (RASS) was used to produce the Northern *ROSAT* All-Sky (NORAS; Böhringer et al., 2000) and *ROSAT*-ESO Flux-Limited X-ray (REFLEX; Böhringer et al., 2001a) galaxy cluster surveys. Several subsamples from NORAS and REFLEX were selected and followed up using *XMM-Newton* and *Chandra*: the Highest X-ray Flux Galaxy Cluster Sample (HIFLUGCS; Reiprich and Böhringer, 2002), a survey of 63 of the brightest clusters at $z \lesssim 0.1$ (with a few extremely luminous exceptions up to $z = 0.2010$); the Representative *XMM-Newton* Cluster Structure Survey (REXCESS; Böhringer et al., 2007), a survey of 33 clusters in the range $0.055 < z < 0.183$ which is the subject of this dissertation; and the *ROSAT*-ESO Flux-Limited Distant X-ray Luminous survey (REFLEX-DXL; Zhang et al., 2006), a sample of clusters in the range $0.27 < z < 0.31$. These were to be complementary to further analysis of surveys based on the systematic analysis of the archive of *ROSAT* pointed observations: the 160 degree² *ROSAT* Survey (Vikhlinin et al., 1998a,b) in the range $0.015 < z \lesssim 0.8$ and the *ROSAT* Deep Cluster Survey (RDCS; Rosati et al., 1998) in the range $0.05 < z < 0.8$.

One key issue when using X-ray observations to investigate cosmology, is that the most accessible observable – X-ray luminosity L_X – has a large scatter with respect to the cluster mass M which is the quantity of real interest. In addition, the *scaling relation*

which links M and L_X is complicated by the structure and history of each cluster – whether it has undergone a recent merger, or has a cool core. A good calibration of the relationship between these two parameters, in a way which was unbiased with respect to the appearance of clusters, would allow better cosmological constraints to be calculated using surveys where the observations were not deep or detailed enough to measure and correct for effects due the structure of individual clusters.

The REXCESS survey was designed to be agnostic to structure during the selection process, and therefore be a representative sample which could be used to calibrate scaling relations. The survey methodology is described in detail in Böhringer et al. (2007). It was also designed with the properties of *XMM-Newton* in mind so in Section §2.1 we outline the telescope properties before describing the survey itself. A description of the optical follow-up dataset collection and reduction is described in Section §2.2. The galaxy catalogue creation is described in Section §2.3, and the calibration of the catalogues is described in Section §2.4.

2.1 REXCESS and *XMM-Newton*

2.1.1 *XMM-Newton*

The European Space Agency’s X-ray Multi-Mirror Mission, known as *XMM-Newton*, is an X-ray telescope orbiting the Earth at geocentric radii r_{\oplus} between $(7 \times 10^6 - 1.14 \times 10^8)$ m with an orbital period of ~ 48 h (Jansen et al., 2001).

It carries three Wolter telescopes, each consisting of 58 nested mirrors, which focus X-ray photons onto imaging and spectroscopic detectors by reflecting them at glancing angles. We use data from the three European Photon Imaging Camera (EPIC) detectors: two metal oxide semiconductor charge-coupled-device (CCD) arrays *MOS1* and *MOS2*, and the pn-junction based detector *PN*. Each of these is served by one of the telescopes. Two Reflection Grating Spectrometers (RGS) share telescopes with *MOS1* and *MOS2*, and $\sim 50\%$ of the light entering the telescope is directed away from the MOS to the RGS detectors (den Herder et al., 2001).

The *field of view* (FOV) is $\sim 30'$ across. The pattern into which light from a point source like an AGN or star is focussed is called the *point spread function* (PSF). For photons with energies (1.5–9) keV, this has full width at half maximum FWHM $\sim (5-6)''$ at the image centre on the optical axis, but this size increases substantially towards the edge of the FOV.

The MOS and PN detectors detect the energies of individual photons by making a series of short integrations, reading out the array each integration and locating groups of pixels where an X-ray photon has deposited charge. The *pattern* of energy deposition is measured and can be used to discriminate partly between photons and spurious detections from non-X-ray sources.

Photons with energies (0.15–15) keV can be detected with an energy resolution of $\frac{E}{\delta E} \sim 20-50$ [FWHM $\sim (20-200)$ eV]. At these energies, the MOS detectors have

quantum efficiency above 0.1, and PN above 0.6 (Strüder et al., 2001; Turner et al., 2001). The EPIC cameras' energy range means they are well suited to observations of massive galaxy clusters with ICM temperatures $k_{\text{B}}T_{\text{ICM}} > 2 \text{ keV}$. As each photon is recorded independently, measurements of the rate of photon incidence over time, images in different bands as well as spectra of moderate resolution can be drawn from the same observations.

There is a finite chance that two or more photons will deposit their energy in the same region during one short exposure – *pile-up*, and this can be detected by measuring the rate of different detection patterns, since these are distributed differently when piled-up compared with under ordinary conditions. This effect is important for bright sources with high count rates, but less important for distant galaxy clusters. Pile-up is also dependent on the spectrum of photon energies and position in the FOV because both of these parameters affect the PSF.

2.1.2 XMM-Newton backgrounds

XMM-Newton observations are affected by several background sources, which vary with time and telescope pointing. X-ray backgrounds include thermal sources (e.g. hot gas), unresolved cosmological point sources like AGN, Solar wind charge exchange and spurious reflections from outside the field of view. Particles can also interact with XMM-Newton's detectors. The main source is soft protons from Solar flares, but X-ray fluorescence of the telescope structure due to cosmic ray impacts is also significant.

The particle and fluorescent backgrounds are not focussed by the telescopes. However, they do interact with the structure of the spacecraft, which means that their distribution is not uniform across the exposed field of view. A model of the distribution of the detections from these particles can be found by making observations with the detector obscured by a filter which blocks essentially all the X-rays. The EPIC detectors are designed such that there is a shielded region which is never exposed to the X-rays focussed by the telescopes. It is possible to make a reasonable estimate of the particle background distribution by scaling the *filter-wheel closed observations* using the detection rates measured in the unexposed regions during science observations.

Observation periods with very high soft proton background rates must be discarded. These periods can usually be detected by analysing the change of the total count rate with time (light-curve) for the whole observation duration, looking for periods where the count is spuriously high. In cases where the soft proton background is very high for most or all of the duration of an observation, the whole observation must be repeated.

2.1.3 Survey and observation parameters

The light collecting power, sensitivity, spectral resolution and FOV of the EPIC detectors can be used to define a set of constraints on the properties of a systematic galaxy cluster survey. For good characterisation of the dark matter, the FOV needed to cover the region within r_{500} . Simulations had shown that the ICM would be detectable within this

radius, and that observations would allow good characterisation of the cluster dark matter (Evrard et al., 1996). In addition, the FOV must include a region outside of r_{500} , which is needed to allow good background characterisation. This had to be balanced with ensuring a reasonable X-ray flux within an attainable observation time, since several thousand X-ray photons from a galaxy cluster are required for reasonable signal-to-noise ratios and good determination of ICM temperature and density profiles.

The final selection of the 33 galaxy clusters in REXCESS is described in Böhringer et al. (2007). Most of the clusters have angular radii on the sky in the range $7' < \frac{r_{500}}{D_A} < 9'$ where D_A is the angular diameter distance, but the nearest, lowest luminosity clusters have $10' < \frac{r_{500}}{D_A} < 12'$. For a typical cluster with angular radius $\frac{r_{500}}{D_A} = 7'$, the PSF FWHM $\sim 6''$ corresponds to features of scale $\sim 0.014 r_{500}$. The total photon count rates from the target clusters in the (0.5–2) keV band are between (0.198–0.57) s^{-1} in the *ROSAT* Position Sensitive Proportional Counter (PSPC) observations, and about an order of magnitude higher when observations from the three *XMM-Newton* detectors are combined. After cleaning the data for intervals where the background level is raised, the mean exposure times were $(1.4 \pm 0.7) \times 10^4$ s for the PN sensors and $(2.1 \pm 0.9) \times 10^4$ s for the MOS detectors. The clusters were selected to have estimated $T_{\text{ICM}} k_B > 2$ keV, excluding galaxy groups.

In Chapter 4 we compare the radial ICM density profiles with galaxy count density profiles, and use the results to infer the relative importance of different processes which go on during the interactions between gas and galaxies. The gas density cannot be measured directly, and must be inferred from X-ray surface brightness profiles which are dependent on the projected gas densities along each line of sight, on the temperature, and on the PSF of the telescope. Croston et al. (2008) de-projected and de-convolved the surface brightness profiles using information about the *XMM-Newton* PSF to produce high resolution gas density profiles for each cluster.

As part of the analysis described in Chapter 5 we use 2D surface brightness maps of X-ray emission to detect any substantial gas reserves remaining between the galaxies in infalling clumps of galaxies near clusters. We use maps of X-ray emission in the (0.5–2) keV band, chosen because it maximises the signal to noise for ICM observations. These maps are shown in Appendix A.

2.2 Observations using the MPG/ESO 2.2 m telescope Wide Field Imager

Optical observations of the REXCESS galaxy clusters were made using the Max Planck Gesellschaft/European Southern Observatory 2.2 m telescope's Wide Field Imager (WFI@2.2 m) at La Silla, high in the Atacama desert in Chile. WFI@2.2 m is well suited for *XMM-Newton* follow-up due to its comparable field of view. In this section we outline the telescope and instrument system (using information found in the WFI manual; La Scilla SciOps, 2005).

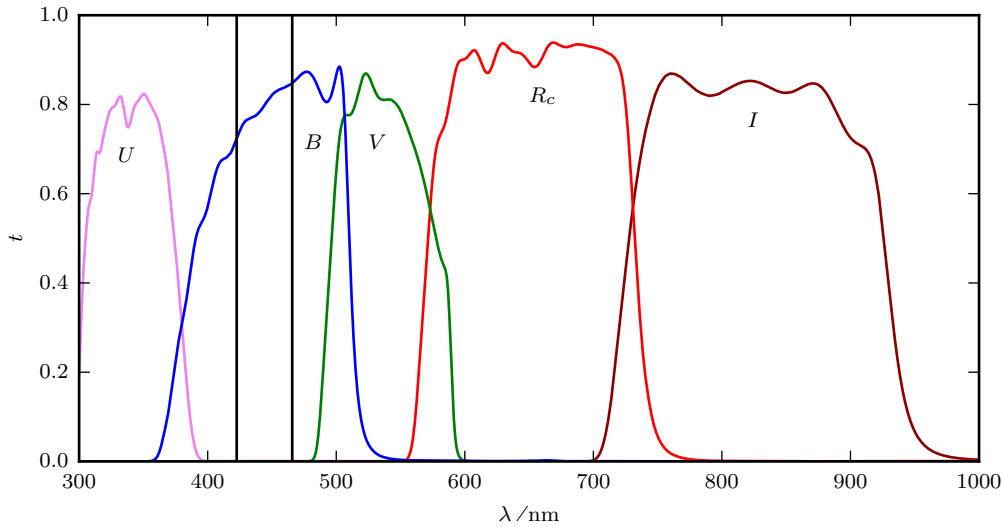


Figure 2.1: WFI@2.2m bandpasses for the standard *UBVRI* filter set. t is the nominal transmittance. The vertical lines bound the range of observed wavelengths of the 400 nm spectral break characteristic of elliptical galaxies discussed in Section §1.3.2.4, given the range of z in the REXCESS sample.

2.2.1 Telescope and instrument parameters

The MPG/ESO 2.2m telescope is of Ritchey–Chrétien–Cassegrain design and has an equatorial fork mount. The main mirror has a 2.200 m diameter free aperture and the secondary mirror has a diameter of 0.844 m. It has a focal ratio of f/8.0. The vignetting-free field of view has an angular diameter 33'. It is located at 70°44'12.0" W, −29°15'28.2" S, 2335 m above sea level.

The WFI@2.2m is mounted at the Cassegrain focus and has a f/5.90 focal reducer converting the intrinsic plate scale of 0.00234" μm^{-1} to 0.01587" μm^{-1} . It has a 34' \times 33' field of view filled with a 4 \times 2 mosaic of 2 kpixel \times 4 kpixel CCDs with a nominal scale of 0.238" pixel^{−1}. Its quantum efficiency is > 40% at wavelengths λ in the range (350–850) nm, and has maximum throughput of 67.5% at 501 nm. It is fitted with a range of 46 broad-, medium- and narrow-band filters, including an (approximately) standard *UBVRI* broad-band set which we use. The *R* filter is slightly wider than in standard sets, and is labelled *R_c*. The bandpasses are shown in Figure 2.1.

2.2.2 Observation parameters

Light collected by the telescope from target objects is accompanied by light from astronomical foreground and background sources, light scattered by the Earth's atmosphere,

and thermal/electronic noise due to the detector.¹ Exposure lengths must be planned to take these other sources of light and scattering effects into account, and be long enough to capture a sufficient number of photons from the faintest sources of interest to determine their brightness, colour and location.

The dimming of astronomical light by scattering in the atmosphere is known as *extinction*. The shortest path to the edge of the atmosphere is towards the zenith, so observations are planned such that objects are observed at their highest point in the sky. For small angles measured away from the zenith θ_z , the *airmass* is given by $Z_M = \sec \theta_z$, and absorption in magnitudes is given by $Z_M e_M$. e_M is band and atmosphere dependent; for WFI@2.2 m, typical values under excellent observing conditions are $e_{R_c} = (0.07 \pm 0.01)$ mag, $e_V = (0.11 \pm 0.01)$ mag and $e_B = (0.22 \pm 0.02)$ mag (ESO, 2003), but these vary and are monitored using nightly calibration. Observations were typically restricted to $Z_M < 1.5$, corresponding to $\theta_z < 48.25^\circ$. The scattered light is also seen as a diffuse background, the brightness of which varies slowly over the sky.

Bad pixels and *chip gaps* between the 8 CCDs in WFI@2.2 m can be compensated for by taking several *dithered exposures* in directions slightly offset from the target field centre. The gaps and bad pixels overlay different points on the sky in each frame, and only data from good pixels is stacked to produce a final image. In addition, using stacked short exposures rather than fewer long exposures increases the brightness threshold at which objects saturate, increasing the image dynamic range.

Taking all of these issues into account, observation times for each band can be planned in order to reach a specified signal-to-noise ratio for a galaxy of the lowest required brightness. The target objects in the REXCESS sample are galaxies in galaxy clusters, which are typically red with colours $C_{B-V} \sim 0.6$ and $C_{B-R_c} \gtrsim 1.2$ (shown in Section §4.3.5). Along with the increased atmospheric scattering and higher background levels in the blue band, this means that substantially longer exposures need to be made to measure the magnitude of faint objects in the B band than in R_c .

For REXCESS, observations of total duration 0.5 h were used for the R_c and V bands, and 0.75 h for the B band. Individual exposure times were ~ 200 s in the R_c and V bands, and ~ 300 s in the B band. The magnitude limits reached in these observations are discussed in detail in Section §4.3.3.1.

2.2.3 Image point spread function

Focussing optics like telescopes and eyes work by collecting light at different points in an aperture, and then compensating for the phase shifts introduced by different path lengths from the aperture to the focal plane in order to focus the light. Light from different points in the aperture interferes, and the resulting PSF diffraction pattern is called an *Airy disc*. For telescopes with circular apertures, the first minimum of the diffraction pattern falls

¹Thermal noise is minimised by housing the CCDs in a Dewar maintained at 167 K. The electronics were designed with minimisation of noise in mind.

at an angle (in radians) of

$$\theta = \frac{1.22\lambda}{D}, \quad (2.1)$$

from the centre of the pattern, where D is the telescope aperture and λ is the wavelength. Examples of the PSF for Cassegrain telescopes with central obstructions due to the secondary mirror are shown in panel iii.) of Figure 2.2a and Figure 2.2c.

Light passing through the turbulent boundaries between layers of atmosphere at different temperatures is imprinted with additional phase shifts, as shown in panel ii.) of Figures 2.2b and 2.2d. These lead to a breakup of the Airy disc, as shown in panel iii.) of Figures 2.2b and 2.2d. During long exposures, the phase screen changes as the turbulent air moves and mixes, which causes smearing out of the PSF as shown in panel iv.) of Figures 2.2b and 2.2d. The final PSF is often modelled as a 2D Gaussian, the FWHM of which is given the name *atmospheric seeing*. The final PSF in cases where the seeing is larger than the intrinsic Airy disc PSF of the telescope is largely independent of the telescope size. Stars (apart from the Sun) with the largest apparent angular sizes have diameters $< 0.1''$ (e.g. Young et al., 2000), well below the resolution of WFI@2.2 m. Stars are therefore ideal unresolved point sources for the measurement of the PSF.

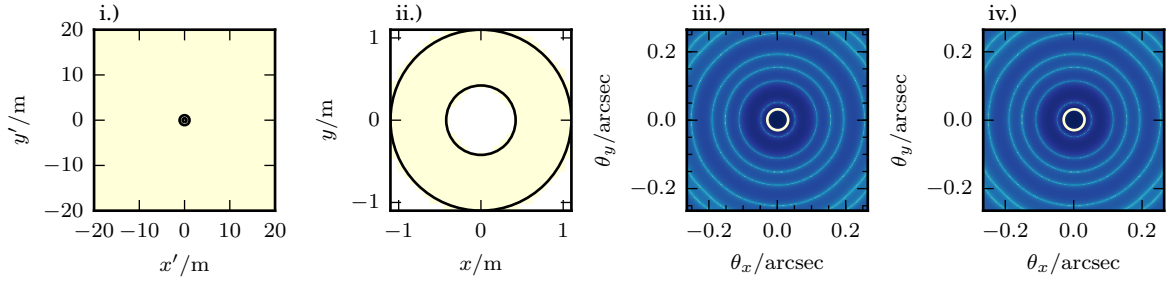
During observations it is necessary to monitor the seeing, since atmospheric conditions may change and planned observations may not be possible. Often, observatories operate a *differential image motion monitor* (DIMM) – a relatively small telescope (e.g. $D = 0.35$ m; Sarazin and Roddier, 1990) with an obscured aperture that only allows light through two circular gaps in the obscuring material. The rate at which the two images produced within the telescope move in relation to each other is dependent on the atmospheric seeing. If the DIMM is mounted separately to the science telescope, effects due to the surroundings, dome and optical tube assembly of the science telescope are not represented in the DIMM measurements. A large change in the difference between measurements from the DIMM compared with the science image may point to a problem with the science telescope.

2.2.4 Calibration and artefact correction

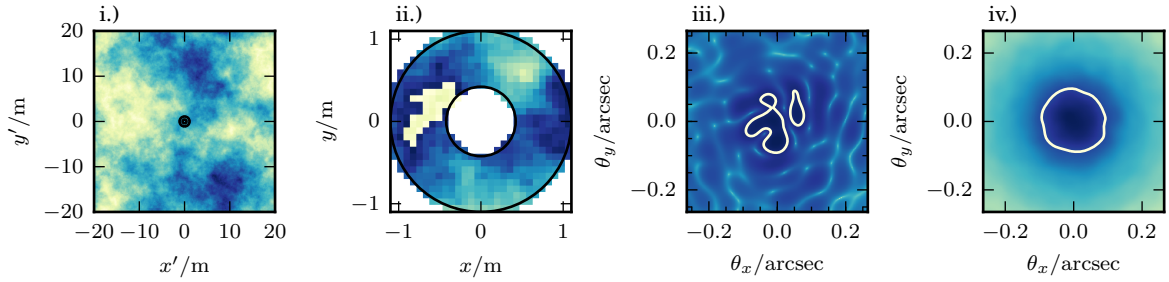
Before the final science images can be produced by stacking individual exposures together, corrections must be made for *artefacts* (spurious measurements), sensitivity variations and systematic biases in the individual exposures.

CCDs usually produce *biased* values offset from 0 even when not exposed. In addition, thermal noise in the sensor – *dark current* – leads to image values proportional to the exposure time. Dark current plus bias can be measured on individual frames using the *overscan regions* at the edge of a CCD chip, which are not exposed to light, and on dark exposures carried out for instrument calibration. Faulty pixels are noted as part of these measurements. The first step in processing raw images is to subtract the dark and bias values, and to mask bad pixels.

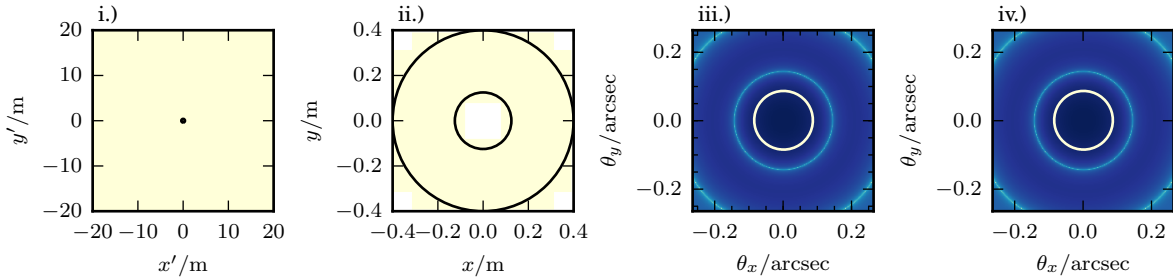
Spatial variations in the sensitivity of the sensor, in the transmissivity of light through the telescope and filters from different directions on the sky leads to variations in the



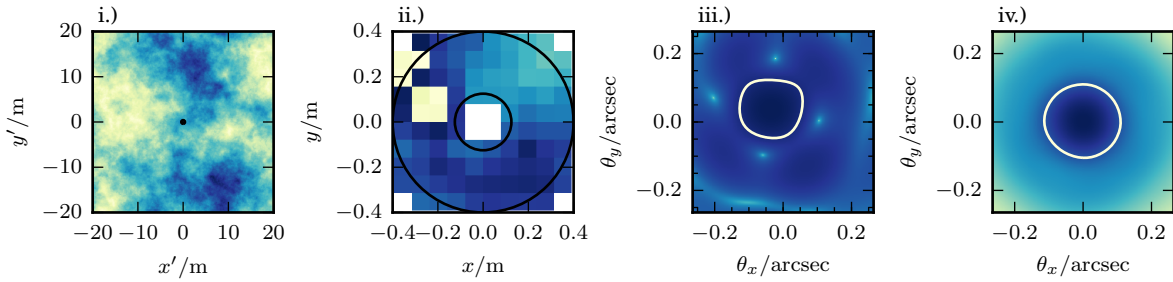
(a) Point spread function simulation for a space-based $D = 2.2$ m telescope (no atmospheric effects).



(b) Point spread function for a ground based $D = 2.2$ m telescope.



(c) Point spread function simulation for a space based $D = 0.8$ m telescope (no atmospheric effects).



(d) Point spread function simulation for a ground based $D = 0.8$ m telescope (turbulence as in Figure 2.2b).

Figure 2.2: Simulated point spread functions for short and long exposures with different telescope sizes and atmospheric conditions. In each case i.) shows the turbulent phase screen with a Kolmogorov power spectrum and a mark showing the aperture size; ii.) is a detail of the phase shifts $0-2\pi$ across the aperture; iii.) and iv.) show the snapshot PSF and long exposure PSF respectively – dark is high light intensity, and the contour is at $\frac{1}{2} \times$ the maximum value.

measured brightness of sources with the same intrinsic brightness. Sensitivity of the telescope–sensor system is calibrated with observations of *flat fields* which are meant to provide uniform illumination. Ideally, the flat fields are as far away as possible from the telescope, so that any focus-dependent effects are minimised. Several uniform sources may be used including observations of the sky background with stars removed, observations of the twilight sky or observations of a screen within the telescope dome. Science images are corrected for all the sensitivity variations by dividing them by the flat field.

Satellite trails are straight bright lines across the image field which are sufficiently rare and noticeable that they can be reliably masked by hand. Cosmic ray strikes must be masked automatically because they occur very frequently. Direct detection of these in individual exposures is outlined in Section §2.3.2. Cosmic ray strikes can also be handled by taking the median rather than the mean when stacking images.

Image *registration* – specifying the direction and orientation of a frame with respect to a coordinate system with sub-pixel accuracy – is performed by comparing star positions with a precisely calibrated astrometric catalogue.

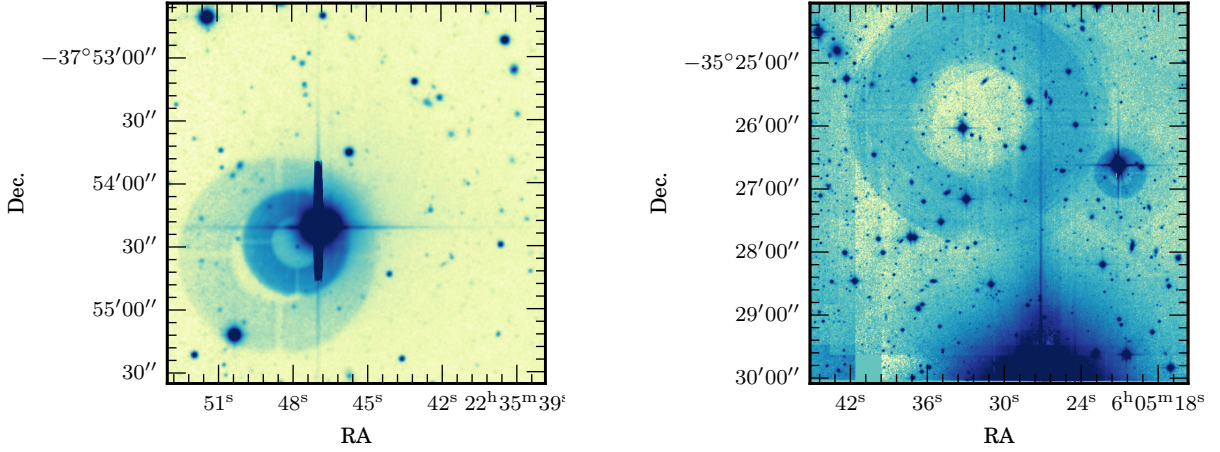
Some artefacts are more difficult to correct. Our place within a galaxy means that thousands of stars are found in each WFI@2.2m image. These can produce image artefacts which are difficult or impossible to correct for once the exposures have been made.

Reflections from within the telescope may be visible. Light from bright stars is reflected from the sensor back into the telescope, where it is reflected back onto the sensor. For very bright stars, several ghost images which can be substantially offset from the centre of the star may be detected. The reflection positions are dependent on the attitude of the telescope with respect to the star, so they shift in individual dithered frames, causing smearing of the reflections in the final images. Examples are shown in Figure 2.3a. The telescope aperture and the structures within the optical path (such as the *spider* which holds the secondary mirror) imprint additional diffraction patterns in the PSF of bright stars, as shown in Figure 2.3b and Figure 2.3a.

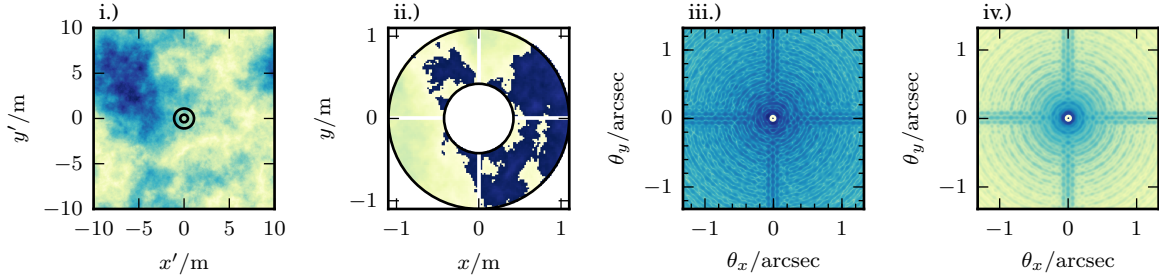
Bright stars can also cause *blooming*, where the CCD well depth is too small to contain all the electrons liberated by absorbed photons, and the electrons spill out along the read-out column in the sensor. Examples are shown in Figure 2.3c.

Where observations are made with the sensor in a fixed orientation with respect to the right ascension axis, blooming columns and diffraction spikes always have the same orientation in the final image, so it is possible that no unaffected data is available for these regions, which may have to be discarded. Blooming effects do not spill over onto adjacent CCDs in the mosaic, so ensuring that a star is dithered onto several chips can ameliorate this problem.

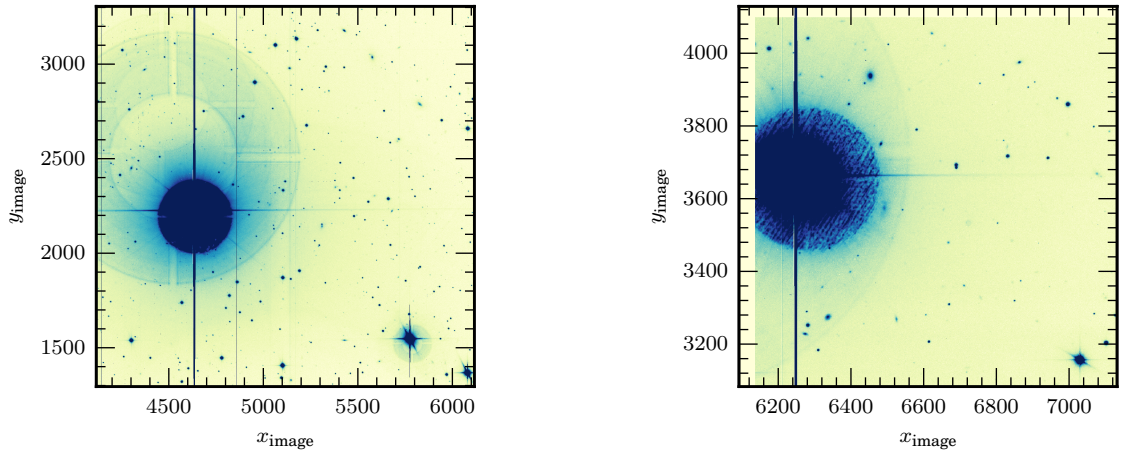
We mask out regions where reflections, blooming and diffraction spikes cause spurious object detections. In principle, it should be possible to detect and model regions affected by diffraction spikes and reflections, with a view to subtracting the model and recovering the underlying data, but we found this to be rather tricky because of the variation in appearance of the image artefacts.



(a) Left: primary and secondary reflections in the shape of the telescope aperture around a bright star. (A saturated region with blooming is also shown). Right: tertiary reflection due to the bright star just outside an observation field. Diffraction spikes are seen emanating from the of the PSF centres.



(b) Simulation of observations using telescope with 4 spider arms of width 5 cm holding the secondary mirror and causing a + shaped diffraction pattern in the short and long exposure PSFs. The telescope is otherwise identical to the 2.2 m telescope in Figure 2.2b. The panels are as described in Figure 2.2, but note that the PSF panel axes iii.) and iv.) scales are much larger in this case.



(c) Raw WFI@2.2m observations with uncorrected blooming spikes and reflections from the REFLEX2 galaxy cluster sample (Böhringer et al., 2013). Left: * 48 Lib in the field of galaxy cluster RXC J1558.3–1410. Right: HD 110662 in the field of galaxy cluster RXC J1244.6–1159.

Figure 2.3: Examples of image artefacts which may be difficult or impossible to correct during image reduction.

2.2.5 Stacked images

The dithered observation frames need to be processed into single images where the gaps between the chips, any bad pixels, satellite tracks, cosmic ray strikes etc. are removed. Once the bias and dark components have been subtracted, the images have been corrected for sensitivity variations by dividing by a flat field, and spurious signals have been masked, the registered individual frames can be stacked to produce a single image for each band.

Seeing conditions vary between observations, but for accurate colour measurements the PSFs of images in different bands must be the same. In the case that the PSF is modelled by a Gaussian, this can be achieved by convolving the stacked images taken under better seeing with a second 2D Gaussian. For a standard deviation $\sigma_0 = \frac{\text{FWHM}}{2\sqrt{2\log 2}}$ in the observed image, and a target standard deviation $\sigma_t > \sigma_0$, the convolving Gaussian standard deviation σ_1 is given by $\sigma_1 = \sqrt{\sigma_t^2 - \sigma_0^2}$.

We use a subset of 14 clusters from REXCESS survey which had reduced follow-up observations in the R_c , V and B bands. The U and I data available for some of the clusters in the subsample were found to be of inhomogeneous quality, and were not used. Colour images for all the clusters in the subsample are shown in Appendix A.

2.3 Object detection and catalogue generation

2.3.1 Detection of objects in optical images

Once the images have been reduced and normalised to have a common PSF, galaxies and stars can be detected. We detect stars and galaxies using SEXTRACTOR (Bertin and Arnouts, 1996), which works by locating contiguous groups of pixels, each with values a certain threshold above a specified background level, and then analysing the properties of those pixels once the background level has been subtracted.

The background is estimated by finding the mean I_{bg} and standard deviation $\sigma_{I_{\text{bg}}}$ of pixel values I_i in a small region; removing pixels with values $-3 < \frac{I - I_{\text{bg}}}{\sigma_{I_{\text{bg}}}} < +3$ and then recomputing I_{bg} and $\sigma_{I_{\text{bg}}}$ until these parameters stabilise. If $\sigma_{I_{\text{bg}}}$ does not change by more than 20% from the first to last iterations, the final I_{bg} is used. If $\sigma_{I_{\text{bg}}}$ does change by more than 20%, $I_{\text{bg}} = 2.5 \text{ median } I - 1.5\bar{I}$ for the pixels selected in the final iteration step.

Contiguous groups of at least n_{pix} pixels with $I > I_{\text{bg}} + 1.5\sigma_{I_{\text{bg}}}$ are treated as objects. Throughout this study, we use $n_{\text{pix}} = 5$ for WFI@2.2 m observations. The SEXTRACTOR parameters we used are listed in Appendix B.

2.3.2 Object analysis and classification

The elongation, orientation, ellipticity, FWHM etc. of a group of pixels can be characterised using image moments which are outlined in Section §5.3.3.1. This shape measurement can be used to define an ellipse enclosing a group of pixels O , not all of which need to be

above the background threshold. It is these elliptical regions we consider when making catalogues of object brightness. Throughout this study we use fluxes within an elliptical boundary specified by the `SEXTRACTOR` `auto_mag` measurement. For details, see Bertin (2010).

The simplest measurement of the total flux from an object is given by $f_I = \sum_O \frac{I - I_{\text{bg}}}{t_{\text{exposure}}}$ where t_{exposure} is the exposure time. This can be converted into an instrumental magnitude $M_{\text{raw}} = -2.5 \log_{10} f_I$.

The use of locally calculated I_{bg} and $\sigma_{I_{\text{bg}}}$ means that the object detection algorithms can be run on images with uncorrected variations in sensitivity and I_{bg} , or where bias and dark frames have not yet been subtracted. This includes raw images straight from WFI@2.2m. We found this to be useful for almost real time monitoring of the seeing PSF from science images during observations, where analysis speed is more important than having accurate magnitude measurements.

2.3.3 Star-galaxy separation

Plotting the FWHM vs. magnitude of the objects in astronomical images produces a characteristic diagram which can be used to classify each of the objects as point-like (star), extended (galaxy or nebula) or as a spurious detection or cosmic ray. An example FWHM–magnitude diagram for objects detected in a raw exposure from WFI@2.2m is shown in Figure 2.4.

Unresolved sources scatter around the PSF FWHM in the FWHM–magnitude diagram, which turns over at the point where they begin to saturate the detector. This overdensity in FWHM space allows them to be detected automatically. Taking the mean FWHM of all of these gives a much better constraint on the PSF than from a single star. These objects can also be used to map PSF variations across the focal plane, as shown in Figure 2.5.

Images of real objects are always convolved with the PSF, which means that objects with smaller FWHM are likely to be spurious – statistical fluctuations in the background level – or cosmic rays. Cosmic rays are not focussed by the telescope optics and as a result they can deposit their energy in a smaller region on the sensor than a group of photons emitted by a point source. Longer or stacked exposures leads to better characterisation and smoothing out of the background level, increasing the number of pixels which can be reliably identified as above the background threshold and allowing measurements of fainter sources.

Other detections are likely to be extended objects like galaxies, and these have a very different distribution in FWHM–magnitude space. `SEXTRACTOR` provides an automated object classifier based on a neural network, which can discriminate between stars and galaxies (Bertin and Arnouts, 1996). This classifier depends on a good estimate of the PSF for an image. It produces a stellarity s in the range 0–1, where $s = 1$ is a star and $s = 0$ is an extended object. Care needs to be taken to deal with misclassifications, which are sometimes quite obvious in the FWHM–magnitude diagram.

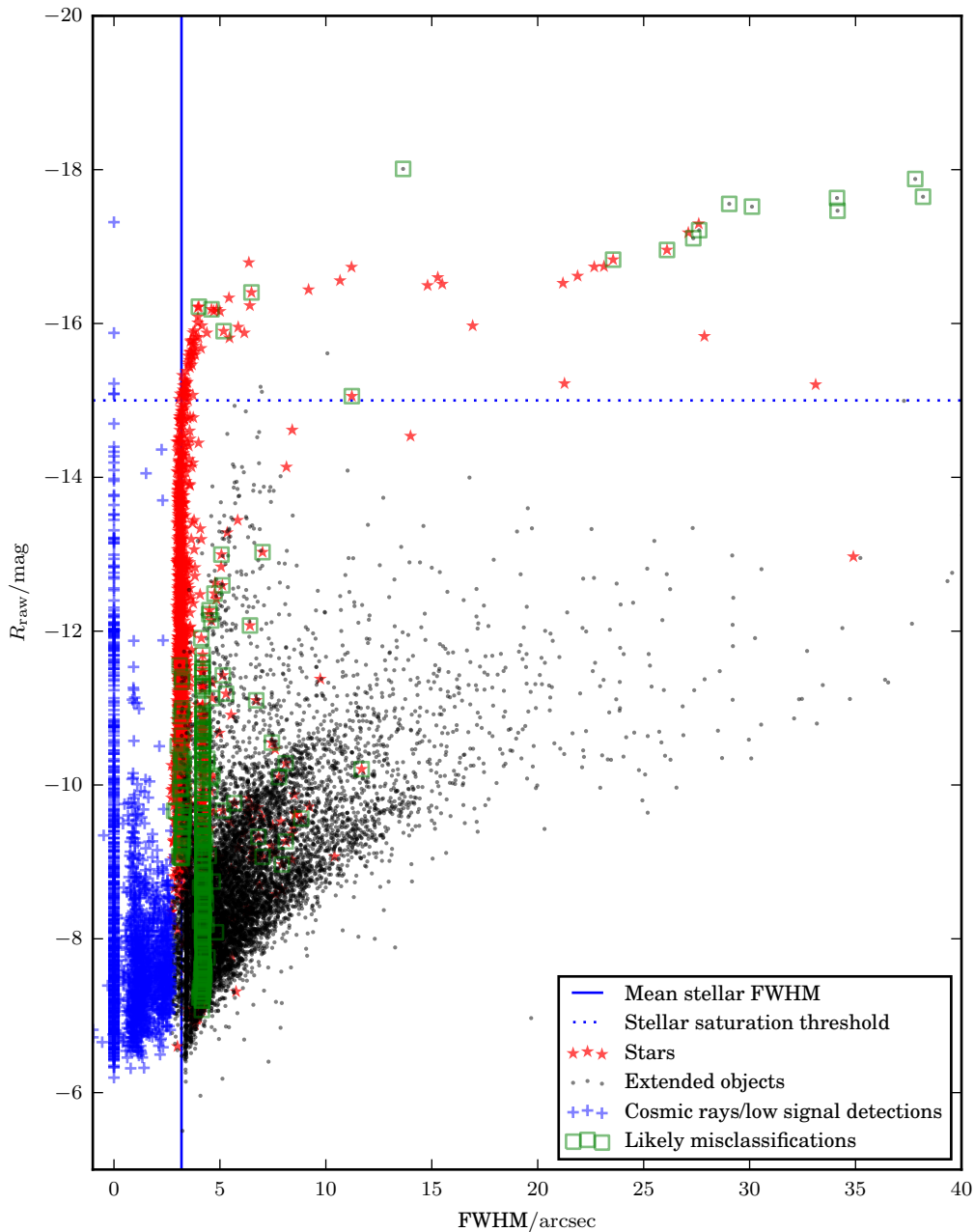


Figure 2.4: FWHM–magnitude diagram for sources detected in a single R_c band WFI@2.2m exposure of RXC J1244.6–1159 with exposure 300s. The line of sources at $\text{FWHM} = 0''$ are cosmic ray strikes or bad pixels. The stars scatter around the seeing disc FWHM up to the saturation threshold. Object classification is performed using a neural network, but very bright or faint objects, or those affected by blooming, may be misclassified. The blooming feature shown in the right panel of Figure 2.3c leads to most of the misclassifications.

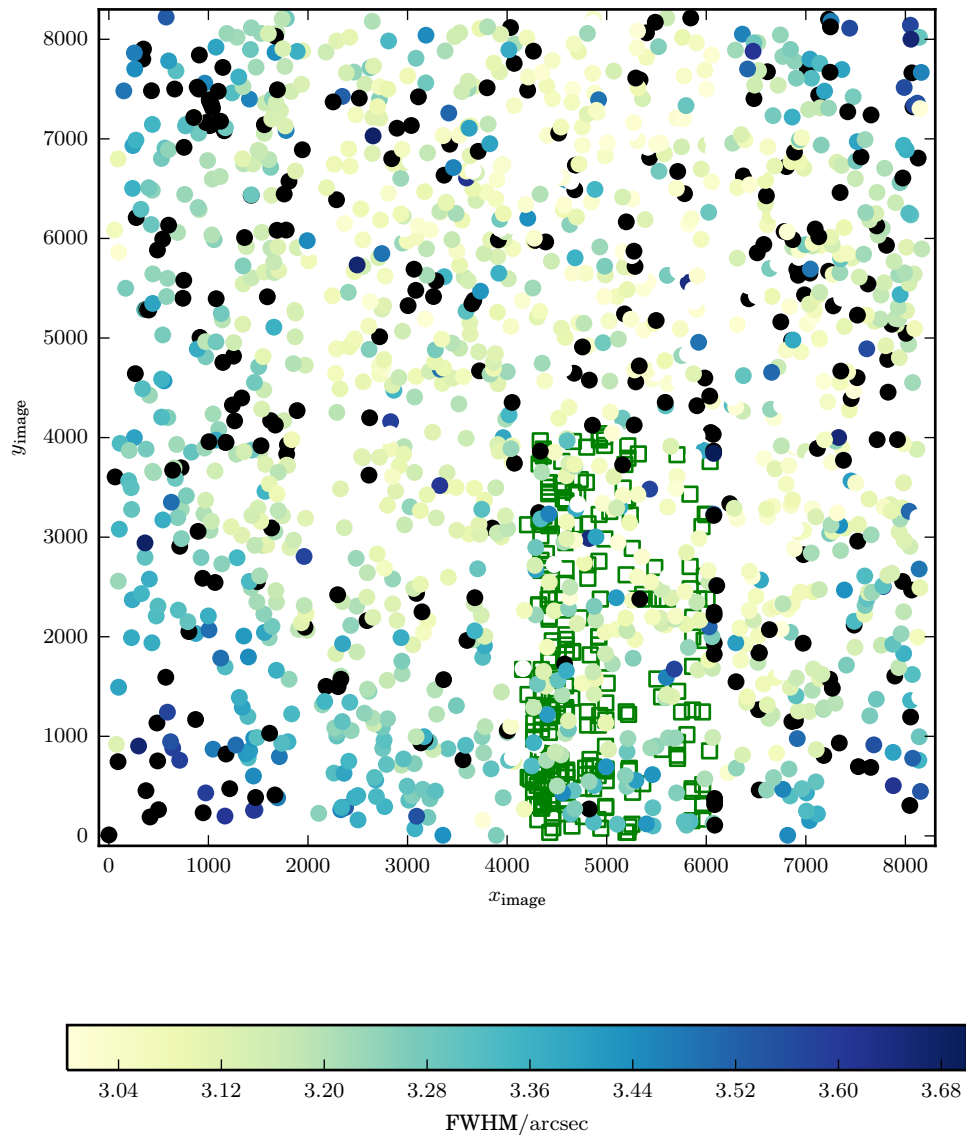


Figure 2.5: FWHM variation across an image, showing the increase in PSF FWHM of unsaturated stars as distance from the image centre increases. The group of stars with larger FWHM scattered across the whole image are saturated. The FWHM–magnitude diagram for this image is given in Figure 2.4. The misclassified objects are marked with squares and are confined to one CCD badly affected by blooming (detail shown in the right panel of Figure 2.3c).

2.3.4 Final catalogue generation

Once the data have been calibrated and PSF-matched images produced, the final catalogue generation can take place. To ensure that the same objects are measured in all bands, we detect object positions and morphology using `SEXTRACTOR` using only the R_c (detection band), and then measure object f_I for each object in each band using a common elliptical aperture.

To avoid any loss of power to discriminate between stars and galaxies due to the PSF normalisation, we also run the star–galaxy separation algorithm on each original image in band M to give value s_M , and set the final $s = \max(s_{R_c}, s_V, s_B)$. These measurements are cross-referenced into the main catalogue using the source position.

The background in images, scattered by the atmosphere, or due to electronic noise, should in principle be spatially uncorrelated – each pixel produces a fair Poisson realisation of the local background level. This lack of correlation means that when the background is convolved with a Gaussian smoothing filter, its variance decreases and more accurate and precise measurements of the local I_{bg} and $\sigma_{I_{\text{bg}}}$ are possible. By convolving an image with a filter which has the profile of the image PSF, this effect is maximised (e.g. North, 1963), allowing more robust detections of faint objects. We applied this method, modelling the PSF of each detection image using a 2D isotropic Gaussian with standard deviation derived from the mean FWHM of stars detected in the FWHM–magnitude diagram.

The final catalogue for each set of images comprises position and morphology data from the detection band, instrumental magnitudes from each of the matched PSF images, and a combined stellarity classification drawn from the original stacked images which were not PSF matched.

2.4 Magnitude and colour calibration

There are temporal variations in the sensitivity of the atmosphere–telescope–sensor system which need to be calibrated. These may include long-term variations in the sensor, filters, mirror reflectivity and lens transmissivity due to degradation or damage, or the atmospheric extinction.

2.4.1 Zero points from standard star observations

Nightly observations of stars of known brightness at different Z_M in all bands can be used to calibrate for all of these changes. Once the atmospheric extinction terms already discussed in Section §2.2.2 are found, the remaining variations are absorbed into a single parameter – the magnitude zero point M_{zero} .

These observations must be made and reduced in an identical manner to the images of the actual observation targets. The relation between the raw magnitude M_{raw} for a star and the standard system magnitude M is $M = M_{\text{raw}} + M_{\text{zero}} - Z_M e_M$.

2.4.2 Zero point reference from the APASS all-sky survey

Should no standard star observations be available, it is possible to find photometry for stars in many fields using all-sky surveys. This precludes the fitting of e_M , but this parameter is not of intrinsic interest in this study. We used B magnitudes from the American Association of Variable Star Observers photometric All-Sky Survey (APASS) to find $B_{e,\text{zero}} = M_{\text{zero}} - Z_M e_M$ for each observation field. Stellar magnitudes for the other bands in our catalogues were not available at the time of analysis.

2.4.3 Colour calibration by stellar locus regression

Zero points for each band are required, so a second method was needed to find $R_{ce,\text{zero}}$ and $V_{e,\text{zero}}$. We use a modified version of the *stellar locus regression* (SLR) method described by High et al. (2009).

If two colours – e.g. (C_{V-R_c}, C_{B-V}) – for main sequence stars are plotted against each other they scatter around a line called the *stellar locus* which is approximately constant across the sky. We used a catalogue of stars detected from a set of WFI@2.2 m observations with known zero points to find the location of the stellar locus. The colours and the fitted stellar locus are shown in Figure 2.6.

In our SLR implementation, we find the shifts required to convert between raw and calibrated colours, by minimizing the Euclidean distances of all the stars in a catalogue from the stellar locus. The zero points are related by the same colour shifts, so when they are used in conjunction with a known zero point in one of the bands, these shifts can be used to calibrate magnitudes as well.

High et al. assume in their implementation that all of the stars observed are behind the dust lanes in the Milky Way, that the dust lanes can therefore be modelled as a thin sheet. This means that the zero points found using the regression method also include the dust absorption terms for extra-Galactic objects. We tested these assumption by converting the calibrated stellar loci from Covey et al. (2007, used by High et al.) into the WFI@2.2 m magnitude system, and comparing them with our calibrated observations. The results are shown in Figure 2.6.

We found that there was a significant difference between the observed and Covey et al. stellar locus shape which increased towards the bluer end of the stellar locus. Blue stars are rarer, have the highest intrinsic brightness and are seen at greater distances compared to fainter, redder stars, only observable if they are nearby. The increasing reddening of more distant stars shows that the dust cannot be treated as a thin sheet.

We chose to assume that the observed stellar locus is constant across the sky, an assumption which may be approximately true for the REXCESS clusters which are all at high Galactic latitude. This assumption introduces a potential colour mis-calibration effect. This step may be the source of the larger scatter in the red sequence intercepts than is seen in the literature. This also affects all luminosity measurements, since we use the R_c luminosities which are cross-calibrated using the colour terms and the B zero points. Since dust absorption is not calibrated in our stellar locus regression implementation,

we correct galaxy magnitudes using the extinction parameters for extra-Galactic objects found in the NASA Extragalactic Database (NED).

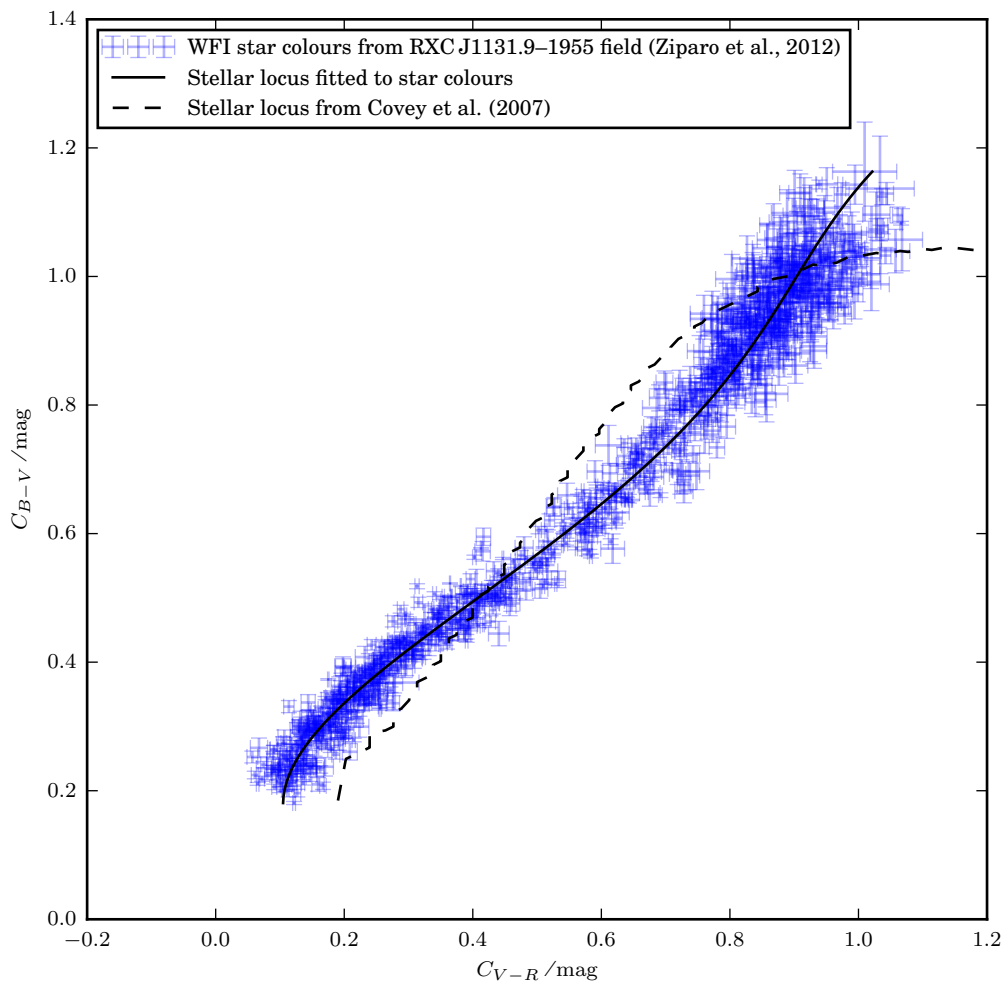


Figure 2.6: Calibrated star colours and fitted stellar locus from the field of RXC J1131.9–1955 (Ziparo et al., 2012). The dashed line shows the shape of the stellar locus derived from the data of Covey et al. (2007), shifted to overlay the observations as closely as possible.

Chapter 3

Galaxy distribution structural analysis techniques

If you torture the data enough,
nature will always confess.

Ronald Harry Coase, *How should
economists choose?*, 1981

We wanted to analyse the structure of galaxy clusters by measuring the distribution of galaxies. In order to understand that distribution, we performed three data reduction steps which are described in detail in this chapter. First, we transform the point distribution of galaxy positions into a continuous 2D smoothed map using the smoothing techniques described in Section §3.1. In the second step we subtract or compensate for the background distribution of galaxies using the techniques described in Section §3.2. We use the term *background* to refer to all points which are not of interest in our study of the target clusters, rather than just those points more distant than the target. We demonstrate variations on these techniques using a simulated dataset similar to the distribution of galaxies in the plane of the sky in and around a cluster. In the third step we detect galaxies belonging to the cluster red sequence in colour–magnitude space, as described in Section §3.3. By selecting red sequence galaxies, we are able to produce a higher SNR measurement of the spatial distribution of old galaxies within a cluster. The REXCESS dataset we analyse in Chapters 4 and 5 does not include any spectroscopic measurements, so we were restricted to using only photometry and spatial position to discriminate between target and background galaxies.

Spatial and colour–magnitude point distributions share a number of characteristics. Both have a range of densities over several orders of magnitude – a high dynamic range, may contain groups of related points, and both may have non-uniform backgrounds. A spatial distribution may reveal a remnant clump of galaxies after a cluster–group merger, and exhibit a variable background due to the large scale structures in which the cluster is embedded. A cluster colour–magnitude distribution usually has a prominent

red sequence, and a background density which varies very strongly with magnitude due to the number counts of field galaxies. The similarities mean that we can, to some extent, use the same methods to handle them both.

In Section §3.1 we describe and compare the results of some general techniques for smoothing point data on a quantised grid. In Section §3.2 we provide a brief account of some background/target discrimination methods which we investigated, which build on the smoothing methods. In Section §3.3 we describe the red sequence detection methods we investigated, which form a crucial part of the analysis in Chapters 4 and 5.

3.1 Density estimate from a 2D point distribution

Density estimates due to discrete data drawn from an unknown distribution can be used to make an estimate of the shape of the original distribution. In point distributions with a high dynamic range where some regions have a high density of counts and other regions are only sparsely populated, care must be taken not to smear out features of interest.

An input density map V can be used to generate a map of discrete counts V_{ct} using $V_{\text{ct},i} = \text{Poisson}(V_i)$ for each pixel i , where $\text{Poisson}(\lambda)$ returns a random integer from the Poisson distribution with expectation value λ . The aim of the density estimate method is to start with V_{ct} and recover V . We investigate 4 methods: simple binned count map, described in Section §3.1.1; fixed scale smoothing, described in Section §3.1.2; density estimates from the Voronoi decomposition of the point distribution, described in Section §3.1.3; and adaptive aperture smoothing described in Section §3.1.4.

Each density estimate method is applied to a simulated point distribution akin to projected galaxy positions within and around a cluster. The target density map τ consists of a large elliptical Gaussian in the field centre, overlaid with two smaller elliptical Gaussians which is similar to a galaxy cluster with sub-clumps. There is a very compact independent target with a low number of counts towards the bottom edge of the field similar to an infalling galaxy group. The background density β varies across the field, and the lowest density region of the background coincides with the position of the compact independent object. The distribution is contrived to show problems with each of the smoothing and background subtraction methods in this Section and in Section §3.2.

τ and β are $256 \text{ pixel} \times 256 \text{ pixel}$ grids. The total density $\omega = \tau + \beta$ is shown in Figure 3.1a and satisfies $\sum_i \omega_i = 2^{10}$ and $\sum_i \tau_i \sim \sum_i \beta_i$.¹ The weight map A is an array with the same shape as ω and the value 1 for each element.² We use the total count map $\omega_{\text{ct}} = \tau_{\text{ct}} + \beta_{\text{ct}}$ as input for the smoothing algorithms. We define $n_t = \sum_i \omega_{\text{ct},i}$.

¹The total count is a little lower than typical galaxy cluster observations in the REXCESS sample with the magnitude limit we use, which have a few hundred target galaxies plus a broader distribution of a few thousand background galaxies.

² A is a map of object completeness, which represents the probability of detecting the objects of interest at that pixel, if they were actually there. In the case of galaxy catalogues, this probability varies with magnitude, being very close to 1 for bright objects, but reducing as the noise limit of the observations is reached. We deal with this variability when running smoothing algorithms on real data by truncating our galaxy catalogues at detection magnitude where we assess them to be near to 100% complete.

A catalogue of points is also produced: for each pixel $V_{\text{ct},i} > 0$, the location of pixel i is added to the catalogue $V_{\text{ct},i}$ times. Whether each point was drawn from τ_{ct} or β_{ct} is also recorded. The catalogue is shown in Figure 3.1b. We use this catalogue in Section §3.2 to assess the effectiveness of background subtraction algorithms.

Each smoothing algorithm produces a map of density estimates S where each pixel is also assigned an uncertainty α_S . S has an identical shape to ω . We show S for each algorithm in Figure 3.2.

Comparisons between ideal and estimated density map values are shown in Figure 3.3. In Figure 3.3a, we show

$$\Sigma = \frac{S - \omega}{\alpha_S}, \quad (3.1)$$

the offset between the smoothed and original maps in terms of the uncertainties produced by the smoothing algorithm. Figure 3.3b shows

$$\Upsilon = \left| \frac{S - \omega}{S} \right|, \quad (3.2)$$

which is the absolute fractional deviation from the ideal value at each pixel. Regions with $-3 < \Sigma < 3$ may have $S \gg \omega$ or $S \ll \omega$ but very large α_S ; Υ is independent of α_S and can reveal these regions.

The simulation is contrived to have densities across several orders of magnitude; broad, sparsely populated, slowly-varying-density regions; regions where object densities are high with expectation values $\gtrsim 1 \text{ pixel}^{-1}$; regions with rapidly varying densities; and a region with an isolated compact object on a scale $< 25 \text{ pixel}$ with a low number of counts < 25 . This provides a sufficient dynamic range and variable background level to demonstrate the advantages and problems associated with each algorithm. Data with continuous coordinates can be quantised by binning onto a grid with whatever resolution is required to resolve the smallest structures of interest, so there is little loss of generality by designing the smoothing methods to run on a grid.

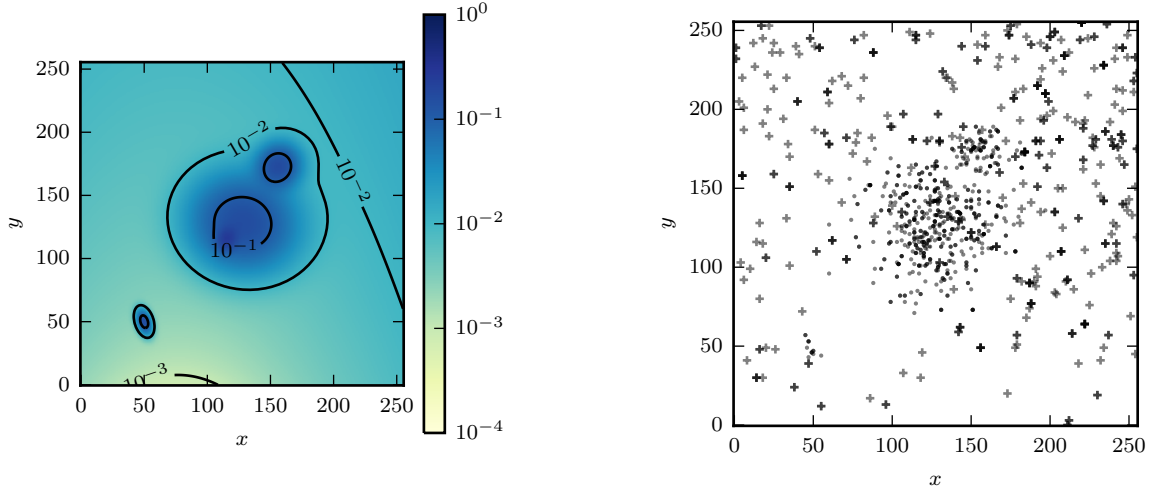
A similar analysis, run on a model of the colour–magnitude diagram of a galaxy cluster, is shown in Section §C.1. Broadly the same results can be seen in both cases.

3.1.1 Simple binned count map

Binning point positions into fixed size bins allows a simple measurement of the local density, but does not produce good representations of the density structure of high dynamic range data.

The binning scale can be defined by a target signal to noise ratio SNR_t , which determines the uncertainty of the final density estimate for each bin. The Poisson uncertainty for a given number of counts n_{bin} is $\sqrt{n_{\text{bin}}}$, so $\text{SNR}_t = \frac{n_{\text{bin}}}{\sqrt{n_{\text{bin}}}} = \sqrt{n_{\text{bin}}}$.

To bin data onto a grid of equal sized squares if the input data range is the same in both coordinates:

(a) Input total density distribution ω .

(b) Simulated point distribution based on Figure 3.1a. Circles are drawn from the target objects, and are drawn from the background.

Figure 3.1: Simulation input density map and the resulting point distribution.

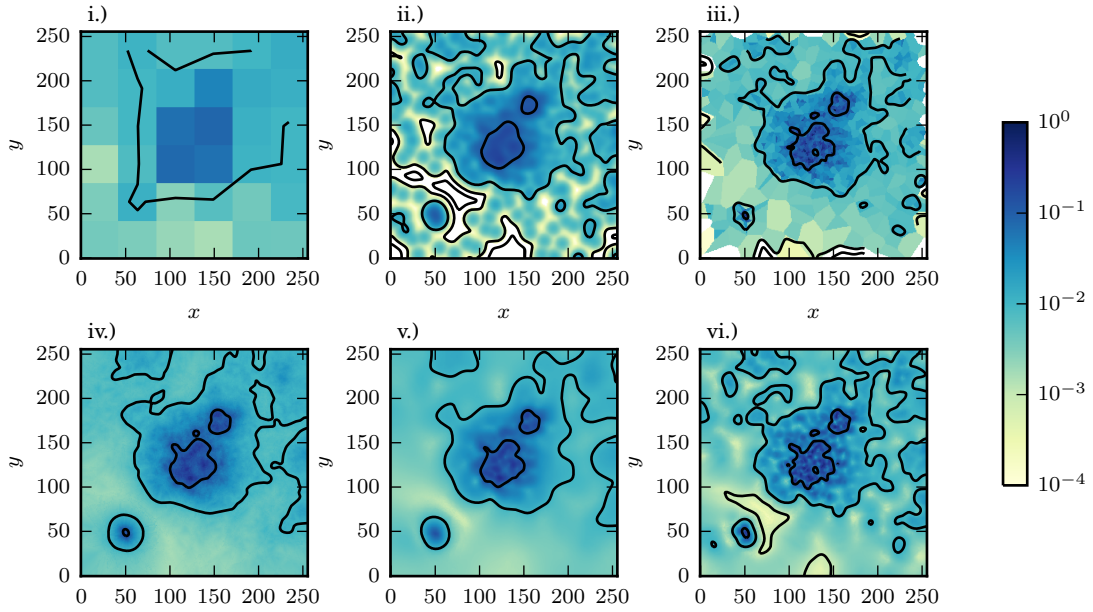
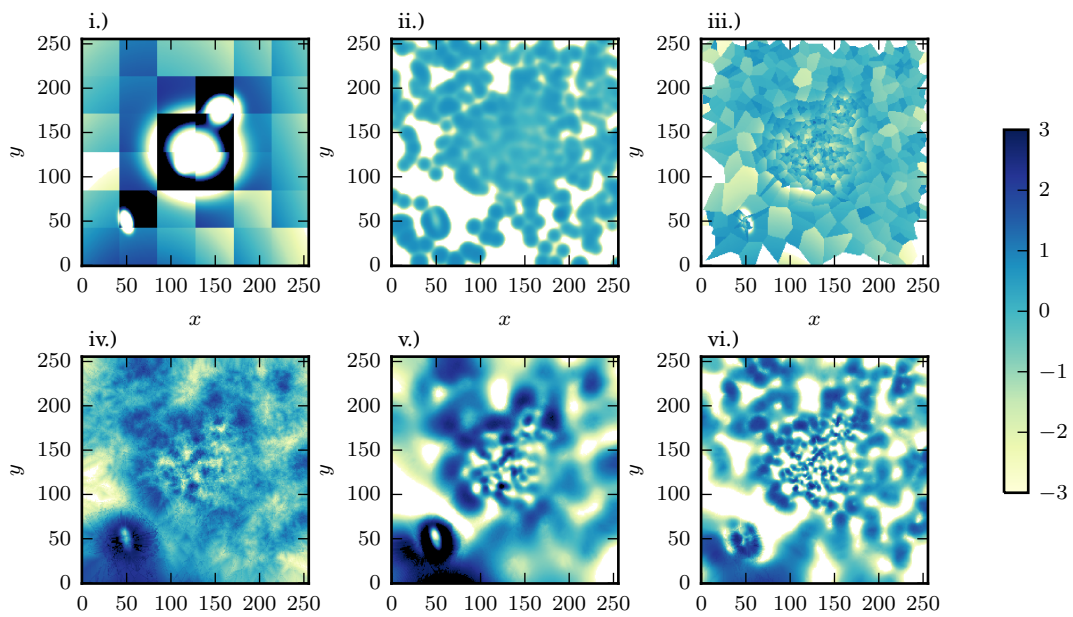
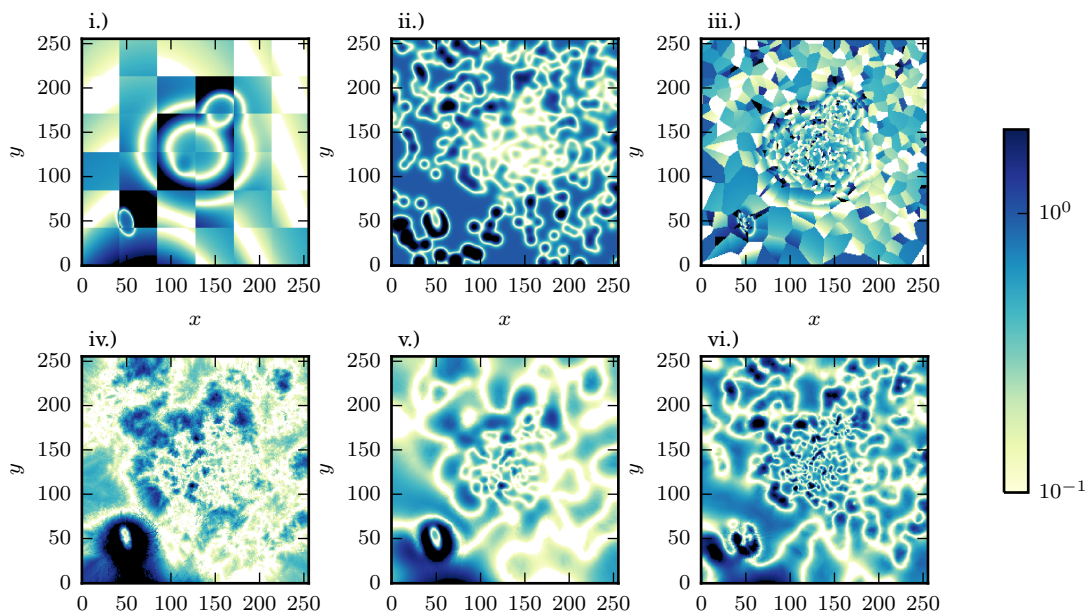


Figure 3.2: Smoothed density maps S based on the point distribution in Figure 3.1b using different algorithms: i.) fixed bin histogram; ii.) fixed aperture smoothing; iii.) Voronoi tessellation; iv.) adaptive top-hat filter with $\text{SNR}_t = 5$; v.) adaptive Gaussian filter with $\text{SNR}_t = 5$; vi.) adaptive Gaussian filter with $\text{SNR}_t = \sqrt{8}$. The contour levels correspond with the levels shown in Figure 3.1a.



(a) Σ difference maps in units of the smoothed density map uncertainty [Σ defined in Equation (3.1)].



(b) Υ absolute difference maps in units of the original density map value [Υ defined in Equation (3.2)].

Figure 3.3: Differences between original input density ω from Figure 3.1a and the smoothed density map S results from Figure 3.2. Values above and below the range shown in the colour bar are shown as black and white respectively.

1. The number of bins between the minimum and maximum values in each coordinate is set as $\text{floor}\left(\sqrt{\frac{n_t}{n_{\text{bin}}}}\right)$, where floor rounds down to the next integer. The total number of bins is then $\sim \frac{n_t}{n_{\text{bin}}}$. We chose $\text{SNR}_t = 5$.
2. The counts in ω_{ct} are binned to make the binned count map C , and the areas in A are binned to make the binned weight map E .
3. The density is $B = \frac{C}{E}$, with uncertainties given by $\alpha_B = \frac{\sqrt{C}}{E}$.
4. We generate S from B and α_S from α_B by taking the value from the nearest bin, such that S and α_S have the same resolution as ω_{ct} .

The results are shown in panel i.) Figure 3.2, and compared with ideal results in panel i.) of Figures 3.3a and 3.3b. The shape of the contours shown in panel i.) of Figure 3.2, compared with the contours in 3.1a show that all fine features – the thin, dense part of the diagram with $\omega > 10^{-1}$ – are not resolved. Panel i.) of Figures 3.3a and 3.3b illustrate the problem in the high density regions where the local density changes very rapidly: the estimate which is taken for the whole bin is only correct for a very thin band of pixels, and large overestimates or underestimates appear either side of this band.

This method is clearly limited by the Nyquist sampling criterion (Nyquist, 1928), which requires bin sizes no larger than half the size of the smallest feature of interest. Introducing interpolation between bin centres can only provide a partial correction to this since it does not deal with the fundamental Nyquist limit.

3.1.2 Fixed aperture smoothing

A common density estimate method is to convolve the point data with a 2D Gaussian kernel:

1. Define σ such that $\pi\sigma^2 n_t = \sum_i A_i$.
2. Define a Gaussian kernel G

$$G(x', y') = \frac{1}{2\pi\sigma^2} \exp\left(-\frac{x'^2 + y'^2}{2\sigma^2}\right). \quad (3.3)$$

3. The smoothed map is given by $S = \frac{\omega_{\text{ct}} * G}{A * G}$, where $*$ is the convolution operator. Errors are estimated as $\alpha_S = \frac{\sqrt{\omega_{\text{ct}} * G}}{A * G}$.

The results are shown in panel ii.) Figure 3.2, and compared with ideal results in panel ii.) of Figures 3.3a and 3.3b. The contours shown in panel ii.) of Figure 3.2 show that the smaller scale provided by the smoothed counts allows a reasonable estimate of the shape of the distribution in the densest image regions with $\omega > 10^{-1}$. This method does a better job of finding the correct contours than the simple binned count map at scales $\omega \geq 10^{-3}$. It also picks out the shape of the compact object at (50, 50), but fails to reveal the region

with $\omega > 10^{-1}$ in the centre of the compact object. Panel ii.) of Figure 3.3b shows that in the high density regions, the density estimates are reasonable, within $\sim 50\%$ of the real value. In sparser regions there is a mottled pattern where single counts are smoothed on much too fine a scale and regions serendipitously devoid of counts have $S = 0$, even though $\omega > 0$.

3.1.3 Voronoi tessellation

Fixed count binning and fixed smoothing both fail to generate sensible density estimates for sparse point data. We were very interested in finding a method where individual points could be assigned a density. The density of points in a situation where all of the points have unique positions can be analysed using a Voronoi diagram:

1. Let $p = \{p_0, p_1, \dots, p_n\}$ be a set of n points in the plane, each with unique locations.
2. The *cell* c_i is the region of the plane which is nearer to p_i than any other p_j , and has area a_i . When two points have the same coordinates, a_i is undefined. Cell boundaries are equidistant between two points, and boundaries meet at nodes which are equidistant from 3 or more points.
3. c_i has density $\rho_i = a_i^{-1}$. We estimate a density uncertainty of $\alpha_{\rho_i} = \rho_i$, due to the 100% Poisson uncertainty for a single count.

This produces almost one density estimate per point.³

The algorithm can be extended to Poisson count data in an array of pixels, where some points are likely to have the same coordinates in dense regions. We do not take into account regions with missing data (for instance in the map of galaxy positions on the sky, where a region around a bright star has been excised) or variations in the weight map values. The algorithm is modified slightly:

1. Let $q = \{q_0, q_1, \dots, q_n\}$ be the coordinates and $u = \{u_0, u_1, \dots, u_n\}$ be the corresponding values of all non-zero pixels in the array.
2. The cell d_i is the region of the plane which is nearer to q_i than any other q_j , and has area b_i . Only point positions are quantised; b_i is measured using fractional pixels, rather than whole pixels, because pixels are often split several ways in dense regions.
3. The density of cell d_i is $\rho_i = \frac{u_i}{b_i}$. We assume a Poisson uncertainty on u_i , so that the density uncertainty is $\alpha_{\rho_i} = \frac{\sqrt{u_i}}{b_i}$.
4. Each pixel in S is assigned the value and uncertainty of the cell into which its centre falls. Pixels on cell boundaries are assigned values at random from their adjacent cells.

³Some points at the edge of the distribution have unbounded cells and therefore undefined areas.

The results are shown in panel iii.) Figure 3.2, and compared with ideal results in panel iii.) of Figures 3.3a and 3.3b. The contours shown in panel iii.) of Figure 3.2 show that this method produces the smoothest results at intermediate densities ($\omega \sim 10^{-2}$) where pixels have values 0 or 1, and counts are sparse. In higher density regions, the densities measured in adjacent cells can be quite different despite the smooth input map. Even in the densest regions, each density estimate suffers from large fractional count errors which arise because the algorithm uses at most a few points to estimate each density.

3.1.4 Adaptive aperture smoothing

Many of the problems associated with the Voronoi diagram method can be attributed to the 100% fractional errors. This issue, and some of the problems associated with smoothing on fixed length scales, can be ameliorated by using a variable smoothing scale whose size depends on the density of points in the region to be smoothed.

We investigated two variations on the adaptive aperture smoothing approach – a 2D top-hat filter, and an isotropic 2D Gaussian filter with its size set by counts within a comparably sized top-hat filter. The method is as follows:

1. Decide a target SNR_t and n_{bin} as outlined in Section §3.1.1
2. Initialise S to consist of null values. The starting aperture radius is defined to be $r_{\text{max}} = 1$ pixel.
3. Define a top-hat kernel,

$$M(x', y') = \begin{cases} 1 & \in |\mathbf{r}'| \leq r_{\text{max}}, \\ 0 & \in |\mathbf{r}'| > r_{\text{max}}, \end{cases} \quad (3.4)$$

where $\mathbf{r}' = \begin{bmatrix} x' \\ y' \end{bmatrix}$.

- (a) For the Gaussian variation, also define a truncated 2D Gaussian filter,

$$G(x', y') = \begin{cases} \frac{1}{2\pi\sigma^2} \exp\left(-\frac{x'^2+y'^2}{2\sigma^2}\right) & \in |\mathbf{r}'| \leq r_{\text{max}}, \\ 0 & \in |\mathbf{r}'| > r_{\text{max}}, \end{cases}$$

$$\sigma = \frac{r_{\text{max}}}{3}.$$

4. Calculate the smoothed count map $C = \omega_{\text{ct}} * M$ (and $D = \omega_{\text{ct}} * G$) and smoothed area map $E = A * M$ (and $F = A * G$).
5. For each pixel i where $C_i \geq n_{\text{bin}}$ and a value for S_i has not yet been assigned, set
 - (a) $S_i = \frac{C_i}{E_i}$ and $\alpha_{S_i} = \frac{\sqrt{C_i}}{E_i}$ in the case of the top-hat variation, and

(b) $S_i = \frac{D_i}{F_i}$ and $\alpha_{S_i} = \frac{D_i}{F_i \sqrt{C_i}}$ in the case of the Gaussian variation.

6. If any pixels in S are still null, increase r_{\max} by 1 pixel and repeat steps 3 to 6.

We handle area normalisation in step 5 rather than in the definition of M for several reasons. Since M has a uniform value of 1, C is the count of galaxies within the aperture around each pixel – rather than the density – and is computationally useful for the selection of pixels which fulfil the SNR criterion for a given r_{\max} in step 5. By calculating the area normalisation in the aperture around each pixel, the method produces correct density estimates in apertures where some pixels have $A = 0$, for instance where data are missing or galaxies are unobservable due to image artefacts around a bright star. This explicit area normalisation step also deals with the non-preservation of counts due to truncation of G . The integrated value of G is 0.989, but this difference from 1 does not contribute to a systematic reduction in S because it contributes to both D_i and F_i and cancels out when $S_i = \frac{D_i}{F_i}$ is calculated.

The results using the top-hat and Gaussian variations with $\text{SNR}_t = 5$ ($n_{\text{bin}} = 25$) are shown in panels iv.) and v.) of Figure 3.2. These are compared with ideal results in panels iv.) and v.) of Figures 3.3a and 3.3b. Inspection of the 10^{-2} and 10^{-1} contour shapes in both cases show that the results are broadly similar. In lower density regions, the Gaussian variation leads to subtly different results. These can be seen in the centre of the compact object at (50, 50). In the top hat smoothed version, the shape of the object is smeared out, but the central density peak is at about the right level. In the Gaussian variation, the shape of the contours is a better match for the ideal contour shape, but the central density peak level is underestimated.

The results after applying the Gaussian variation with a lower $n_{\text{bin}} = 8$ (corresponding to $\text{SNR}_t = \sqrt{8}$) are shown in panel vi.) of Figures 3.2, 3.3a and 3.3b. This method characterises the size and shape of the compact object better than any other method. However, the contours at all densities are less regular than with $n_{\text{bin}} = 25$ and the appearance of the densest region is noisier than the higher SNR_t versions – reminiscent of the results of the Voronoi tessellation method.

3.1.5 Summary

We have shown the effect of a range of smoothing algorithms on a contrived point distribution which has some of the features we expect to see in the spatial distribution of galaxies within galaxy clusters. The fixed width algorithms only work for the range of point densities where there are a substantial number of points per bin/smoothing kernel area. Fixed scale algorithms often under-sample the spatial signal and fail to characterise the peak densities and rapid density changes.

It is clear that the Voronoi tessellation and adaptive smoothing methods give a better estimate of local density from the pure point data. Within these methods, variations using a small number of points per density estimate – Voronoi tessellation with 1 point per estimate, or adaptive smoothing with a low minimum point count per aperture – produce

the noisiest results but allow the characterisation of the smallest local over-densities. A larger number of points per aperture leads to smoother results with a tradeoff of poorer characterisation of small features.

In 5 we use the adaptive top hat technique to generate maps of galaxy count density in clusters. The top hat method gives better estimates of the peak density of sub-clumps than given by the Gaussian adaptive method, and we were primarily interested in the peak densities rather than the overdensity shapes. We ran simulations using more realistic ‘ β -model’ cluster galaxy distributions, varying n_{bin} in the range 2^3 – 2^9 , inspecting the results and comparing them with the original density maps. We found that for data with the same frame size and point density as real WFI@2.2m observations, $n_{\text{bin}} = 2^5$ was sufficiently fine to reveal substructures of interest whilst limiting the appearance of image artefacts.

3.2 Background subtraction

In many cases a method to remove or account for background points in a point distribution is necessary. In cases where a robust model of the target and background distributions exists, the model and background parameters can be found by fitting a model to the point positions. Where similar data which do not contain the target distribution are available, a more direct, non-parametric and model independent background subtraction method can be applied.

We were interested not only in the overall density of points, but also the properties of individual points in the distribution. For this reason, we wanted to perform background subtraction on a point-by-point basis, rather than just dealing with the overall distribution. We investigated two alternatives for background subtraction of point data, which we illustrate using the point distribution from Section §3.1. In Section §C.2 we show that the same approach is applicable to background subtraction in a colour–magnitude diagram.

3.2.1 Stochastic point removal

One way to subtract the background from a target field is to make a guess at which points might be a part of the background, and then to remove them. In *stochastic point removal* (or *Poisson killing*):

1. Generate a point distribution representative of an *empty field* – i.e. an observation in a comparable coordinate space which has a comparable distribution of background objects, but no target structures. This might be derived from a real observation of a comparable region without any structures of interest, or simulated from a background model derived from the target field.
2. Loop through the list of empty field points, removing the nearest point in the target data for each background point.

The final catalogue is the list of target data points which have not been removed after all the background points have been used.

In Figure 3.4 we show the results of running this algorithm on the point distribution from Figure 3.1b in the case where we have a perfect model of the background distribution. We differentiate in the plot between points which were originally due to the background or due to the target objects. The algorithm is successful in removing most of the background points and very few target points in the region $y > 150$. In the region $x < 75$, $y < 75$ about half of the points from the compact object are removed and some background points at the very bottom of the field are left un-killed.

In Figure 3.5 we show the results in a more realistic situation where the background level has not been correctly identified, and is modelled as uniform across the field. This leads to serious problems with the results – a trail of points belonging to the background in the region $x > 200$, $y > 200$ are untouched, and almost all the points in $y < 100$ are removed, including the whole of the compact object and some points from the lower edge of the main elliptical overdensity around $x \sim 100$, $y \sim 100$. We found when we ran this method on the spatial positions of galaxies in the REXCESS sample, that the background level was not uniform across some of the images. We took this to be evidence of structures on scales larger than the clusters themselves appearing in the observation fields.

An obvious extension to this method is to run it several times with different realisations of the background and then combining all of the results to give a weight to each galaxy, rather than a boolean 0 or 1. The fraction of these runs in which a particular point is removed is then the probability that it belongs to the target rather than the background, and the precision with which the weight can be stated depends on the number of iterations. This Monte-Carlo approach allows one to have a better understanding of the probability that each point is in a non-background structure, as long as the background density estimate is correct.

3.2.2 Membership probability from density estimates

Results similar to those from the Monte-Carlo extension of the stochastic point removal method can be arrived at by a more direct route:

1. Given a target and background distribution τ and β (smoothed using one of the methods described earlier, or due to a fitted model), we define a *target probability* map,

$$P_t = \frac{\tau}{\tau + \beta} = 1 - \frac{\beta}{\tau + \beta}. \quad (3.5)$$

2. Each point in the target region catalogue is assigned the value from the corresponding pixel in P_t .

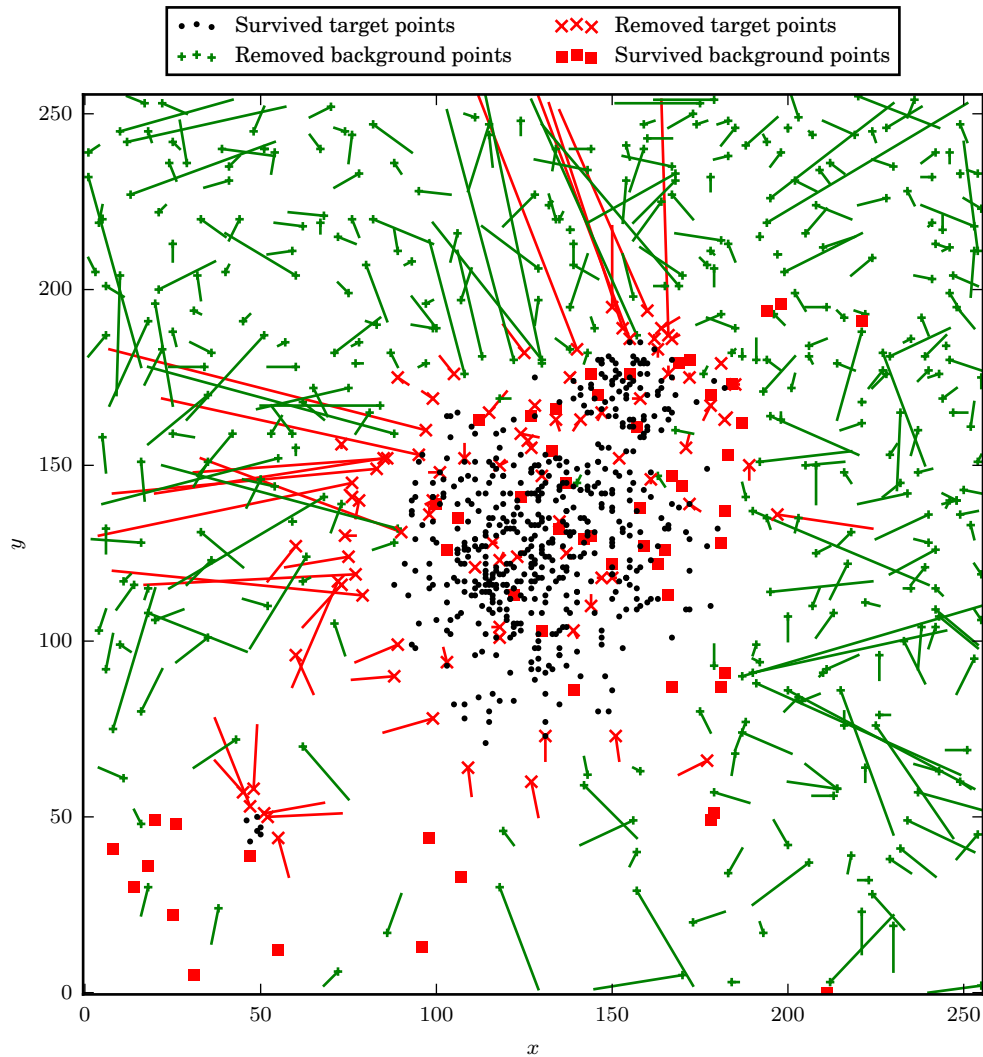


Figure 3.4: Stochastic point removal applied to the point distribution shown in Figure 3.1b, using background points derived from a perfect background map. The red crosses and squares show where the algorithm has erroneously removed a target point or left a background point in the data. Green crosses mark where background points have been removed correctly. A line is shown between the position of each killed point and the location of the empty field point which was responsible for its removal.

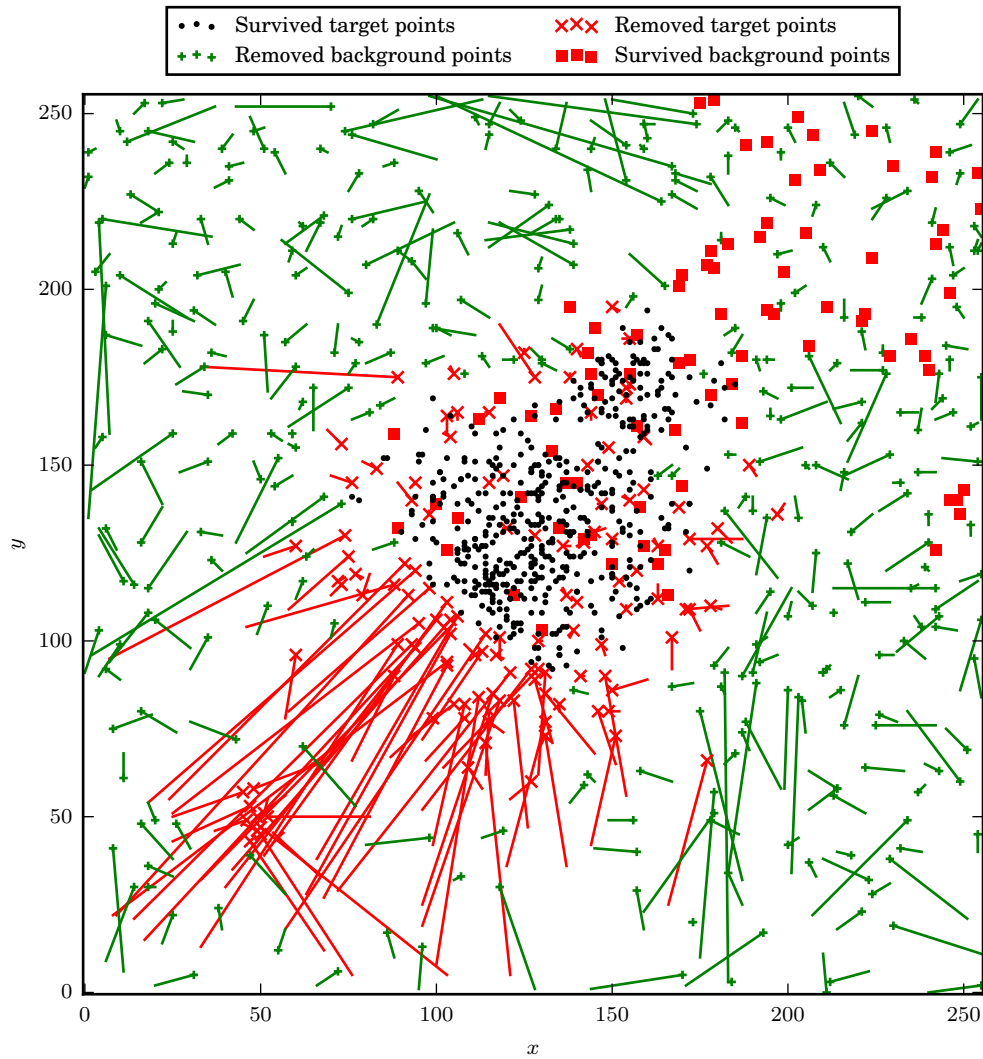


Figure 3.5: Stochastic point removal where the total background expectation value is correct, but is modelled as uniform distribution across the field. The details are as in Figure 3.4.

In real cases, we are likely to have a model of the background Γ and a smoothed observation S . In that case

$$P_t = \frac{S - \Gamma}{S}, \quad (3.6)$$

is equivalent. This can lead to logical inconsistencies with $P_t > 1$ or $P_t < 0$ if (for example): $\Gamma > S$, as may well occur due to a statistical fluctuation in the local density; or S or Γ is undefined, as occurs using Voronoi smoothing methods for points at the edge of the coordinate spaces; or if $S \leq 0$ which may occur using fixed scale smoothing algorithms. These inconsistencies arise from the scatter in the density estimates, and can be reduced by choosing a higher SNR_t in the smoothing algorithm.

The result of applying this measurement to a point distribution is shown in Figure 3.6 with a perfect target and background model, and in Figure 3.7 with a more realistic background model due to the smoothed density map from a simulated empty field observation. The results show that for points in the densest target regions, values of $P_t > 0.5$ are measured. In addition, the points in the compact object at $(50, 50)$ are also assigned $P_t > 0.5$. There are a large number of points misclassified when we apply this simple P_t threshold.

Clearly, we cannot use this method alone to make robust estimates of whether individual points are members of the target – for that one would need much more information like spectroscopic redshifts. Instead, P_t represents the fraction of points with a particular coordinate in a catalogue which belong to the target. In other words, we can use it to weight points in measurements of the properties of the target objects as a whole. We apply this weighting in Section §4.3.9.3 to calculate the total luminosity of galaxies in a cluster, using a 1D NFW radial profile model plus a constant background in place of τ and β .

When applying this weighting, the smoothing algorithm is of critical importance. We investigated this weighting method in parallel with the Voronoi density estimate described in Section §3.1.3 but the P_t results are badly affected by the large fractional errors. Using adaptive smoothing, as shown in Figure 3.7, gives better results.

3.3 Red sequence

A key step in our analysis was to detect the red sequence of galaxies in the galaxy catalogues, a line in the colour–magnitude diagram of cluster galaxies, which can be seen when the two bands used to calculate the colour bracket the 400 nm spectral break of elliptical galaxies (the red sequence was introduced in Section §1.3.2.4). This feature falls in the B band for all of the clusters in this sample, as shown in Figure 2.1, and the red sequence can be seen in (R, C_{B-V}) and (R, C_{B-R}) .

Because the red sequence shifts in colour with z , selecting red sequence galaxies is a form of z selection. Making such a selection reduces the background in measurements of galaxy count density and increases the SNR of the distribution of interest – the cluster galaxies. In addition, red sequence selection allows us to compare the distribution of galaxies which had long been cluster members with the distribution of bluer galaxies

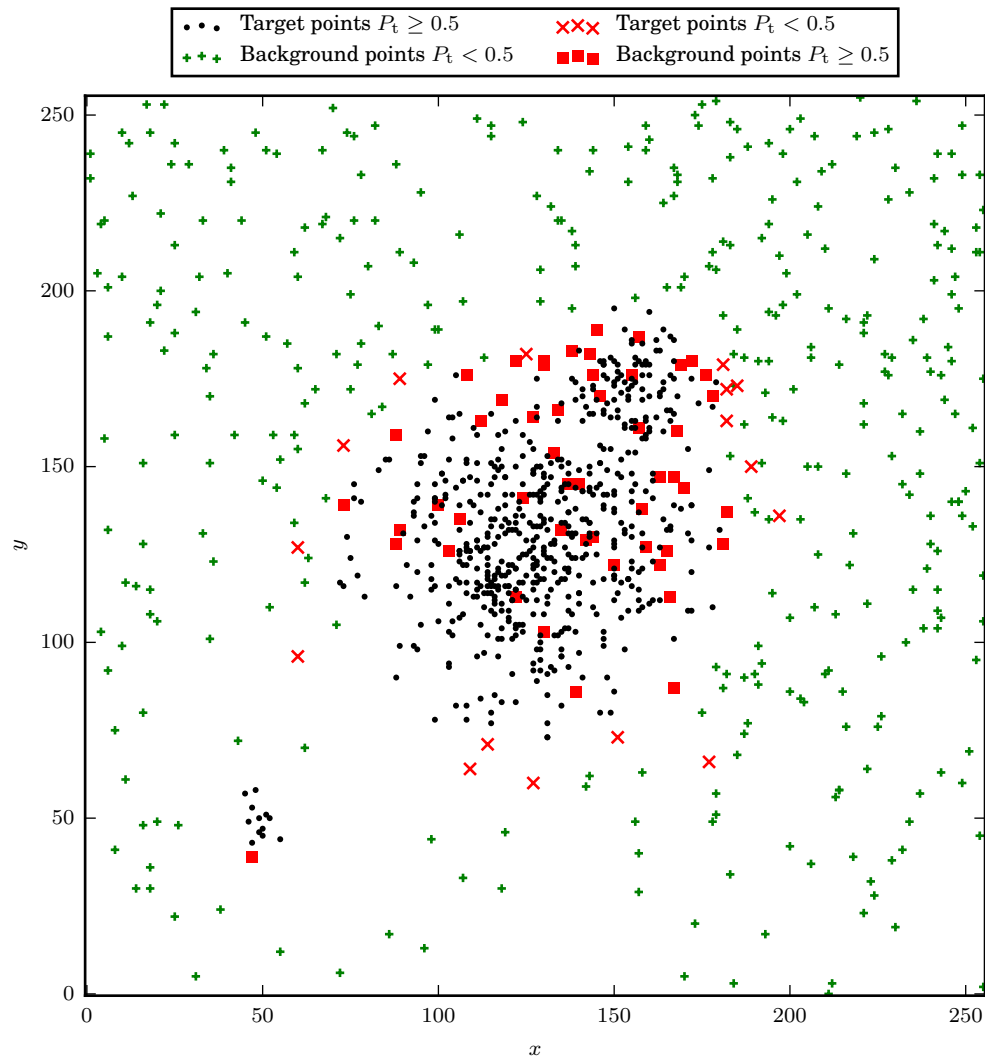


Figure 3.6: Membership probability estimates for the point distribution shown in Figure 3.1b. Probabilities are calculated using Equation (3.5), and the target and background densities used are identical to those used to generate the point data. Each point is assigned a floating point value $0 \leq P_t \leq 1$, but we split the points in this case at $P_t = 0.5$, a threshold which shows the broad trends in the results.

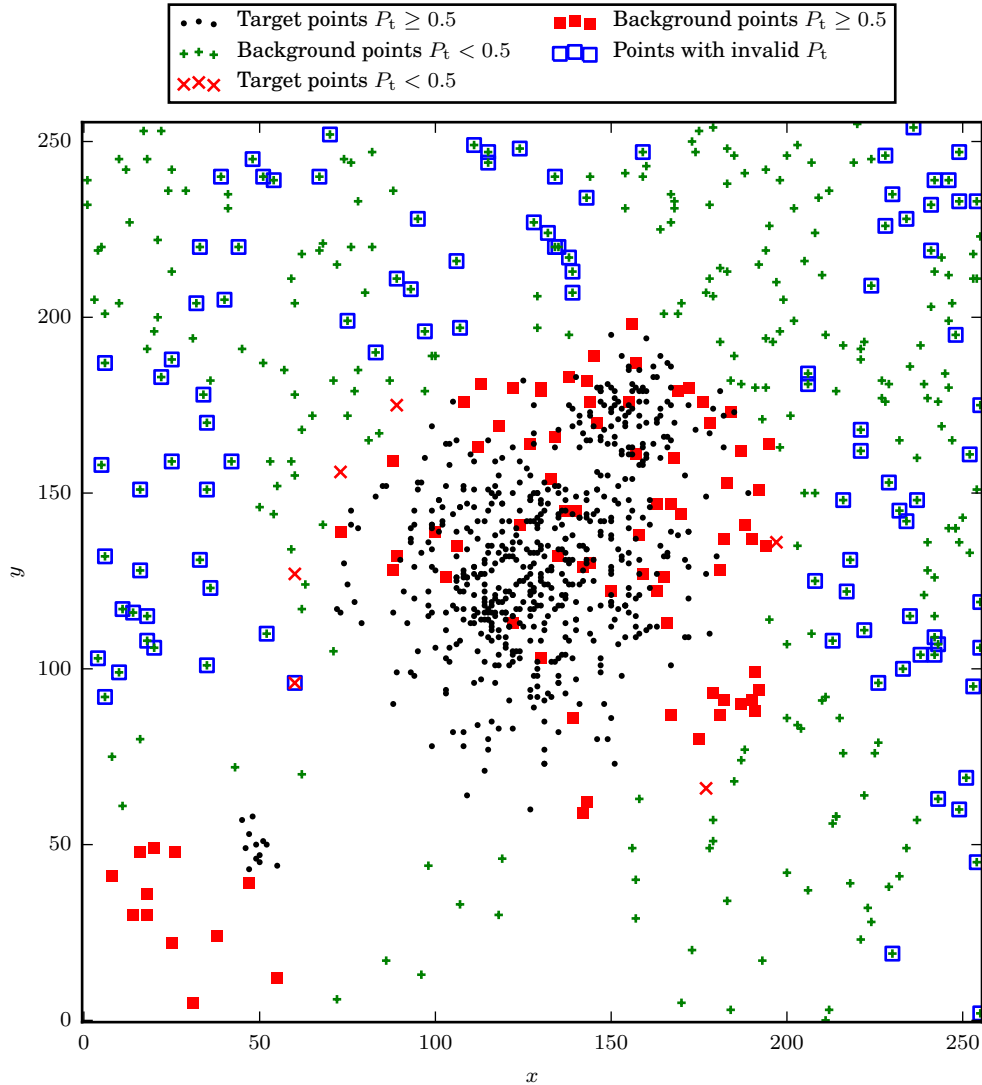


Figure 3.7: Membership probability estimates for the point distribution shown in Figure 3.1b. Probabilities are calculated using Equation (3.6). S and Γ are calculated by applying the adaptive Gaussian smoothing method with $\text{SNR}_t = 5$ to the point distribution shown in Figure 3.1b and the empty field points used in Figure 3.4 respectively. (This means that the background point distribution is a good representation of the real background). The details are the same as in Figure 3.6. Points with invalid $P_t < 0$ or $1 < P_t$ are surrounded with a box.

with substantial gas reservoirs, new to the cluster environment.

In Section §3.3.1 we outline some of the red sequence fitting methods we investigated. In Section §3.3.2 we show the 3D appearance of the red sequence in the (R, C_{B-V}, C_{B-R}) coordinate space, motivating our choice of the C_{B-V} colour for selection of the red sequence in Chapters 4 and 5. Finally, in Section §C.1 we show a simple colour–magnitude density model which can be used to simulate red sequences for testing purposes, and which was developed out of the investigation we outline here.

3.3.1 Fitting methods

We found red sequence detection to be rather tricky. This section outlines the two main classes of fitting methods we used, and why the second is better than the first.

We treat the red sequence as a straight line,

$$C_{\text{model}}(M) = g(M - Z) + k \quad (3.7)$$

where C is the colour, g is the gradient, M is the magnitude, and k is the value of $C_{\text{model}}(M)$ at the *pivot point* Z . In addition, we define the colour residual $C_{\text{residual}}(C, M) = C - C_{\text{model}}(M)$ and the *red sequence displacement*,

$$w_{\text{rs}} = \frac{C_{\text{residual}} - o_r}{\sigma_r},$$

where σ_r measures the width of the red sequence and o_r is a parameter which describes any systematic offset between the true red sequence and C_{model} . For well fitted red sequences, $o_r \simeq 0$. We treat σ_r as the standard deviation in a Gaussian distribution, and define $-3\sigma_r < w_{\text{rs}} < 3\sigma_r$ to be *on the red sequence*.

The colour–magnitude diagram of galaxy clusters usually comprises of a compact red sequence and diffuse cloud of blue galaxies with a single or double Schechter function distribution in magnitude space. This is overlaid on a field of galaxies of a broader range of colours with a much steeper magnitude space distribution. The relative density of the different components is variable between rich and poor clusters in dense or low density regions of the cosmic web. As cluster-centric distance increases, the fraction of galaxies which belong to the red sequence as opposed to the blue cloud decreases, but there is still a population of red sequence galaxies at $> r_{500}$, in the region we use for background subtraction.

3.3.1.1 Iterative clipping methods

Our first attempt at fitting the red sequence in galaxy clusters was a simple iterative line fitting method, operating in 2D colour–magnitude space, and with 3σ clipping:

1. An arbitrary selection of the colour–magnitude points is made, i.e. $R < 20; 0 < C_{B-V} < 1.5; r < r_{500}$. A value for Z is defined; we used the BCG magnitude.

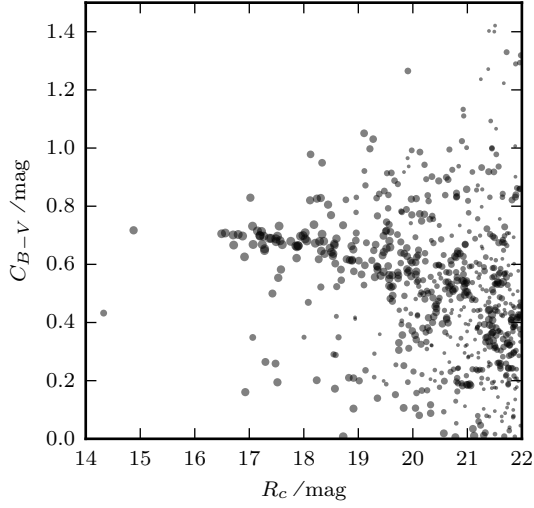
2. The best fit parameters of Equation (3.7) for the selected data points are determined.
3. The 1σ line fit uncertainties are used to define σ_r , which varies with magnitude. (The shape of this region is strongly dependent on the choice of Z .)
4. The points satisfying $-3\sigma_r < w_{rs} < 3\sigma_r$ are selected.
5. If the point selection is the same as in the previous round of fitting, the algorithm stops. Otherwise, steps 2 to 5 are repeated.

We tried a number of variations on the theme of this algorithm, with different methods to calculate the size of the red sequence region, different definitions of the position of the line intercept which change the way the red sequence region flares out at larger magnitudes, using different starting parameters, and using two colours rather than one (the 3D red sequence appearance is discussed in Section §3.3.2). In many cases this kind of approach works because the red sequence is a significantly stronger feature in the colour–magnitude space than any other. In these cases, the algorithm almost always converges, regardless of the variation used. However, there are a few clusters in our sample where the red sequence is relatively weak, and the iteration never actually leads to a line which is consistent with the obvious red sequence.

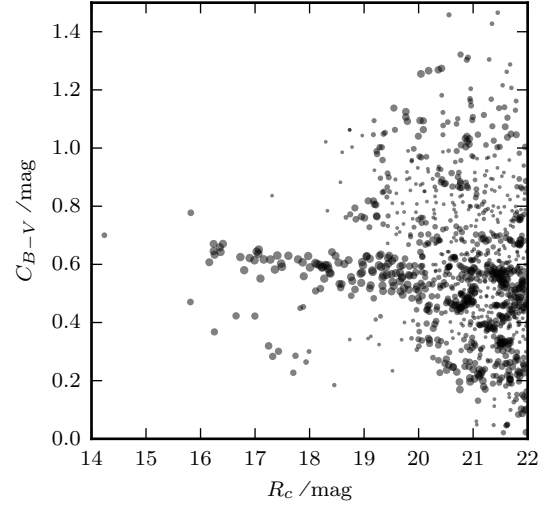
For these tricky cases, we developed the smoothing and weighting tools described in Sections 3.1 and 3.2.2, and applied these to increase the SNR of the red sequence, but these failed to improve the fitting. Examples of the colour–magnitude diagrams weighted using these methods are shown in Figure 3.8.

We found a common pattern in the cases where iterative fitting failed. Where the red sequence is very diffuse, a small overdensity bluer than the red sequence at higher magnitude [e.g. near (21, 0.4) in Figure 3.8c] draws the gradient to steeper values. The similar overdensity at (21, 0.4) in Figure 3.8a does not lead to a failure of the algorithm because the red sequence itself provides a much stronger pull. Weighting or background subtraction methods do not help because the blue cloud is as much a part of the cluster structure as the red sequence. The fundamental problem of fitting red sequences is the presence of the blue cloud of galaxies – the SNR of which is also increased by applying the weighting methods. The admixture of red sequence galaxies in the ‘empty’ region does reduce the signal from the red sequence, but this effect is less important.

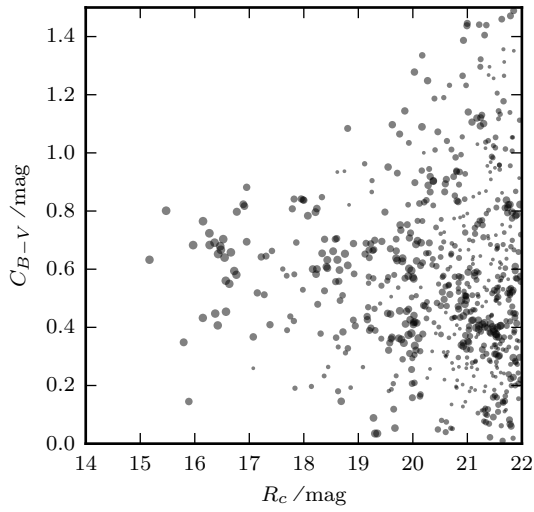
The obvious way to define the red sequence region – based on the uncertainty on the position of the line fit taking into account the uncertainties on intercept and gradient – leads to large differences in the red sequence shapes, whereas we might expect them to be fairly similar across all clusters. This also leads to a situation in some cases where as the line parameters become better bounded, with smaller uncertainties, the selection becomes narrower and narrower, leading to a vicious cycle of artificially low uncertainties on the line fit parameters and even narrower selections.



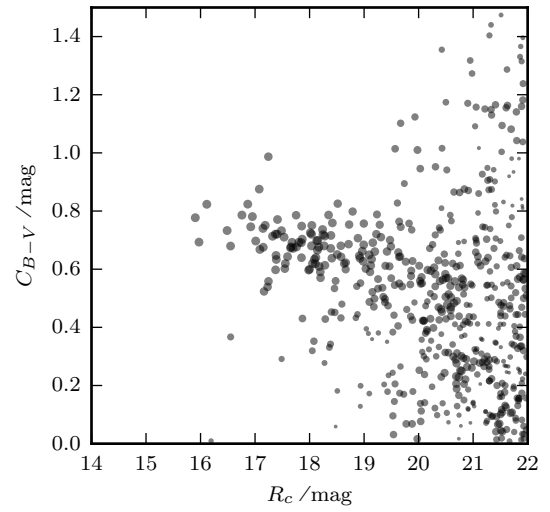
(a) Case with a clear red sequence: RXC J0616.8–4748.



(b) Case with a clear red sequence: RXC J0345.7–4112.



(c) Case with a very unclear red sequence: RXC J2319.6–7313.



(d) Case with a prominent but diffuse red sequence: RXC J0547.6–3152.

Figure 3.8: Colour–magnitude scatter plots with point sizes proportional to P_t [Equation (3.6)]. S was generated by applying the adaptive Gaussian smoothing algorithm with $\text{SNR}_t = 5$ to the catalogue of colour–magnitude points within $< r_{500}$. Γ was generated with the same algorithm, and points $> 1.5r_{500}$. The smoothing algorithm is described in described in Section §3.1.4.

3.3.1.2 Iterative clipping after collapse along red sequence axis

It became clear that iterative fitting was not sufficiently robust. We guessed that the red sequence and blue cloud could be treated as two parallel components, and developed the following method to exploit this property and produce more reliable fits:

1. Guess the red sequence gradient. We took the value $g = -0.044$ from the literature (Valentinuzzi et al., 2011). Since all of the clusters in our sample have similar redshifts, this was expected to change little across the sample.
2. Skew the colour–magnitude space so that lines parallel with the red sequence gradient are horizontal. Equivalently, calculate $C'_{\text{residual}} = C - g(M - Z)$ for each point.
3. Take a histogram of C'_{residual} values. We found that this histogram could be fitted in every case using a double Gaussian model,

$$\begin{aligned} \Psi(C'_{\text{residual}}) &= \psi_r \exp\left(-\frac{(C'_{\text{residual}} - o_r)^2}{2\sigma_r^2}\right) + \psi_b \exp\left(-\frac{(C'_{\text{residual}} - o_b)^2}{2\sigma_b^2}\right), \\ &= \Psi_r(C'_{\text{residual}}) + \Psi_b(C'_{\text{residual}}), \end{aligned}$$

where $\sigma_r < \sigma_b$, the Ψ_r component is the red sequence, the Ψ_b is the blue cloud plus the cosmic background. Crucially, there is no red sequence selection in this step.

4. Select the points satisfying $-3\sigma_r < w_{rs} < 3\sigma_r$.
5. Fit the straight line Equation (3.7) to these red sequence points in the original (un-skewed) colour–magnitude space. This step yields new values for g and k .
6. Repeat steps 2 to 6 until the red sequence position stabilises. If the position never stabilises and the algorithm goes into a loop, choose the red sequence line which led to the narrowest red sequence Gaussian in step 3.

The algorithm stacks the data from all magnitudes to increase the SNR of the red sequence distribution during the point selection step, and is not affected by the same vicious cycle of narrowing selection which plagues iterative fit method. The initial gradient guess must be sufficiently accurate that it leads to a strong red sequence spike in the colour histogram. In many cases, taking an initial gradient estimate of 0 was sufficient, but in the case of some clusters with very high background or diffuse red sequences (like the one shown in Figure 3.8c), this led to a red sequence spike which was too smeared-out.

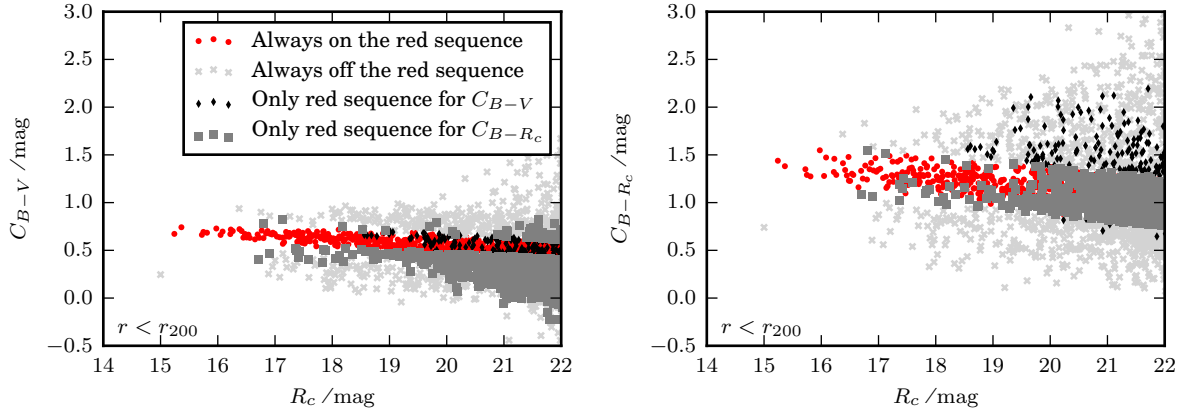
This method is applied in Chapter 4 and Chapter 5 for red sequence detection. We make a comparison of the red sequence fitting results against those from the literature in Section §4.3.5.

3.3.2 3D appearance

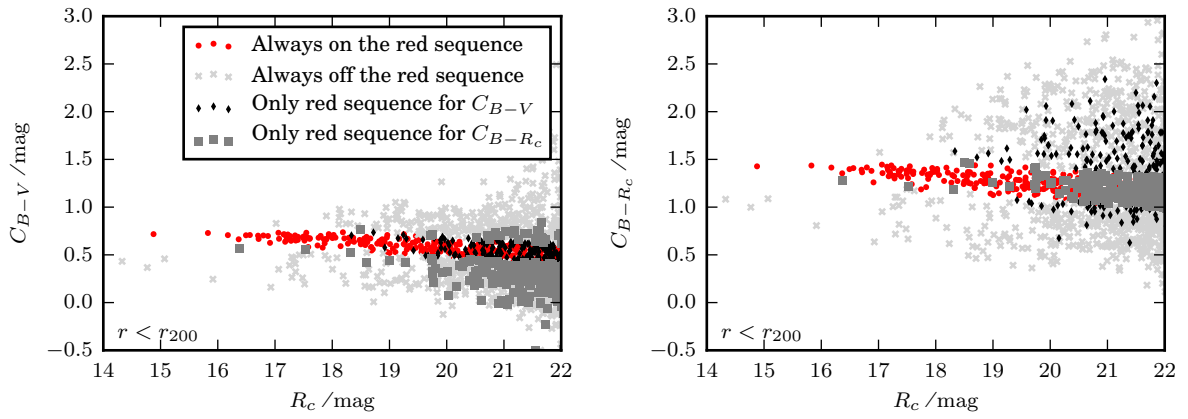
Since both C_{B-V} and C_{B-R} bracket the 400 nm spectral break, it is of interest to compare the appearance of the red sequence in each colour. In Figure 3.9, (R, C_{B-V}) and (R, C_{B-R}) colour–magnitude diagrams for clusters in the REXCESS sample are shown. We applied the fitting method described in Section §3.3.1.2 to each band independently, and we show the differences between the selections of red sequence objects for the two bands.

The data show that the colour with the smaller wavelength difference between the bands – C_{B-V} – has the tighter red sequence. The data also show that there is a population of galaxies which are selected as red sequence members in one band, but not in the other. A large fraction of red sequence galaxies are classified as such in both colours.

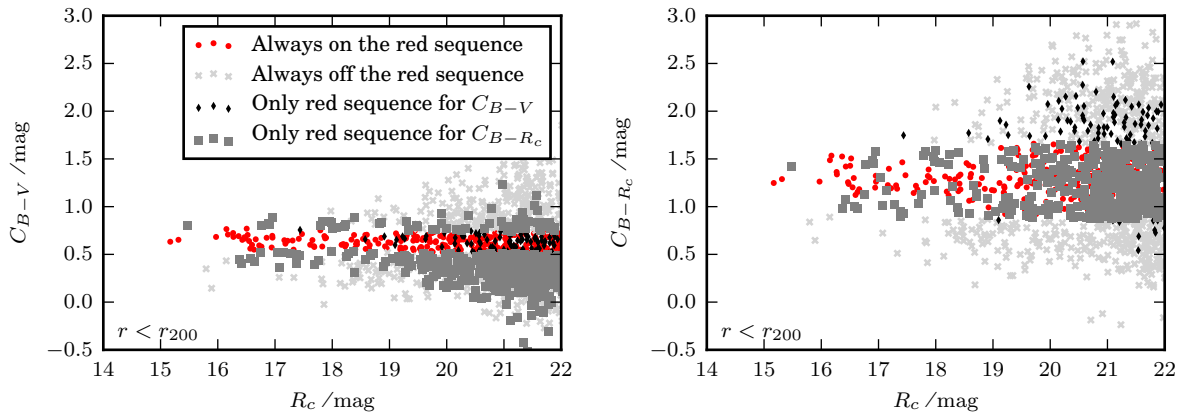
We have not investigated the spectra of red sequence galaxies in any detail, but we suspect that the galaxies which have different classifications might be non-cluster members which are serendipitously in the same colour–magnitude space as the red sequence due to their z . Regardless of the reason, C_{B-V} has many fewer potential misclassifications of galaxies and exhibits a tighter red sequence. We elected to use this single band pair for red sequence classification in Chapters 4 and 5, rather than a joint classification based on both C_{B-V} and C_{B-R} , because the 2-colour scheme was unnecessarily complex given the marginal increase in discriminatory power.



(a) RXC J0006.0-3443



(b) RXC J0616.8-4748



(c) RXC J2319.6-7313

Figure 3.9: Galaxy colour-magnitude diagrams for the $< r_{200}$ region in the REXCESS sample showing two band pairs in each case. Points which are part of the fitted red sequence in one band but not in the other are marked.

Chapter 4

Optical and X-ray profiles in the REXCESS sample of galaxy clusters

John G. Holland, Hans Böhringer, Gayoung Chon and Daniele Pierini

Monthly Notices of the Royal Astronomical Society, 2015 448 (3): 2644-2664
doi:10.1093/mnras/stv097

Abstract

Galaxy clusters' structure, dominated by dark matter, is traced by member galaxies in the optical and hot intra-cluster medium (ICM) in X-rays. We compare the radial distribution of these components and determine the mass-to-light ratio vs. system mass relation.

We use 14 clusters from the REXCESS sample which is representative of clusters detected in X-ray surveys. Photometric observations with the Wide Field Imager on the 2.2m MPG/ESO telescope are used to determine the number density profiles of the galaxy distribution out to r_{200} . These are compared to electron density profiles of the ICM obtained using *XMM-Newton*, and dark matter profiles inferred from scaling relations and an NFW model.

While red sequence galaxies trace the total matter profile, the blue galaxy distribution is much shallower. We see a deficit of faint galaxies in the central regions of massive and regular clusters, and strong suppression of bright and faint blue galaxies in the centres of cool-core clusters, attributable to ram pressure stripping of gas from blue galaxies in high density regions of ICM and disruption of faint galaxies due to galaxy interactions. We find a mass-to-light ratio vs. mass relation within r_{200} of $(251.1 \pm 33.7) h M_{\odot} L_{\odot}^{-1}$ at $10^{15} M_{\odot}$ with slope 0.11 ± 0.14 , consistent with most previous results.

4.1 Introduction

Galaxy clusters are the most massive gravitationally bound and virialised objects in the observable Universe, with masses up to a few $\times 10^{15} M_{\odot}$ (e.g. Köhlinger and Schmidt (2014) measure the projected mass within 200 kpc of RXC J1347.5–1145 – one of the most X-ray luminous clusters found – to be in the range $(2.19–2.47) \times 10^{15} M_{\odot}$). Superclusters of galaxies can be more massive and bound, but are unvirialised, e.g. Chon, Böhringer, and Nowak (2013). Galaxy clusters are interesting as their contents are reasonably representative of the contents of the universe as a whole and they contain a population of coeval galaxies whose appearance is affected by a whole range of astrophysical processes and the interactions between the processes.

The dominant baryonic component of galaxy clusters is the intracluster medium, (ICM), a hot ($>10^7$ K), X-ray emitting plasma which contains most of the baryonic mass (e.g. Lin et al., 2003). The gas becomes X-ray luminous after being heated by adiabatic compression and shocks during cluster collapse (e.g. Gunn and Gott, 1972; Kravtsov and Borgani, 2012). A fraction of the clusters have a centre where the density is high and where entropies can be low enough that cooling should take place on the order of the Hubble time (Fabian, 1994), but feedback mechanisms quench cooling flows (Bower et al., 2006; Fabian, 2012 is a recent review), adding additional energy to the initially gravitationally heated gas and causing it to be more broadly distributed than the dark matter potential. Cluster mass profile estimates from X-ray data, including ICM density measurements, are limited to the region in which robust temperature measurements can be made. For *XMM-Newton* and *Chandra*, this is typically $\lesssim r_{500}$; *Suzaku* and *ROSAT* can reach r_{200} with substantially lower spatial resolution (Reiprich et al., 2013) (Δ is the ‘halo overdensity’ and r_{Δ} refers to the radius of the volume in which the mean density is Δ times the critical density of the universe).

Cluster galaxies can be used to probe the cluster environment to greater cluster-centric distances than gas and can be treated as approximately collisionless particles moving in the dark matter potential well of the cluster. The well known morphology-density relation – higher fractions of elliptical galaxies in high density environments like galaxy clusters, compared to low fractions of elliptical galaxies in the lower density field environment (Dressler, 1984) – is caused by the ICM and the presence of other galaxies, but a precise description of the way the different components involved interact is not yet available. The critical processes are: ram-pressure stripping, where weakly bound gas is stripped away from galaxies by interaction with the ICM (Gunn and Gott, 1972); strangulation, where galaxies are starved of cool gas in their haloes – gravitational heating combined with the active galactic nucleus (AGN)/wind/supernova feedback mechanisms already mentioned lead to ICM entropy which is too high for effective cooling and replenishment of the cool gas (Larson et al., 1980); harassment – gravitational interactions between galaxies which increase internal energy and lead to morphological change (Farouki and Shapiro, 1981; Moore et al., 1996; Moore, Lake, and Katz, 1998); and galactic cannibalism, where dynamical friction reduces the velocity of satellites relative to the central galaxy below the velocity dispersion of the satellite, allowing it to be accreted on to the central galaxy

(Ostriker and Hausman, 1977). Galaxies at low cluster-centric distances are preferentially harassed and starved due to the high ICM density and more frequent encounters with other cluster galaxies, including cD galaxies which are often the brightest cluster galaxy (BCG). Faint and dwarf galaxies with the weakest dark matter haloes and the weakest hold on their gas reservoirs fare the worst in this environment such that the population of cluster galaxies seen at $z > 0.4$ which includes a large fraction of star forming galaxies changes by $z = 0$ into a population dominated by galaxies with very low star formation rates (Butcher and Oemler, 1984; Dressler et al., 1994; Oemler et al., 1997; Popesso et al., 2006; Boselli and Gavazzi, 2006).

It should be noted that an X-ray selected sample like the Representative *XMM-Newton* Cluster Structure Survey (REXCESS, Böhringer et al., 2007), used in the present study, preferentially represents objects with higher ICM densities, so we could expect that any ICM-dominated effects would be stronger in our results than in other, optically selected samples (e.g. Carlberg et al., 1997) or partially optically selected samples (e.g. Popesso et al., 2004). They also preferentially include clusters with deep potential wells and thus more time available for galactic evolution. Böhringer et al. (2004) show that cool-cores in clusters must be preserved on very long time-scales and we could expect these to cause distinctive features in the population of galaxies. Conversely, if we assume clusters which show disturbances in their X-ray morphology are relatively recent mergers, we would expect their galactic populations to be less evolved than in other types of cluster and might also show some trace of disturbance in the galaxy distribution.

In this work we study the relationship between the optical density profiles of the galaxy distribution and the density profiles of X-ray emitting gas in X-ray selected galaxy clusters. We explore the extent to which galaxies and gas trace one-another and the underlying dark matter. We also investigate how the red and blue galaxy populations are distributed. We investigate the total mass to optical light ratio of galaxy clusters, and measure how this varies with respect to total cluster mass and morphology (presence/absence of cool-cores, regular/disturbed ICM). By taking into account the morphology of our sample, we show clear differences in the distribution of different types of galaxies in the centres of clusters which have had relatively stable morphology for a long period of time – massive clusters or those which have cool-cores – when compared to clusters with signs of more radical recent evolution – disturbed and non cool-core clusters.

The paper is structured as follows. In Section §4.2 the sample characteristics, X-ray data and optical data are described. In Section §4.3 we describe all stages of the analysis including object detection, classification, optical data calibration, red sequence fitting, radial profile generation and luminosity measurements, along with the results generated at each stage. The results are discussed in Section §4.4. The conclusions are summarised in Section §4.5.

Throughout this paper, radial distances are measured in units of r_{500} . The influence of the cluster may extend further than this, so we typically use the region outside $1.5 r_{500} \sim r_{200}$ as the off-target region. ($r_{200} = 1.51r_{500}$ for a concentration $c_{500} = 3.2$, (Arnaud, Pointecouteau, and Pratt, 2007)). Magnitudes M in a given broad band filter (R, V, B) are signified by a subscript suffix, AB magnitudes by $_{AB}$, Johnson magnitudes by $_J$ and

K-correction by K . We adopt a flat cosmology where $h = 0.7$ (and $h = 0.7 h_{70}$), $\Omega_m = 0.3$, $\Omega_\Lambda = 0.7$ and $H_0 = 100 h \text{ km s}^{-1} \text{ Mpc}^{-1}$.

4.2 Sample description

4.2.1 REXCESS sample

The REXCESS sample has been compiled as a galaxy cluster sample, representative of clusters detected by their X-ray luminosity and independent of their morphology. The sample selection is described in Böhringer et al. (2007). The clusters have redshifts between $z = 0.055$ and $z = 0.183$ and luminosities above $0.4 \times 10^{44} h_{70}^{-2} \text{ erg s}^{-1}$ in the (0.1–2.4) keV band. The r_{500} region, where the mean density is $500 \times$ the critical density, plus a region outside where the background can be estimated are within the *XMM-Newton* field-of-view ($\sim 30'$). The mass range of the clusters is $M_{200} = (1.36 - 10.8) \times 10^{14} M_\odot$. They represent a relatively homogeneous population in X-ray luminosity, L_X .

The 14 objects comprising the subset of the REXCESS sample used in this work are tabulated with their key parameters in Table 4.1 and comprise approximately half of the complete REXCESS sample. The objects were selected by right ascension for ease of follow-up observation scheduling, and were observed first.

4.2.2 X-ray data

The X-ray observations are described in Böhringer et al. (2007). Each cluster was observed using all three detectors (MOS1, MOS2 and PN), and the mean final exposure after cleaning was $(1.4 \pm 0.7) \times 10^4 \text{ s}$ for PN and $(2.1 \pm 0.9) \times 10^4 \text{ s}$ for each of the MOS detectors. All exposures were cleaned from times of high background due to Solar flares and the PN data were corrected for out-of-time events. The mean fraction of exposure time lost to Solar flares was ~ 0.35 for PN and ~ 0.25 for MOS1/2.

Cluster centres were set by finding the density peak of the X-ray image on a scale of $8.2''$ (corresponding to $2 \times$ the PN pixel width), and all radial distances, r , were measured from these centres. r_{500} values are from Pratt et al. (2009) and were found through iteration of the $r_{500} - Y_X$ relation for morphologically relaxed clusters (eq. 1 in Pratt et al., 2009, Arnaud et al., 2007). Electron density profiles are from Croston et al. (2008). They were derived from surface brightness profiles using the non-parametric method of Croston et al. (2006) which performs a direct deprojection based on the assumption of spherical symmetry and a regularisation procedure, and involves a point spread function deconvolution, rather than fitting of a pre-determined gas density distribution to the surface brightness profile.

Table 4.1: Overview of the REXCESS clusters analysed in this paper. CC = cool-core, D = disturbed, M = massive. Abell Name, RA, Dec, z and L_x are from table 3 in Böhringer et al. (2007). r_{500} , CC and D are from table 1 in Pratt et al. (2009); M_{500} was derived from r_{500} and z using the fiducial cosmology. Massive objects are those with M_{500} above the median of the entire REXCESS population, $2.95 \times 10^{14} M_{\odot}$. ID is used in Figures in Section §4.3.9.4 to distinguish between the clusters in the sample.

Object	Abell Name	RA	Dec.	z	L_x 10^{37} W	r_{500} kpc	M_{500} $10^{14} M_{\odot}$	D	CC	M	ID
RXC J0006.0-3443	A2721	00 ^h 06 ^m 03.0 ^s	-34°43'27.0"	0.1147	1.875	1059.3	4.21	D		M	1
RXC J0049.4-2931	S0084	00 ^h 49 ^m 24.0 ^s	-29°31'28.0"	0.1084	1.503	807.8	1.84				2
RXC J0345.7-4112	S0384	03 ^h 45 ^m 45.7 ^s	-41°12'27.0"	0.0603	0.495	688.4	1.04		CC		3
RXC J0547.6-3152	A3364	05 ^h 47 ^m 38.2 ^s	-31°52'31.0"	0.1483	4.667	1133.7	5.53			M	4
RXC J0605.8-3518	A3378	06 ^h 05 ^m 52.8 ^s	-35°18'02.0"	0.1392	4.478	1045.9	4.26		CC	M	5
RXC J0616.8-4748		06 ^h 16 ^m 53.6 ^s	-47°48'18.0"	0.1164	1.597	939.2	2.95	D			6
RXC J0645.4-5413	A3404	06 ^h 45 ^m 29.3 ^s	-54°13'08.0"	0.1644	7.139	1280.0	8.23			M	7
RXC J0821.8+0112	A0653	08 ^h 21 ^m 51.7 ^s	+01°12'42.0"	0.0822	0.673	755.9	1.44				8
RXC J2023.0-2056	S0868	20 ^h 23 ^m 01.6 ^s	-20°56'55.0"	0.0564	0.411	739.5	1.28	D			9
RXC J2048.1-1750	A2328	20 ^h 48 ^m 10.6 ^s	-17°50'38.0"	0.1475	3.215	1078.0	4.75	D		M	A
RXC J2129.8-5048	A3771	21 ^h 29 ^m 51.0 ^s	-50°48'04.0"	0.0796	0.767	900.6	2.42	D			B
RXC J2218.6-3853	A3856	22 ^h 18 ^m 40.2 ^s	-38°53'51.0"	0.1411	3.516	1130.1	5.40	D		M	C
RXC J2234.5-3744	A3888	22 ^h 34 ^m 31.0 ^s	-37°44'06.0"	0.1510	6.363	1283.2	8.06			M	D
RXC J2319.6-7313	A3992	23 ^h 19 ^m 41.8 ^s	-73°13'51.0"	0.0984	0.937	788.7	1.68	D	CC		E

4.2.3 Optical data

We used the Wide Field Imager on the MPG/ESO 2.2 m Telescope at La Silla, which is well suited to *XMM-Newton* follow up as it has a similar field of view ($34' \times 33'$). Each set of optical data cover the cluster and a region outside r_{200} which we use for the background assessment. The nominal resolution is $0.238'' \text{ pixel}^{-1}$ and the detector is a 4×2 array of $2 \text{ kilopixel} \times 4 \text{ kilopixel}$ CCDs.

Dithered observations with total exposure times listed in Table 4.2 were taken in B , V and R bands (ESO filters B/123, V/89, and Rc/162). The raw frames were reduced and co-added using ESO/MVM (ALAMBIC). These were aligned (shifted and rotated), then cropped to exclude regions where any band was missing using the IRAF task `wregister`. SEXTRACTOR (version 2.8.6; Bertin and Arnouts, 1996) was run on each image and the seeing measured by taking the median full width at half maximum (FWHM) of objects in the unsaturated part of the stellar locus in the FWHM-Magnitude diagram. Bright but unsaturated isolated point sources, with SEXTRACTOR-measured stellarity > 0.965 in all three bands, were confirmed as point sources by eye and used to calculate convolution kernels with which to degrade each set of images to a common seeing for photometry measurements using the IRAF task `psfmatch`. The final seeing was equal to the worst seeing in each set of three images. Star-galaxy separation was performed on the original, non-PSF-matched images.

Examples of stacked, flat-fielded images where stars have been excised are shown in Figures D.1, D.2, D.3 and D.4.

4.2.4 Subsamples

We use subsamples of the 14 objects in our catalogue, based on their X-ray parameters as given in Table 4.1. We use the morphological classifications of Pratt et al. (2009, §2.3).

‘Massive’ objects are those with M_{500} above the median of the entire REXCESS population $2.95 \times 10^{14} M_{\odot}$.

‘Cool-core’ objects have central electron density $h(z)^{-2} n_{e,0} > 4 \times 10^2 \text{ cm}^{-3}$ and have central cooling times $< 10^9 \text{ yr}$ (Pratt et al., 2009, §2.3.1).

‘Disturbed’ objects are classified based on their X-ray centroid shifts w_i ; $w_i = d_i/r_{500}$ for d_i the projected separation between the X-ray peak and centroid in apertures with radii in the range $(0.1 - 1) r_{500}$. If the standard deviation $\langle w_i \rangle$ is above the threshold value $0.01 r_{500}$, the object is classified as disturbed. A detailed description of the determination of this morphological parameter is given in Böhringer et al. (2010, §2.4).

4.3 Analysis

4.3.1 Source detection and classification

Source detection and measurement was carried out on PSF-matched images (see Section §4.2.3) using SEXTRACTOR in double image mode, with R as the detection band.

Table 4.2: Details of optical observations. Seeing was measured from the images, and the observation date refers to the date when the observations were started. $A_{r>r_{500}}$ and $A_{r>r_{200}}$ are the areas of the regions outside r_{500} and r_{200} which can be used for background estimation.

Object	R_{exp} h	V_{exp} h	B_{exp} h	R_{see} arcsec	V_{see} arcsec	B_{see} arcsec	R_{date}	V_{date}	B_{date}	$A_{r>r_{500}}$ arcmin ²	$A_{r>r_{200}}$ arcmin ²
RXC J0006.0-3443	0.50	0.50	0.75	0.99	0.96	1.05	2008-09-24	2008-09-24	2008-09-24	647.6	416.7
RXC J0049.4-2931	0.50	0.61	1.25	0.99	0.97	1.03	2008-09-23	2008-09-23	2008-09-23	711.4	561.5
RXC J0345.7-4112	0.50	0.50	0.75	0.88	0.97	1.03	2007-11-19	2007-11-19	2007-11-19	602.5	268.0
RXC J0547.6-3152	0.50	1.00	0.50	0.76	1.04	0.95	2000-01-19	2000-01-18	2007-11-14	454.7	315.9
RXC J0605.8-3518	0.50	0.50	1.37	0.76	0.78	0.92	2007-11-27	2007-11-27	2007-11-15	730.6	586.3
RXC J0616.8-4748	0.50	0.50	0.75	0.93	1.02	1.08	2007-11-15	2007-11-15	2007-11-15	740.9	572.4
RXC J0645.4-5413	0.50	0.50	0.75	1.06	1.08	1.19	2000-01-03	2000-01-03	2000-01-03	765.0	606.2
RXC J0821.8+0112	0.83	0.58	0.62	0.95	0.98	1.12	2007-11-15	2007-11-16	2007-11-16	633.1	414.1
RXC J2023.0-2056	0.56	0.67	1.00	0.90	1.01	1.19	2008-07-01	2008-07-01	2008-07-01	462.3	85.8
RXC J2048.1-1750	0.50	0.50	0.75	0.78	0.90	0.99	2008-07-01	2008-07-01	2008-07-03	667.7	526.6
RXC J2129.8-5048	0.50	0.50	0.75	1.21	1.25	1.40	2008-06-30	2008-06-30	2008-06-30	574.0	249.2
RXC J2218.6-3853	0.50	0.50	0.87	1.18	1.15	1.04	2008-09-20	2008-09-20	2008-09-20	744.9	573.5
RXC J2234.5-3744	0.50	0.50	0.75	1.11	1.22	1.41	2008-06-30	2008-06-30	2008-06-30	674.8	477.6
RXC J2319.6-7313	0.44	0.56	0.75	1.07	1.06	1.15	2008-09-21	2008-09-21	2008-09-21	733.2	562.3

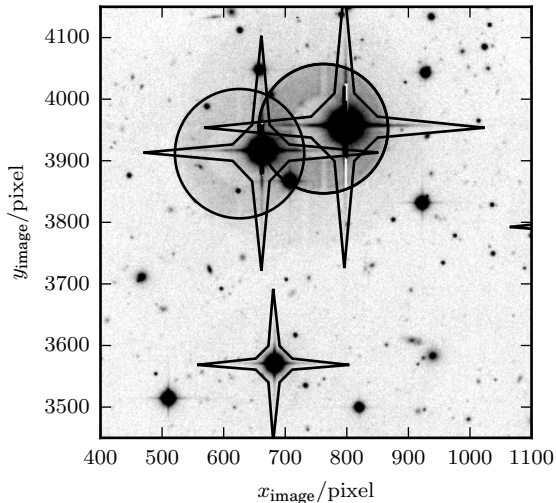


Figure 4.1: Example masks produced by hand for bright objects. The circles have radius $25''$.

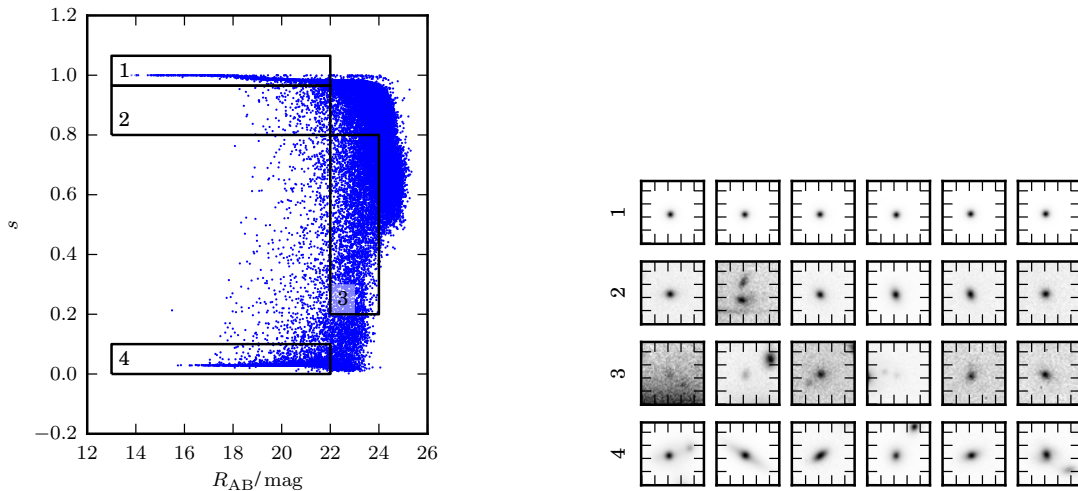
Groups of ≥ 5 pixels with values $\geq 2\sigma$ above the median filtered background per pixel were treated as objects. We used `auto_mag` in `SEXTRACTOR` for magnitude measurements.

Masks were placed on stars:

- magnitude $M_{\text{GSC}} < 14$ in the Guide Star Catalogue 1.2 (Morrison et al., 2001),
- and/or with prominent diffraction or blooming spikes,
- and/or with prominent secondary or higher order reflections.

Initial placement of the masks was performed using a modified version of `automask.sh` from `THELI` (Erben et al., 2005) and then finely positioned and scaled by hand. Examples are shown in Figure 4.1. Masking introduces sharp edges which produce spurious detections not present when using unmasked images, so objects which only appeared in masked images were ignored. When a bright object overlaid the edge of a mask, that object was masked individually to avoid blending it with nearby extended objects. Objects from partially exposed regions at the edges of the images – a result of the telescope dithering and frame stacking – were filtered out of the catalogues.

The `SEXTRACTOR` star-galaxy classifier is a neural network trained on a sample of simulated point-source and non-point-source images to return a stellarity s in the range $0-1$, where 1 is a point-source and 0 is not. We found that good star-galaxy separation was achieved when the maximum stellarity from all three un-degraded images was considered, and objects with $s > 0.965$ in one of the bands were considered to be stars.



(a) Stellarity vs. detection band magnitude.

(b) Examples of the objects contained in the boxes in Figure 4.2a.

Figure 4.2: Point source discrimination using SEXTRACTOR's object classifier. Any objects with $s < 0.965$ are treated as galaxies. Objects in box 1 are stars, objects in box 2 were checked by eye, objects in box 3 ($R_{AB} > 22$) could not be classified and are assumed to be galaxies, and objects in box 4 are clearly extended. Stars $R_{AB} < 13$ do not appear as they have been masked (note that $M_{GSC} \neq R_{AB}$). These examples come from the images of RXC J0006.0–3443.

Bright objects which were not definitively classified ($s > 0.8$, $R_{AB} < 21$) were checked by eye. An example stellarity-magnitude diagram with images of some objects is shown in Figure 4.2. The figure shows good discrimination (a value close to either 1 or 0) of objects which are obviously point-like or extended at bright magnitudes ($R_{AB} < 20$). At dimmer magnitudes, classifications become increasingly random. Because of the finite thickness of the Galactic disc and a finite upper magnitude on the star population, we expect the number of stars to drop rapidly above the magnitude at which we can no longer properly classify stars. Objects at higher magnitudes which are unclassified in the un-degraded images are always assumed to be galaxies. By applying the degrading filter, the signal to noise ratio of these objects is increased – the spatially uncorrelated background is suppressed, whereas spatially correlated objects on the scale of the kernel used for degradation are enhanced – so they can be detected.

4.3.2 Magnitude calibration

Magnitudes from SEXTRACTOR were converted into AB magnitudes by making an atmospheric correction and a zero point correction. We fixed the B band zero point B_{zero} using Data Release 7 of the AAVSO Photometric All-Sky Survey (APASS DR7) cata-

Table 4.3: Zero points for each of the observations. We found B_{zero} using comparison to the APASS catalogue, and then fitted the two colour offsets κ_{B-V} and κ_{V-R} to a stellar locus from the literature in order to constrain V_{zero} and R_{zero} . The large variation in the zero points is due the atmospheric absorption on the observation nights; since the extinction coefficients e_M were not independently determined during observations it was impossible to disentangle extinction from the zero point variation.

Object	R_{zero} mag	V_{zero} mag	B_{zero} mag
RXC J0006.0–3443	24.37 ± 0.02	24.17 ± 0.02	24.70 ± 0.02
RXC J0049.4–2931	23.93 ± 0.03	23.92 ± 0.02	24.52 ± 0.02
RXC J0345.7–4112	24.52 ± 0.05	24.31 ± 0.05	24.87 ± 0.05
RXC J0547.6–3152	24.27 ± 0.02	24.14 ± 0.02	24.44 ± 0.02
RXC J0605.8–3518	24.38 ± 0.02	24.11 ± 0.02	24.61 ± 0.02
RXC J0616.8–4748	24.45 ± 0.02	24.20 ± 0.02	24.71 ± 0.02
RXC J0645.4–5413	24.41 ± 0.02	24.13 ± 0.02	24.61 ± 0.02
RXC J0821.8+0112	24.46 ± 0.03	24.21 ± 0.03	24.73 ± 0.03
RXC J2023.0–2056	24.31 ± 0.03	24.10 ± 0.03	24.65 ± 0.03
RXC J2048.1–1750	24.34 ± 0.02	24.15 ± 0.02	24.71 ± 0.02
RXC J2129.8–5048	24.39 ± 0.02	24.19 ± 0.02	24.76 ± 0.02
RXC J2218.6–3853	24.30 ± 0.02	24.09 ± 0.02	24.65 ± 0.02
RXC J2234.5–3744	24.35 ± 0.02	24.16 ± 0.02	24.69 ± 0.02
RXC J2319.6–7313	24.04 ± 0.03	23.79 ± 0.03	24.11 ± 0.03

logue, which has good coverage of almost all of our fields, and sufficient coverage ($>30\%$) in those fields where coverage was incomplete.

Using the observations and zero points from Ziparo et al. (2012), we generated a calibrated stellar locus. By minimizing the offset of the stellar locus in each observation set from this calibrated stellar locus, we found colour offsets $\kappa_{B-V} = B_{\text{zero}} - V_{\text{zero}}$ and $\kappa_{V-R} = V_{\text{zero}} - R_{\text{zero}}$. This method is similar to that of High et al. (2009). The resulting zero points are given in Table 4.3.

No attempt was made to correct for galactic extinction whilst constructing the stellar locus diagram as we found that the assumption that the galactic dust could be modelled as a thin sheet was incorrect, and that bluer stars (brighter and typically further away) tended to be more reddened than redder stars (dimmer and typically closer). Instead, we assumed that the observed stellar locus was independent of position on the sky (at least away from the galactic plane, where all of our targets are) and that we could cross-calibrate with similar observations.

Conversion of magnitudes and colour gradients to the Johnson system (for comparisons with the literature) was carried out using colour terms from the ESO WFI web page.¹ The conversion between raw magnitudes M_{raw} and Johnson magnitudes M_J is described by

¹<https://www.eso.org/sci/facilities/lasilla/instruments/wfi/inst/zeropoints.html> [Accessed: 2013-07-24]

Table 4.4: Magnitude conversion parameters. The offsets O_M were taken from the ESO MAG2FLUX tool at <http://archive.eso.org/mag2flux/>.

Band	c_M	e_M	O_M
R	0.0 ± 0	0.070 ± 0.010	$+0.23$
V	-0.13 ± 0.01	0.11 ± 0.01	$+0.14$
B	0.25 ± 0.02	0.22 ± 0.01	-0.07

$$\begin{pmatrix} R_{\text{raw}} \\ V_{\text{raw}} \\ B_{\text{raw}} \end{pmatrix} = \begin{bmatrix} 1 + c_R & -c_R & 0 \\ -c_V & 1 + c_V & 0 \\ 0 & -c_B & 1 + c_B \end{bmatrix} \begin{pmatrix} R_J \\ V_J \\ B_J \end{pmatrix} + \begin{pmatrix} Z_R e_R \\ Z_V e_V \\ Z_B e_B \end{pmatrix} - \begin{pmatrix} R_{\text{zero}} \\ V_{\text{zero}} \\ B_{\text{zero}} \end{pmatrix}, \quad (4.1)$$

for M_{zero} the zero point in band M , c_M the colour term, Z_M the airmass of the observation and e_M the extinction parameter. This equation can be inverted in order to find standard magnitudes given raw magnitudes. The conversion between raw magnitudes and AB magnitudes is described by

$$\begin{pmatrix} R_{\text{AB}} \\ V_{\text{AB}} \\ B_{\text{AB}} \end{pmatrix} = \begin{pmatrix} R_{\text{raw}} \\ V_{\text{raw}} \\ B_{\text{raw}} \end{pmatrix} - \begin{pmatrix} Z_R e_R \\ Z_V e_V \\ Z_B e_B \end{pmatrix} + \begin{pmatrix} O_R \\ O_V \\ O_B \end{pmatrix} + \begin{pmatrix} R_{\text{zero}} \\ V_{\text{zero}} \\ B_{\text{zero}} \end{pmatrix}, \quad (4.2)$$

for O_M the AB offset for band M . The values of the parameters are given in Table 4.4, and the AB corrections O_M were taken from the ESO MAG2FLUX tool².

The results in the rest of this paper are based on AB system magnitudes.

4.3.3 Luminosity function analysis

4.3.3.1 Galaxy catalogue completeness from off-target observations

The number counts of field galaxies arise from the summation of luminosity functions at many redshifts, which themselves are influenced by galaxy evolution. We use the number counts histogram to estimate catalogue completeness at different magnitudes, and to compare the relative over- or under-density of galaxies in the off-target regions of our observations to other regions in the sky.

²<http://archive.eso.org/mag2flux/>

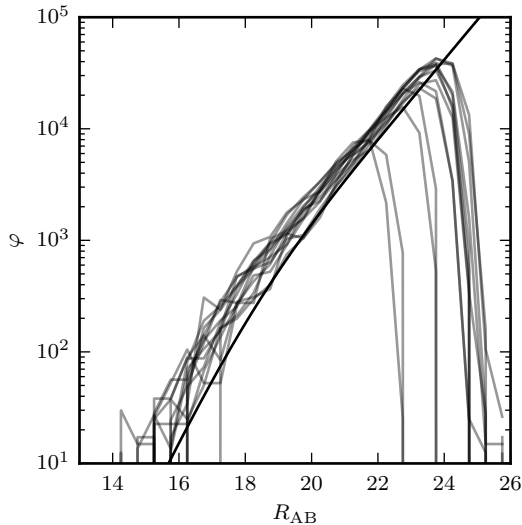


Figure 4.3: The off-target number count surface densities S for each cluster in the sample are shown in grey, along with the expected number counts from data compiled by Metcalfe in solid black [see Footnote (3)].

Metcalfe compiled a set of number count measurements³ from Jones et al. (1991); Metcalfe et al. (1991, 1995, 1996); McCracken et al. (2000); Metcalfe et al. (2001); Frith et al. (2003); Buswell et al. (2004); Metcalfe et al. (2006). The dataset has an intrinsic scatter of ~ 0.3 dex, corresponding to a factor of ~ 2 . We use a 5th order polynomial spline fit $\xi_{\text{Metcalfe}}(R)$ as an empirical shape for our field number counts histogram fitting. The number count surface densities S for all of the off-target regions in the sample are plotted in Figure 4.3, along with ξ_{Metcalfe} .

We assume that the fall-off at the magnitude limit can be described by the logistic function $\xi_{\text{falloff}}(M) = \left[1 + \exp\left(\frac{M - M_{\text{falloff}}}{W_{\text{falloff}}}\right)\right]^{-1}$. This function was chosen since it goes smoothly from ~ 1 to ~ 0 over a characterisable distance, but we make no claim that it precisely describes the fall-off. The 50% completeness limit is at M_{falloff} in this model.

We fit the function $\Xi = f_g \xi_{\text{Metcalfe}} \xi_{\text{falloff}}$ where f_g is a normalisation factor, to the off-target number counts histogram for each cluster in our sample (measured in region $r > 1.5 r_{500}$), and the results are given in Table 4.5. We also include the fall-off magnitude as a K-corrected absolute magnitude at the cluster redshift, $R_{\text{AB abs K falloff}}$. The K-corrections are made using the data of Poggianti (1997), assuming that the galaxies are E-galaxies.

The observed galaxy counts were all between $1\times$ and $2\times$ the empirically determined density, consistent with our galaxy clusters occupying denser regions of the cosmic web, and within the expected bounds of the scatter from Metcalfe’s galaxy counts dataset. In

³<http://astro.dur.ac.uk/~nm/pubhtml/counts/counts.html> Metcalfe, (2010) [Accessed: 13-05-2013]

Table 4.5: Off-target number counts fit results. $R_{\text{ABfalloff}}$ is the detection band falloff magnitude in the observer’s magnitude system and $R_{\text{AB abs Kfalloff}}$ is the corresponding K-corrected absolute magnitude. f_g is the normalisation factor by which the literature number counts function was multiplied.

Object	$R_{\text{ABfalloff}}$ mag	$R_{\text{AB abs Kfalloff}}$ mag	W_{falloff} mag	$f_g R_{\text{AB}}$
RXC J0006.0–3443	24.07 ± 0.03	-14.71 ± 0.03	0.153 ± 0.014	1.49 ± 0.06
RXC J0049.4–2931	23.10 ± 0.03	-15.53 ± 0.03	0.157 ± 0.014	1.33 ± 0.05
RXC J0345.7–4112	24.40 ± 0.04	-12.81 ± 0.04	0.150 ± 0.011	1.16 ± 0.06
RXC J0547.6–3152	23.34 ± 0.03	-16.09 ± 0.03	0.150 ± 0.014	1.39 ± 0.06
RXC J0605.8–3518	23.99 ± 0.03	-15.28 ± 0.03	0.154 ± 0.011	1.53 ± 0.06
RXC J0616.8–4748	23.74 ± 0.02	-15.08 ± 0.02	0.150 ± 0.008	1.37 ± 0.05
RXC J0645.4–5413	23.74 ± 0.03	-15.96 ± 0.03	0.151 ± 0.011	1.17 ± 0.05
RXC J0821.8+0112	24.07 ± 0.03	-13.89 ± 0.03	0.146 ± 0.012	1.27 ± 0.05
RXC J2023.0–2056	24.34 ± 0.03	-12.73 ± 0.03	0.158 ± 0.009	1.26 ± 0.05
RXC J2048.1–1750	24.25 ± 0.02	-15.16 ± 0.02	0.142 ± 0.009	1.46 ± 0.05
RXC J2129.8–5048	24.02 ± 0.04	-13.86 ± 0.04	0.152 ± 0.012	1.10 ± 0.05
RXC J2218.6–3853	22.25 ± 0.03	-17.04 ± 0.03	0.159 ± 0.014	1.19 ± 0.05
RXC J2234.5–3744	24.11 ± 0.03	-15.37 ± 0.03	0.150 ± 0.010	1.39 ± 0.05
RXC J2319.6–7313	21.93 ± 0.05	-16.46 ± 0.05	0.143 ± 0.014	1.71 ± 0.10

Table 4.6: Schechter function fitting results, valid for the MPG/ESO 2.2 m Telescope WFI filters.

Band	M^* mag	α	χ_r^2
$R_{\text{AB abs K}}$	-22.39 ± 0.17	-1.18 ± 0.04	2.03
$V_{\text{AB abs K}}$	-21.90 ± 0.25	-1.27 ± 0.07	3.62
$B_{\text{AB abs K}}$	-21.59 ± 0.26	-1.23 ± 0.09	3.55

addition, the shapes of the off-target number counts in Figure 4.3 do not closely trace the curve expected from the literature, suggesting that the galaxy overdensity of the cluster extends beyond r_{500} .

4.3.3.2 Initial cluster luminosity function analysis

For each cluster, we measured the on-target luminosity function in the region $r < r_{500}$ in the R band, subtracting the off-target number counts histogram measured from the region $r > 1.5 r_{500}$. Each function was normalised by the mean density in $-21 < R < -17$. We truncated each function well below the 50% completeness limit, at $M_{\text{falloff}} - 4W_{\text{falloff}}$ as fitted in the off-target region (see Section §4.3.3.1). We fitted a Schechter function $\Phi(L) = \phi \left(\frac{L}{L^*}\right)^\alpha \exp\left(\frac{-L}{L^*}\right)$ for L^* the Schechter luminosity (with the corresponding magnitude M^*), α the slope parameter and ϕ a normalisation factor to the mean luminosity function. The function and its fit for the detection band are shown in Figure 4.4, and the fitting results for all three bands are given in Table 4.6.

Given the detection band Schechter magnitude R^* , we define three groups of galaxies

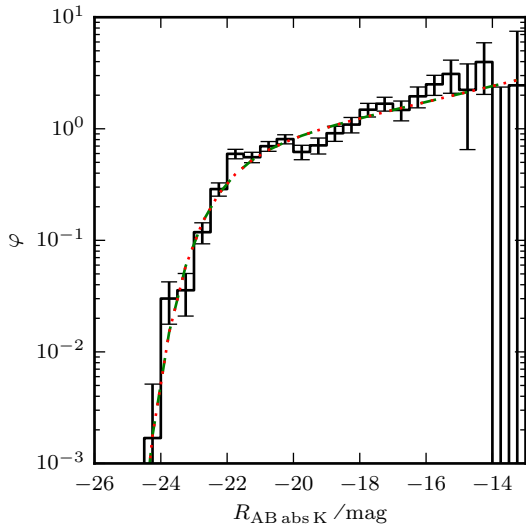


Figure 4.4: Mean cluster luminosity function in the detection band and best fitting Schechter function model. Before stacking, the off-target number count density was subtracted, and each profile divided by the remaining object count in $-21 < R_{\text{AB abs K}} < -17$.

in each cluster: ‘bright’ galaxies are those satisfying ($R < R^* + 2.5$), i.e. ($L/L^* > 0.1$); ‘faint’ galaxies satisfy ($R^* + 2.5 < R < R^* + 5$), i.e. ($0.1 > L/L^* > 0.01$); and ‘dwarf’ galaxies satisfy ($R > R^* + 5$), i.e. ($L/L^* < 0.01$). Additionally, we define the symbols $R^{*+2.5} = R^* + 2.5$ and $R^{*+5} = R^* + 5$.

The dwarf galaxy population (described in, e.g. Popesso et al., 2006) is not always obvious in our data due to different image depths in different observations. The detection band data are sufficiently deep to reach the faint limit, $R^* + 5$, so in the rest of this paper we use the ‘bright’ and ‘faint’ galaxies, ignoring the dwarfs.

By imposing a magnitude cut at $R^* + 5$, we lose a fraction of the total luminosity in each cluster. By integrating the fitted luminosity functions beyond the cut and extrapolating for very faint objects we can estimate the ratio between the total luminosity in galaxies we observe and the total integrated luminosity in the luminosity function. Luminosities based on the ‘faint’ cut need to be increased by 2.5% in R , 3.9% in V and 3.3% in B .

A more exhaustive assessment of the luminosity functions, as well as total luminosity measurements informed by the count density profiles is given in Section §4.3.9.

4.3.4 Catalogue contamination by misidentified stars

We estimate an upper bound on the number of stars at each magnitude in our catalogues by fitting star counts with respect to magnitude at magnitudes where star-galaxy separation is robust, and extrapolating this to higher magnitudes. (These count estimates

Table 4.7: Contamination fraction for each catalogue measured at the bright limit, the faint limit, and the 50% detection limit.

Object	$K_{R < R^* + 2.5}$	$K_{R < R^* + 5}$	$K_{M_{\text{falloff}}}$
RXC J0006.0-3443	-0.00 ± 0.05	-0.002 ± 0.013	0.003 ± 0.005
RXC J0049.4-2931	-0.00 ± 0.08	-0.036 ± 0.014	-0.002 ± 0.008
RXC J0345.7-4112	0.00 ± 0.26	-0.01 ± 0.05	-0.005 ± 0.004
RXC J0547.6-3152	-0.00 ± 0.14	0.123 ± 0.024	0.154 ± 0.017
RXC J0605.8-3518	-0.00 ± 0.13	0.274 ± 0.012	0.319 ± 0.004
RXC J0616.8-4748	-0.00 ± 0.19	0.215 ± 0.019	0.270 ± 0.007
RXC J0645.4-5413	0.04 ± 0.08	0.340 ± 0.009	0.365 ± 0.007
RXC J0821.8+0112	0.00 ± 0.32	0.11 ± 0.05	0.324 ± 0.004
RXC J2023.0-2056	0.0 ± 0.5	0.21 ± 0.07	0.474 ± 0.004
RXC J2048.1-1750	-0.00 ± 0.11	0.426 ± 0.009	0.5358 ± 0.0033
RXC J2129.8-5048	0.00 ± 0.29	0.06 ± 0.05	0.183 ± 0.005
RXC J2218.6-3853	-0.00 ± 0.14	0.387 ± 0.009	0.277 ± 0.021
RXC J2234.5-3744	-0.00 ± 0.06	-0.077 ± 0.019	0.017 ± 0.006
RXC J2319.6-7313	-0.00 ± 0.18	0.085 ± 0.035	0.222 ± 0.015
Mean	0.00 ± 0.06	0.150 ± 0.009	0.2241 ± 0.0025

are upper bounds since the star counts drop off at a faster rate at higher magnitudes.) The number of stars which are expected given the power law, but not seen, are assumed to have been misidentified as galaxies. The contamination fraction K measured in each catalogue at selected magnitudes is given in Table 4.7.

4.3.5 Red sequence selection

The red sequence is a line in colour-magnitude space around which elliptical galaxies in clusters tend to scatter (e.g. Bower, Lucey, and Ellis, 1992; Valentinuzzi et al., 2011). The origin of the red sequence and its relation to the mass-metallicity relation was explored in a seminal paper by Arimoto and Yoshii (1987). The position of the line changes with redshift, and can be used to detect new galaxy clusters and estimate cluster redshifts (e.g. Gladders and Yee, 2000). Spiral galaxies in clusters tend to be bluer than the red sequence and migrate on to it as star formation fades. The scatter of field galaxies in colour space is usually much larger than the scatter of the red sequence galaxies and in this study we use this observation to increase the signal to noise ratio of our radial profiles.

We fit a line to the red sequence described by $C_{\text{model}}(M) = g(M - Z) + k$ where C is a colour, g is the gradient, M is a magnitude, and k is the colour at a ‘pivot point’ Z . The distribution of cluster galaxies perpendicular to the red sequence comprises a red sequence of galaxies with a relatively narrow scatter (≤ 0.05 mag in this case) centred on the line, and a blue cloud of galaxies with a larger scatter (~ 0.5 mag) centred some distance below the red sequence. We model this as a distribution of the form

$$\Psi(C_{\text{residual}}) = \psi_r \exp\left(-\frac{(C_{\text{residual}} - o_r)^2}{2\sigma_r^2}\right) + \psi_b \exp\left(-\frac{(C_{\text{residual}} - o_b)^2}{2\sigma_b^2}\right), \quad (4.3)$$

with $C_{\text{residual}}(C, M) = C - C_{\text{model}}(M)$, where o_r is the offset of the distribution of red sequence galaxies from the line C_{model} , σ_r the width of the red sequence, and ψ_r the density of the red sequence; o_b , σ_b and ψ_b are equivalent quantities for the blue cloud. For well fitted red sequences, o_r/σ_r should be small ($\ll 1$). We also define

$$w_{\text{rs}} = \frac{C_{\text{residual}} - o_r}{\sigma_r}, \quad (4.4)$$

which is the scaled displacement of a point from the red sequence in units of the width of the red sequence; galaxies with $-3 < w_{\text{rs}} < 3$ are taken to be on the red sequence and those with $w_{\text{rs}} < -3$ are blue cloud objects.

We consider red sequences in the $(R, B - V) = (M, C)$ colour-magnitude space (in the AB system), and fit to the galaxies satisfying $R < 20$ and $r < r_{500}$.

The fitting procedure was:

1. Fit of the straight line C_{model} to the colour-magnitude points, using a least squares method. (On the first iteration, this step was skipped, and we assumed a gradient of -0.044 .)
2. Compute the histogram of C_{residual} for all points within the magnitude limits.
3. Fit of the scatter model Ψ to the histogram.
4. Select points $|w_{\text{rs}}| < 3$ and use these as the input for the straight line fit 1.

Steps 1 to 4 were repeated enough times that the results stabilized (~ 5 iterations was usually sufficient). In cases where the solutions oscillated, the solution with the narrowest σ_r was selected. The fit results are shown in Figure 4.5.

To compare our red sequence parameters to those in the literature we refitted g and k in $(R, B - R)$ and $(R, V - R)$ using the same method, before using (4.1) and (4.2) to transform g and k into the Johnson-Cousins $(V_J, B_J - V_J)$ colour-magnitude space. K-corrections were made assuming that red sequence objects are elliptical galaxies, using values from Poggianti (1997). The parameters are shown in Table 4.8. Valentinuzzi et al. (2011, fig. 3) give values for the K-corrected red sequence normalisation k_{JK} and gradient g_J for 72 clusters in the $(V_J, B_J - V_J)$ colour-magnitude space. The mean values are $\bar{k}_{\text{JK}} = 0.87 \pm 0.06$ (at $V_{\text{abs}} = -20$) and $\bar{g}_J = -0.044 \pm 0.009$. These values are in reasonable agreement with our results in Table 4.8.

The red sequence for RXC J2319.6–7313 is unclear and achieving a reasonable fit for this object depended on the selection of the solution with the narrowest σ_r . This is the target with the most southerly declination in the REXCESS sample, is only visible from ESO La Silla at relatively high airmass (~ 1.5) and the observation image depth was somewhat lower than for most of the other targets (as shown in Table 4.5). We suspect that the uncertainties on the measured colours may be underestimated, making the red sequence more difficult to see. Before finding the fitting method described above, we investigated several alternative fitting algorithms in an attempt to get robust fits for

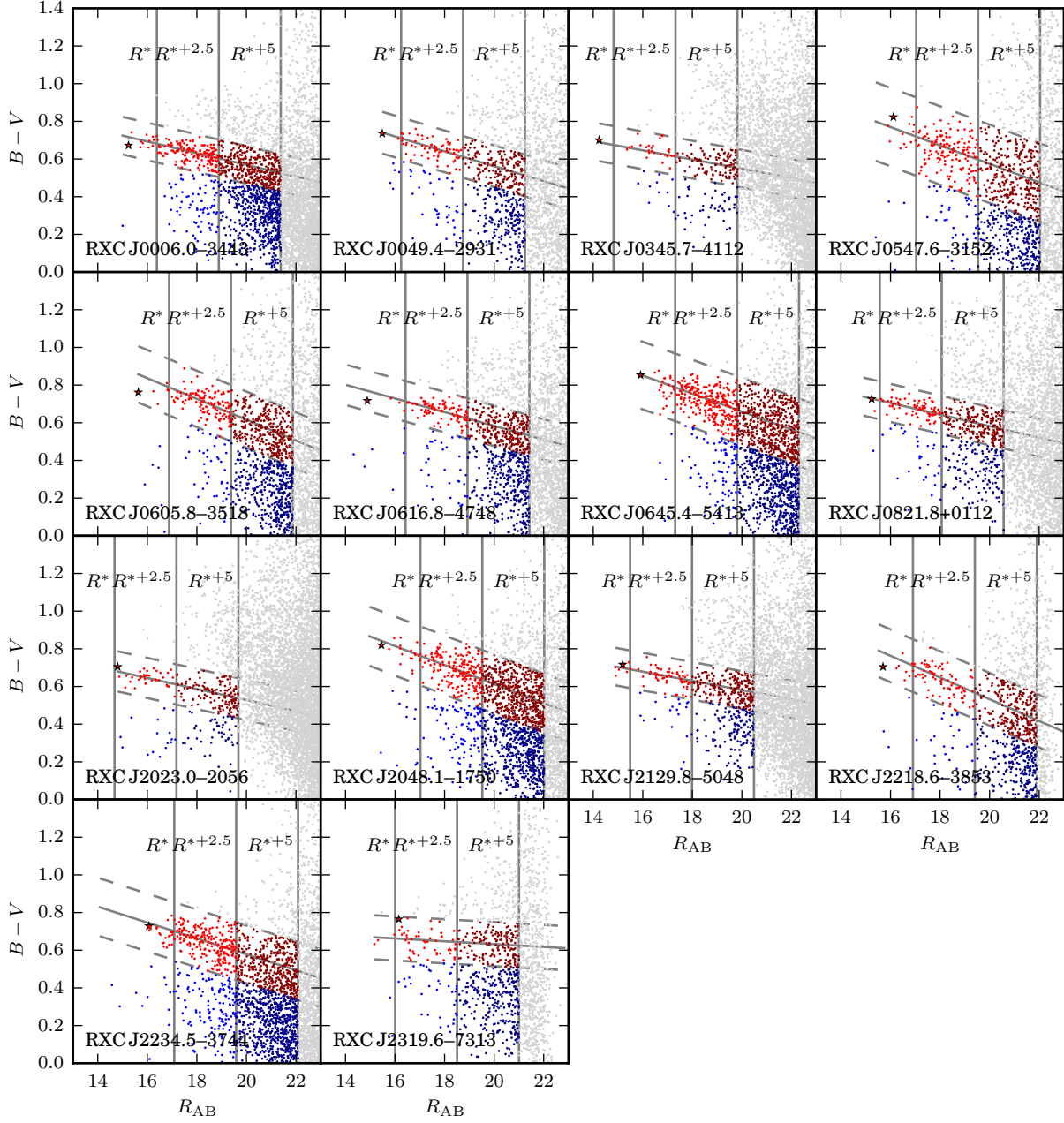


Figure 4.5: Fitted red sequences for all the clusters in the sample. The red sequence best-fitting line is shown as a solid line, and the dashed lines show $\pm 3w_{rs}$. The vertical lines show the Schechter magnitude, R^* , and the bright and faint magnitude limits, $R^{*+2.5}$ and R^{*+5} respectively. The star denotes the BCG. Objects below the lower dashed line are ‘blue,’ and objects between the dashed lines are ‘on the red sequence.’

Table 4.8: Red sequence parameters in the Johnson-Cousins colour-magnitude space ($V_J, B_J - V_J$), where g_J is the gradient, and $k_J = V_J, B_J - V_J$ at $V_{\text{abs}} = -20$. k_{JK} are compensated for evolution and redshift dependence on colour using values from Poggianti (1997) assuming that the red-sequence comprises of E-galaxies.

Object	g_J	k_J mag	k_{JK} mag
RXC J0006.0–3443	-0.063 ± 0.024	1.12 ± 0.16	0.74 ± 0.16
RXC J0049.4–2931	-0.035 ± 0.026	1.23 ± 0.16	0.87 ± 0.16
RXC J0345.7–4112	-0.05 ± 0.10	0.995 ± 0.171	0.84 ± 0.17
RXC J0547.6–3152	-0.059 ± 0.015	1.18 ± 0.16	0.71 ± 0.16
RXC J0605.8–3518	-0.077 ± 0.017	1.11 ± 0.16	0.66 ± 0.16
RXC J0616.8–4748	-0.045 ± 0.022	0.963 ± 0.150	0.57 ± 0.15
RXC J0645.4–5413	-0.071 ± 0.012	1.15 ± 0.16	0.64 ± 0.16
RXC J0821.8+0112	-0.028 ± 0.010	1.11 ± 0.15	0.85 ± 0.15
RXC J2023.0–2056	-0.038 ± 0.042	1.10 ± 0.15	0.92 ± 0.15
RXC J2048.1–1750	-0.064 ± 0.021	1.03 ± 0.16	0.56 ± 0.16
RXC J2129.8–5048	-0.032 ± 0.009	1.12 ± 0.15	0.86 ± 0.15
RXC J2218.6–3853	-0.055 ± 0.057	1.22 ± 0.18	0.77 ± 0.18
RXC J2234.5–3744	-0.066 ± 0.007	0.997 ± 0.143	0.51 ± 0.14
RXC J2319.6–7313	$+0.007 \pm 0.034$	1.15 ± 0.16	0.83 ± 0.16
Mean	-0.049 ± 0.010	1.11 ± 0.04	0.74 ± 0.04
St. dev.	$+0.022 \pm 0.008$	0.0828 ± 0.0445	0.13 ± 0.04

RXC J2319.6–7313. Of particular interest was fitting in several bands simultaneously, i.e. iteration of line fitting in $(R, B - R, V - R)$ space with an iterative cut based on perpendicular distance from the line. We found that there is a substantial population of galaxies which are identified as ‘on the red sequence’ using the single band-pair method, but which are excluded from it in the multi-band method. Apart from scatter in the colour measurements, possible reasons for the offsets in the other band pairs are that the galaxies may lie at a substantially different redshift, have substantial dust attenuation or AGN activity, or be influenced by the spread in star formation histories. The improved discrimination of cluster and background galaxies in this case would lead to lower background levels overall and higher signal-to-noise ratios on the radial profiles. However, this method required excellent starting values, and was particularly susceptible to blue objects at fainter magnitudes. For RXC J2319.6–7313, with its broad red sequence which is poorly separated from the blue cloud, the method failed.

There is no significant change in the the red sequence results here – or the subsequent results based on the red sequence selection – for the other clusters when using the other fitting algorithms we investigated.

Table 4.9: Concentration parameters c_Δ with respect to the critical density. The values of $c_{200,m}$ were calculated using equation (12) in Dolag et al. (2004). c_{200} and c_{500} were derived from $c_{200,m}$ assuming our fiducial cosmology.

Object	$c_{200,m}$	c_{200}	c_{500}
RXC J0006.0–3443	7.46 ± 0.07	4.43 ± 0.04	2.907 ± 0.030
RXC J0049.4–2931	8.16 ± 0.06	4.87 ± 0.04	3.217 ± 0.028
RXC J0345.7–4112	9.04 ± 0.07	5.43 ± 0.04	3.609 ± 0.029
RXC J0547.6–3152	7.04 ± 0.07	4.17 ± 0.04	2.724 ± 0.031
RXC J0605.8–3518	7.29 ± 0.07	4.32 ± 0.04	2.833 ± 0.030
RXC J0616.8–4748	7.72 ± 0.06	4.60 ± 0.04	3.024 ± 0.029
RXC J0645.4–5413	6.67 ± 0.07	3.93 ± 0.05	2.560 ± 0.032
RXC J0821.8+0112	8.57 ± 0.06	5.14 ± 0.04	3.400 ± 0.028
RXC J2023.0–2056	8.89 ± 0.07	5.33 ± 0.04	3.539 ± 0.029
RXC J2048.1–1750	7.16 ± 0.07	4.24 ± 0.04	2.775 ± 0.030
RXC J2129.8–5048	8.15 ± 0.07	4.87 ± 0.04	3.213 ± 0.029
RXC J2218.6–3853	7.10 ± 0.07	4.21 ± 0.04	2.751 ± 0.031
RXC J2234.5–3744	6.76 ± 0.07	3.99 ± 0.05	2.600 ± 0.033
RXC J2319.6–7313	8.31 ± 0.06	4.97 ± 0.04	3.284 ± 0.028
Mean	7.737 ± 0.018	4.608 ± 0.011	3.031 ± 0.008
St. dev.	0.785 ± 0.019	0.496 ± 0.012	0.346 ± 0.008

4.3.6 Radial density model

We assume a generalised NFW model for the radial density profiles, namely

$$\rho(r) = \frac{\rho_0}{\left(\frac{r}{r_s}\right)^\gamma \left(1 + \left(\frac{r}{r_s}\right)^\alpha\right)^{\frac{\beta-\gamma}{\alpha}}}, \quad (4.5)$$

where ρ_0 is a density normalisation, Δ is the factor by which the halo is overdense with respect to the critical density of the universe at the object redshift, $r_s = 1/c_\Delta$ is a characteristic scale length measured in units of r_Δ , γ is the inner slope, β is the outer slope and $\alpha = 1$. All parameters are calculated in terms of $\Delta = 500$.

There is a strong degeneracy between β and r_s when fitting the generalised NFW profile, so we estimated a value of c_{500} for each cluster using equation (12) from Dolag et al. (2004) to be used in subsequent calculations. The values are shown in Table 4.9. When analysing stacked profiles, we assume the mean value of c_{500} from all the contributing clusters.

4.3.7 Brightest cluster galaxy properties and positions

Large cD galaxies in the cluster central region are expected to have a significant impact on the distribution of fainter galaxies, which are less tightly bound and more susceptible to disruption than larger bright galaxies. Their distances from the cluster centres and sizes are given in Table 4.10.

Table 4.10: BCG parameters. $R_{\text{AB abs K}}$ is the absolute magnitude of the BCG and L_R is the corresponding luminosity. r is the distance of the BCG from the X-ray peak. A_c is the ratio of the area of the BCG to $\pi(0.1 r_{500})^2$. a_{Kron} is the semi-major axis of the elliptical aperture used to measure the BCG luminosity.

Object	$R_{\text{AB abs K}}$	L_R $10^{11} L_{\odot}$	r r_{500}	A_c	a_{Kron} kpc
RXC J0006.0–3443	-23.534 ± 0.025	1.88 ± 0.04	0.00	0.11267 ± 0.00008	55.590 ± 0.028
RXC J0049.4–2931	-23.151 ± 0.026	1.319 ± 0.031	0.01	0.06321 ± 0.00008	21.180 ± 0.020
RXC J0345.7–4112	-22.97 ± 0.05	1.12 ± 0.06	0.00	0.099439 ± 0.000031	23.026 ± 0.005
RXC J0547.6–3152	-23.312 ± 0.023	1.530 ± 0.032	0.02	0.05545 ± 0.00009	28.507 ± 0.034
RXC J0605.8–3518	-23.633 ± 0.022	2.06 ± 0.04	0.00	0.08959 ± 0.00008	35.869 ± 0.023
RXC J0616.8–4748	-23.935 ± 0.023	2.72 ± 0.06	0.01	0.14889 ± 0.00010	57.391 ± 0.028
RXC J0645.4–5413	-23.789 ± 0.024	2.37 ± 0.05	0.01	0.10326 ± 0.00011	53.77 ± 0.04
RXC J0821.8+0112	-22.718 ± 0.025	0.885 ± 0.020	0.01	0.042928 ± 0.000019	18.431 ± 0.005
RXC J2023.0–2056	-22.264 ± 0.028	0.583 ± 0.015	0.01	0.064183 ± 0.000027	19.517 ± 0.006
RXC J2048.1–1750	-23.963 ± 0.023	2.79 ± 0.06	0.17	0.07459 ± 0.00005	30.889 ± 0.016
RXC J2129.8–5048	-22.690 ± 0.024	0.863 ± 0.019	0.11	0.041114 ± 0.000023	21.526 ± 0.009
RXC J2218.6–3853	-23.598 ± 0.023	1.99 ± 0.04	0.03	0.06235 ± 0.00013	32.02 ± 0.05
RXC J2234.5–3744	-23.412 ± 0.023	1.68 ± 0.04	0.15	0.041763 ± 0.000029	29.832 ± 0.014
RXC J2319.6–7313	-22.242 ± 0.031	0.571 ± 0.016	0.01	0.06545 ± 0.00027	24.68 ± 0.07

The BCGs in REXCESS were studied by Haarsma et al. (2010). In this paper we use variable aperture elliptical magnitudes, whereas Haarsma et al. used magnitudes measured in a $12 h^{-1} \text{kpc}$ fixed aperture metric radius, and as a consequence the magnitudes we measure here are higher.

4.3.8 Radial density profiles

By measuring the shape of the radial density profiles of galaxy clusters, we can assess the extent to which galaxies (effectively collisionless particles) trace gas (a collisional fluid) and dark matter (which we assume to be a collisionless fluid) in galaxy clusters of different morphological types and masses. Since the evolutionary history of a galaxy may be quite different if it is on the red-sequence as opposed to in the blue cloud, or bright as opposed to faint, we must consider each sub-population of galaxies (red and bright, red and faint, blue and bright, and blue and faint) separately.

We produced radial surface density profiles S for individual clusters by summing object counts in radial bins around the cluster centres (see Section §4.2.2 for details on the centring method), with annular bin edges at (0, 0.1, 0.15, 0.2, 0.25, 0.35, 0.5, 0.7, 1, 1.25, 1.5, 2.5 and 5) r_{500} . The number counts were divided by the total exposed area in each annulus to get the surface density.

4.3.8.1 Count density profile fitting

We fitted the generalised NFW model profile defined in Equation (4.5) to each of the individual galaxy count density profiles. This measurement is used to constrain the

Table 4.11: NFW fitting results for each of the galaxy population filters – bright and faint; red sequence and blue. The full length table is given in Table D.1.

Object	Galaxy filter	β	S_0 r_{500}^{-3}	S_{bgNFW} r_{500}^{-2}
RXC J0006.0–3443	Bright, red	2.7 ± 0.5	49.7 ± 9.0	7.2 ± 2.1
RXC J0049.4–2931	Bright, red	3.4 ± 0.4	60.2 ± 10.7	1.9 ± 0.5
RXC J0345.7–4112	Bright, red	3.0 ± 0.9	10.5 ± 3.3	2.1 ± 0.6
RXC J0547.6–3152	Bright, red	2.65 ± 0.34	50.7 ± 6.7	5.5 ± 1.4
RXC J0605.8–3518	Bright, red	3.1 ± 0.4	54.9 ± 8.8	7.2 ± 0.8
RXC J0616.8–4748	Bright, red	2.54 ± 0.28	29.2 ± 3.5	2.6 ± 0.6
RXC J0645.4–5413	Bright, red	2.87 ± 0.26	112.3 ± 12.9	9.9 ± 1.3
RXC J0821.8+0112	Bright, red	2.4 ± 0.4	22.5 ± 3.4	1.4 ± 0.9

background count density and to provide an estimate of the total galaxy count within a particular radius.

When fitting the model profile to projected quantities like the observed galaxy count density profiles, we integrate $\rho(r)$ numerically along the line of sight, and allow an additional uniform surface density component S_{bgNFW} as background, which is not projected. We fixed $\alpha = \gamma = 1$ because the statistics of the individual profiles were too poor to constrain these parameters.

An additional limit, $\rho(r > r_{\text{cutoff}}) = 0$ is imposed so that the integrals converge and to break the degeneracy between β and S_{bgNFW} . We found that values of S_{bgNFW} were consistent within their uncertainties for $r_{\text{cutoff}} = (2.5, 5 \text{ and } 10) r_{500}$ for the red populations which have good statistics, but that the poor statistics of the blue populations led to some cases of negative S_{bgNFW} if $r_{\text{cutoff}} > 2.5 r_{500}$. Whilst there are indications that the cluster extends beyond $2.5 r_{500}$, our data outside that radius are too sparse to make reasonable measurements, so we set $r_{\text{cutoff}} = 2.5 r_{500}$. This limit is also used where we estimate the projected total mass profile within the cluster, and the projected gas density profile.

To generate estimates of the total number of galaxies n_g in each cluster, we integrated the fitted density profiles out to the relevant r_Δ . This was done for each galaxy population (combinations of red/blue and bright/faint) as well as for the combined total population (red and blue, down to the faint limit).

Count density profiles for all of the individual clusters are shown in Figures D.5 to D.8 and their best fitting radial density profile parameters are given in Table 4.11 (full length table is given in Table D.1).

4.3.8.2 Background count density analysis

Before stacking the count density profiles of the clusters, the density of galaxies which are in the same line of sight as the cluster but not physically bound to it must be estimated and subtracted. Having already established that the objects may be embedded in more dense regions of the large scale structure (in Section §4.3.3.1), we made a number of different estimates of the local background for each observation set, with the aim of

assessing whether the background level was high because the cluster itself is extended, or due to a uniform surface density of objects across the observation field.

The simplest estimate S_{bgsimple} was found by taking the count density in the region bounded by $r > 1.5 r_{500}$. This method is susceptible to contamination by the wings of the galaxy density distribution, including virialised galaxies and structures like infalling subclusters and filaments.

We control for infalling structures which are not azimuthally symmetric by making n independent estimates S_{bgsector} (with standard deviation $\sigma_{S_{\text{bgsector}}}$) of the background level in annular sectors in the same bounded region. If the objects in the sectors are spatially uncorrelated and obey Poisson statistics, we would expect that the combined uncertainty of the n independent samples of the background density, $\alpha_{S_{\text{bgsector}}} = \sigma_{S_{\text{bgsector}}}/\sqrt{n}$, would be the same as the Poissonian value for the complete region, i.e. $\alpha_{S_{\text{bgsector}}} \sim \alpha_{S_{\text{bgsimple}}}$. On the other hand, spatially correlated objects are not drawn from a single Poisson distribution and appear significantly more frequently in some the sectors, leading to a higher $\alpha_{S_{\text{bgsector}}}$, i.e. we would expect $\alpha_{S_{\text{bgsector}}} > \alpha_{S_{\text{bgsimple}}}$ if local structures are present.

To control for broad wings of the galaxy density distribution, we fitted the NFW model described in Equation (4.5) - including a constant surface density component S_{bgNFW} - to the individual cluster profiles. S_{bgNFW} is sensitive to uniform density across the field, whereas S_{bgsimple} includes the cluster wings and infalling structures as well. $S_{\text{bgsimple}}/S_{\text{bgNFW}} > 1$ indicates that S_{bgsimple} is contaminated by the wings of the cluster and overestimates the background level.

The results of these measurements for the red galaxies down to the faint magnitude limit are given in Table 4.12, and Table 4.13 includes comprehensive results for all of the galaxy populations used in the radial profiles (the full length table is given in Table D.2).

Comparing $\alpha_{S_{\text{bgsector}}}$ and $\alpha_{S_{\text{bgsimple}}}$, we see that 7 of the clusters have $\alpha_{S_{\text{bgsector}}}/\alpha_{S_{\text{bgsimple}}} > 1.5$, consistent with the existence of localised substructures within some of the sectors. We conclude that in half of the sample, filamentary structure or infalling objects contribute to the high background in the cluster outskirts.

Values of > 1 for the ratio $S_{\text{bgsimple}}/S_{\text{bgNFW}}$ are suggestive that, in most cases, S_{bgsimple} is an overestimate contaminated by the wings of the cluster profile. (In the case of RXC J2023.0-2056, S_{bgNFW} is consistent with zero.) Measurements of the remnant luminosity function in this region, once a model of the field galaxy density is removed, are presented in Section §4.3.9.2.

We can also compare $S_{\text{bgsimple}}/S_{\text{bgNFW}}$ with f_g from Table 4.5. In RXC J0345.7-4112, RXC J0645.4-5413, RXC J0821.8+0112 and RXC J2129.8-5048, $S_{\text{bgsimple}}/S_{\text{bgNFW}} \geq f_g$, so at least a portion of the overdensity seen in the number counts function is likely due to contamination from the cluster itself, rather than the large scale structure along the line of sight.

The least contaminated estimate of the background galaxy count density appears to be S_{bgNFW} , so we use that to generate background subtracted count density profiles. Whilst relying on a background measurement which is dependent on a prior cluster shape rather than one which is shape independent is not ideal, there is sufficient scope in the NFW model to make a reasonable characterisation of most of the clusters we see.

Table 4.12: Background count density measurements for the red bright and faint galaxy population: simple count density S_{bgsimple} including Poisson uncertainties; standard error measured from sectors $\alpha_{S_{\text{bgsector}}}$; constant density component from an NFW fit S_{bgNFW} . Comprehensive results for red-bright, red-faint, blue-bright and blue-faint galaxy populations are given in Table 4.13.

Object	S_{bgsimple} arcmin ⁻²	$\alpha_{S_{\text{bgsector}}}$ arcmin ⁻²	S_{bgNFW} arcmin ⁻²	$\frac{S_{\text{bgsimple}}}{S_{\text{bgNFW}}}$	$\frac{\alpha_{S_{\text{bgsector}}}}{\alpha_{S_{\text{bgsimple}}}}$
RXC J0006.0–3443	0.87 ± 0.05	0.04	0.74 ± 0.08	1.17	0.9
RXC J0049.4–2931	0.490 ± 0.029	0.04	0.471 ± 0.019	1.04	1.4
RXC J0345.7–4112	0.120 ± 0.021	0.02	0.088 ± 0.032	1.37	1.0
RXC J0547.6–3152	0.93 ± 0.05	0.10	0.81 ± 0.09	1.15	1.9
RXC J0605.8–3518	1.13 ± 0.04	0.08	1.09 ± 0.06	1.04	1.9
RXC J0616.8–4748	0.73 ± 0.04	0.04	0.67 ± 0.06	1.09	1.1
RXC J0645.4–5413	1.35 ± 0.05	0.14	1.19 ± 0.08	1.14	2.9
RXC J0821.8+0112	0.344 ± 0.029	0.05	0.26 ± 0.05	1.30	1.9
RXC J2023.0–2056	0.13 ± 0.04	0.04	0.06 ± 0.09	2.19	1.0
RXC J2048.1–1750	1.66 ± 0.06	0.10	1.43 ± 0.17	1.17	1.8
RXC J2129.8–5048	0.321 ± 0.035	0.07	0.269 ± 0.027	1.19	1.9
RXC J2218.6–3853	0.83 ± 0.04	0.07	0.83 ± 0.04	1.00	1.9
RXC J2234.5–3744	1.19 ± 0.05	0.06	1.06 ± 0.06	1.12	1.2
RXC J2319.6–7313	0.514 ± 0.030	0.02	0.46 ± 0.05	1.11	0.8

Table 4.13: Background count density measurements. In the case of the RXC J2023.0–2056 bright blue filter, no objects are detected in the region used for measuring S_{bgsimple} . The full length table is provided in Table D.2.

Object	Galaxy filter	S_{bgsimple} arcmin ⁻²	$\alpha_{S_{\text{bgsector}}}$ arcmin ⁻²	S_{bgNFW} arcmin ⁻²	$\frac{S_{\text{bgsimple}}}{S_{\text{bgNFW}}}$
RXC J0006.0–3443	Bright, red	0.166 ± 0.020	0.02	0.12 ± 0.04	1.34
RXC J0006.0–3443	Faint, red	0.70 ± 0.04	0.04	0.62 ± 0.06	1.13
RXC J0006.0–3443	Bright, blue	0.128 ± 0.017	0.02	0.102 ± 0.029	1.25
RXC J0006.0–3443	Faint, blue	1.15 ± 0.05	0.07	0.67 ± 0.19	1.72
RXC J0049.4–2931	Bright, red	0.064 ± 0.011	0.01	0.050 ± 0.013	1.27
RXC J0049.4–2931	Faint, red	0.427 ± 0.027	0.03	0.413 ± 0.020	1.03
RXC J0049.4–2931	Bright, blue	0.074 ± 0.011	0.01	0.054 ± 0.022	1.38
RXC J0049.4–2931	Faint, blue	0.82 ± 0.04	0.04	0.797 ± 0.023	1.02

4.3.8.3 Comparison profiles and normalisation

With the given count statistics and binning, a deprojection of the count density profiles produces very noisy profiles and therefore comparisons are best made with other projected profiles.

The deprojected electron density profiles of Croston et al. (2008) do not extend to r_{cutoff} (the edge of our galaxy density model) because the cluster X-ray emission becomes too faint to observe, so these were extrapolated using a generalised NFW profile (described in Equation (4.5)) fit to Croston’s data, assuming c_{500} from Table 4.9 and allowing β , γ and ρ_0 to vary.

We also wished to compare the galaxy count density profiles with some model of the total mass of the cluster. Since this is dominated by dark matter, we assumed the NFW density profile form described in Equation (4.5) with $\beta = 3$ and $\alpha = \gamma = 1$, and the relevant c_{500} from Table 4.9.

The electron and total mass profiles were projected using the same numerical integrator as used for the galaxy count density profile fitting, in the same radial bins and with the same r_{cutoff} . Typically, the projected electron density profiles are dominated outside of $\sim 0.8 r_{500}$ by extrapolated densities.

Since the electron, total mass and galaxy count density profiles each have different normalisation, we plot $S / \sum_{r < r_{500}} S a$, where a is the total area in the annulus, wherever they are compared.

4.3.8.4 Stacked profiles

We produce stacked galaxy density profiles for all clusters and each subsample by taking the mean of $S_{\text{norm}} = (S - S_{\text{bgNFW}}) / n_{\text{g,r+b}}$ where $n_{\text{g,r+b}}$ is the total galaxy count for the cluster measured from the radial profile of all red and blue galaxies down the faint limit (see Section §4.3.8.1). The units of S_{norm} and S are r_{500}^{-2} . We produce stacked electron density profiles by taking the mean of $S_{\text{e,norm}} = S_{\text{e}} / \sum_{r < r_{500}} S_{\text{e}} a$, where $S_{\text{e,norm}}$ and S_{e} have units r_{500}^{-2} . Similarly, we produce stacked total mass profiles by taking the mean of $S_{M,\text{norm}} = S_M / \sum_{r < r_{500}} S_M a$, where $S_{M,\text{norm}}$ has units r_{500}^{-2} and S_M has units $M_{\odot} r_{500}^{-2}$. The mean profiles for the whole sample are shown in Figure 4.6.

The bright red profile follows the total mass profile reasonably well. The faint red profile is a little broader and there is a 3σ ($3\times$ the galaxy count density uncertainty) deficit of faint red galaxies in the central bin. The blue profiles are both substantially broader than the total mass profile. There appears to be suppression of faint blue objects compared to the overall trend which is limited to the region $< 0.15 r_{500}$; with respect to the NFW total mass curve (shown in grey) the deficit is around 5σ . The presence of a cD brightest cluster galaxy in the cluster core could make the detection of faint objects more difficult, but since the BCG occupies a small fraction of the area of the central bin – if indeed it is positioned there – this effect is negligible (see Table 4.10 for BCG sizes relative to the central bin area, and the distance of the BCG from the X-ray peak). Additionally, we would expect to see a similar effect for the red sequence galaxies, for

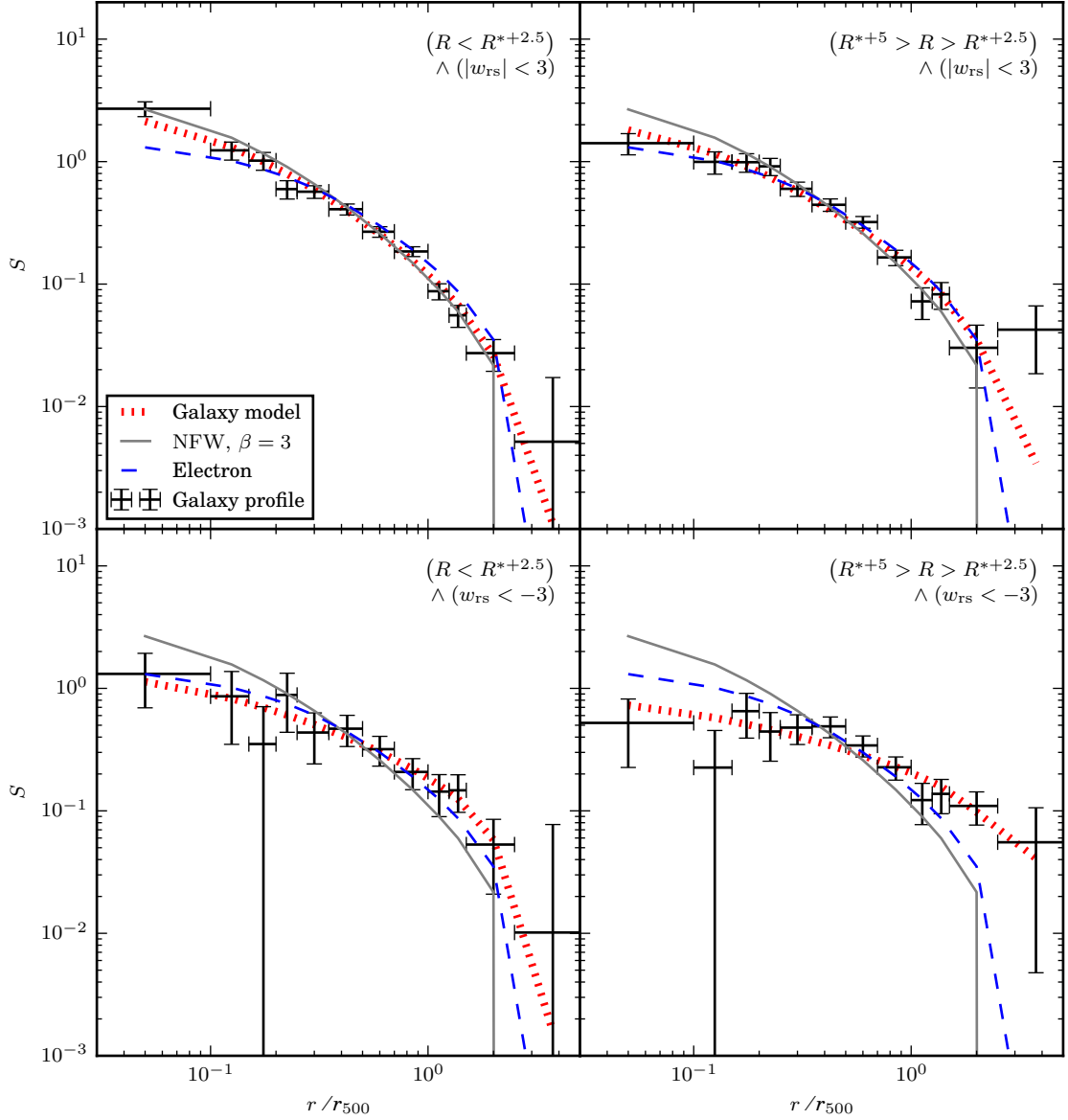
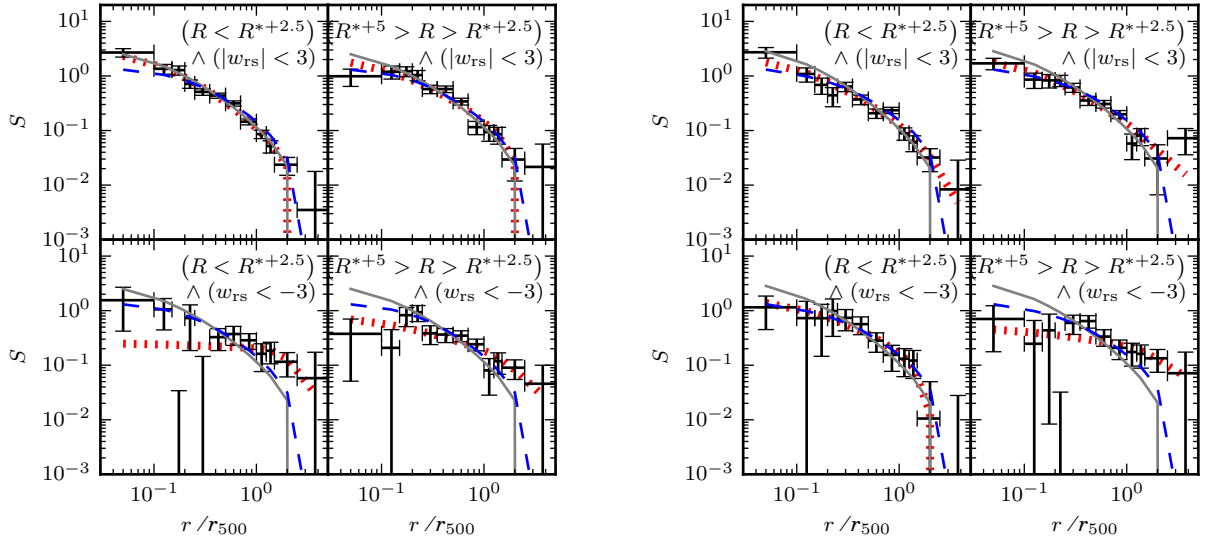


Figure 4.6: Mean projected radial profile of all of the clusters. Galaxy number density profiles are shown as black points with error bars, with the best fitting NFW model shown as a red dotted line. The projected electron density is shown as a blue dashed line. The NFW profile with parameters ($\alpha = 1, \beta = 3, \gamma = 1$) and c_{500} from Table 4.9 is shown in grey. The upper panels represent galaxies on the red sequence, and the lower panels include only galaxies bluer than the red sequence. The panels on the left are ‘bright’ and the panels on the right are ‘faint’ galaxies. The radial densities S shown are unitless, having been normalised by the mean S of all of the annuli within r_{500} , such that they overlay each other as closely as possible.



(a) Massive clusters: RXC J0006.0–3443,
 RXC J0547.6–3152, RXC J0605.8–3518,
 RXC J0645.4–5413, RXC J2048.1–1750,
 RXC J2218.6–3853, RXC J2234.5–3744

(b) Low mass clusters: RXC J0049.4–2931,
 RXC J0345.7–4112, RXC J0616.8–4748,
 RXC J0821.8+0112, RXC J2023.0–2056,
 RXC J2129.8–5048, RXC J2319.6–7313

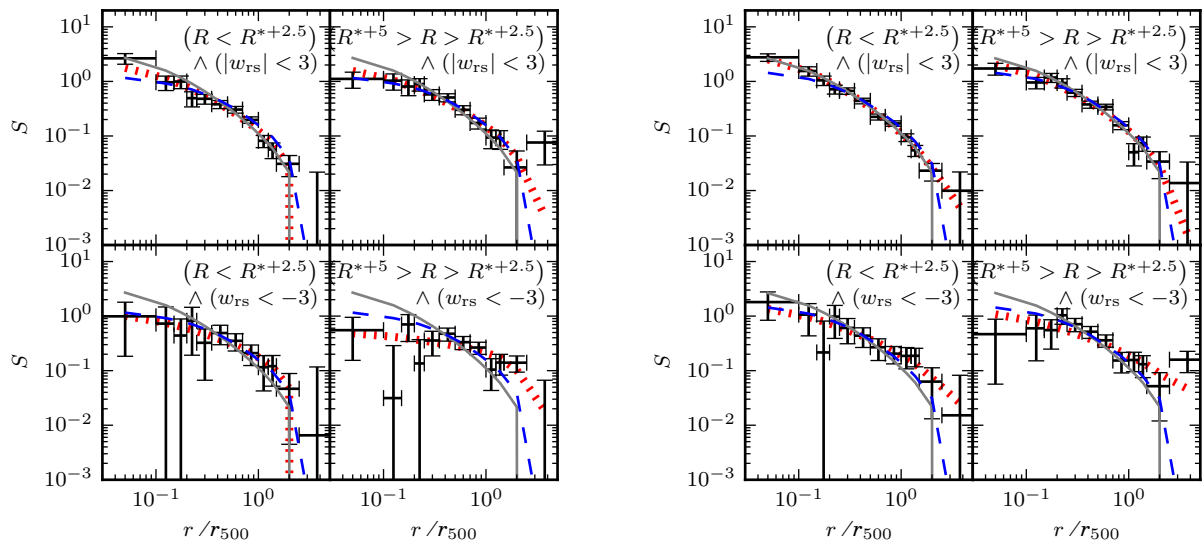
Figure 4.7: Stacked, projected radial number density profiles for clusters above and below the median mass in the population. The lines are the same as described in Figure 4.6.

which there is no evidence.

In Section §4.2.4 we described subsamples of the REXCESS dataset based on morphological classifications and cluster total mass. Mean profiles for the massive and low mass subsamples are shown in Figure 4.7, for the disturbed and regular subsamples in Figure 4.8, and for the cool-core and non-cool-core subsamples in Figure 4.9.

The subsample profiles appear to show that the suppression of faint blue galaxies in the cluster cores is driven by the massive subsample where this effect is marked, and is absent in the low mass subsample (both in Figure 4.7). The massive subsample also shows suppression of the faint red galaxies in the innermost radial bin ($< 0.1 r_{500}$), not seen in the mean profile for the whole sample. Figure 4.9 shows that there is even stronger suppression of faint blue galaxies in the cores of the cool-core clusters (only one of which is classified as massive), and this effect appears in all three cool-core clusters’ individual profiles (see Section §D.2). Additionally, suppression of bright blue galaxies is noted in the cool-core cluster cores, an effect not seen at all in the stacked profile for the full sample. In the cool-core clusters the red populations appear to be unaffected.

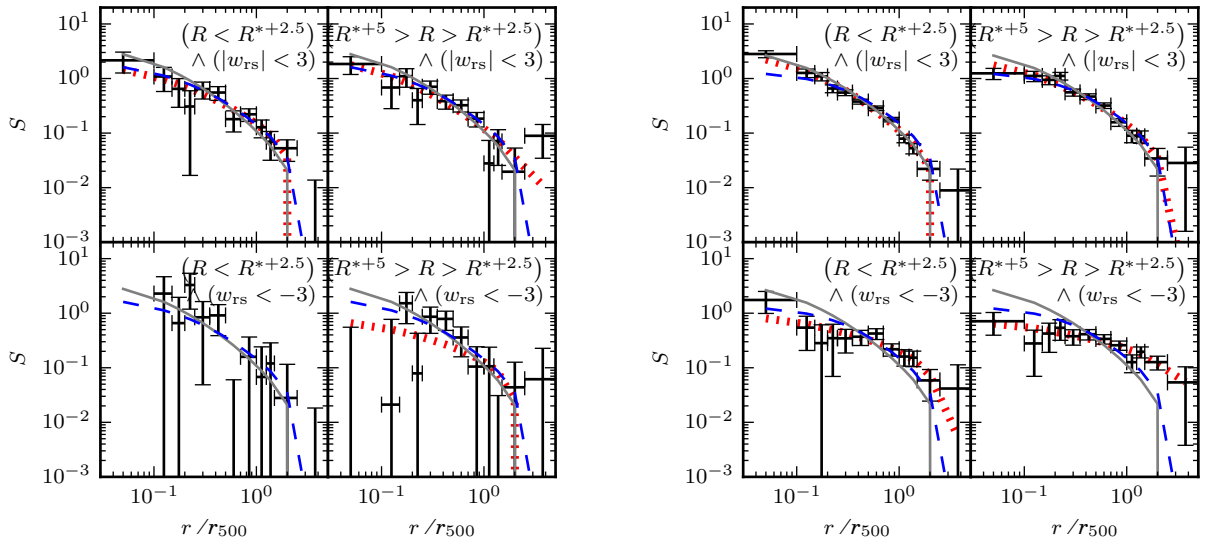
There is some suppression of faint blue galaxies in the centres of the regular clusters, but other than that the profiles for the regular and disturbed clusters appear qualitatively very similar to one another. In particular, we find no evidence from this analysis that there is any substantial difference between the two subsamples which might give a measure of



(a) Disturbed clusters: RXC J0006.0–3443,
 RXC J0616.8–4748, RXC J2023.0–2056,
 RXC J2048.1–1750, RXC J2129.8–5048,
 RXC J2218.6–3853, RXC J2319.6–7313

(b) Regular clusters: RXC J0049.4–2931,
 RXC J0345.7–4112, RXC J0547.6–3152,
 RXC J0605.8–3518, RXC J0645.4–5413,
 RXC J0821.8+0112, RXC J2234.5–3744

Figure 4.8: Stacked, projected radial number density profiles for disturbed and regular clusters. The lines are the same as described in Figure 4.6.



(a) Cool-core clusters: RXC J0345.7–4112,
RXC J0605.8–3518, RXC J2319.6–7313

(b) Non-cool-core clusters: RXC J0006.0–
3443, RXC J0049.4–2931, RXC J0547.6–
3152, RXC J0616.8–4748, RXC J0645.4–
5413, RXC J0821.8+0112, RXC J2023.0–
2056, RXC J2048.1–1750, RXC J2129.8–5048,
RXC J2218.6–3853, RXC J2234.5–3744

Figure 4.9: Stacked, projected radial number density profiles for cool-core and non-cool-core clusters. The lines are the same as described in Figure 4.6.

the dynamical state to complement the X-ray based centre shifts parameter used for the disturbed/regular classification (see Section §4.2.4). The difference which is seen could be statistical noise.

There is strong evidence that the profiles extend at least up to the $2.5 r_{500}$ limit, as the outer bins of the stacked profiles have a significant positive residual even after background subtraction.

We fitted projected generalised NFW models to the stacked galaxy count density profiles using the same method as used for the individual clusters to yield β_g , allowing for a constant density component S_{bgNFW} in case the background subtraction before stacking was incomplete. We include for comparison the mean electron density profile outer slope $\overline{\beta_e}$, which is calculated by taking the mean β_e of all the clusters in the subsample. The parameters are tabulated in Table 4.14 and the fits are shown in Figures 4.6 to 4.9.

The best fitting profiles for both bright and faint red sequence galaxies have outer slopes which are flatter than, but nevertheless in rough agreement with $\beta = 3$, the slope of the assumed total mass profile. The bright blue profile is substantially broader than the NFW, and the best fitting has outer slope inconsistent with $\beta = 3$. The faint blue profile is similar, with a best fitting outer slope consistent with the outer slope for the bright blue galaxies but with large uncertainties.

The cumulative fraction of red galaxies for the full sample, and for the high and low mass clusters is shown in Figure 4.10. These measurements reflect the morphology-density relation for ellipticals and spirals (e.g. Dressler, 1984), and our measured blue fraction at the limit of our observations – well within the cluster region of influence – is substantially lower than the field spiral population. Comparing the low mass and massive clusters, we see that outside $0.2 r_{500}$, the red fraction reaches a plateau in the low mass clusters, but in the massive clusters it is still higher than 90% and doesn't reach the same plateau level even at the limit of our observations. Even in low mass clusters, the red fraction approaches 100% in the central regions.

4.3.9 Luminosity measurements

4.3.9.1 Variation of the cluster luminosity function with radius

Since we see a reduction in the faint galaxy counts in cluster centres, we produced background subtracted luminosity functions for the projected annuli with edges at (0, 0.15, 0.5 and 1.0) r_{500} for the full galaxy population and for the red sequence galaxies. A selection of these luminosity functions are shown in Figure 4.11. The method of generation, normalisation and stacking is described in Section §4.3.3.2; the only difference is that we now impose an additional catalogue selection based on the red sequence fit.

Figure 4.11 shows that the red sequence luminosity functions outside of $0.15 r_{500}$ are all extremely similar. The inner luminosity functions have a break at around $R_{\text{AB abs K}} = -18$, above which the function drops below the trend. This suppression is largely due to the massive clusters. The uncertainties on the inner luminosity function for the low mass clusters are too large to conclude that there is suppression; within the uncertainties

Table 4.14: Stacked cluster best fitting parameters. ¹No error is quoted where the fitting routine failed to estimate the covariance matrix.

Object	Galaxy filter	β_g	β_e
All clusters	Bright, red	2.76 ± 0.16	2.936 ± 0.026
Massive	Bright, red	2.97 ± 0.17	3.131 ± 0.032
Low mass	Bright, red	2.54 ± 0.30	2.74 ± 0.04
Disturbed	Bright, red	2.53 ± 0.25	2.853 ± 0.034
Regular	Bright, red	3.00 ± 0.12	3.02 ± 0.04
Cool-core	Bright, red	2.20 ± 0.34	2.70 ± 0.06
Non-cool-core	Bright, red	2.85 ± 0.17	3.001 ± 0.028
All clusters	Faint, red	2.51 ± 0.22	2.936 ± 0.026
Massive	Faint, red	2.45 ± 0.35	3.131 ± 0.032
Low mass	Faint, red	2.54 ± 0.29	2.74 ± 0.04
Disturbed	Faint, red	2.29 ± 0.27	2.853 ± 0.034
Regular	Faint, red	2.70 ± 0.25	3.02 ± 0.04
Cool-core	Faint, red	2.6 ± 0.5	2.70 ± 0.06
Non-cool-core	Faint, red	2.43 ± 0.24	3.001 ± 0.028
All clusters	Bright, blue	1.80 ± 0.24	2.936 ± 0.026
Massive	Bright, blue	-0.3 ± 1.8	3.131 ± 0.032
Low mass	Bright, blue	1.85 ± 0.22	2.74 ± 0.04
Disturbed	Bright, blue	1.67 ± 0.30	2.853 ± 0.034
Regular	Bright, blue	2.04 ± 0.32	3.02 ± 0.04
Cool-core	Bright, blue	1.31^1	2.70 ± 0.06
Non-cool-core	Bright, blue	1.4 ± 0.4	3.001 ± 0.028
All clusters	Faint, blue	1.4 ± 0.4	2.936 ± 0.026
Massive	Faint, blue	1.5 ± 0.6	3.131 ± 0.032
Low mass	Faint, blue	0.9 ± 1.2	2.74 ± 0.04
Disturbed	Faint, blue	0.8 ± 0.7	2.853 ± 0.034
Regular	Faint, blue	1.9 ± 0.6	3.02 ± 0.04
Cool-core	Faint, blue	1.4 ± 1.4	2.70 ± 0.06
Non-cool-core	Faint, blue	1.3 ± 0.4	3.001 ± 0.028

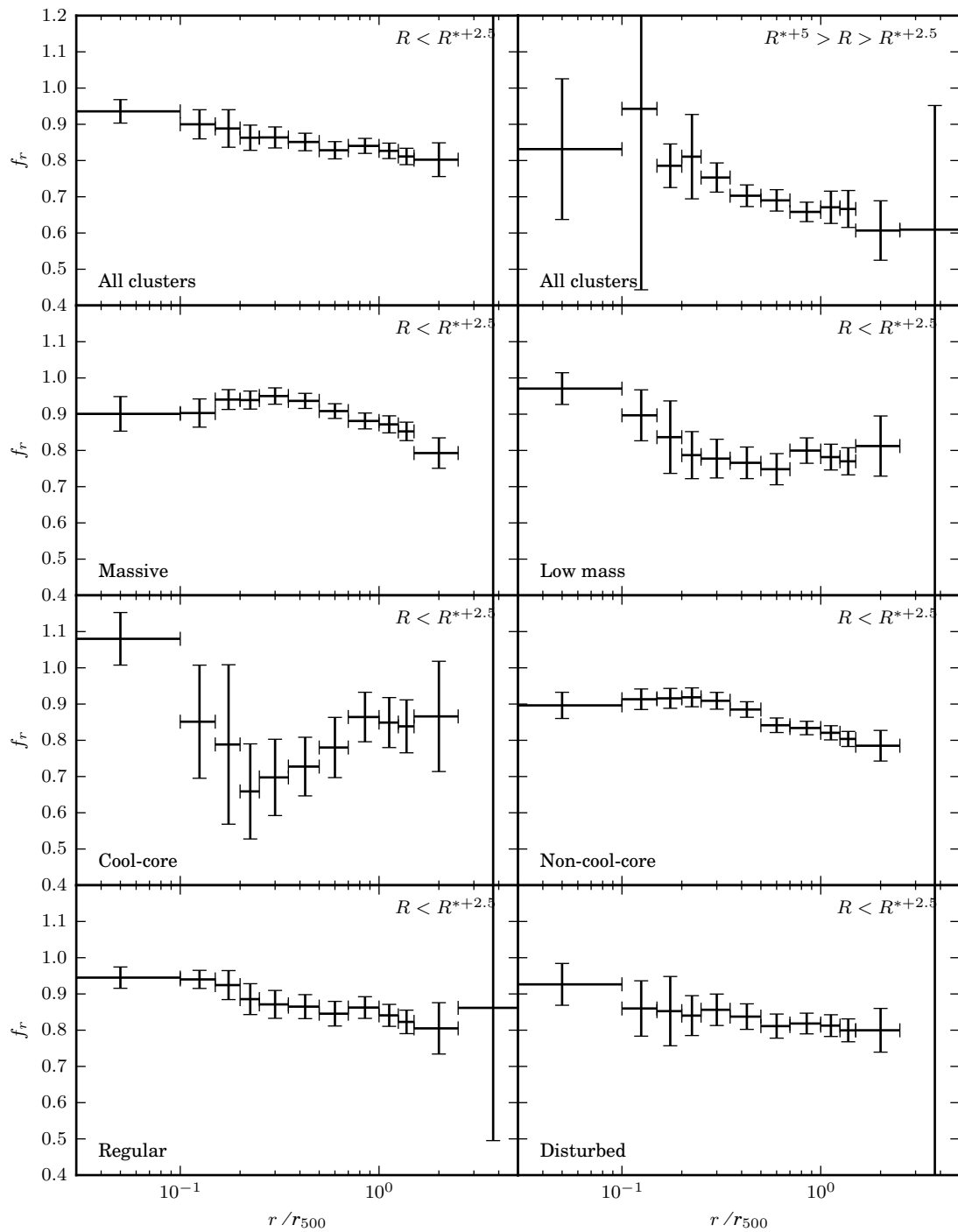
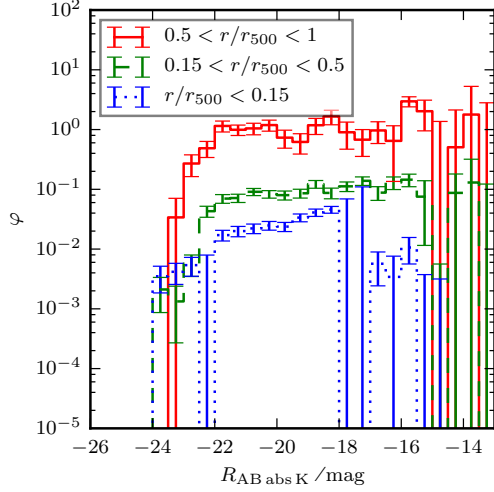
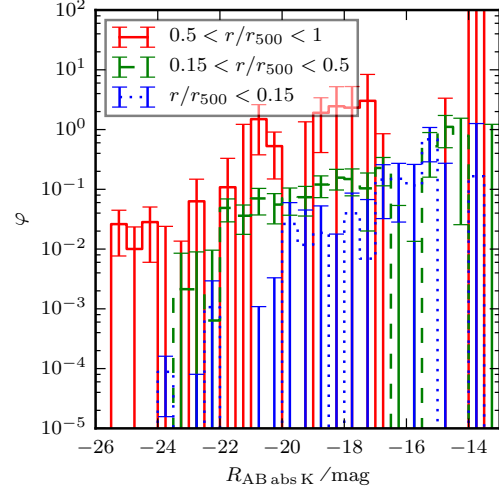


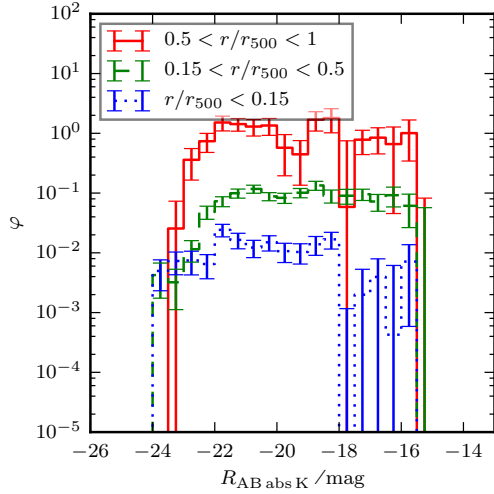
Figure 4.10: Cumulative fraction of red galaxies. The top two panels show (left) bright and faint galaxies for the whole sample and (right) only bright galaxies for the whole sample. The remaining panels show bright and faint galaxies for the specified subsamples.



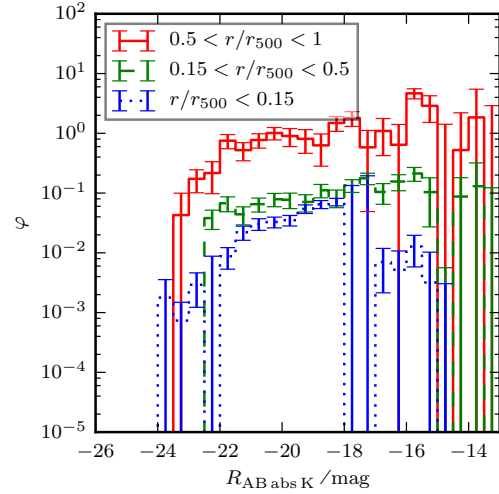
(a) Stacked luminosity functions for all the clusters in the dataset, including red sequence galaxies satisfying $|w_{rs}| < 3$.



(b) Stacked luminosity functions for all the clusters in the dataset, including blue galaxies satisfying $w_{rs} < -3$.

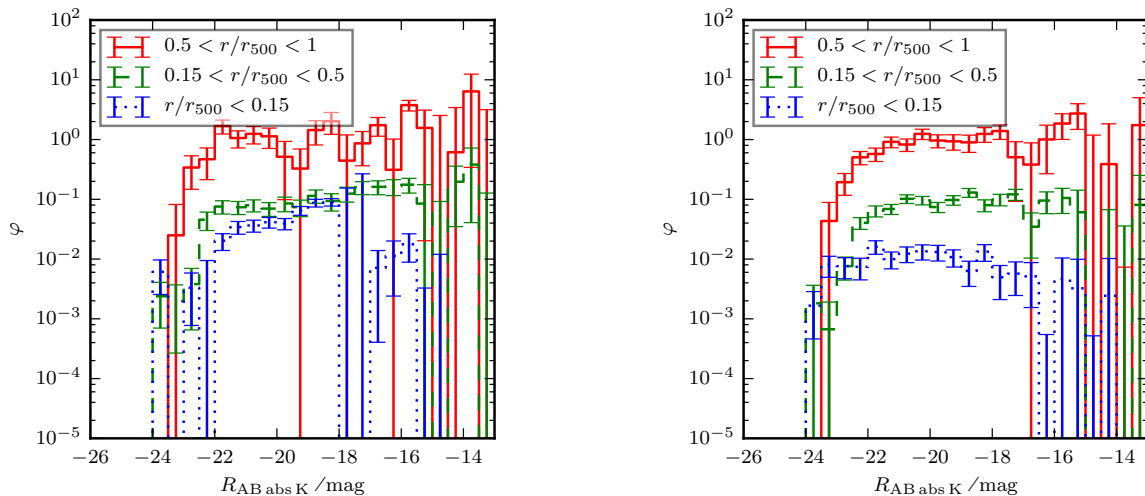


(c) Stacked luminosity functions for massive clusters, including red sequence galaxies satisfying $|w_{rs}| < 3$.



(d) Stacked luminosity functions for low mass clusters, including red sequence galaxies satisfying $|w_{rs}| < 3$.

Figure 4.11: Stacked luminosity functions for the annuli bounded by $(0, 0.15, 0.5$ and $1.0) r_{500}$. The functions are normalised and then artificially separated by a factor of 10.



(a) Stacked luminosity functions for disturbed clusters, including red sequence galaxies satisfying $|w_{rs}| < 3$.

(b) Stacked luminosity functions for regular clusters, including red sequence galaxies satisfying $|w_{rs}| < 3$.

Figure 4.12: Stacked luminosity functions for the annuli bounded by $(0, 0.15, 0.5$ and $1.0) r_{500}$. The functions are normalised and then artificially separated by a factor of 10.

it appears that the faint galaxy count continues the trend seen at brighter magnitudes. We note that the massive clusters are more distant on average, and that the magnitude limit is lower for these observations, but not sufficiently low that it explains the break at $R_{AB,abs,K} = -18$. Additionally, the stacking procedure – normalising to a complete part of the luminosity function and ensuring that truncated magnitude bins do not contribute to the mean – should minimize any influence of the completeness limit on the final luminosity function shapes. There is some evidence that the massive sample luminosity function is a little flatter than the low mass sample one, but given the size of the uncertainties it is difficult to be certain.

The blue object luminosity functions vary strongly with respect to cluster-centric distance. Figure 4.11b shows an excess of bright galaxies in the outer cluster regions ($0.5 < r/r_{500} < 1$) which isn't seen at smaller radii, and we found that there was an excess of bright blue galaxies in the off-target region as well. In the two inner regions sampled ($r/r_{500} < 0.15$ and $0.15 < r/r_{500} < 0.5$) there is strong variation in shape of the luminosity function, away from a simple Schechter function.

There is no evidence of a difference between the luminosity function of disturbed and regular clusters, shown in Figure 4.12. Any differences which are apparent are consistent with being statistical effects.

4.3.9.2 Residual cluster luminosity function in the off-target region

Given the evidence of structures in the off-target region in Section §4.3.8.2 and Section §4.3.8.4, we re-analysed the luminosity function in the $r_{200} < r$ region to try to find a residual cluster luminosity function, once our assumed field galaxy function was subtracted.

The possible excess of cluster galaxies outside r_{500} means that the normalisation factor f_g found for the assumed field galaxy function ξ_{Metcalfe} (see Section §4.3.3.1) may be slightly overestimated. However, since the cluster luminosity function is largely invariant with distance from the cluster centre, we can attempt to fit both cluster and field simultaneously for the full image. This should give an improved estimate of f_g , which can be used with ξ_{Metcalfe} as the background.

Assuming values for α and M^* from Table 4.6⁴ we fitted a combined model $\xi_{\text{falloff}}(\Phi(L) + f_g \xi_{\text{Metcalfe}})$ to the luminosity histogram of each full field, making no magnitude or red-sequence based selections since these may alter the field number counts. The ξ_{Metcalfe} component was subtracted from the count histogram in the off-target region, and the results are shown in Figure 4.13.

The shape of the residual in Figure 4.13 appears, in most cases, inconsistent with the shape of the background number counts function which is also shown. The residual often resembles the cluster luminosity function. This is consistent with the tentative conclusion drawn in Section §4.3.8.2, that the cluster does extend some distance outside of r_{200} . Compared with the on-target luminosity functions shown in Section §4.3.9.1, these residuals have denser faint components, with an upturn at fainter magnitudes similar to the dwarf upturn seen in Popesso et al. (2006), but are also consistent with being due to some remnant field contamination.

4.3.9.3 Total cluster luminosity

The total cluster luminosity and the related mass-to-light ratio are useful parameters when assessing the efficiency or disruption of star formation in different types of galaxy clusters. Since we are dealing with projected data, a correction needed to be made for the cluster galaxies outside of r_{500} or r_{200} but, when seen in projection, in one of the annular bins.

We considered two populations of galaxies when calculating the total cluster luminosities: $|w_{\text{rs}}| < 3$ which includes only galaxies on the red sequence, and $w_{\text{rs}} < 3$ which includes both the red sequence and the blue cloud, but excludes objects redder than the red sequence. To ensure that the correction to the total luminosity required due to the magnitude limit was approximately equal for all the clusters in the sample, we considered galaxies satisfying $R < R^* + 5$.

⁴ α and M^* were fitted to the entire sample. Since the cluster luminosity function is invariant with distance from the cluster centre, the background subtraction performed before the stacking operation in Section §4.3.3.2 should not bias the shape of the final luminosity function, despite the small residual of cluster galaxies in the region used as the background.

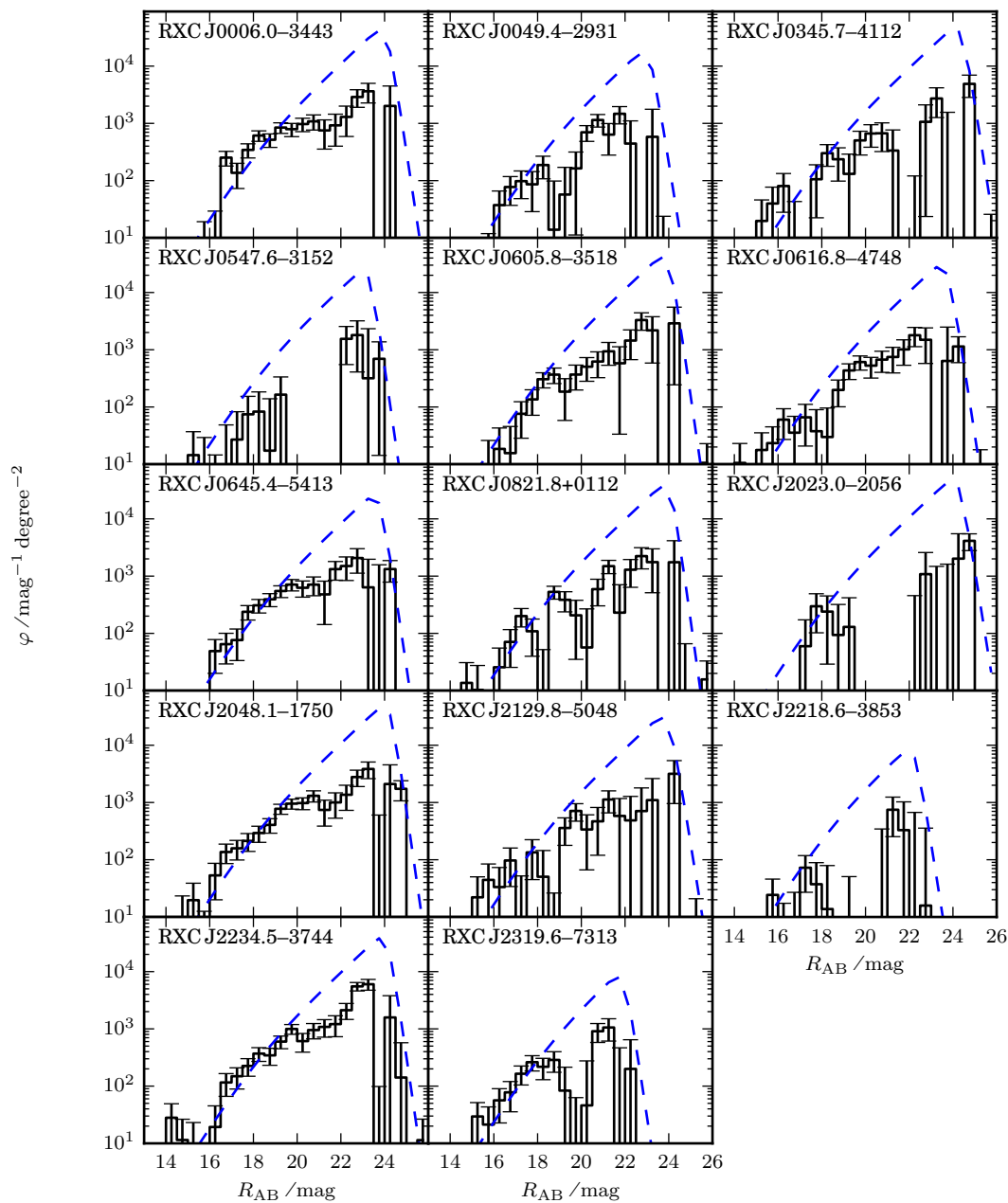


Figure 4.13: Off-target region ($r_{200} < r$) residual cluster luminosity function. The assumed background model (including the falloff component) is shown as a dashed line for comparison.

Using the best fitting NFW models – which include a background estimate – for each of the galaxy populations, we assign a weight w which represents the probability that a galaxy seen in a particular radial bin is within r_Δ . If the total best fitting model count density for a particular radial bin is $S_{\text{total}} = S_{\text{bgNFW}} + S_{\text{NFW}, r_{\text{cutoff}}=2.5r_{500}}$ (as described in Section §4.3.8.1), the weight assigned to each galaxy in that radial bin is $w_\Delta = S_{\text{NFW}, r_{\text{cutoff}}=r_\Delta} / S_{\text{total}}$, where S_{NFW} is found by integrating the volume density model ρ in annuli along the line of sight, and setting $\rho = 0$ where $r > r_{\text{cutoff}}$. The total luminosity within r_Δ is then the sum $\sum_i w_{\Delta i} L_i$, and the total count is $\sum_i w_i$ for all galaxies i in the particular population. The major source of uncertainty in this calculation is the uncertainty on w , arising from the uncertainties on the fitting parameters in the model. The BCG is assigned $w = 1$, but other galaxies are not specially treated. Typical values of w are around 0.9 in the innermost radial bins.

Since the radial count density profiles for the bright red, faint red, bright blue and faint blue populations are different, we calculate luminosities for all four subpopulations separately, and then sum the relevant sub-populations to get total red or red plus blue luminosities. In cases where the best fitting model is consistent with there being no overdensity for a particular population and has very large uncertainties on the relevant fit parameters this subpopulation is not included in the final total luminosity. Only the RXC J0345.7–4112 faint blue population is affected by this step.

The total luminosities for each cluster are given in Table 4.15.

4.3.9.4 Mass-to-light ratio relation

M_{500} and M_{200} were calculated using r_{500} from Table 4.1, concentration parameters from Table 4.9 (to transform between r_{500} and r_{200}) and the fiducial cosmology. We calculated mass-to-light ratios M_Δ/L_Δ for each of the clusters, which are plotted against M_Δ in Figure 4.14. Using $M_\Delta/L_\Delta = \eta (M_\Delta/M_{\text{pivot}})^\epsilon$ as a model, with $M_{\text{pivot}} = 5 \times 10^{14} M_\odot$, we found best fitting parameters to the mass-to-light vs. mass relation, which are given in Table 4.16.

Three objects – RXC J0345.7–4112 (cool-core), RXC J00605.8–3518 (cool-core and massive) and RXC J2218.6–3853 (massive and disturbed) – lie slightly above the fitted mass-to-light relationship, but do not significantly affect the fit.

We find a slope ϵ of 0.01 ± 0.10 for the red sequence within r_{200} , and 0.11 ± 0.14 for the red plus blue galaxy population within r_{200} . The increase in slope when the blue luminosity is included compared with the case with just the red sequence luminosity is consistent with a decrease in blue fraction at high masses, already noted in Section §4.3.8.4 and shown in Figure 4.10. The increase in the mean luminosity of blue galaxies as cluster mass increases and faint galaxies are disrupted/otherwise suppressed is insufficient to compensate for the decreased blue fraction.

Popesso et al. (2007) measured M_{200}/L_{200} for red sequence objects and quote a slope $\epsilon = 0.18 \pm 0.04$, once projection effects are taken into account. Whilst this result is in fair agreement with our measurements given the uncertainties, both of our best estimates for the red sequence are somewhat flatter.

Table 4.15: Total R band luminosities.

Object	Galaxy filter	L_{500} $10^{12} L_{\odot}$	L_{200} $10^{12} L_{\odot}$
RXC J0006.0–3443	Bright and faint, red	1.70 ± 0.19	2.52 ± 0.28
RXC J0006.0–3443	Bright and faint, red and blue	2.03 ± 0.20	3.23 ± 0.32
RXC J0049.4–2931	Bright and faint, red	1.16 ± 0.13	1.47 ± 0.16
RXC J0049.4–2931	Bright and faint, red and blue	1.39 ± 0.17	1.98 ± 0.26
RXC J0345.7–4112	Bright and faint, red	0.283 ± 0.028	0.36 ± 0.04
RXC J0345.7–4112	Bright and faint, red and blue	0.330 ± 0.033	0.41 ± 0.05
RXC J0547.6–3152	Bright and faint, red	2.48 ± 0.20	3.42 ± 0.29
RXC J0547.6–3152	Bright and faint, red and blue	2.62 ± 0.26	3.7 ± 0.4
RXC J0605.8–3518	Bright and faint, red	1.34 ± 0.10	1.75 ± 0.13
RXC J0605.8–3518	Bright and faint, red and blue	1.39 ± 0.11	1.82 ± 0.14
RXC J0616.8–4748	Bright and faint, red	1.10 ± 0.07	1.64 ± 0.13
RXC J0616.8–4748	Bright and faint, red and blue	1.39 ± 0.11	2.13 ± 0.17
RXC J0645.4–5413	Bright and faint, red	4.34 ± 0.28	6.0 ± 0.4
RXC J0645.4–5413	Bright and faint, red and blue	4.43 ± 0.28	6.2 ± 0.4
RXC J0821.8+0112	Bright and faint, red	0.82 ± 0.07	1.31 ± 0.13
RXC J0821.8+0112	Bright and faint, red and blue	1.06 ± 0.09	1.80 ± 0.19
RXC J2023.0–2056	Bright and faint, red	0.49 ± 0.10	0.68 ± 0.16
RXC J2023.0–2056	Bright and faint, red and blue	0.64 ± 0.14	0.88 ± 0.22
RXC J2048.1–1750	Bright and faint, red	2.55 ± 0.28	4.1 ± 0.5
RXC J2048.1–1750	Bright and faint, red and blue	3.09 ± 0.29	5.3 ± 0.5
RXC J2129.8–5048	Bright and faint, red	0.98 ± 0.14	1.23 ± 0.21
RXC J2129.8–5048	Bright and faint, red and blue	1.02 ± 0.15	1.32 ± 0.21
RXC J2218.6–3853	Bright and faint, red	1.20 ± 0.26	1.44 ± 0.30
RXC J2218.6–3853	Bright and faint, red and blue	1.35 ± 0.27	1.71 ± 0.33
RXC J2234.5–3744	Bright and faint, red	3.98 ± 0.16	5.23 ± 0.21
RXC J2234.5–3744	Bright and faint, red and blue	4.52 ± 0.23	6.5 ± 0.5
RXC J2319.6–7313	Bright and faint, red	0.50 ± 0.06	0.86 ± 0.10
RXC J2319.6–7313	Bright and faint, red and blue	0.62 ± 0.08	1.02 ± 0.12

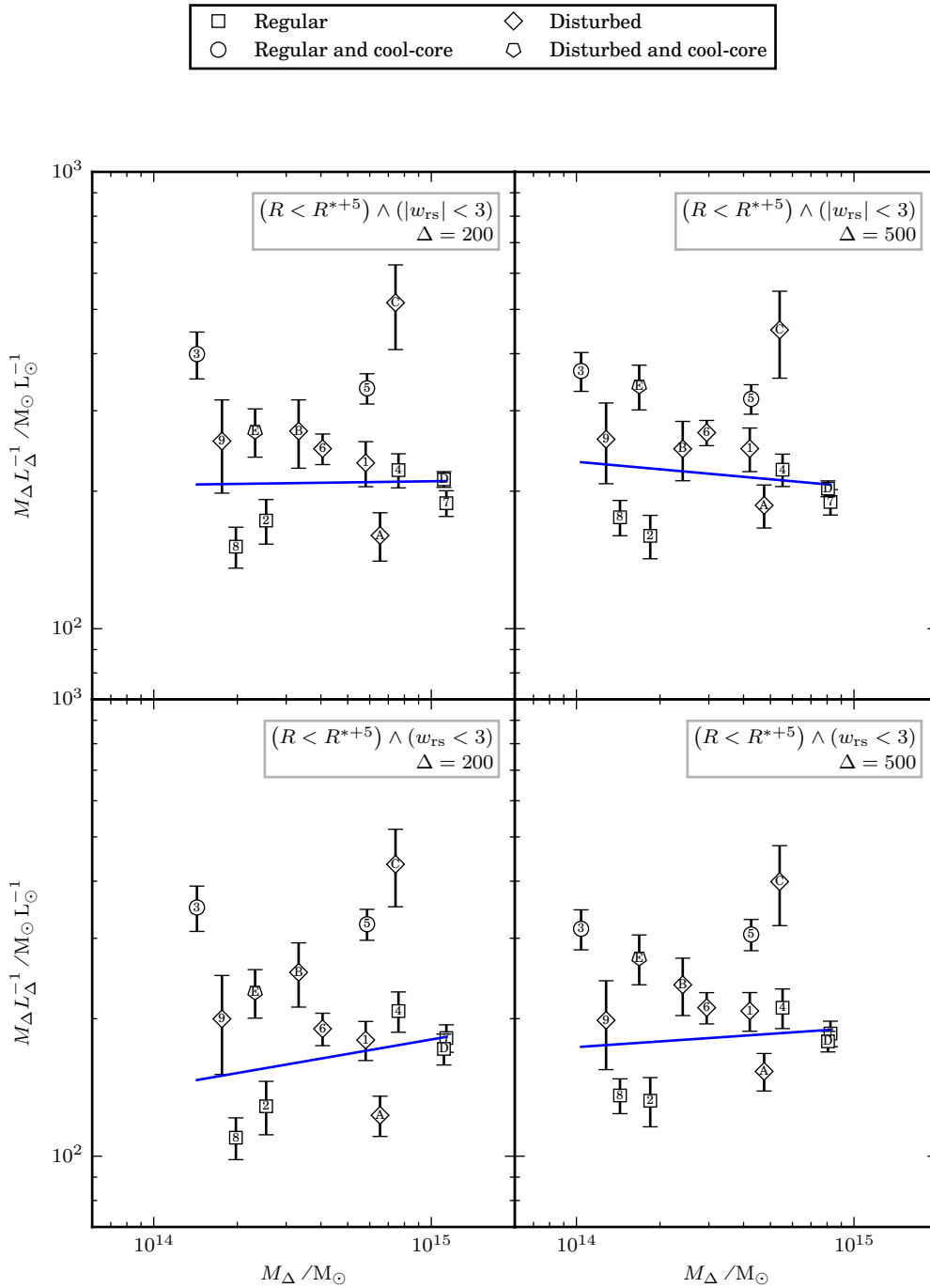


Figure 4.14: Mass-to-light relations. The marker labels are the IDs given in Table 4.1. The uncertainties only take into account the luminosities; mass uncertainties have not been considered.

Table 4.16: Best fitting parameters to the mass-to-light ratio relation $M_{\Delta}/L_{\Delta} = \eta (M_{\Delta}/M_{\text{pivot}})^{\epsilon}$ where $M_{\text{pivot}} = 5 \times 10^{14} M_{\odot}$. The values of the $M_{\Delta} L_{\Delta}^{-1}$ measured at $10^{14} M_{\odot}$ and $10^{15} M_{\odot}$ are corrected for the magnitude cut at $R < R^* + 5$ using the correction factor described in Section §4.3.3.2. η is not corrected for the magnitude cut.

Galaxy filter	Δ	η $M_{\odot} L_{\odot}^{-1}$	ϵ	$M_{\Delta} L_{\Delta}^{-1} (10^{14} M_{\odot})$ $M_{\odot} L_{\odot}^{-1}$	$M_{\Delta} L_{\Delta}^{-1} (10^{15} M_{\odot})$ $M_{\odot} L_{\odot}^{-1}$	$M_{\Delta} L_{\Delta}^{-1} h^{-1} (10^{15} M_{\odot})$ $M_{\odot} L_{\odot}^{-1}$
Bright and faint, red	200	209.0 ± 14.4	0.01 ± 0.10	$(2.0 \pm 0.3) \times 10^2$	$(2.1 \pm 0.2) \times 10^2$	$(2.9 \pm 0.3) \times 10^2$
Bright and faint, red	500	212.4 ± 13.1	-0.05 ± 0.09	$(2.3 \pm 0.4) \times 10^2$	$(2.0 \pm 0.2) \times 10^2$	$(2.9 \pm 0.2) \times 10^2$
Bright and faint, red and blue	200	167.5 ± 15.5	0.11 ± 0.14	$(1.4 \pm 0.3) \times 10^2$	$(1.8 \pm 0.2) \times 10^2$	$(2.5 \pm 0.3) \times 10^2$
Bright and faint, red and blue	500	185.3 ± 13.4	0.04 ± 0.10	$(1.7 \pm 0.3) \times 10^2$	$(1.9 \pm 0.2) \times 10^2$	$(2.7 \pm 0.3) \times 10^2$

Sheldon et al. (2009b) quote a logarithmic slope on the mass-to-light ratio of $\epsilon = 0.33 \pm 0.02$ for objects in the MaxBCG catalogue of galaxy clusters in the Sloan Digital Sky Survey measured in the i band, a value in fair agreement with our measurement for the red and blue populations, but in this case too, our result is flatter.

The $\sim (5 \times 10^{12} - 10^{15}) h^{-1} M_{\odot}$ range in M_{200} available to both Popesso et al. and Sheldon et al. is substantially larger than the single order of magnitude mass range in REXCESS, lending their analyses greater power to resolve mass dependent effects.

Carlberg et al. (1997) quote an asymptotic value $(289 \pm 50) h M_{\odot} L_{\odot}^{-1}$ for the Gunn r band, in excellent agreement with our value of $(251.1 \pm 33.7) h M_{\odot} L_{\odot}^{-1}$ for the red and blue galaxies in the R band, measured at $10^{15} M_{\odot}$.

4.4 Discussion

Both the invariance of the cluster luminosity function with respect to radius (outside of cluster centres, i.e. $r > 0.15 r_{500}$) and suppression of faint galaxies in the central regions of galaxy clusters have been noted before (Popesso et al., 2006). Popesso et al. found significant suppression in the late type luminosity function (corresponding to our blue population) for small cluster-centric distances; we find that there is substantial change in the red luminosity function close to the cluster core as well.

The colour-magnitude relation parameters drawn from the WINGS clusters (Valentinuzzi et al., 2011) are quite similar to the values we see here, although the gradient scatter from our sample is twice as large as that from WINGS. That sample is also X-ray selected, but from clusters with lower redshifts. Whilst it may be the case that there is a tightening of the distribution of red sequence parameters at redshifts approaching $z = 0$, it is difficult to distinguish this effect from the increased measurement uncertainties introduced by increasing numbers of field galaxies in the same region of colour-magnitude space.

Of particular interest to us was any indication that the galaxy density profile of disturbed clusters is also disturbed. Both the slope of the galaxy count density distribution (β_g) and the luminosity functions could have shown differences, but there is no significant evidence of a difference in either of these two properties in the disturbed and regular subsamples. The similarity in the luminosity functions echoes the findings of De Propris et al. (2013) where luminosity functions of collisional and normal clusters in a sample selected by X-ray, optical and weak and strong lensing were studied.

We suggest that two main processes can be invoked to explain the distribution of red and blue, bright and faint galaxies in clusters. Ram pressure stripping occurs as a galaxy moves with velocity v through the intracluster medium (ICM) with density ρ , and the gas in the galaxy is subjected to pressure $P \propto \rho v^2$ (Gunn and Gott, 1972). The pressure ablates cool gas from the halo, slowing star formation and turning blue galaxies redder. This effect should be more pronounced in regions of galaxy clusters with high gas densities, in particular in cool-cores. The galaxy infall velocity is related to the cluster mass M by $v^2 \propto M$, so ram pressure stripping should also be stronger for more massive clusters. Because this process affects bright (as well as faint) galaxies, which

dominate the total luminosity of the cluster, it should lead to a decrease in fraction of the cluster luminosity provided by the blue galaxy population as cluster mass increases. As it affects star formation as a whole, it should also lead to decreased overall star formation efficiency in more massive clusters and to a positive slope on the mass-to-light ratio relation measured using just red sequence galaxies.

The second main process, harassment, occurs as weakly bound galaxies interact tidally with more massive objects. Parts of the weakly bound galaxy are stripped away, or the galaxy is completely disrupted. The remnants are a source of intracluster light (ICL). This process is strongest in regions where galaxy count densities and velocities are highest and affects more weakly bound (less massive/lower luminosity) galaxies more. Because the galaxy count densities in the central regions of the clusters are not strongly dependent on mass, this effect is expected to be less mass dependent than ram pressure stripping.

There are several key pieces of evidence we can use to disentangle the two processes. The suppression of faint galaxies independent of the galaxy colour in the densest regions of the galaxy clusters, with the strongest effect in the most massive clusters, suggests harassment – a gravitational process independent of gas density and star formation in the affected galaxy – is important. The steeper mass-to-light ratio relation for the blue plus red galaxies vs. the red sequence alone, as well as decreasing blue galaxy fraction with higher mass, is evidence that ram pressure stripping – a process which primarily affects blue galaxies – is increasingly effective in reducing star formation rates as infall velocities of galaxies rise. From the flatter blue galaxy count density profiles in all of the clusters, it is clear that the blue galaxy population does not survive long enough to relax into the cluster potential before being stripped of its cold gas and becoming part of the red population. There is some evidence that the suppression of blue galaxies is most pronounced in the regions with the highest gas densities at the centres of cool-core clusters, but given the small sample size we cannot be certain that this is not a statistical anomaly.

The REXCESS sample was selected by X-ray luminosity, ensuring that only clusters which are well evolved and have deep gravitational potential wells with hot, dense ICM are selected. This is in contrast to clusters in optically selected samples which are not always as well evolved, and consequently may not have a sufficiently dense ICM for efficient ram pressure stripping. Böhringer et al. (2004) note that cool-cores in clusters are long-lived, which may allow more time for processes which disrupt galaxies and stop star formation from taking place.

Both the red sequence and red plus blue mass-to-light ratio relation slopes we measure are flatter than in the literature, compared to both X-ray selected samples (Popesso et al., 2007) or optically selected samples (Sheldon et al., 2009a). Given the scatter in the relation and the relatively large uncertainties on the best fitting parameters, as well as the fact that the REXCESS sample contains only clusters spanning one order of magnitude at the highest masses, it is impossible using these data to distinguish between the case where the differences between the slopes measured here and in the literature are purely statistical in nature, or due to different physical processes in the two samples – e.g. stronger ICM effects.

The ICL has not been taken into account in this work, but if the relative density of the ICL in the centres of massive clusters were higher than in low mass clusters, then this would be further evidence for increased harassment. If we assume that 10% of the light of galaxy clusters is ICL (e.g. Zibetti et al., 2005), our mass-to-light ratio normalisations may be overestimated by a factor of ~ 1.1 , leading to a correction of comparable size to the normalisation uncertainties. However, based on the measurements of the BCG sizes and luminosities as compared with Haarsma et al. (2010) described in Section §4.3.7, it seems likely that a substantial fraction of the intracluster light is included in the BCG luminosity we measure, so the correction may well be smaller.

Gonzalez et al. (2007) and Gonzalez et al. (2013) discuss the reduced efficiency of ICL generation in more massive objects which is coupled with a higher X-ray gas fraction. Zibetti et al. (2005) find that the ICL surface brightness is correlated with BCG luminosity, but that the total fraction of light contributed by the ICL is almost independent of cluster richness and BCG luminosity. Given the open discussion on the ICL light fraction as a function of cluster mass, it is too premature to include the effect of the ICL in the mass-to-light ratio in our results.

4.5 Summary and conclusions

We have used a sample of 14 galaxy clusters from the REXCESS survey to investigate radial density profiles of galaxies and intra-cluster medium.

- The red galaxy density traces the dark matter density closely outside of the cluster centres (in the region $r > 0.15 r_{500}$). The best fitting NFW model outer-slopes β_g are roughly consistent with $\beta_g = 3$, with a best estimate $\beta_g = 2.76 \pm 0.16$, fitted to the stacked bright red sequence galaxy density profile of all the clusters.
- The blue sequence count density profile slopes are substantially shallower than the $\beta = 3$ total mass model, with a best estimate $\beta_g = 1.80 \pm 0.24$, fitted to the stacked bright blue galaxy density profile of all the clusters.
- The mean outer slope for the gas density profiles of the full sample is $\beta_e = 2.936 \pm 0.026$. Within the cluster centres the gas and dark matter profiles tend to diverge.
- We find that faint blue galaxies are suppressed in the centres of massive and regular clusters. Faint red galaxies are also suppressed in the centres of massive clusters. Both bright and faint blue galaxies are heavily suppressed in the centres of cool-core clusters, but the faint red galaxies are unaffected. This is consistent with the idea that the suppression of star formation is driven by ram pressure stripping of gas from galaxies, but that wholesale disruption of galaxies is caused by galaxy interactions in regions with high galaxy densities.
- Our measurement of the logarithmic slope ϵ of the galaxy cluster mass-to-light relation within r_{200} of 0.11 ± 0.14 for all galaxies, measured in the R band, is in fair

agreement with $\epsilon = 0.33 \pm 0.02$ from Sheldon et al. (2009b), measured in the i band. Our measurement of the mass to light ratio normalisation of $(251.1 \pm 33.7) h M_{\odot} L_{\odot}^{-1}$ (evaluated at $10^{15} M_{\odot}$) in the R band is in excellent agreement with Carlberg et al. (1997) measured in the Gunn r band.

- There is no evidence of any difference in the galaxy count density profiles when comparing clusters classified as having disturbed X-ray morphology with those which are regular.

Acknowledgements

We acknowledge support from the DFG Transregio Programme TR33 ‘Dark Universe’ and the Munich Excellence Cluster ‘Structure and Evolution of the Universe.’ GC acknowledges support from DLR through project 50 OR 1305. DP acknowledges the financial support from Labex OCEVU. The X-ray data used here are based on observations with *XMM-Newton*, an ESA science mission with instruments and contributions directly funded by ESA member states and NASA. This research has made use of the SIMBAD database, operated at CDS, Strasbourg, France. This research has made use of the NASA/IPAC Extragalactic Database (NED) which is operated by the Jet Propulsion Laboratory, California Institute of Technology, under contract with the National Aeronautics and Space Administration. This research has made use of NASA’s Astrophysics Data System. This research made use of *ASTROPY*, a community-developed core *PYTHON* package for astronomy (Astropy Collaboration et al., 2013). Additional analysis was carried out using *SCIPY* and plots were made using *MATPLOTLIB* (Hunter, 2007). This research was made possible through the use of the AAVSO Photometric All-Sky Survey (APASS), funded by the Robert Martin Ayers Sciences Fund.

Chapter 5

Optical and X-ray substructure in the REXCESS sample of galaxy clusters

John G. Holland, Hans Böhringer, Gayoung Chon and Daniele Pierini

Abstract

Gas and galaxies behave differently during galaxy cluster mergers, retaining complementary information about past cluster evolution. We study the gas and galaxies in 14 clusters in the REXCESS galaxy cluster survey to find this complementary information. *XMM-Newton* X-ray surface brightness maps of the intracluster medium (ICM) are compared with smoothed galaxy count density maps based on *BVR* data from the 2.2 m MPG/ESO telescope. Both datasets are characterised with various structure and substructure algorithms, and sub-clump catalogues for each cluster are produced.

We find weak correlation between the centre shift parameter measured on X-ray images and the distribution of red sequence galaxies, but no correlation with blue cloud galaxies. There is good correlation between ellipticity and orientation in the red sequence galaxy distribution and ICM, but the blue galaxy distribution does not trace the ICM. Sub-clumps are detected in the red sequence galaxy distribution in clusters which are regular when measured in X-rays. We attribute this to the longer relaxation time of sub-clumps of galaxies as compared with the ICM. No correlation is found between the density of optical clumps in the cluster or its nearby environment and the X-ray centre shift parameter; the lack of correlation is observed because almost all of the clusters have significant optical substructure which remains long after the ICM relaxes. We use complementary information available in X-ray and optical maps to characterise a subset of the clusters as pre- and post-merger systems, and find that X-ray or photometric optical measurements alone are insufficient to characterise cluster dynamical state unambiguously.

5.1 Introduction

Galaxy clusters are useful cosmological tracers because they are the largest bound and virialised objects in the observable Universe. They have properties fundamentally linked with the initial conditions of the Universe's expansion, with the history of cosmic expansion, and with the gravitational processes which dominate dynamics of astrophysical systems on large scales (reviewed in Kravtsov and Borgani, 2012). Their matter constituents are roughly consistent with those of the universe as a whole. They each contain a sample of galaxies which have evolved under quite similar circumstances. Galaxy clusters show a range of morphologies (Bautz and Morgan, 1970) which presumably represent different evolutionary histories.

They contain several matter components whose dynamics are quite different and are, to some extent, independent. These different matter components retain the signatures of major events like mergers with other clusters or galaxy groups, allowing these processes to be studied and compared with cosmological simulations. Their gas makeup and dynamics is affected by feedback from their constituent galaxies in addition to gravitational processes.

We are interested in looking for correlations and complementary information about galaxy cluster dynamical state which can be gained by comparing X-ray observations of the intracluster medium (ICM) and optical observations of the galaxy populations within clusters. In the last two decades several groups have performed joint X-ray–optical analysis on individual clusters and cluster samples (e.g. Zabludoff and Zaritsky, 1995; Kolokotronis et al., 2001; Hashimoto et al., 2007; Ramella et al., 2007; Haarsma et al., 2010; Verdugo et al., 2012; Mahdavi et al., 2013). In this study, we present an analysis based on high quality *XMM-Newton* and wide field optical follow-up data for a representative sample of X-ray luminous clusters, selected independent of morphological type.

The dominant component of galaxy clusters is the dark matter halo composed of collisionless particles, which can be detected by the influence it has on the dynamics of gas and galaxies in clusters, and because it acts as a gravitational lens for light from more distant galaxies.

The dominant baryonic component, the hot intra cluster medium (ICM), is a plasma which can be treated as a collisional fluid and – because it can redistribute linear momenta – relaxes more quickly than the dark matter halo (e.g. Gunn and Gott, 1972). Gas can be stripped away from the dark matter halo of a galaxy or sub-cluster by ram pressure interactions with other gas clouds (Gunn and Gott, 1972; McCarthy et al., 2008). In the centres of clusters, runaway cooling is moderated by feedback from active galactic nuclei (AGN) and supernovae (Bower et al. 2006; Hlavacek-Larrondo et al. 2013; Mittal et al. 2009; Nulsen and McNamara 2013; O'Greehan et al. 2010; AGN feedback was reviewed in Fabian, 2012).

Galaxies act as a collisionless fluid and relax slowly, and therefore their distribution retains disturbances induced by mergers for longer than the ICM. Galaxies show a range of colours dependent on star formation rate. Those forming large numbers of stars are bluer and contain cool gas clouds, which, if poorly bound, can be stripped away by ram

pressure interaction with the ICM. The majority of galaxies in clusters have low star formation rates and redder colours, and follow a colour-magnitude relation – the red-sequence (e.g. Gladders and Yee, 2000). The brightest galaxy in the red sequence is often a large cD type galaxy at the centre of the cluster, often coincident with the X-ray peak (Haarsma et al., 2010) and with the reddest colour. Galaxies on the red sequence have progressively bluer colours at fainter magnitudes. The colour magnitude relation gradient and intercept for a particular colour-magnitude pair varies with redshift due to red-shifting of the spectral energy distribution and due to changes in the evolution of galaxies in clusters over cosmic time. A minority of galaxies in clusters are substantially bluer than the red sequence and form a scattered cloud in colour-magnitude space. The red fraction decreases with increasing cluster-centric distance and redshift (Loh et al., 2008), and in low density field environments bluer galaxies predominate (Verdugo et al., 2012).

The thermodynamics of the ICM can only be observed in detail with X-ray telescopes within the region where the gas is shock heated, dense and luminous Markevitch and Vikhlinin (shocks are reviewed in 2007); Kravtsov and Borgani (shocks are reviewed in 2012). Using *XMM-Newton* and *Chandra* this is typically the region bounded by radius r_{500} , defined such that the mean total matter density enclosed is $500\times$ the critical density of the Universe at the time the cluster is observed (e.g. Allen et al., 2011). Galaxies, which are self luminous, can be observed at larger distances. Simulations have shown that the radius outside of which infalling galaxies are in the majority is r_{200} , analogously defined (Balogh et al., 2000; Moore et al., 2004). In the REXCESS sample r_{500} is typically on the order of ~ 1 Mpc and $r_{200} \sim 1.5 r_{500}$.

The baryonic components' dynamics are very different, but they are related by the common gravitational potential which is dominated by the dark matter distribution. Because of the different behaviour of gas and galaxies during events like mergers, we can use complementary observations of the two components to learn more about the structure and history of clusters. In the hierarchical structure formation scenario which forms the basis of the concordance cosmology, galaxy clusters were the most recent structures to form, with massive clusters only emerging after $z = 2$. Clusters' growth continues today and is characterised by constant smooth accretion of matter, punctuated by violent mergers with other massive systems. Mergers cause distinctive morphological characteristics.

If infalling clumps are sufficiently massive and not too near to the primary cluster, they may be identified in X-ray observations as an asymmetry in or as an independent overdensity near the primary object's X-ray emission. As these accrete, the gas haloes of the primary and infalling object collide causing a disturbance in the X-ray appearance of the primary which may be measurable. The gas from the infalling cloud is rapidly merged into the primary's ICM. However, because the galaxies and dark matter associated with the infalling clump are collisionless, their structure is not as readily disrupted, and longer term gravitational processes are required to merge the secondary galaxy distribution with the primary. Sub-clumps of galaxies may be detected long after the gas cloud with which they were originally associated has been assimilated into the primary ICM.

By measuring asymmetry and detecting sub-clumps in galaxy clusters, we are able

in some circumstances to characterise the current dynamical state of a cluster – whether a merger is happening now, is about to occur, or has just happened (all three of which may be the case for a single cluster at a single time). By looking for substructures traced by bluer galaxies, which are rapidly stripped of gas and become red during infall, it may be possible to detect recently accreted clumps, or a signal of smooth accretion from the environment, e.g. along a filament.

In our previous study of the same sample (Holland et al., 2015, henceforth H2015) we compared the distribution of galaxies and X-ray luminous gas in terms of radial density profiles and showed that whilst galaxies on the red sequence in clusters follow the ICM density profiles reasonably well, the blue galaxies are distributed differently to the ICM. It was also found that there is no significant difference in the average radial profiles of clusters classified as having disturbed or regular intracluster media. In this paper, we extend that analysis of the galaxy and ICM distributions into 2D and find that the differences in the radial profiles between red and blue galaxy populations are not purely statistical or restricted to the cluster centres where the highest gas densities are found, but are a consequence of fundamental differences in the way the two components are distributed. We use several widely used techniques to quantify galaxy and gas distributions in our data. In Böhringer et al. (2010, henceforth B2010) the centre shifts technique, which parametrises the variability of the centroid of X-ray surface brightness at scales in the range $(0.1 - 1) r_{500}$, was applied to X-ray observations of the REXCESS clusters. Here, the same method is applied to the red and blue galaxy populations to discover if galaxy density maps can be analysed in the same way. We compare the orientation and ellipticity of X-ray gas and galaxies in order to check if the galaxy distribution is broadly similar to the gas on very large scales. Finally, we make a survey of optically detected sub-clumps of galaxies within individual clusters' X-ray and galaxy density maps to inform our understanding of the distributions and to try to identify clusters in pre- and post-merger states.

The REXCESS cluster sample, optical catalogues and X-ray data are described in Section §5.2. The density map analysis methods are described in Section §5.3. Centre shift and shape analysis results, individual clump descriptions and a summary of the trends found in the whole sample of galaxy count density maps are given in Section §5.4. The results are discussed in Section §5.5 and the conclusions recapitulated in Section §5.6.

A flat cosmology with $h = 0.7$, $H_0 = 100 h \text{ km s}^{-1} \text{ Mpc}^{-1}$, $\Omega_m = 0.3$ and $\Omega_\Lambda = 0.7$ is adopted.

5.2 Sample description

REXCESS is a sample of galaxy clusters, which is representative of those selected by their X-ray luminosity and is independent of morphology. The sample and the X-ray data are described in detail in Böhringer et al. (2007). Clusters have redshifts between $0.055 - 0.183$ and X-ray luminosities $L_X > 0.4 \times 10^{44} h_{70}^{-2} \text{ erg s}^{-1}$ in the $(0.1 - 2.4) \text{ keV}$ band. They are distributed relatively homogeneously in X-ray luminosity. The mass range is $M_{200} =$

$(1.36 - 10.8) \times 10^{14} M_{\odot}$. Angular size is such that r_{500} and a background region outside this are within the *XMM-Newton* and WFI@2.2 m field of view (both $\sim 30'$).

We use approximately half of the REXCESS sample. Our subsample was selected for ease of follow up observation by right ascension. A table of cluster details is shown in Table 5.1.

The X-ray surface brightness maps are based on combined data from the MOS and PN detectors of *XMM-Newton*. Exposures were cleaned of times of high background and the fraction of time lost was ~ 0.35 for PN and ~ 0.25 for MOS1/2, leading to mean final exposure times of $(2.1 \pm 0.9) \times 10^4$ s for MOS1/2 and $(1.4 \pm 0.7) \times 10^4$ s for PN. PN data were corrected for out-of-time events. The data from the three sensors were stacked.

Optical follow up was carried out using the Wide Field Imager on the MPG/ESO 2.2 m Telescope at La Silla, which has a similar field of view to *XMM-Newton* and is therefore well suited for follow-up observations. The optical observations and galaxy catalogues are described in detail in H2015. Dithered observations were made in ESO filters B/123, V/89, and Rc/162 (henceforth *B*, *V* and *R* respectively). Individual exposures were reduced and co-added using ESO/MVM (ALAMBIC). Regions with low exposure times in any of the bands were excluded. The PSF was equalised across all the images in each band.

Galaxy catalogues were generated from the images using SEXTRACTOR (version 2.8.6; Bertin and Arnouts, 1996) including magnitudes and colours.

All the catalogues were found to have close to complete coverage down to $R^* + 5$, where R^* is the Schechter magnitude in the *R* band, determined from the catalogues themselves. Two groups of objects are defined based on R^* : ‘bright’ objects with $R < R^* + 2.5$ and ‘faint’ objects with $R^* + 2.5 < R < R^* + 5$. The 50% completeness limit for the *R* observations was typically > 23 mag, except in RXC J2218.6–3853 [(22.25 \pm 0.03) mag] and RXC J2319.6–7313 [(21.93 \pm 0.05) mag].

The slope, intercept and width of the red sequence for each cluster was determined using the algorithm described in H2015. The spread of the red sequence was fitted in colour space with a Gaussian profile centred on the colour-magnitude relation. Each galaxy was assigned a ‘red sequence distance’ value w_{rs} – the displacement from the centre of the fitted Gaussian in units of the standard deviation (RMS width). Two further groups of objects are defined: objects ‘on the red sequence’ have $|w_{rs}| < 3$ and objects ‘bluer than the red sequence’ have $w_{rs} < -3$. Objects redder than $w_{rs} = 3$ are assumed to be at higher redshift than the cluster and are not considered.

5.3 Methods

5.3.1 Cluster X-ray peak centred coordinate system

We define a coordinate system for the cluster which has its origin at the cluster X-ray peak, as measured with the brightest point on the X-ray image smoothed on a scale of $8.2''$. The $(x_{\text{Cluster}}, y_{\text{Cluster}})$ coordinate system is aligned with the RA–Dec axes at the

Table 5.1: Summary of galaxy cluster properties in the first half of the REXCESS sample. RA, Dec, z and X-ray luminosity L_x were taken from Böhringer et al. (2007). r_{500} is from Pratt et al. (2009). The X-ray centre shift parameter w_{B2010} is taken from B2010, and clusters with $w_{B2010} > 0.01$ are classified as disturbed and marked D.

Object	ID	Abell Name	RA	Dec.	z	L_x 10^{37} W	r_{500} kpc	w_{B2010}	D
RXC J0006.0-3443	1	A2721	00 ^h 06 ^m 03.0 ^s	-34°43'27.0"	0.1147	1.875	1059.3	0.0130 ± 0.0014	D
RXC J0049.4-2931	2	S0084	00 ^h 49 ^m 24.0 ^s	-29°31'28.0"	0.1084	1.503	807.8	0.0023 ± 0.0008	
RXC J0345.7-4112	3	S0384	03 ^h 45 ^m 45.7 ^s	-41°12'27.0"	0.0603	0.495	688.4	0.0052 ± 0.0009	
RXC J0547.6-3152	4	A3364	05 ^h 47 ^m 38.2 ^s	-31°52'31.0"	0.1483	4.667	1133.7	0.0070 ± 0.0006	
RXC J0605.8-3518	5	A3378	06 ^h 05 ^m 52.8 ^s	-35°18'02.0"	0.1392	4.478	1045.9	0.0059 ± 0.0004	
RXC J0616.8-4748	6		06 ^h 16 ^m 53.6 ^s	-47°48'18.0"	0.1164	1.597	939.2	0.0131 ± 0.0015	D
RXC J0645.4-5413	7	A3404	06 ^h 45 ^m 29.3 ^s	-54°13'08.0"	0.1644	7.139	1280.0	0.0039 ± 0.0004	
RXC J0821.8+0112	8	A0653	08 ^h 21 ^m 51.7 ^s	+01°12'42.0"	0.0822	0.673	755.9	0.0045 ± 0.0014	
RXC J2023.0-2056	9	S0868	20 ^h 23 ^m 01.6 ^s	-20°56'55.0"	0.0564	0.411	739.5	0.0167 ± 0.0015	D
RXC J2048.1-1750	A	A2328	20 ^h 48 ^m 10.6 ^s	-17°50'38.0"	0.1475	3.215	1078.0	0.042 ± 0.004	D
RXC J2129.8-5048	B	A3771	21 ^h 29 ^m 51.0 ^s	-50°48'04.0"	0.0796	0.767	900.6	0.042 ± 0.020	D
RXC J2218.6-3853	C	A3856	22 ^h 18 ^m 40.2 ^s	-38°53'51.0"	0.1411	3.516	1130.1	0.0155 ± 0.0005	D
RXC J2234.5-3744	D	A3888	22 ^h 34 ^m 31.0 ^s	-37°44'06.0"	0.1510	6.363	1283.2	0.0075 ± 0.0006	
RXC J2319.6-7313	E	A3992	23 ^h 19 ^m 41.8 ^s	-73°13'51.0"	0.0984	0.937	788.7	0.0217 ± 0.0009	D

Table 5.2: Cluster X-ray peak positions. In each case, the point represents the brightest pixel of the X-ray surface density map, when smoothed using an $8.2''$ kernel.

Object	RA	Dec.
RXC J0006.0–3443	1.49844	–34.72189
RXC J0049.4–2931	12.34573	–29.52059
RXC J0345.7–4112	56.44281	–41.20401
RXC J0547.6–3152	86.90890	–31.87123
RXC J0605.8–3518	91.47558	–35.30256
RXC J0616.8–4748	94.21554	–47.79458
RXC J0645.4–5413	101.37207	–54.22781
RXC J0821.8+0112	125.46083	1.19777
RXC J2023.0–2056	305.74489	–20.95001
RXC J2048.1–1750	312.04039	–17.83328
RXC J2129.8–5048	322.40369	–50.81452
RXC J2218.6–3853	334.66804	–38.90045
RXC J2234.5–3744	338.61683	–37.73337
RXC J2319.6–7313	349.91751	–73.22730

cluster centre position such that x increases with decreasing RA.

This redefinition with respect to the more complex algorithm and selection implemented in B2010 (where dipole minimisation or similar peak detection on an image smoothed with a similar $\sim 8''$ kernel was used) should not have a large impact any of the results. Changes of the origin of the cluster centred coordinate system may have a marginal effect on the normalised clump count described in Section §5.4.3.2, which includes a region selection around the origin. The origin of the coordinate system for each of the clusters is shown in Table 5.2.

5.3.2 Smoothed density map generation

We can recover a reasonable approximation of the galaxy density distribution by smoothing the galaxy count maps, which represent one realisation of points sampled from the distribution. Using smoothed maps makes several stages of our analysis simpler. Algorithms to perform background subtraction on un-smoothed point maps are difficult to implement. Those relying on stochastic removal of a background density of points rely on excellent background level measurements, which are dependent on reliable algorithms to exclude structured regions from the background measurement. In particular, we found it extremely difficult to apply this type of method to galaxy catalogues which have background count density gradients (which may be statistical or may be structures on scales larger than the field of view).

Algorithms to perform background subtraction on smoothed density maps are much less complicated and measurements made on smoothed density maps which are background subtracted are more robust to changes in the background level measurement.

Smoothing algorithms can be designed to ameliorate regions with missing data – e.g. where stars have been excised, or there is a gap in the exposure. (It is possible to fill

such regions with simulated data, but generating the simulated data requires running a smoothing algorithm on the image.)

After smoothing, the X-ray and optical data can be analysed with precisely the same algorithms, so we can make direct comparisons between the two bands.

5.3.2.1 Smoothing algorithm

Taking each pixel in the image as a centre, we find the minimum sized aperture around that pixel which includes at least $c_i > 32$ count. The exposed area a_i – equal to the aperture area minus the area of any masked pixels – is measured, and the surface count density is given by $S_i = c_i/a_i$. We found in tests on simulated observations that 32 counts as a minimum c_i produced reasonable smoothness whilst limiting the unwanted introduction of spurious large artefacts in regions with low counts. The Poisson uncertainties associated with 32 counts allow us to measure 18% over-densities at the 1σ level.

The convolution of the adaptive aperture with the count map and exposure map to compute c_i and a_i at each scale is accelerated using Fourier transforms.

A series of 30 resampled count maps S_{resamp} were also produced for each original red or blue count map, to assist in assessing uncertainties on parameters. The value of each pixel in a resampled map is generated by passing the smoothed count map pixel value as the expectation value into a Poisson random number generator, which generates a sparse array of positive small integers in a field of zeroes. The adaptive smoothing algorithm is run on each of the resampled count maps independently.

5.3.2.2 Background level estimate

Background levels S_{bg} are estimated using the approach of H2015. A radial profile is made around the origin of the coordinate system in the cluster, and the profile is fitted using a Navarro-Frenk-White model (NFW, Navarro et al., 1997) with a free outer slope parameter plus a uniform component which we use as the background. Uncertainty on the background is the fit uncertainty in the Levenberg-Marquadt algorithm used to get the best fit.

We found in H2015 that the red sequence/blue cloud, bright/faint galaxy populations have different distributions. Taking this into account, we calculate an independent background density for each colour-magnitude selection. Wherever a measurement based on the total red sequence or total blue cloud background-subtracted density is made, it is calculated independently for the two magnitude selections, and the results are combined.

Total object counts after background subtraction for each colour-magnitude selection are given in Table 5.3.

5.3.2.3 Overdensity contours

We need to estimate the overdensity of a particular smoothed density map region with respect to its surroundings – the background or the bulk of the cluster – in order to discriminate between noise and real substructures.

Table 5.3: Total galaxy counts n in each full WFI@2.2 m field after background subtraction. Subscript B refers to the bright subsample, F to the faint subsample, r to the red sequence subsample and b to the blue cloud subsample.

Object	n_{Br}	n_{Fr}	n_{Bb}	n_{Fb}
RXC J0006.0–3443	132.4 ± 34.2	$(1.6 \pm 0.6) \times 10^2$	51.3 ± 26.5	$(4.9 \pm 1.6) \times 10^2$
RXC J0049.4–2931	67.5 ± 14.8	71.3 ± 26.2	43.5 ± 20.2	29.5 ± 32.6
RXC J0345.7–4112	14.0 ± 8.4	78.1 ± 31.3	3.1 ± 4.3	0.5 ± 9.0
RXC J0547.6–3152	145.5 ± 24.8	$(1.5 \pm 0.5) \times 10^2$	8.6 ± 22.8	$(2.0 \pm 0.8) \times 10^2$
RXC J0605.8–3518	94.7 ± 24.0	$(1.2 \pm 0.6) \times 10^2$	7.6 ± 17.6	$(0.7 \pm 1.0) \times 10^2$
RXC J0616.8–4748	91.4 ± 16.4	$(1.0 \pm 0.6) \times 10^2$	18.4 ± 13.3	$(1.7 \pm 0.6) \times 10^2$
RXC J0645.4–5413	270.8 ± 35.4	$(3.5 \pm 0.9) \times 10^2$	$(2.3 \pm 3.7) \times 10^1$	$(1.4 \pm 0.7) \times 10^2$
RXC J0821.8+0112	78.4 ± 16.5	$(1.4 \pm 0.4) \times 10^2$	32.2 ± 15.2	$(1.3 \pm 0.6) \times 10^2$
RXC J2023.0–2056	31.6 ± 10.7	73.5 ± 25.8	12.9 ± 9.2	8.8 ± 12.1
RXC J2048.1–1750	$(2.2 \pm 0.5) \times 10^2$	$(2.9 \pm 1.0) \times 10^2$	98.8 ± 30.0	$(2.6 \pm 0.7) \times 10^2$
RXC J2129.8–5048	50.8 ± 16.8	97.4 ± 26.1	3.5 ± 5.9	$(1.4 \pm 0.8) \times 10^2$
RXC J2218.6–3853	52.6 ± 25.7	$(3.9 \pm 4.0) \times 10^1$	16.0 ± 16.0	$(1.0 \pm 4.7) \times 10^1$
RXC J2234.5–3744	218.4 ± 23.9	$(1.4 \pm 0.7) \times 10^2$	$(1.0 \pm 0.7) \times 10^2$	$(3.9 \pm 6.4) \times 10^1$
RXC J2319.6–7313	58.8 ± 13.6	$(5.7 \pm 4.6) \times 10^1$	10.9 ± 13.8	$(5.6 \pm 6.1) \times 10^1$

The measured surface count density is $S = S_{\text{bgsub}} + S_{\text{bg}}$ where S_{bgsub} is the background-subtracted count density we want to characterise. We assume a squared uncertainty on S_{bgsub} , $\alpha_{S_{\text{bgsub}}}^2 = \alpha_S^2 + \alpha_{S_{\text{bg}}}^2$ where α_S and $\alpha_{S_{\text{bg}}}$ are the uncertainties on S and S_{bg} respectively. This should be a reasonable upper bound as S and S_{bg} are not independent. Using the relation $\frac{S}{\alpha_S} = \sqrt{c}$ this leads to $\alpha_{S_{\text{bgsub}}}^2 = \alpha_{S_{\text{bg}}}^2 + \frac{S^2}{c}$. We generate overdensity contours ς_i using

$$\varsigma_0 = S_{\text{bg}}, \quad (5.1)$$

$$\varsigma_{i+1} = \varsigma_i + \sqrt{\alpha_{S_{\text{bg}}}^2 + \frac{\varsigma_i^2}{c}}, \quad (5.2)$$

with increases in S_{bgsub} of 1σ at each contour.

Galaxy count density maps overlaid with these contours for the red and blue galaxy populations in each cluster are shown in Section §E.1.

5.3.3 Image analysis

Simple tools to find centroids and alignment of elliptical features in images will be required to calculate the centre shift parameter and for comparison of the ellipticity and orientation of the X-ray and galaxy density distributions in the following sections.

5.3.3.1 Moments

For an image V with pixels i , at positions (x_i, y_i) , pixel intensity I_i the 2D moment is given by

$$M_{pq} = \sum_i (x_i^p y_i^q) I_i. \quad (5.3)$$

The centroid of the image is

$$\text{centroid}(V) = (x_c, y_c) = (M_{10}/M_{00}, M_{01}/M_{00}), \quad (5.4)$$

and the central 2D moment (invariant under translation) is

$$\mu_{pq} = \sum_i [(x_i - x_c)^p (y_i - y_c)^q] I_i. \quad (5.5)$$

Defining $\mu'_{pq} = \mu_{pq}/\mu_{00}$, the covariance matrix of the sub-image is

$$\text{cov}(I) = \begin{bmatrix} \mu'_{20} & \mu'_{11} \\ \mu'_{11} & \mu'_{02} \end{bmatrix}. \quad (5.6)$$

The orientation and ellipticity of the sub-image can be recovered from the eigenvectors $\boldsymbol{\lambda}_{\text{major}}$ and $\boldsymbol{\lambda}_{\text{minor}}$ corresponding to eigenvalues λ_{major} and λ_{minor} respectively, where $\lambda_{\text{major}} \geq \lambda_{\text{minor}}$. The direction of the eigenvector with the largest eigenvalue is along the semi-major axis. The ellipticity of the image is given by

$$\epsilon = \frac{\sqrt{\lambda_{\text{major}}} - \sqrt{\lambda_{\text{minor}}}}{\sqrt{\lambda_{\text{major}}}}. \quad (5.7)$$

Differences in orientation between the galaxy and ICM distributions are of interest, and we need a coordinate-system-independent way of measuring the offset. The difference in orientation between axes aligned with two vectors $\boldsymbol{\lambda}_0$ and $\boldsymbol{\lambda}_1$ is

$$\Theta_{01} = \arccos(|\boldsymbol{\lambda}_0 \cdot \boldsymbol{\lambda}_1|), \quad (5.8)$$

which is invariant under reversal of either of the vectors and always returns a value in the range $0 - \frac{\pi}{2}$.

5.3.3.2 Centroiding algorithm

A robust centroiding algorithm for circular apertures is required for the following centre shift and shape analyses. We need to be able to characterise the centroid of different types of smooth or clumpy, symmetric or irregular density maps, potentially with low counts on a range of scales, from a few pixels up to most of the image. It was found that iterative re-centring techniques did not reliably find the centroid of simple test data with similar statistics to the galaxy catalogues without both excellent starting values (with the target centre within the central half of the aperture) and fudges to the algorithm, like additional smoothing at aperture edges. In cases where there was increased degeneracy, like a ‘ridge’ of high density (e.g. in the smoothed density map of RXC J0006.0–3443 shown in 5.1b) or several possible centres (like many of the clumpy blue count density maps), iterative algorithms often failed.

We wish to locate a stable centre on an image V within an aperture of radius r_{max} . Let W be a circular sub-image of V with radius r_{max} centred on a guess for the centroid

(x_j, y_j) . The centroid offset in W is $\boldsymbol{\delta}_j = \text{centroid}(W) - (x_j, y_j)$. In iterative centroiding methods, the calculation $(x_{j+1}, y_{j+1}) = (x_j, y_j) + \boldsymbol{\delta}_j$ is repeated until a convergence criterion is satisfied – usually that the length $f_i = |\boldsymbol{\delta}_i|$ drops below a threshold (typically 1 pixel on an image), or an iteration limit is reached. The final (x_j, y_j) is taken as the centre.

By calculating $\boldsymbol{\delta}_i$ for all pixels in the image, we can directly find centres which satisfy the convergence criterion $f = \min(f_i)$ locally for a given r_{\max} . Using aperture functions defined by

$$M(x', y') = \begin{cases} 1 & \in |\mathbf{r}'| \leq r_{\max}, \\ 0 & \in |\mathbf{r}'| > r_{\max}, \end{cases} \quad (5.9)$$

$$X(x', y') = x' M(x', y'), \quad (5.10)$$

$$Y(x', y') = y' M(x', y'), \quad (5.11)$$

where $\mathbf{r}' = \begin{bmatrix} x' \\ y' \end{bmatrix}$ (and $\mathbf{r} = \begin{bmatrix} 0 \\ 0 \end{bmatrix}$ at the centre of each aperture), we compute the convolved images $\mathcal{X} = V * X$, $\mathcal{Y} = V * Y$ and $\mathcal{M} = V * M$ which lead to $\boldsymbol{\delta}_i = \left(\frac{\mathcal{X}_i}{\mathcal{M}_i}, \frac{\mathcal{Y}_i}{\mathcal{M}_i} \right)$. We accelerate the convolutions using fast Fourier transforms.

Local stable centres are located by finding pixels with the lowest f in a moving square aperture of side-length r_{\max} . From these, we select a global centroid $\mathbf{r}_{\text{COM},i}$ for each r_{\max} by finding the stable centre with the highest \mathcal{M}_i (which is necessary to avoid finding stable, but empty, regions in the density map).

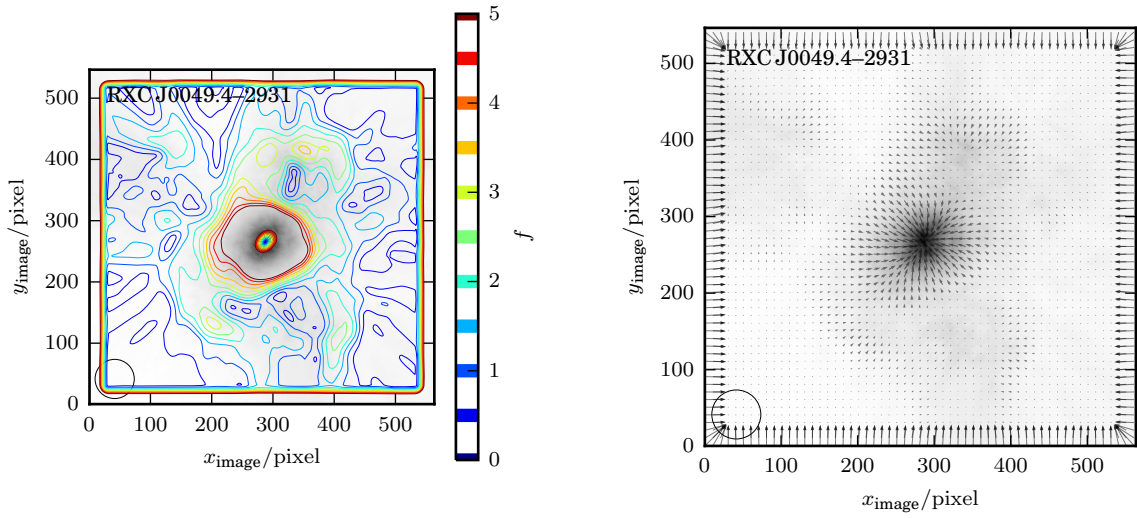
The new algorithm is different from the centroid implemented in B2010, as it is effectively a brute force search of the image field for the most stable region for a given aperture, but produces the same results if the starting parameters of the iterative method are appropriately set. It also overcomes the issue of nowhere-stable and looping solutions – where $\min(f_i) > 1$ pixel – which can affect iterative centroiding.

Both looping solutions and no stable path cases exist in the REXCESS smoothed galaxy density map dataset, so the use of iterative centroiding or dipole minimisation was not appropriate. Diagrams showing stable and unstable centroiding paths versus the cost function minimisation algorithm in two cases of the current dataset are shown in Figure 5.1.

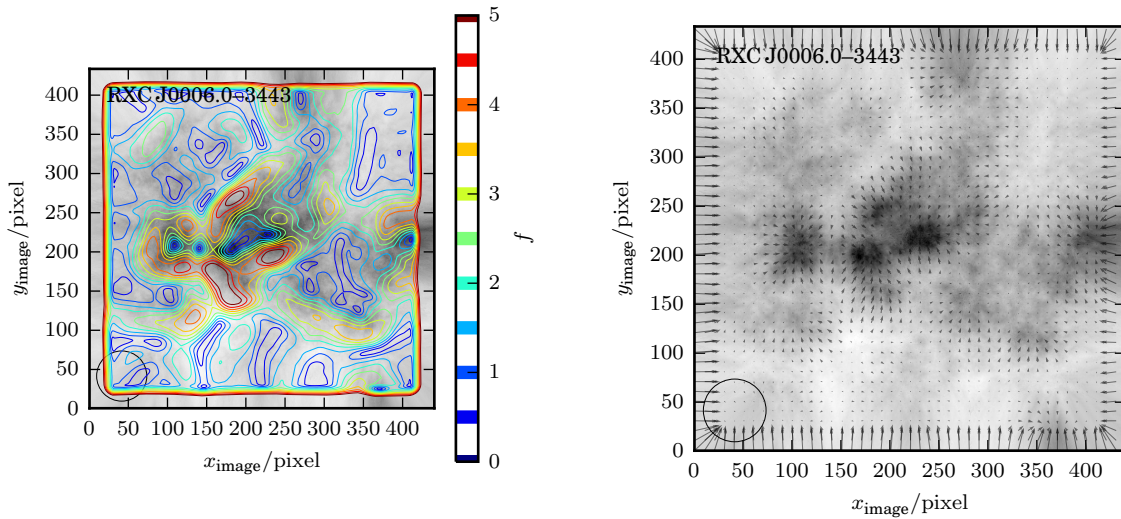
It is potentially computationally costly, but the use of fast Fourier transforms and array multiplication to compute the convolution step rather than implementing direct convolution increase its speed by several orders of magnitude.

5.3.4 Centre shifts

The centre shift parameter is a simple measurement which is suited to characterising scale dependent offsets in perturbed modal distributions at multiple scales. It produces intuitive results and has been proven to be useful on X-ray data in the past (Mohr et al. 1993, 1995; O'Hara et al. 2006; Poole et al. 2006; B2010).



(a) Example density map of a cluster which appears reasonably regular in optical galaxy count density, showing a clear minimum in f (left panel) and many stable routes to the centre (right panel).



(b) Example density map of a cluster which appears irregular in optical galaxy count density, showing a ridge of minima in f (left panel) and few stable routes to this ridge (right panel).

Figure 5.1: The left panels show plots of the f field over the smoothed optical density map. The right panels show the offset of the centre of mass measured in a circular aperture around a sample of pixels (where the tail of the arrow shows the starting pixel, and the head of the arrow points to the centre of mass). The aperture size is shown as a circle in the bottom left corner of each plot.

Using the method from Section §5.3.3.2 we locate the stable centroids of ten apertures with n radii r_{\max} (0.1, 0.2, ..., 1.0) r_{500} on 3 maps: X-ray, red galaxy density and blue galaxy density.

Given some fiducial centre \mathbf{r}_{fc} , we calculate the centre shift $\Delta_i = |\mathbf{r}_{\text{COM},i} - \mathbf{r}_{\text{fc}}|$, and the mean $\bar{\Delta}$, and define the centre shift parameter as

$$w = \frac{1}{r_{500}} \sqrt{\frac{\sum_{i=1}^n (\Delta_i - \bar{\Delta})^2}{n - 1}}. \quad (5.12)$$

To reduce dependence on assumptions about the cluster morphology and shape and to minimise w , we take $\mathbf{r}_{\text{fc}} = \overline{\mathbf{r}_{\text{COM},i}}$, the mean centre of all of the apertures.

An identical process is run on each of the resampled smoothed galaxy density maps described in Section §5.3.2.1, and we use the 32nd and 68th percentiles w as the uncertainty bounds. A simple standard deviation is not used because the distribution of results is non-Gaussian.

5.3.5 Ellipticity and orientation

One widely used metric of disturbance in X-ray clusters is the ellipticity of the surface brightness. Ellipticity is increased during pre-mergers where the infalling gas appears to be an anisotropic extension of the primary, and in post-mergers the infalling CDM halo can overshoot, drawing ICM into an elongated structure. We calculate the ellipticity ϵ and semi-major axis λ_{major} within each of the n apertures defined in Section §5.3.4 using the methods described in Section §5.3.3.1, on the red, blue and X-ray cluster images. We also calculate the orientation offsets between the 3 semi-major axes for each r_{\max} using Equation (5.8).

The same measurements are made independently on each pair of the resampled galaxy count density maps. Uncertainties on ellipticity and orientation offset are found by taking the standard deviation of the values measured on resampled maps with respect to the un-sampled result. The uncertainties on ellipticity and orientation are much larger on the galaxy density maps, as these have many fewer counts than the X-ray data.

5.4 Results

5.4.1 Centre shift parameter

Figure 5.2 shows the correlation between the centre shift parameter measured in B2010 and using the algorithm in Section §5.3.4. The results are correlated, but do not trace each other tightly. In B2010, the offset comparison is made with respect to the X-ray peak position, whereas we use the mean centre at all scales. Here in addition, no correction is made for the presence of cool cores. These changes are known to make a significant difference to measured parameters.

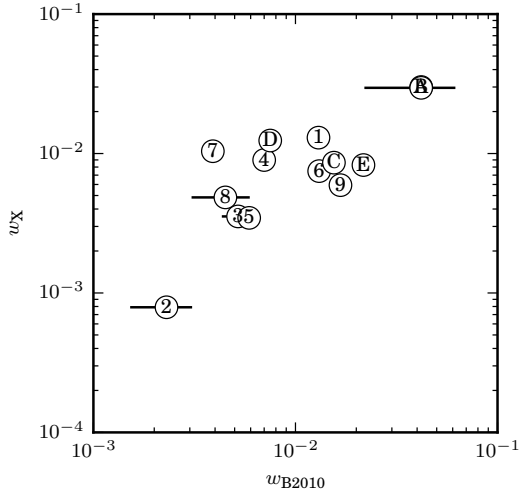
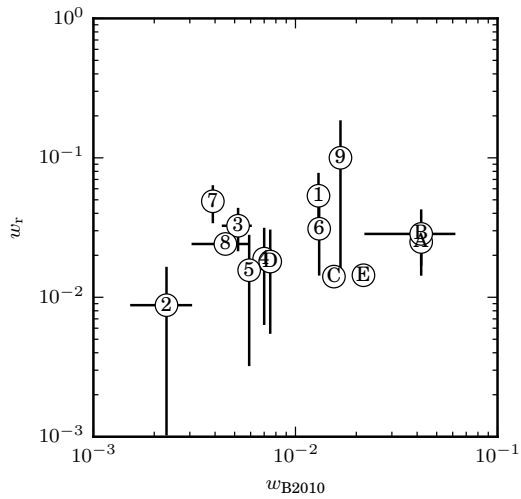
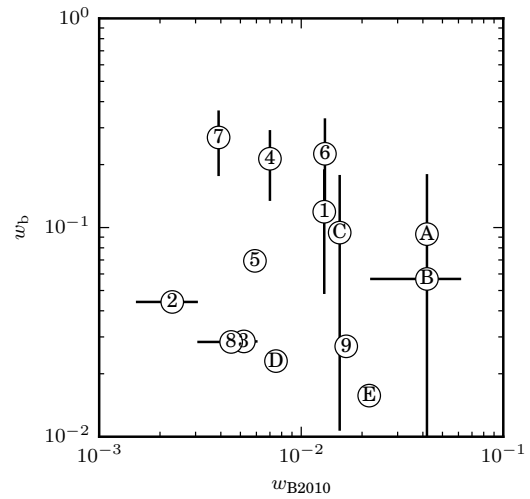


Figure 5.2: w_{B2010} vs. w_X using the algorithm defined in this paper. The point labels correspond to the ID column in Table 5.1.



(a) w_{B2010} vs. w_r .



(b) w_{B2010} vs. w_b .

Figure 5.3: Optical centre shift parameters w measured in apertures (0.1, 0.2, ..., 1.0) r_{500} on red and blue smoothed galaxy density maps compared with w_{B2010} from B2010. The point labels correspond to the ID column in Table 5.1.

The centre shift parameters of smoothed density maps of red sequence galaxies and galaxies bluer than the red sequence, to a magnitude limit of $R^* + 5$, were calculated in apertures $(0.1, 0.2, \dots, 1.0) r_{500}$. The results are shown in Figure 5.3.

The calculation of the X-ray uncertainties using the method of B2010 was not reproduced for the galaxy distribution because the assumption of approximate circular symmetry is more often than not unacceptable for the galaxy density maps.

Figures 5.3a and 5.3b show the centre shift parameter measured on X-ray surface brightness maps in B2010 compared with a similar measure on red and blue galaxy count density maps. There is weak correlation between the centre shift parameter of the red sequence galaxy distribution and X-ray surface brightness, but no correlation between the parameter when measured on the blue cloud galaxy distribution and compared to the X-ray. The mean $\frac{w_r}{w_x} = 3.6$.

The centre shift measurement is good at measuring relatively small asymmetries in a dominant clump. If very strong asymmetries and clumpiness are apparent (as is clearly the case in some of the galaxy density maps), the relation between ‘perceived substructure’ by inspection and ‘measured substructure’ by the centre shift parameter breaks down.

There are also cases where there is clearly something of interest occurring in the galaxy density map which is not picked up by the centre shift parameter – e.g. in the RXC J2218.6–3853 map – but because the disturbance is largely symmetrical this is not detected.

Given the relatively low counts of galaxies versus X-ray photons, the uncertainties on the centre shift parameter measured on galaxy density maps are necessarily quite large, making a correlation analysis difficult.

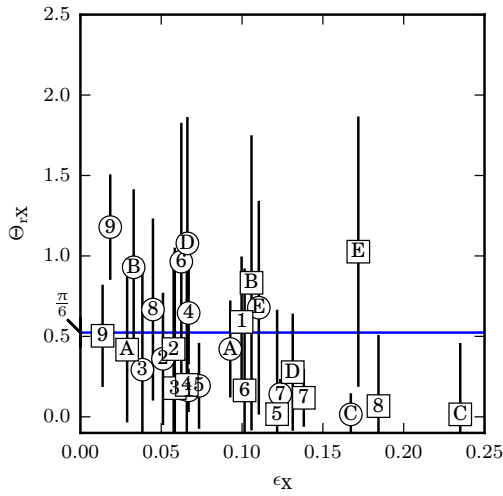
5.4.2 Cluster shape analysis

Using the smoothed density map within each of the apertures produced in the centre shifts measurement, measurements of ellipticity ϵ and semi-major axis orientation based on 2D central moments were made with respect to the cluster centred coordinate system. These shape measurements were also run on the X-ray maps. Figure 5.4 shows comparisons of X-ray ellipticity ϵ_x vs. red and blue ellipticity ϵ_r, ϵ_b at each scale r_{\max} , and the red–X-ray and blue–X-ray orientation offsets Θ_{rX} and Θ_{bX} vs. ϵ_x .

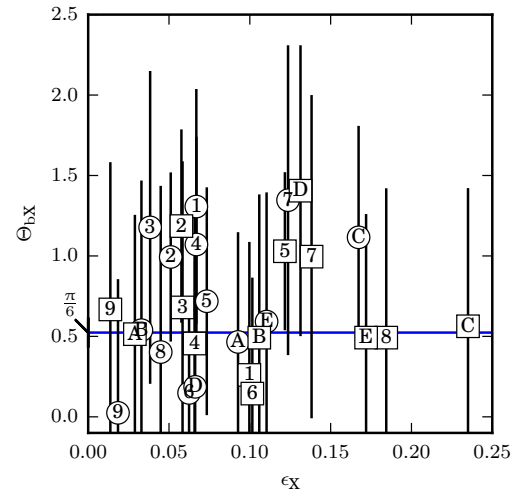
Figure 5.4a shows that the red galaxy population orientation is increasingly aligned with the X-ray gas as the X-ray ellipticity increases. (The exceptional case of RXC J2319.6–7313 is discussed in Section §5.4.4.)

Based on the large scatter of X-ray orientation offsets at low ellipticities shown in Figure 5.4a, we surmise that orientations cannot be compared reliably in cases where $\epsilon_x < 0.05$.

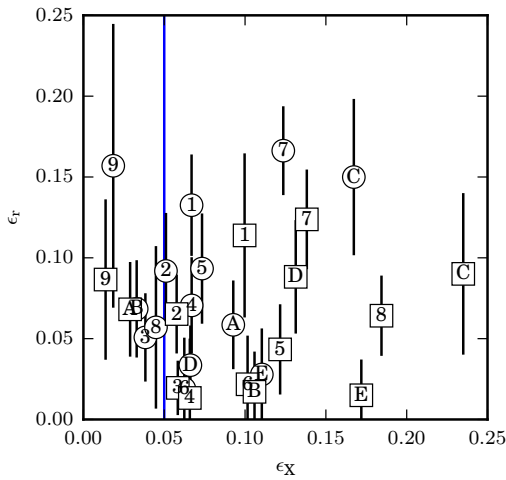
We found that the distribution of orientation offset between blue and X-ray orientations shown in Figure 5.4b was consistent with chance. A possible signal of correlation within objects with X-ray centre shift parameter $w_{B2010} > 0.01$ (the ‘disturbed’ subsample) was investigated but was found not to be significant at the 2σ level.



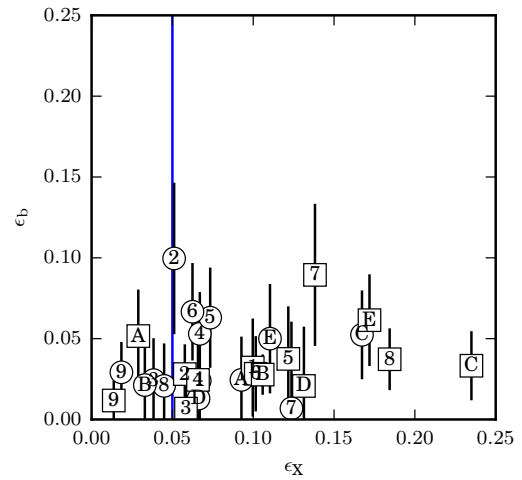
(a) Orientation offsets between X-ray and red galaxy distribution measurements with respect to X-ray ellipticity. The horizontal line marks $\frac{\pi}{6} = 30^\circ$.



(b) Orientation offsets between X-ray and blue galaxy distribution measurements with respect to X-ray ellipticity. The horizontal line marks $\frac{\pi}{6} = 30^\circ$.



(c) Comparison of X-ray and red galaxy distribution ellipticity. The vertical line marks $\epsilon_X = 0.05$; red orientation offsets appear to be random when $\epsilon_X < 0.05$.



(d) Comparison of X-ray and blue galaxy distribution ellipticity. The vertical line marks $\epsilon_X = 0.05$; red orientation offsets appear to be random when $\epsilon_X < 0.05$. The scale is the same as in Figure 5.4c.

Figure 5.4: Orientation and ellipticity comparison in red and blue galaxy distribution and X-ray surface brightness. The labels correspond to the ID column in Table 5.1. Each cluster has two measurements in each plot: the result for an r_{500} sized aperture is marked with a circle and that for the $0.5 r_{500}$ with a square.

Figures 5.4c and 5.4d show that there is no clear relationship between X-ray and red/blue galaxy population ellipticity.

5.4.3 Sub-clumps within clusters

The detection of individual sub-clumps within clusters gives us a more intuitive way to measure optical ‘disturbance,’ where the key indicators that something of interest has happened are individual collisionless over-densities of galaxies, rather than the global disturbances characteristic of collisions between gas clouds. In the following sections, we outline a method to detect sub-clumps, and then investigate the similarities and mismatches when using sub clump count and X-ray centre shifts parameter to describe galaxy clusters.

5.4.3.1 Clump detection and significance measurement

It was shown in H2015 that the 1D radial density distributions of the red and blue galaxies within this sample are quite different, and that the red galaxies approximately trace the ICM. From inspection of the density maps shown in Section §E.1, one can see that the structure traced by red galaxies can usually be described by a circularly symmetric primary overdensity $C0$ and background, centred at the X-ray centre $(x_{\text{Cluster}}, y_{\text{Cluster}}) = (0, 0)$, plus approximately circularly symmetric sub-clumps $Ci = (C1, C2, \dots)$. We adopt a model where we expect individual sub-clumps to be traced by red galaxies, and then test whether they have significant X-ray or blue components. Clumps identified by their red sequence, even those outside of r_{200} , are likely to be at the cluster z .

We inspected the map of overdensity contour levels described in Section §5.3.2.3 for the red galaxies, and marked all approximately circular regions with a peak at least two contour levels (2σ) above their surroundings. This is a variation on the method of Geller and Beers (1982).

The significance of the red and blue galaxy count within each projected sub clump region was measured.

First, a radial count density profile was produced centred at $(x_{\text{Cluster}}, y_{\text{Cluster}}) = (0, 0)$, excluding all the regions Ci . This profile includes both $C0$ and the background component which is implicitly taken to be uniform. The profile was computed with equal width annuli, where the total number of bins was set by dividing the total number of galaxies in the profile region by 25, and then ensuring that the annuli had width $0.05 < \frac{w}{r_{500}} < 0.25$. For each clump, the observed count c_o and expected count c_e due to the $C0$ /background profile were calculated. Where sub-clumps overlapped, those with lower numbers were fitted first, excluding any regions where they intersected clumps with higher numbers. When the higher numbered sub clump was fitted, the density of the intersecting region was taken into account in the background estimation step. The probability $P(c_o \geq c_e)$ was calculated, assuming a Poisson distribution. We took clumps with $P < 0.05$ as significant.

A similar procedure was used to estimate the significance of any X-ray overdensity within each sub-clump region. A radial density profile with annulus width $0.05 r_{500}$ was produced for C0 plus the background, excluding all sub-clumps, where the mean and standard deviation of pixels in each annulus were taken as the density and uncertainty. The mean and standard deviation \overline{S}_o and α_{S_o} within each clump region were calculated. The mean expected density due to the C0/background profile \overline{S}_e and its uncertainty α_{S_e} were calculated. The probability $P(c_o \geq c_e)$ was calculated, assuming a Gaussian distribution with mean \overline{S}_e and $\sigma = \alpha_{S_e}$. We took clumps with $P < 0.05$ as significant.

The significant sub-clumps are listed in Table 5.4. Clump maps with all of the regions are shown in Section §E.1. Clumps with significant blue components are rare, and most of these are outside r_{500} . A similar number of clumps have significant X-ray components, and 4 out of 6 of these have significant blue components as well.

5.4.3.2 Normalised clump count

Based on the significant clumps detected in the previous section, we investigated the relative number of galaxies in the sub-clumps in each cluster compared with the number of galaxies in C0. This can be compared with the X-ray centre shift parameter to investigate the relationship between X-ray disturbance and the presence of merger remnants within a cluster, and with clumps near to a cluster.

We calculated a uniform background for each cluster count density map by finding the total galaxy density in the region $> r_{200}$, excluding any areas identified as possibly containing sub-clumps. This allowed us to subtract the background and produce a count density profile for C0 alone.

We estimated the the total number of galaxies within $< r_{500}$ of C0 by multiplying the density by the total area of each annulus (thus correcting for any masked or sub-clump regions), and then summing the result out to r_{500} . No correction is included for projection effects. The total count of galaxies within each sub-clump was produced by calculating the observed density in each sub-clump, less the density due to the C0/background profile, and then multiplying by the sub-clump area. No projection correction is applied to the counts for C_i . The count within each sub-clump was divided by the number of galaxies in C0 to give a normalised count \mathcal{N} .

The normalised clump count $\mathcal{N}_{r < r_{200}}$ is the sum over these normalised counts in the $r < r_{200}$. A similar measure $\mathcal{N}_{r > r_{200}}$ is the sum over normalised counts in the $r > r_{200}$ region, divided by the exposed area in units of Mpc^2 calculated at the cluster z . The results are tabulated in Table 5.5 and plotted against the X-ray centre shift parameter in in Figure 5.5.

The results show no clear trend. When we ignore the outliers RXC J0006.0–3443 and RXC J2218.6–3853, the normalised clump count – X-ray centre shift parameter relationship is flat. Loosening the probability threshold for significance to $P < 0.2$ (a 1σ detection) does not substantially change the results because clumps with low counts have little influence on the final result even if they are included. Fewer than half of the clusters have significant clumps within r_{500} , but those without detectable sub-clumps

Table 5.4: Significant sub-clumps selected using the red galaxy distribution. P_x is the probability that the sub-clump excess in map x arose by chance and \mathcal{S}_x is shown when $P_x < 0.05$; subscript r represents the map of red galaxies, subscript b represents the map of blue galaxies and subscript X represents the X-ray surface brightness.

Object	Region	r r_{500}	P_r	P_b	\mathcal{S}_b	P_X	\mathcal{S}_X
RXC J0006.0–3443	C1	0.57	0.000	0.793		0.000	\mathcal{S}_X
RXC J0006.0–3443	C2	1.15	0.000	0.005	\mathcal{S}_b	0.012	\mathcal{S}_X
RXC J0006.0–3443	C5	1.79	0.006	0.123		0.437	
RXC J0006.0–3443	C6	1.93	0.022	0.166		0.439	
RXC J0049.4–2931	C1	1.39	0.003	0.643		0.319	
RXC J0049.4–2931	C3	1.77	0.034	0.143		0.614	
RXC J0049.4–2931	C4	2.77	0.007	0.275		0.399	
RXC J0547.6–3152	C1	0.88	0.000	0.142		0.570	
RXC J0605.8–3518	C1	1.37	0.033	0.754		0.190	
RXC J0605.8–3518	C2	2.04	0.024	0.056		0.445	
RXC J0605.8–3518	C3	2.67	0.000	0.001	\mathcal{S}_b	0.423	
RXC J0605.8–3518	C5	1.23	0.014	0.941		0.688	
RXC J0616.8–4748	C1	0.64	0.024	0.884		0.920	
RXC J0616.8–4748	C2	2.15	0.030	0.314		0.555	
RXC J0616.8–4748	C3	2.51	0.003	0.054		0.574	
RXC J0616.8–4748	C5	1.16	0.047	0.074		0.016	\mathcal{S}_X
RXC J0645.4–5413	C1	1.87	0.010	0.340		0.450	
RXC J0645.4–5413	C2	2.19	0.000	0.134		0.465	
RXC J0645.4–5413	C3	2.06	0.004	0.910		0.536	
RXC J0645.4–5413	C4	1.82	0.000	0.387		0.218	
RXC J0821.8+0112	C1	1.44	0.000	0.005	\mathcal{S}_b	0.008	\mathcal{S}_X
RXC J2023.0–2056	C1	0.78	0.000	0.168		0.441	
RXC J2048.1–1750	C1	1.11	0.006	0.239		0.157	
RXC J2048.1–1750	C2	1.76	0.000	0.051		0.003	\mathcal{S}_X
RXC J2048.1–1750	C3	1.88	0.008	0.135		0.532	
RXC J2048.1–1750	C4	2.61	0.019	0.554		0.527	
RXC J2129.8–5048	C1	1.33	0.007	0.165		0.470	
RXC J2218.6–3853	C1	1.37	0.001	0.009	\mathcal{S}_b	0.001	\mathcal{S}_X
RXC J2218.6–3853	C2	2.55	0.000	0.007	\mathcal{S}_b	0.518	
RXC J2218.6–3853	C3	1.28	0.012	0.781		0.539	
RXC J2234.5–3744	C1	1.02	0.009	0.671		0.223	
RXC J2234.5–3744	C2	1.31	0.004	0.353		0.532	
RXC J2234.5–3744	C3	2.17	0.005	0.050		0.623	
RXC J2234.5–3744	C4	1.73	0.005	0.585		0.565	
RXC J2234.5–3744	C5	2.24	0.032	0.826		0.501	
RXC J2319.6–7313	C1	0.95	0.006	0.006	\mathcal{S}_b	0.008	\mathcal{S}_X
RXC J2319.6–7313	C2	1.42	0.049	0.218		0.447	

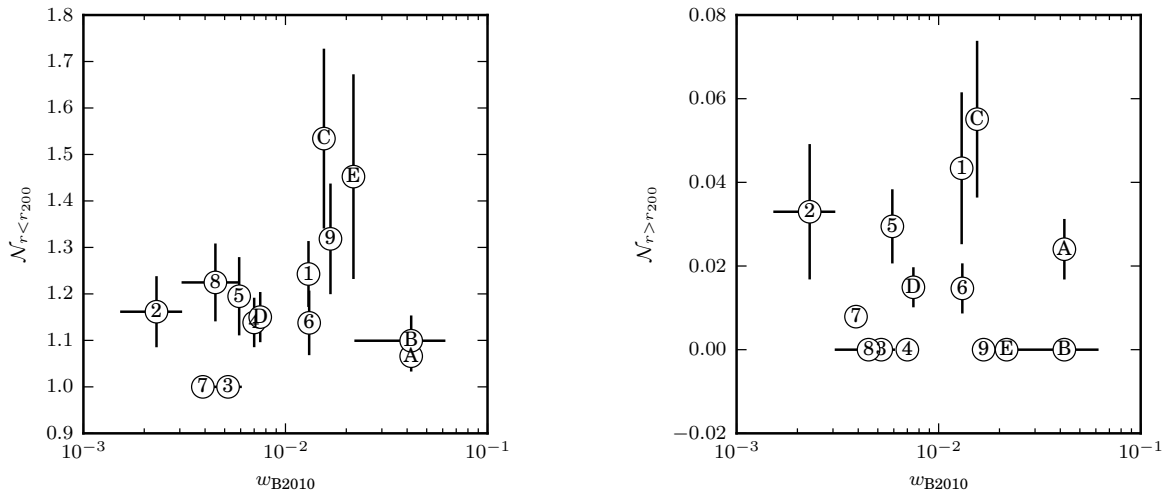
Table 5.5: Cluster normalised clump count and classifications. D means the object was classified as disturbed based on X-ray centre shift criteria in B2010. $\mathcal{N}_{r < r_{200}}$ is the normalised clump count within r_{200} , and objects marked D_O have $\mathcal{N}_{r < r_{200}} > \text{median}(\mathcal{N}_{r < r_{200}})$. $\mathcal{N}_{r > r_{200}}$ is the normalised clump count outside r_{200} which is normalised by the exposed area in Mpc^2 , and points marked C _{$r > r_{200}$} have $\mathcal{N}_{r > r_{200}} > \text{median}(\mathcal{N}_{r > r_{200}})$.

Object	D	$\mathcal{N}_{r < r_{200}}$	D _O	$\mathcal{N}_{r > r_{200}}$	C _{$r > r_{200}$}
RXC J0006.0-3443	D	1.2 ± 0.1	D _O	0.043 ± 0.018	C _{$r > r_{200}$}
RXC J0049.4-2931		1.2 ± 0.1	D _O	0.033 ± 0.016	C _{$r > r_{200}$}
RXC J0345.7-4112		1.0 ± 0		0.0 ± 0	
RXC J0547.6-3152		1.1 ± 0.1		0.0 ± 0	
RXC J0605.8-3518		1.2 ± 0.1	D _O	0.029 ± 0.009	C _{$r > r_{200}$}
RXC J0616.8-4748	D	1.1 ± 0.1		0.015 ± 0.006	C _{$r > r_{200}$}
RXC J0645.4-5413		1.0 ± 0		0.0079 ± 0.0016	
RXC J0821.8+0112		1.2 ± 0.1	D _O	0.0 ± 0	
RXC J2023.0-2056	D	1.3 ± 0.1	D _O	0.0 ± 0	
RXC J2048.1-1750	D	1.1 ± 0.0		0.024 ± 0.007	C _{$r > r_{200}$}
RXC J2129.8-5048	D	1.1 ± 0.1		0.0 ± 0	
RXC J2218.6-3853	D	1.5 ± 0.2	D _O	0.055 ± 0.019	C _{$r > r_{200}$}
RXC J2234.5-3744		1.2 ± 0.1		0.015 ± 0.005	C _{$r > r_{200}$}
RXC J2319.6-7313	D	1.5 ± 0.2	D _O	0.0 ± 0	

still represent the full range of X-ray morphology from very regular to very disturbed. To assist in the discussion of the individual morphologies which follow, we introduce an optical disturbance criterion where clusters with $\mathcal{N}_{r < r_{200}} > \text{median}(\mathcal{N}_{r < r_{200}})$ are classified as optically disturbed (and labelled D_O).

The background density estimates derived from the C0 profile were compared with those from the NFW background model described in H2015 and were found to be systematically higher by 19% on average for the red galaxies and by lower by 15% for the blue. The slightly higher result is expected for the red, because the NFW background model includes the effect of the low density tail of the NFW profile, which using the sub clump method is always subsumed into the background count. The difference in the background density for the blue galaxies is due to the fact that the assumption of symmetry used for the 1D method for the blue is incorrect. The uncertainties introduced by these differences are too small to affect the overall trends.

Ways to improve the background estimate, and thus increase the detectability of clumps outside r_{200} but still within the WFI@2.2m field-of-view, are limited. Although it is possible to make observations of ‘empty fields’ devoid of galaxy clusters, these may not represent the background we aim to subtract from the galaxy clusters studied. The scatter in the surface density of field galaxies along the lines of sight in the regions $r > r_{200}$ around the REXCESS clusters spans a factor of 2 and is always above the density expected from measurements of non-cluster fields (figure 3 in H2015), due to the the location of galaxy clusters in regions of enhanced large scale structure.



(a) Normalised clump count in the region $r < r_{200}$ vs. X-ray centre shift parameter.

(b) Normalised clump count in the region $r > r_{200}$, which is divided by the observed area, vs. X-ray centre shift parameter.

Figure 5.5: Normalised clump count versus the X-ray centre shift parameter.

5.4.4 Optical morphology and mismatched classifications of disturbance

The reasons for the lack of correlation between the $r < r_{200}$ normalised clump count and X-ray centre shift parameter deserve closer scrutiny. Even a cursory inspection of the individual cluster density maps reveals that cluster structures are much more complicated than a simple model where red galaxies follow the form laid down by the ICM, and blue galaxies are a low density admixture.

In this section, we look at the individual cluster morphologies, and put them in context with whether the X-ray and optical disturbance classifications based on the X-ray centre shift parameter and normalised count density match or are mismatched.

5.4.4.1 Matched: optically- and X-ray-regular

Despite being the subgroup of regular clusters where one might expect nothing of interest to be happening, some clusters in this group have curious morphological features.

RXC J0345.7–4112 This is the most optically regular cluster in the sample. There are no detectable substructures.

RXC J0547.6–3152 This cluster has one red sub clump C1 which is coincident with an apparent X-ray enhancement that fails the significance test. Its blue structure is much

more complex, comprising several knots of galaxies which encircle the X-ray–red central density peak. If these blue galaxies are at the cluster redshift, their distribution suggests the presence of a large scale structure at the position angle of C1.

RXC J0645.4–5413 Despite being classified as regular using the X-ray centre shift parameter, this cluster has an obvious NW–SE elongation in X-ray surface brightness which aligns with the elongation of the red galaxy distribution measured in Section §5.4.2, and several over-densities on its outskirts which appear to be contiguous with the primary red overdensity (C0).

RXC J2234.5–3744 This is the only case with a compact blue region which coincides with the main X-ray and red galaxy density peak (as opposed to a broad blue overdensity which is detectable across the whole of C0).

5.4.4.2 Matched: optically- and X-ray-disturbed

This group appears to include cases where there is a pre-merger group about to cross the main cluster but still at a sufficient distance to be detectable in both galaxy count density and X-ray surface brightness, or in cases with a recent merger where the ICM has not yet relaxed but the remnant red galaxy distribution of the impinging object is far enough from the centre to be detectable.

RXC J0006.0–3443 There are two candidate pre-merger sub-clumps with a significant X-ray component, C1 and C2. C2 is slightly offset from the the centre of a circularly symmetric blue galaxy density peak, which may be the true centre of C2, if we relax our assumption that infalling clumps are primarily traced by red galaxies. Most of the prominent galaxies within C2 have z comparable with the cluster $z = 0.114$ (Teague et al., 1990). There is a large region with a significant blue density across most of C0.

RXC J2218.6–3853 C1 is a candidate pre-merger with a significant X-ray component. The C1–C3 axis is in excellent alignment with the X-ray elongation measured in Section §5.4.2. The configuration is consistent with a scenario where C3 is the remnant clump after a crossing on the C1–C3 axis. However, given the small number of galaxies in C3 (~ 10), this could equally well be a pre-merger where the X-ray component is too faint to see.

RXC J2319.6–7313 We noted RXC J2319.6–7313 in H2015 as having a particularly difficult to detect red sequence. It has a candidate pre-merger clump C1 with excess X-ray emission. The orientation comparison in Section §5.4.2 showed a large offset between the X-ray and red galaxy density orientations, despite very strong X-ray ellipticity. Inspection of the density maps shows that the red galaxy overdensity is substantially offset from the X-ray peak, in the direction of the X-ray elongation. The BCG of the cluster is precisely

centred at the X-ray peak. The line passing through the main red cloud, the main blue cloud, the BCG, a clump identified as being infalling by its X-ray excess C1, and the smeared out region of blue of galaxies extending away from the cluster is in good alignment with the ICM elongation axis. The observations here are consistent with a scenario where the galaxies accreted from the direction of C1 are stripped of their gas reserves during the first crossing, and become red sequence objects by the time they reach the other side. Given the weak red sequence in this cluster, it may be the case that the infalling population is not completely stripped of gas on the first pass.

RXC J2023.0–2056 This cluster has been handled differently to the others in terms of clump detection; C1 appears to be a uniform density extension with no significant blue component, but is only distinguishable from C0 if we take into account the location of the blue overdensity centred near the X-ray centre. If C1 were a major merger, which seems likely given its extent, we would expect it to cause either X-ray disturbance in the post-crossing phase, or to perhaps be identifiable as an X-ray overdense region in the pre-merger phase. Neither of these markers is present. There are two prominent red sequence galaxies north of the nominal centre of C1 at $20^{\text{h}}23^{\text{m}}38.40^{\text{s}} - 20^{\circ}55'18.7''$ and $20^{\text{h}}23^{\text{m}}37.72^{\text{s}} - 20^{\circ}55'51.6''$ (J2000), but we found no redshifts for these in the SIMBAD database.

5.4.4.3 Mismatched: optically-disturbed and X-ray-regular

This group appears to include several cases where sub-clumps are observed at relatively large distances from the centre of the cluster. This is consistent with a post-merger scenario where the ICM has relaxed but the red galaxy distribution has not, perhaps due to insufficient time. This does not exclude pre-mergers, so long as the infalling clump is at a sufficient distance not to affect the X-ray centre shift parameter.

RXC J0049.4–2931 This cluster has a regular primary clump C0, and several moderately sized sub-clumps at a moderately large distance from the cluster centre. It has a blue galaxy overdensity largely restricted to one side of the cluster centre. This cluster has a very regular X-ray appearance.

RXC J0605.8–3518 This cluster is regular, but appears to have symmetric lobes C5 and C1. The C5–C1 axis is aligned with the X-ray elongation. There is a cluster-like clump C3 at large cluster-centric distance, which is largely outside the *XMM-Newton* field, and shows no sign of X-ray excess. There is a faint trail of blue galaxies between the cluster centre and C3.

RXC J0821.8+0112 C1 is a candidate pre-merger with X-ray excess. X-ray point sources have been excised from the X-ray surface brightness map in the same region. The internal cluster structure is of particular interest in this case. The overall shape of the

red galaxy distribution echoes the very disturbed distribution of the ICM, but no clump is detected. This is an exceptional case where there is a significant blue galaxy density across the whole of the primary red overdensity C0.

5.4.4.4 Mismatched: optically-regular and X-ray-disturbed

The objects in this group can be characterised as having few or no detectable red galaxy sub-clumps within r_{500} , but include the two clusters with the highest X-ray centre shift parameter which appear to be current major mergers. Serendipitous alignment of the two cluster centres may be the reason why no sub-clumps can be detected in these two cases.

RXC J0616.8–4748 This cluster has a candidate pre-merger clump C5 with a significant X-ray component. Within r_{500} there is a single sub clump C1, and the cluster has a non-circular overall appearance with a low density trail of red galaxies extending SW to the field edge. There is a blue galaxy overdensity which appears to be restricted to one side of the X-ray density peak and is contiguous to the SE edge of the field.

RXC J2048.1–1750 This cluster has an irregular red galaxy density distribution, albeit with a clearly defined density peak slightly offset from the BCG position, but no detectable red sub-clumps within r_{500} , and one candidate pre-merger clump C2. Its blue galaxy density distribution is unique amongst the clusters in this sample – there is a blue galaxy overdensity opposite the red overdensity peak with the BCG and X-ray peak between. The axis connecting the red peak – X-ray peak – blue peak is aligned with the X-ray elongation of the cluster as a whole. The red galaxy density peak appears to be encircled by two arms comprising of blue galaxies. The offset of the main red galaxy density peak from the X-ray centre suggests a current merger where the two merging clumps are approximately overlaid.

RXC J2129.8–5048 No sub-clumps are detected within r_{500} and the red galaxy distribution appears very circularly symmetric and regular, and with very low ellipticity. There is a red galaxy density enhancement north of the cluster centre which is not well aligned with the X-ray distribution and where no independent sub-clumps can be detected. The central X-ray morphology has two closely spaced peaks, which are each overlain with a prominent elliptical galaxy. The larger and brighter of the two – the actual BCG – overlays the slightly broader X-ray peak. The fainter elliptical galaxy overlays a sharper X-ray peak which is chosen by the algorithm in Section §5.3.1 as the origin of the cluster centred coordinate system because it is slightly more dense when smoothed on $\sim 8''$ scales. Redshifts available in the literature for the two objects show that the BCG has recessional velocity $v = (21\,625 \pm 45) \text{ km s}^{-1}$, and the smaller elliptical has $v = (22\,173 \pm 31) \text{ km s}^{-1}$ (Jones et al., 2009). The redshifts and recessional velocities are consistent with a current head on collision approximately in the line of sight.

5.5 Discussion

We showed in H2015 that under azimuthal averaging, red galaxies appear to trace an assumed dark matter dominated NFW model potential of the cluster out to $\sim r_{200}$. Using the data presented here, it is clear that the primary dominant clump of red galaxies of the cluster does follow an approximately symmetric distribution, usually around the ICM density peak. They typically have a dominant primary clump with a common central density peak position. The red galaxy distribution shows increasing alignment with the ICM as the ICM ellipticity increases, but at X-ray ellipticities $\epsilon < 0.05$, orientation offsets between the X-ray and red galaxy distribution become increasingly scattered and appear to be random.

However, the red galaxy distribution is usually less regular than the ICM, with identifiable clumps within r_{200} in most clusters. Extremely strong disturbance of the ICM, where several identifiable peaks can be picked out, is rare, and so it can usually be treated as being regular with a perturbation. 2/14 clusters have catastrophically disrupted ICM appearance where the assumption of a smooth gas distribution with perturbations breaks down, whereas 6/14 clusters have major detectable red sequence sub-clumps projected within r_{500} but are still largely symmetrical. 3/14 clusters have a significant offset between the densest clump of red sequence galaxies and the X-ray centre.

We showed in H2015 that the blue galaxy distribution was substantially shallower than an assumed NFW model of the dark matter potential, and that regions of high ICM density are usually associated with blue under-densities. The results presented here show very clearly that blue galaxies are usually found in irregular patterns rather than tracing the ICM. The distribution of offsets between ICM and blue galaxy distribution orientations is consistent with being random. These data make clear that the assumption of azimuthal symmetry for the blue galaxy distribution is inappropriate.

Blue cloud galaxy over-densities within r_{500} which are contiguous with candidate pre-mergers often terminate before reaching the cluster centre and are restricted to the side of the cluster towards the infalling clump. This is consistent with the rapid transformation of galaxies from blue to red during infall (Verdugo et al., 2012), on timescales of less than the crossing time. Some exceptions are noted: in RXC J0547.6–3152, an apparent ring of clumps is seen which encircles the centre; in RXC J2048.1–1750, a large ($\sim r_{500}$) approximately symmetrical structure with a dense peak offset from the cluster centre is seen; in only one case, RXC J2234.5–3744, is there a substantial compact blue overdensity near the ICM peak. The blue galaxy distribution irregularity, and the circumstantial evidence of blue distributions being restricted to one side of a cluster are consistent with the distribution of blue galaxies being subjected to baryonic processes which disrupt star formation and transform them into red galaxies on timescales shorter than those required for relaxation of the galaxies into the cluster potential.

There is no obvious morphological difference between disturbed and regular clusters in the morphology of the red sequence galaxy distribution. Clusters which are disturbed or regular according to X-ray classifications have the same form of red galaxy distribution characterised by a dominant primary clump with a number of strong additional overdense

regions. We take this as evidence that the red galaxy distribution of clusters retains signatures of disturbance for much longer than the ICM; almost all clusters ought to be classified as ‘disturbed’ using optical criteria.

Using the centre shift formulation described here and B2010 we find that the optical centre shift parameter has a normalisation a few times higher than the X-ray, and that there is a weak correlation between the centre shift parameter of the red sequence galaxy distribution and X-ray surface brightness map. There is no correlation between the centre shift parameter measured on the density map of blue cloud galaxies and X-ray surface brightness map. This result is in agreement with Kolokotronis et al. (2001), where it was found that a centroid estimator normalised using Monte-Carlo simulations showed weak correlation between optical and X-ray centroid shift measures, with a high scatter.

The centre shift parameter we use is most sensitive to cases where there is a dominant primary clump with a single small perturbation, which leads to moderate offsets of the centroid position measured on different scales. This is not the case in the REXCESS optical dataset where relatively strong sub-clumps – compared to the relative size of most perturbations in the X-ray dataset – are seen at all distances from the cluster centre.

The uncertainties on the optical centre shift parameter based on centroid shifts calculated on resampled galaxy density maps are up to an order of magnitude larger than those from X-ray measurements. It was remarked in B2010 that the uncertainties on X-ray centre shift parameters were quite large; with the reduced counts which the optical galaxy catalogues have compared to the X-ray data, this increase of uncertainty is unsurprising.

Detection of substructure clumps by measuring their significance enables us to describe morphological trends in the data qualitatively. The prevalence of ‘optical substructure’ in clusters is reported to be in the range $\sim (40-70)\%$ (Geller and Beers, 1982; Rizza et al., 1998; Kolokotronis et al., 2001), and our measurement criteria prefer a higher prevalence since only 2/14 of the clusters have no detectable sub-clumps within r_{200} . In clusters with strong ICM disturbance, the optical data are usually consistent with a current merger, and none of the clusters with regular ICM have extremely high optical sub-clumps. ICM disturbance appears to be a better indicator of a very recent merger, since the galaxy distribution retains merger signals for longer.

We were interested in the possibility that clusters with more disturbed ICM morphology might be situated in denser regions of the cosmic web, where clump infall might be more frequent and more clumps might be detected in the region $> r_{200}$. However, the low number of significant clumps seen in these regions – a handful in each field – means that this measurement lacks discriminatory power.

A more robust method, compared to the normalised clump count we employ, would be to use wider field data to locate and measure the density of filaments surrounding each cluster. The 2σ primary galaxy count overdensity contour extends at least to the edge of the WFI@2.2m field and suggests the presence of structures on scales larger than the cluster in RXC J0006.0–3443, RXC J0616.8–4748, RXC J0645.4–5413, RXC J0821.8+0112, RXC J2129.8–5048 and RXC J2218.6–3853. However, the field of view of order ~ 5 Mpc is too small for robust detection.

Verdugo et al. (2012) showed that a 20 Mpc wide field spectroscopic catalogue of a cluster and its environs can be used for a direct assessment of the local density, and allowing the clusters to be assessed in context, rather than as quasi-isolated entities as we have shown in this analysis.

5.6 Conclusions

Red galaxy distributions are dominated by a large central overdensity where the peak density is coincident with the ICM peak density. Where ICM ellipticities can be measured, increasing ICM ellipticity is correlated with increasing alignment between ICM and red galaxy distribution. Unlike the ICM, infalling sub-clumps retain their identities for long periods after accreting onto the cluster, which means that most red galaxy distributions in clusters have significant substructures within r_{200} long after the ICM has relaxed. Consequently, we are unable to identify any unambiguous purely optical parameters with which to identify merging clusters – one is unable to distinguish a current/pre-merger from an older post-merger clump using purely optical images. This also leads to the large scatter seen in the correlation of the centre shift parameter measured on the red galaxy distribution compared with the X-ray surface brightness.

Blue galaxy distributions are dominated by baryonic effects, and are very dissimilar to the ICM distribution. In particular it is very rare that a blue overdensity is found at the ICM density peak, and there is no correlation between blue galaxy distribution orientation and the ICM orientation. Contiguous regions of blue galaxy overdensity are often restricted to one side of the cluster, consistent with a model where infalling blue galaxies are stripped of their cool gas and turn red during the first pass through the densest regions of the ICM.

The centre shift parameter is a poor metric of substructure for galaxy point data. Sub-clumps in the galaxy distribution retain their identities for long periods and increase the centre shift parameter normalisation by an order of magnitude with respect to values measured for the ICM. The uncertainties on centre shifts measured using galaxy point data are larger because the number of counts for each cluster is substantially smaller than the X-ray photon count.

Acknowledgments

We acknowledge support from the DFG Transregio Programme TR33 ‘Dark Universe’ and the Munich Excellence Cluster ‘Structure and Evolution of the Universe.’ GC acknowledges support from DLR through project 50 OR 1305. DP acknowledges the financial support from Labex OCEVU. The X-ray data used here are based on observations with *XMM-Newton*, an ESA science mission with instruments and contributions directly funded by ESA member states and NASA. This research has made use of the SIMBAD database, operated at CDS, Strasbourg, France. This research has made use of the

NASA/IPAC Extragalactic Database (NED) which is operated by the Jet Propulsion Laboratory, California Institute of Technology, under contract with the National Aeronautics and Space Administration. This research has made use of NASA's Astrophysics Data System. This research made use of `ASTROPY`, a community-developed core `PYTHON` package for astronomy (Astropy Collaboration et al., 2013). Additional analysis was carried out using `SCIPY` and plots were made using `MATPLOTLIB` (Hunter, 2007). This research was made possible through the use of the AAVSO Photometric All-Sky Survey (APASS), funded by the Robert Martin Ayers Sciences Fund.

Chapter 6

Summary of findings and outlook

So much Universe, and so little time.

Terry Pratchett, *The Last Hero*, 2001

6.1 Summary of findings

We showed how the synthesis of optical galaxy position catalogues and X-ray observations can be used to give insights about the recent merger history of individual galaxy clusters. In particular, we identified some groups of galaxies just outside clusters with a red sequence suggesting they are at the same redshift, which also have significant X-ray emission indicative that they have not crossed the cluster with which they are associated. We also identified some cases where the distribution of galaxies on the outskirts of clusters was irregular but where the X-ray emission was regular, suggesting a post-merger state where the ICM had already relaxed but the galaxy distribution retained the signature of previous merger events.

We were motivated by a wish to explore whether X-ray and optical photometric observations showed highly correlated or complementary results. The literature is awash with spectroscopic investigations of the dynamics of galaxies in clusters, but wide field imaging and photometry allows deeper catalogues of galaxies to be produced, giving a clearer understanding of the projected spatial distribution of galaxies with less observation time.

The whole analysis pivots around the robust and repeatable detection of the red sequence of galaxies in colour–magnitude measurements of the galaxies in galaxy clusters. A range of approaches were tried before the final method based on fitting two distributions for the red sequence and blue cloud simultaneously was found. The description in Chapter 3 of the process by which the different methods were investigated is much simpler than the process itself was. It only became clear after the fact, that the fundamental problem could not be solved using clever background subtraction techniques; what was required to understand the data was a shift in the assumptions about a reasonable model.

Only once this understanding was in place could the rest of the analysis proceed.

The galaxies on the red sequence are the old guard of the galaxies within a cluster – poor in the gas which allows star formation, they have undergone harassment, strangulation and ram pressure stripping over a long period of time to relax into virialised orbits within the cluster. In Chapter 4, we compared the projected count density of red galaxies with the projected density of electrons observed with *XMM-Newton* and showed that the 1D radial count density profile of red sequence galaxies appeared to trace the ICM. In Chapter 5 we extended the analysis to 2D where we found clumps of galaxies within clusters which corresponded to unexplained peaks in the radial count density profiles. Our expectation that the red galaxy distribution would be approximately symmetrical and follow the ICM was confirmed.

The blue galaxy distribution is more interesting and confusing, since blue galaxies are evolutionarily much younger than red galaxies and much more strongly affected by the processes which drive evolution of galaxies within clusters. In Chapter 4 we showed that the 1D radial count density profile of blue galaxies was much flatter than we would expect if they followed the same kind of relaxed virialised orbits typical of red sequence galaxies. We also showed that they were not found in the regions with the highest gas densities. The 2D analysis in Chapter 5 showed that their distribution was generally clumpy, asymmetric, and not at all like the red sequence galaxies. Blue galaxies do not survive long after falling into a cluster – the evidence suggests that they can lose most of their star forming gas during the time it takes to cross the cluster once.

In Chapter 5 we searched for correlations between the result of 2D structural analysis of optical galaxy catalogues and X-ray surface brightness maps of the ICM. We found increasing correlation between the orientation of the red galaxy distribution and the X-ray surface brightness as the X-ray ellipticity increased. After an event like a merger between a cluster and a smaller group, the ICM relaxes quickly, whereas the red galaxies from the infalling object can be detected as a small group and density peak for longer. The blue galaxies trace infall of galaxies on the shortest timescales, turning red as quickly as their gas reserves are depleted.

6.2 Outlook

Dark matter and dark energy, which make up the vast majority of the Universe’s energy budget, are the two key unexplained phenomena facing physicists today. Another major challenge is the approaching glut of data which will be produced by surveys and compiled by collaborations in the near future.

Very wide field astronomical surveys with unprecedented depth are expected in the next few decades: the Extended Roentgen Survey with an Imaging Telescope Array (*eROSITA*) will allow the detection with X-rays of tens of thousands of galaxy clusters, and the 8 m-class Large Synoptic Survey Telescope (LSST) will be able to survey the whole southern sky in three days. Collaborations to pool and share data, like the International Virtual Observatory Alliance (IVOA) will likewise put a great deal of data in the hands

of scientists.

The analysis of these data will doubtless be complicated. Observational astronomers face becoming computer scientists first and theoreticians second. Even with the relatively small amount of data used for this project, image handling and processing in such a way that results could be repeated, cross-checked and verified became a major undertaking. The problem is magnified with each new instrument and with each new analysis step, but the payoff is a rich dataset spanning many wavelengths, spatial scales and time scales.

The methods we used for data calibration, 2D density mapping, red sequence detection and background subtraction are directly applicable to the expected survey data. This type of analysis will allow us to probe the new datasets, to gain insights into the interactions and evolution of galaxies in clusters, the dynamics of the ICM and the distribution and dynamics of dark matter in both finer detail and on much larger scales. The Universe has never been as ready to give up its secrets as it is today.

Appendix A

X-ray surface brightness maps and optical wide field images

Figures A.1 to A.28 show X-ray surface brightness maps and enhanced colour optical wide field images of each of the cluster fields.

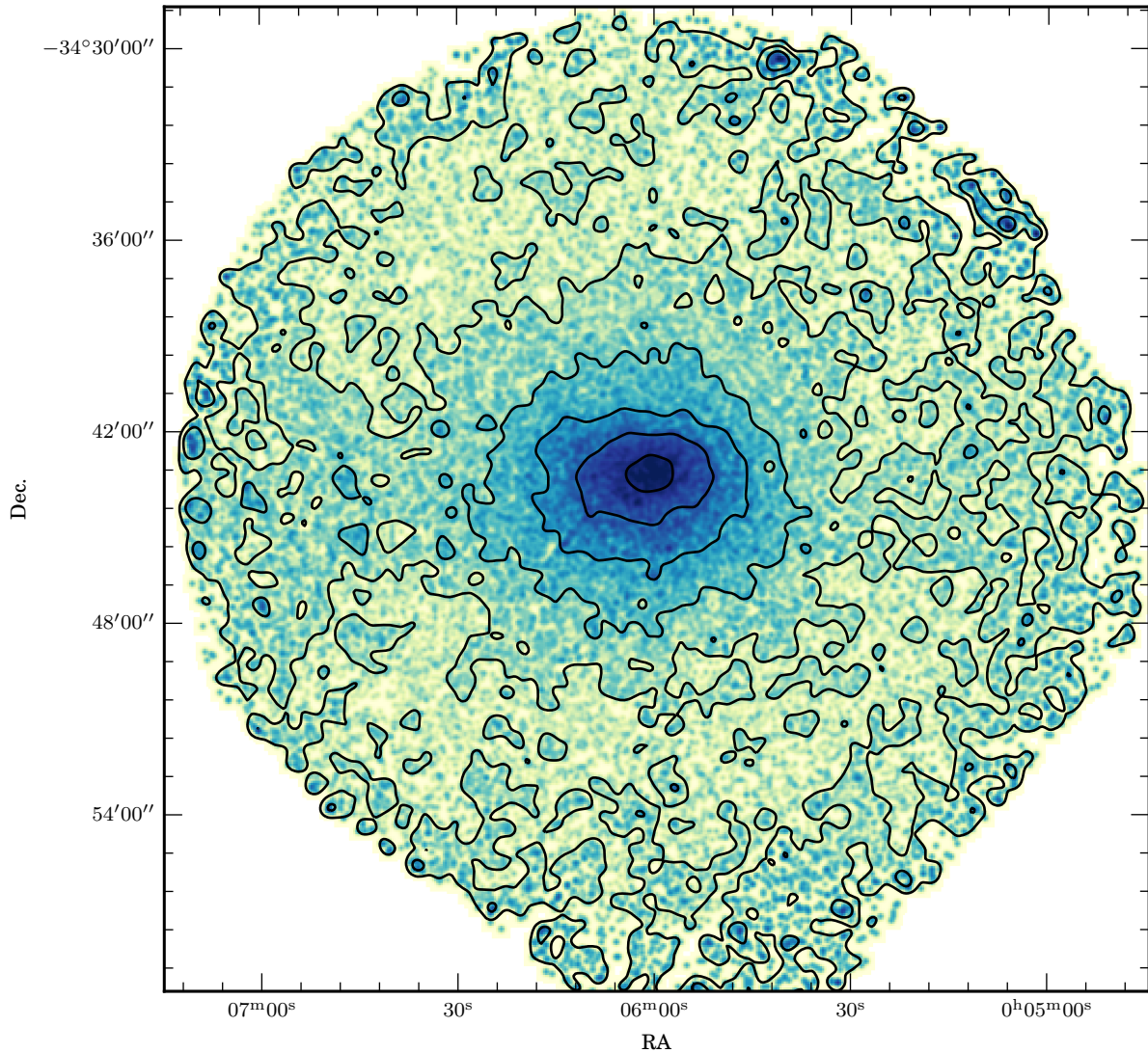


Figure A.1: X-ray flux density map of RXC J0006.0-3443 in the (0.5–2) keV band. The lowest contour is at $3 \times 10^{-5} \text{ s}^{-1} \text{ pixel}^{-1}$ and subsequent contours represent a $2\times$ increase in flux density. The pixel size is $4'' \times 4''$.

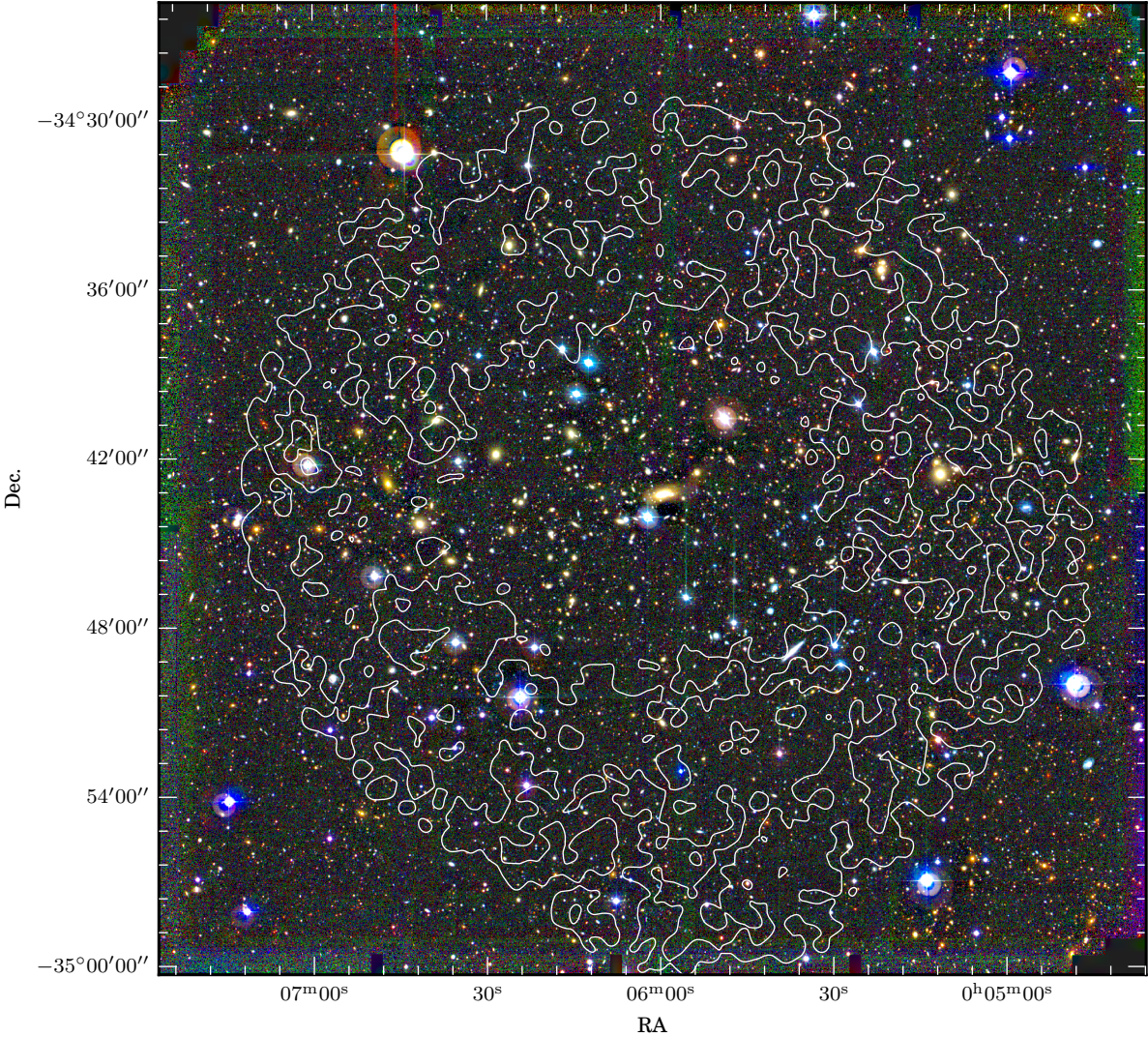


Figure A.2: Optical image of RXC J0006.0-3443 where the WFI@2.2m R_c , V and B bands are mapped to the red, green and blue channels respectively. The $3 \times 10^{-5} \text{ s}^{-1} \text{ pixel}^{-1}$ flux density contour from the (0.5-2) keV X-ray band image (on the facing page) is also shown.

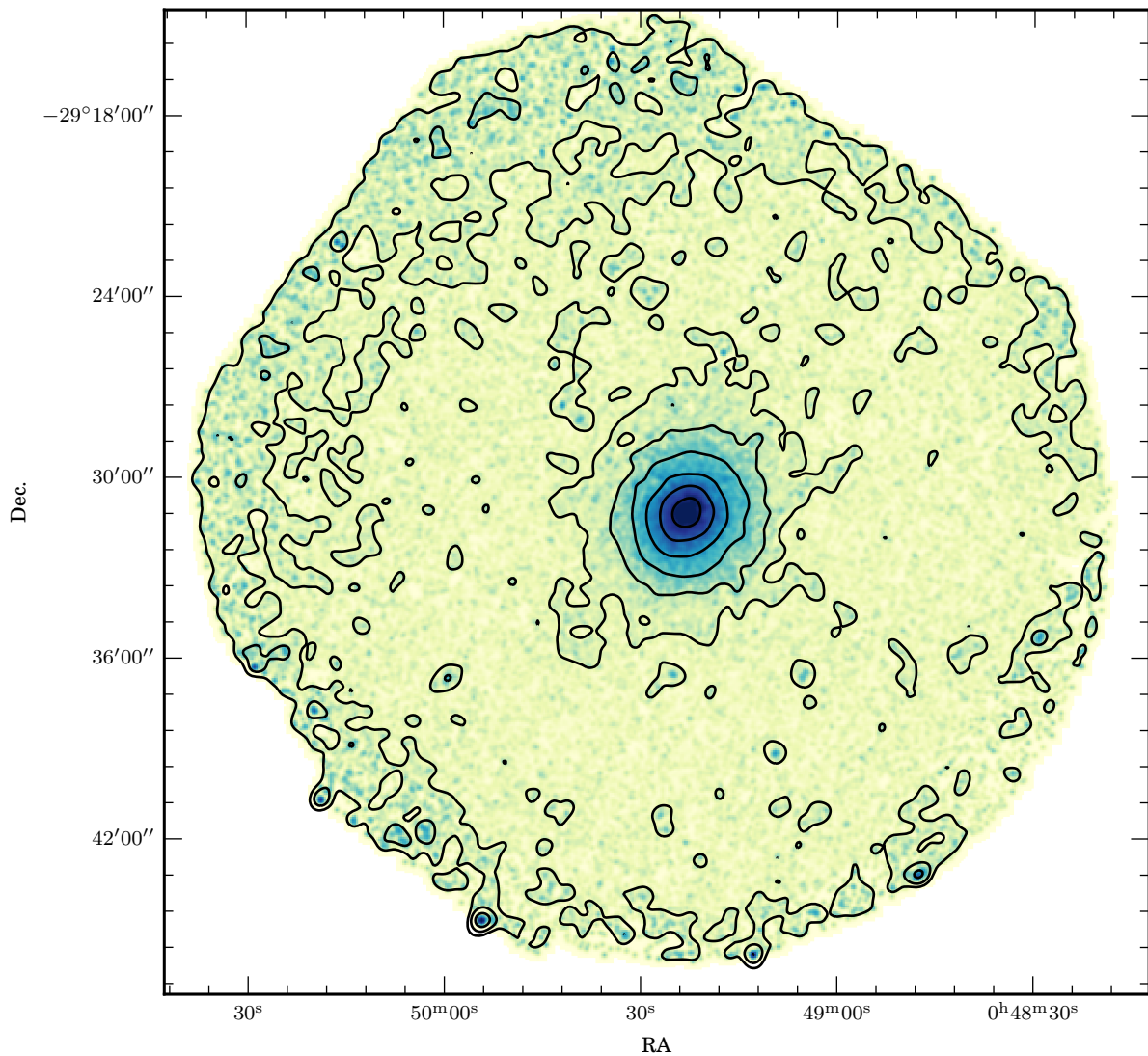


Figure A.3: X-ray flux density map of RXC J0049.4-2931 in the (0.5–2) keV band. The lowest contour is at $3 \times 10^{-5} \text{ s}^{-1} \text{ pixel}^{-1}$ and subsequent contours represent a $2\times$ increase in flux density. The pixel size is $4'' \times 4''$.

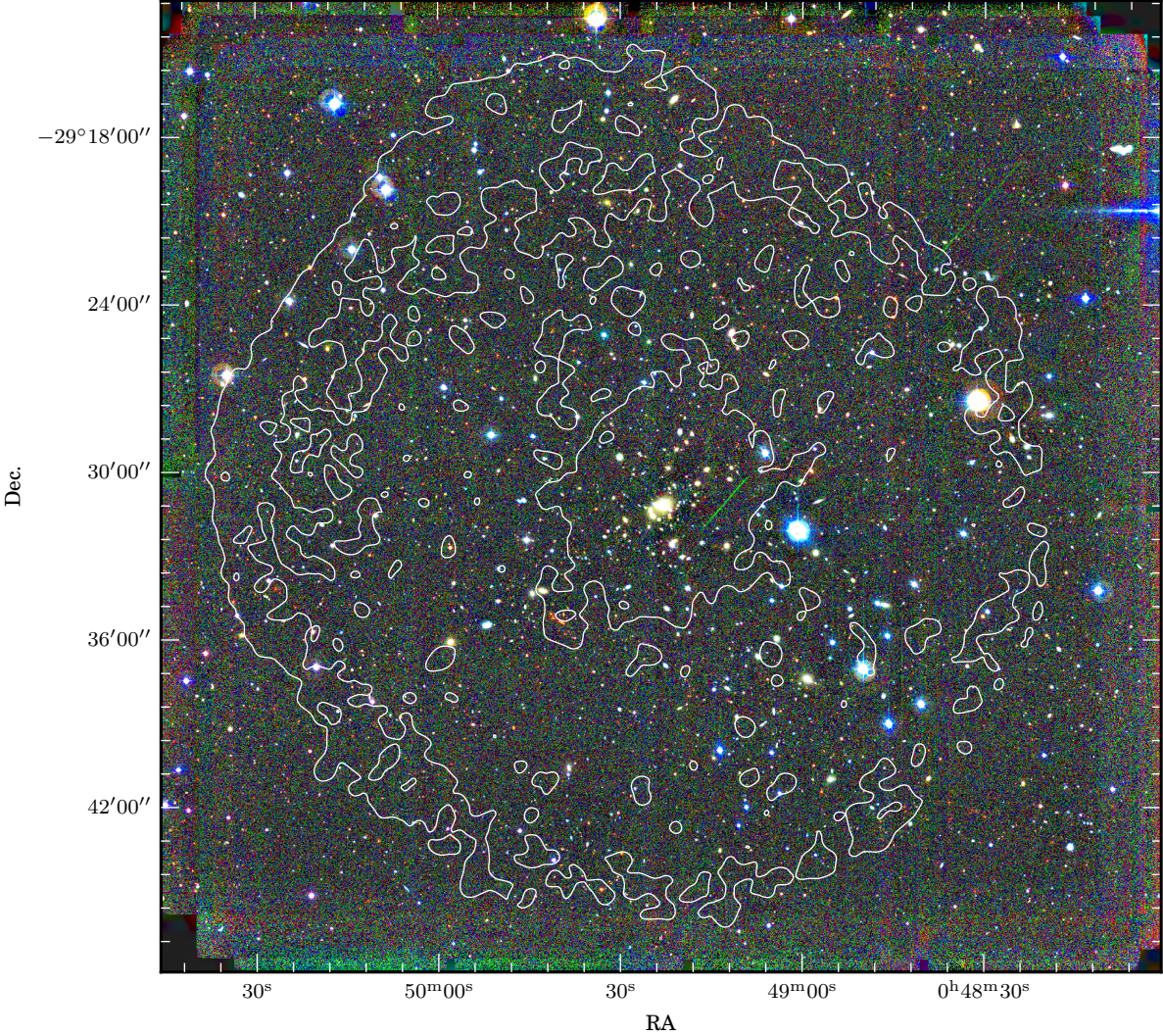


Figure A.4: Optical image of RXC J0049.4-2931 where the WFI@2.2m R_c , V and B bands are mapped to the red, green and blue channels respectively. The $3 \times 10^{-5} \text{ s}^{-1} \text{ pixel}^{-1}$ flux density contour from the $(0.5-2)$ keV X-ray band image (on the facing page) is also shown.

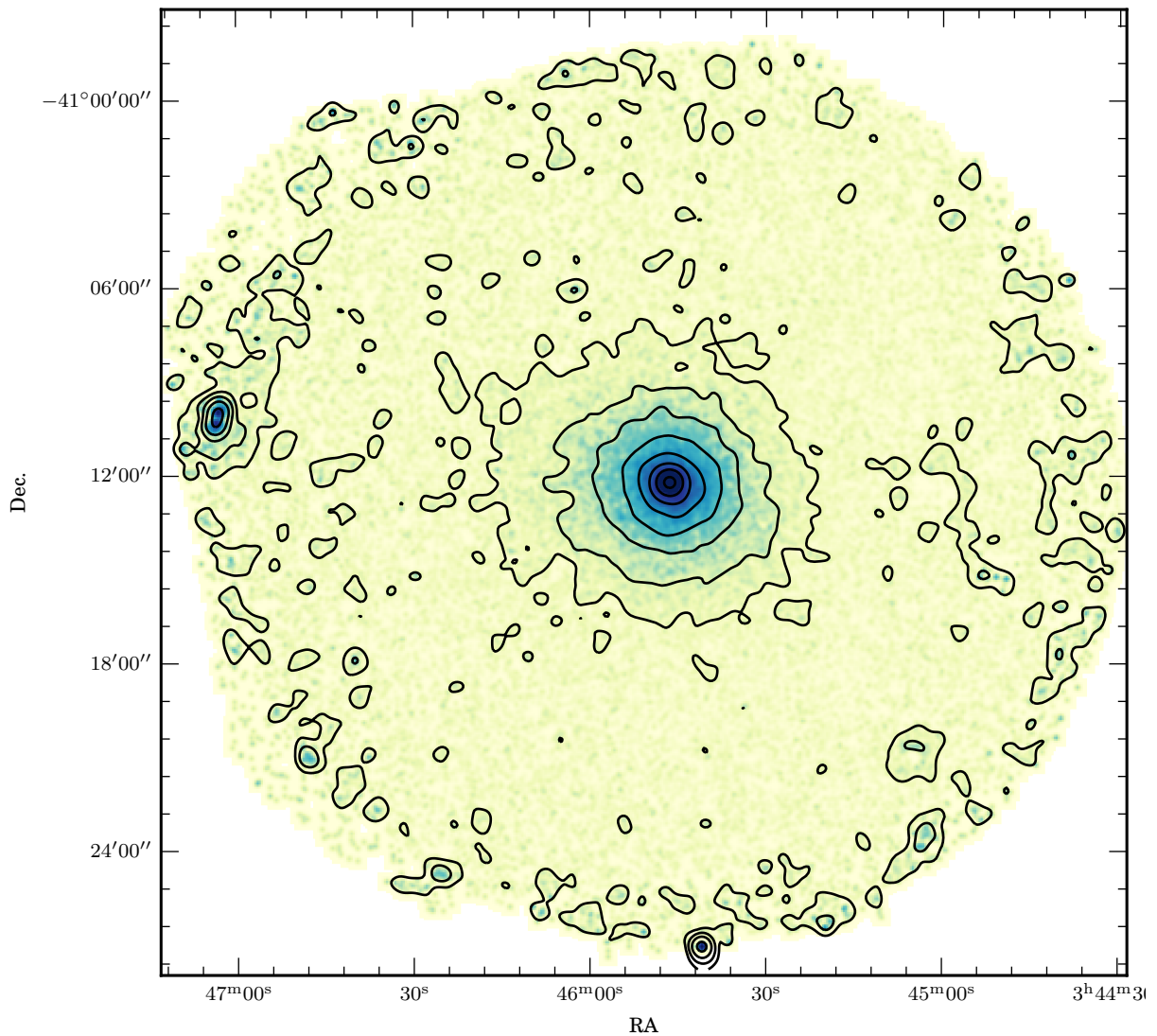


Figure A.5: X-ray flux density map of RXC J0345.7–4112 in the (0.5–2) keV band. The lowest contour is at $3 \times 10^{-5} \text{ s}^{-1} \text{ pixel}^{-1}$ and subsequent contours represent a $2\times$ increase in flux density. The pixel size is $4'' \times 4''$.

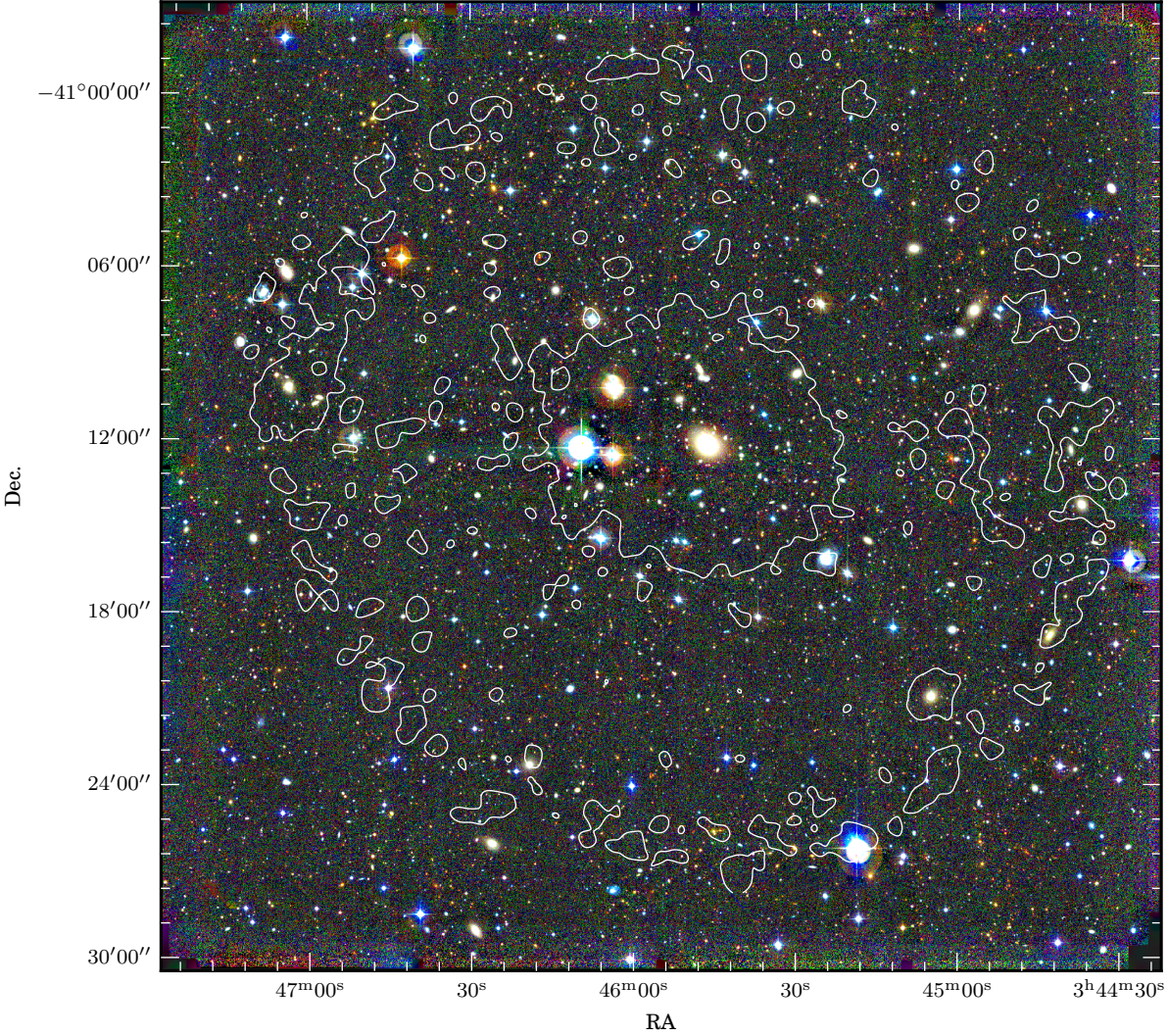


Figure A.6: Optical image of RXC J0345.7–4112 where the WFI@2.2m R_c , V and B bands are mapped to the red, green and blue channels respectively. The $3 \times 10^{-5} \text{ s}^{-1} \text{ pixel}^{-1}$ flux density contour from the (0.5–2) keV X-ray band image (on the facing page) is also shown.

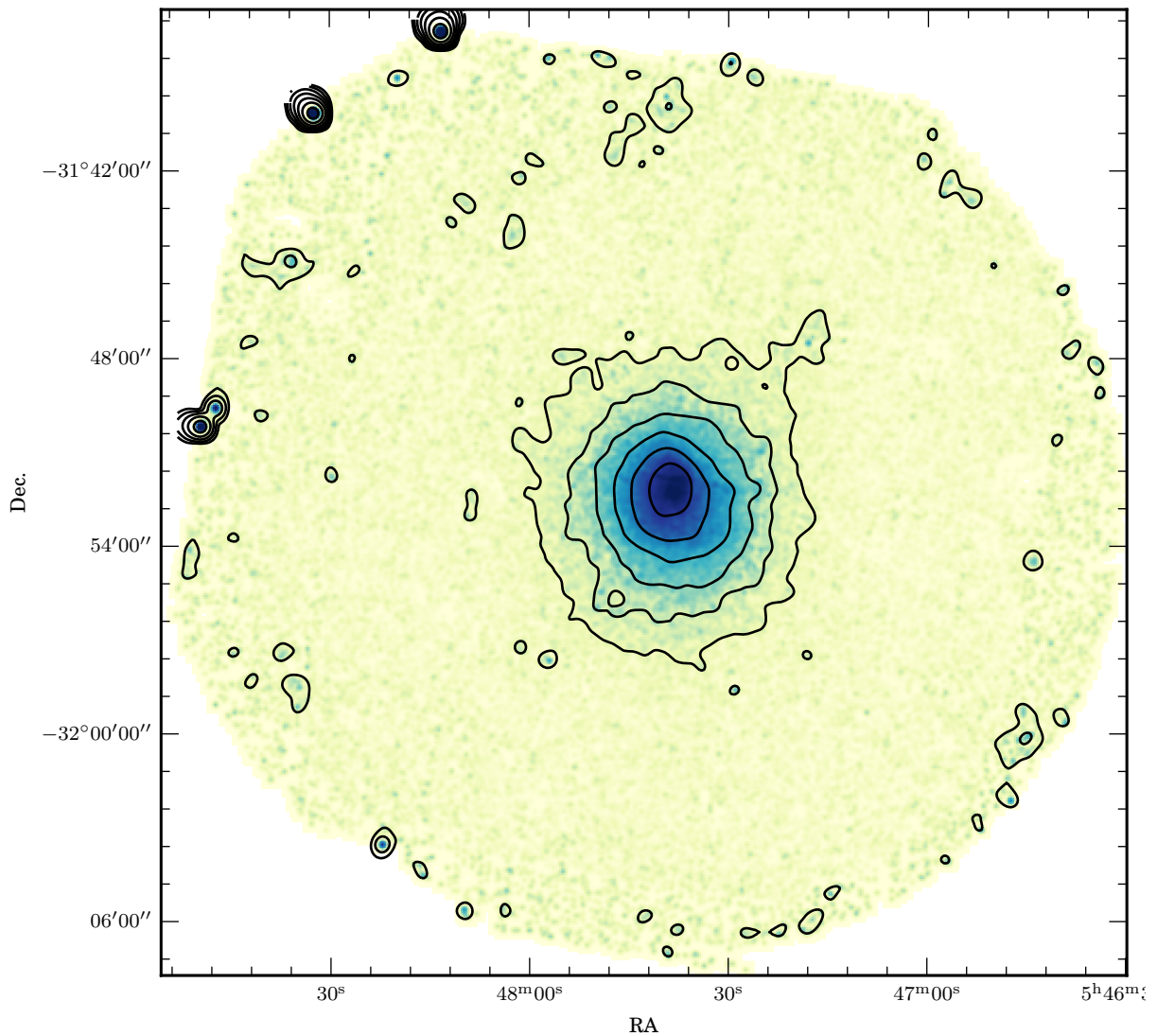


Figure A.7: X-ray flux density map of RXC J0547.6-3152 in the (0.5–2) keV band. The lowest contour is at $3 \times 10^{-5} \text{ s}^{-1} \text{ pixel}^{-1}$ and subsequent contours represent a $2\times$ increase in flux density. The pixel size is $4'' \times 4''$.

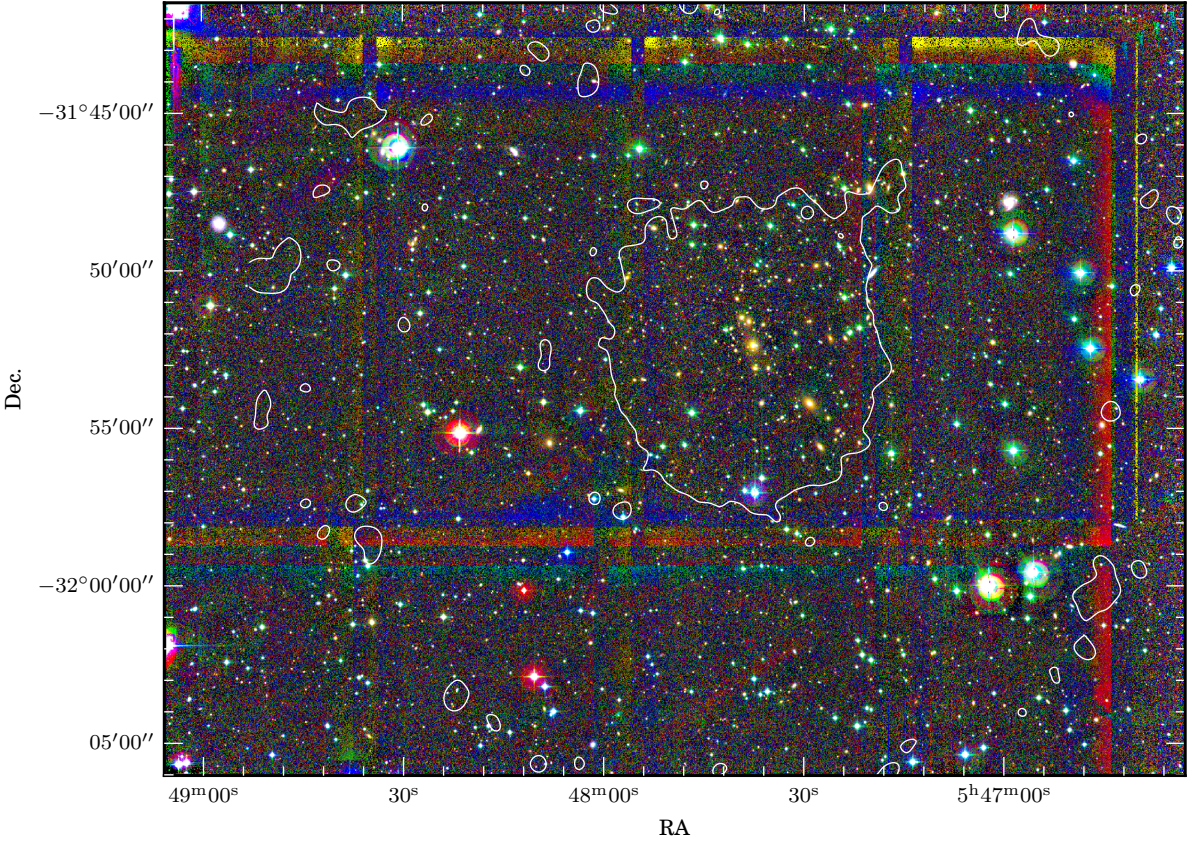


Figure A.8: Optical image of RXC J0547.6-3152 where the WFI@2.2m R_c , V and B bands are mapped to the red, green and blue channels respectively. The $3 \times 10^{-5} \text{ s}^{-1} \text{ pixel}^{-1}$ flux density contour from the (0.5-2) keV X-ray band image (on the facing page) is also shown.

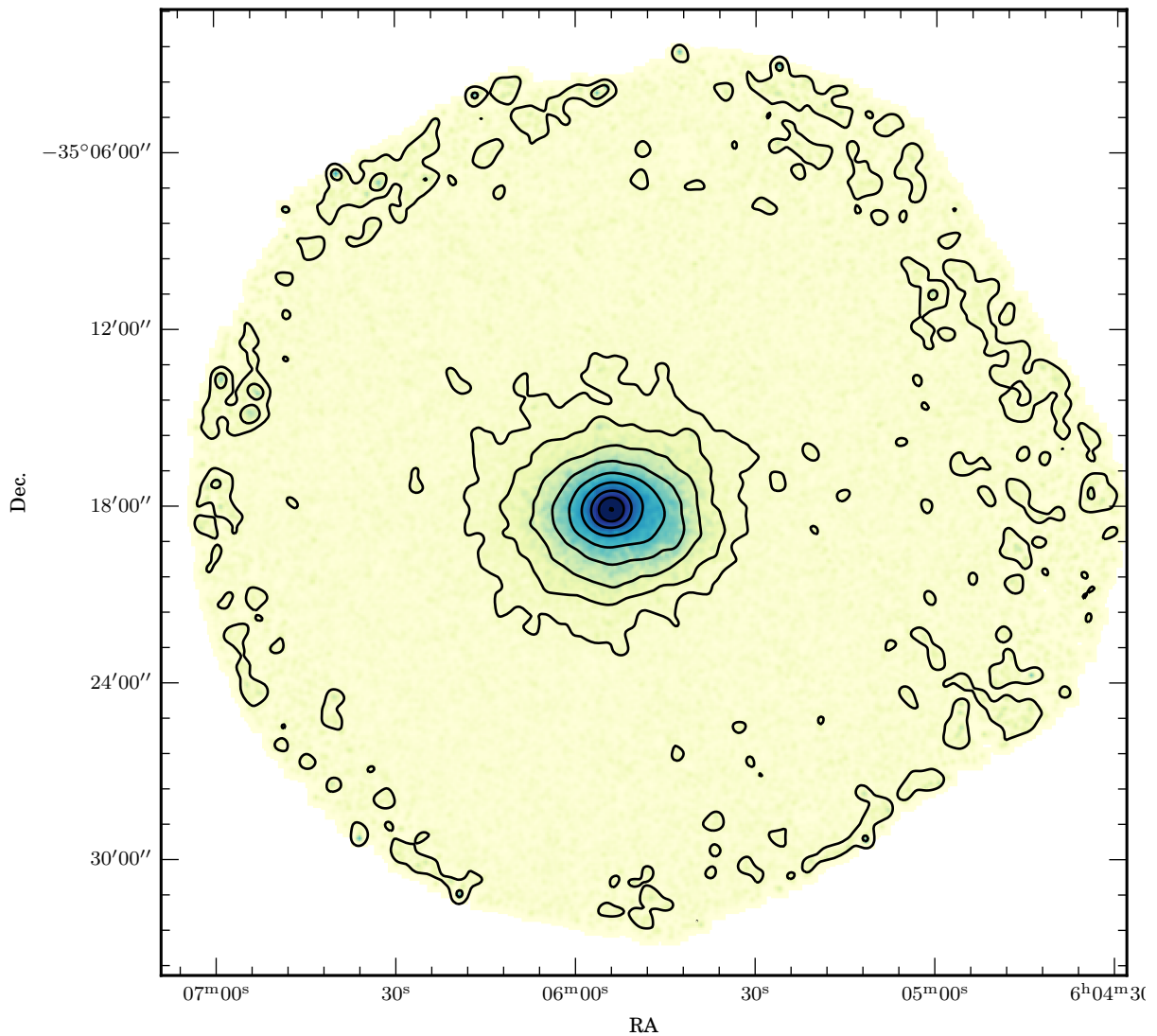


Figure A.9: X-ray flux density map of RXC J0605.8-3518 in the (0.5–2) keV band. The lowest contour is at $3 \times 10^{-5} \text{ s}^{-1} \text{ pixel}^{-1}$ and subsequent contours represent a $2\times$ increase in flux density. The pixel size is $4'' \times 4''$.

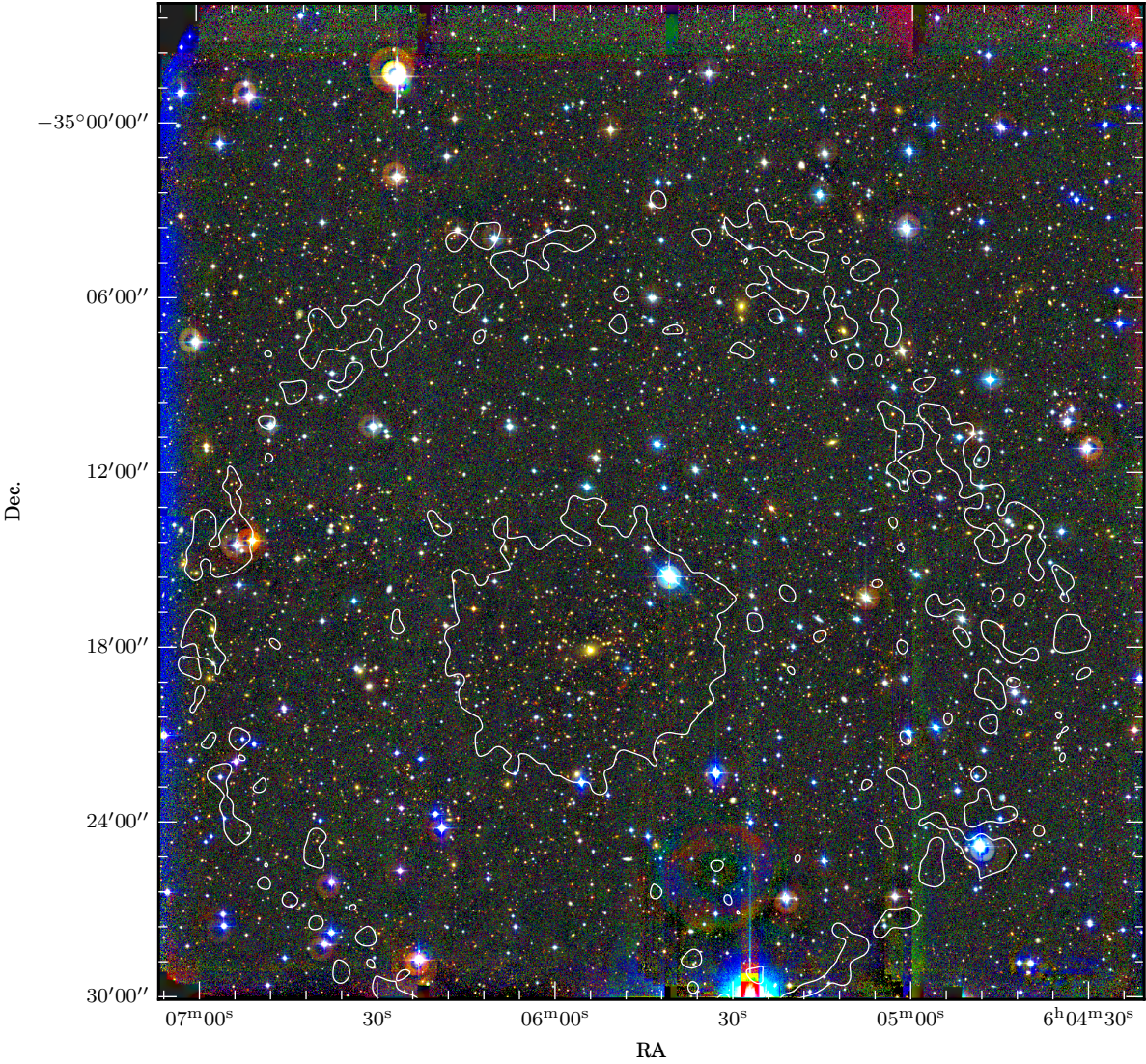


Figure A.10: Optical image of RXC J0605.8-3518 where the WFI@2.2m R_c , V and B bands are mapped to the red, green and blue channels respectively. The $3 \times 10^{-5} \text{ s}^{-1} \text{ pixel}^{-1}$ flux density contour from the $(0.5-2) \text{ keV}$ X-ray band image (on the facing page) is also shown.

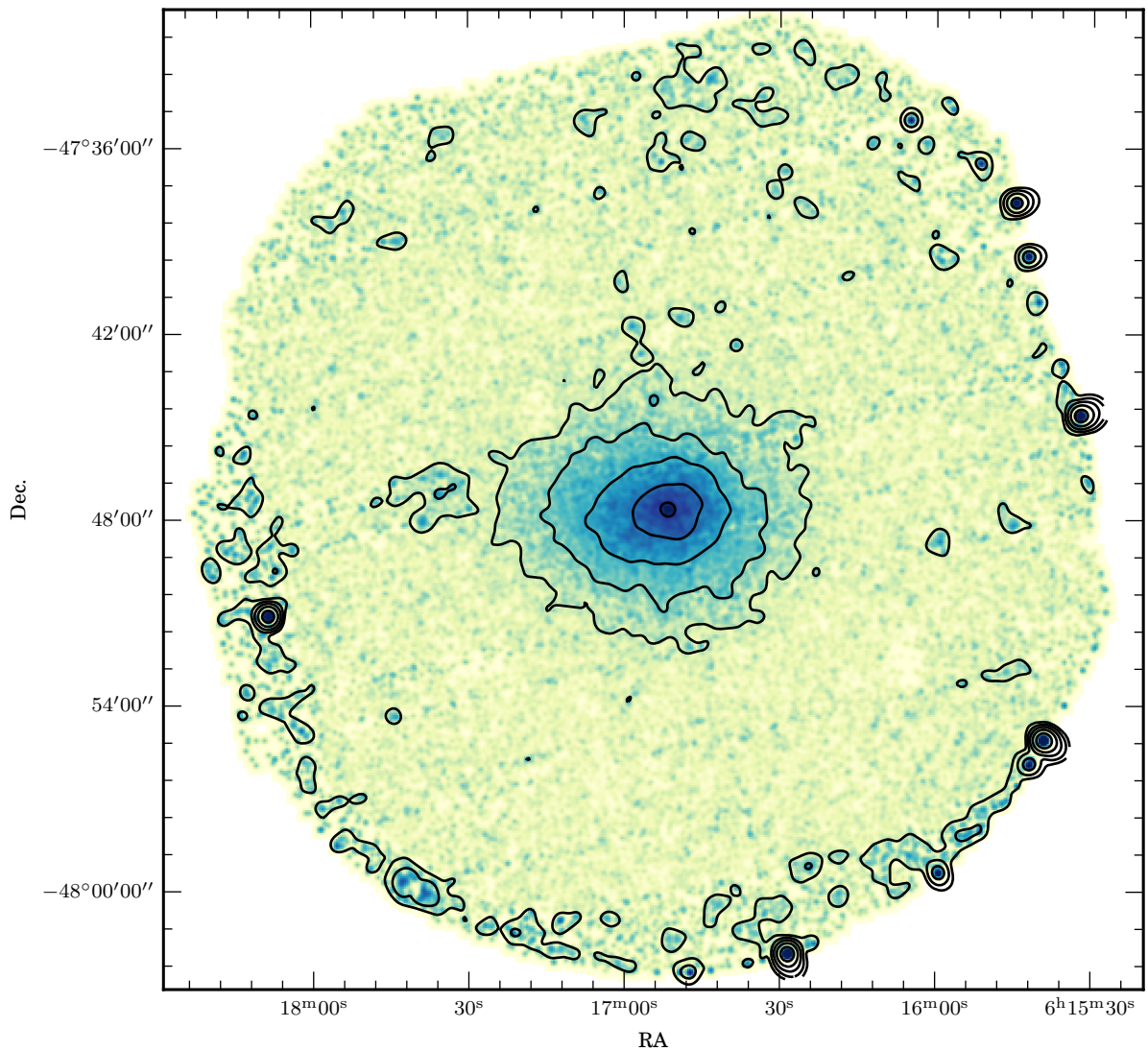


Figure A.11: X-ray flux density map of RXC J0616.8–4748 in the (0.5–2) keV band. The lowest contour is at $3 \times 10^{-5} \text{ s}^{-1} \text{ pixel}^{-1}$ and subsequent contours represent a $2\times$ increase in flux density. The pixel size is $4'' \times 4''$.

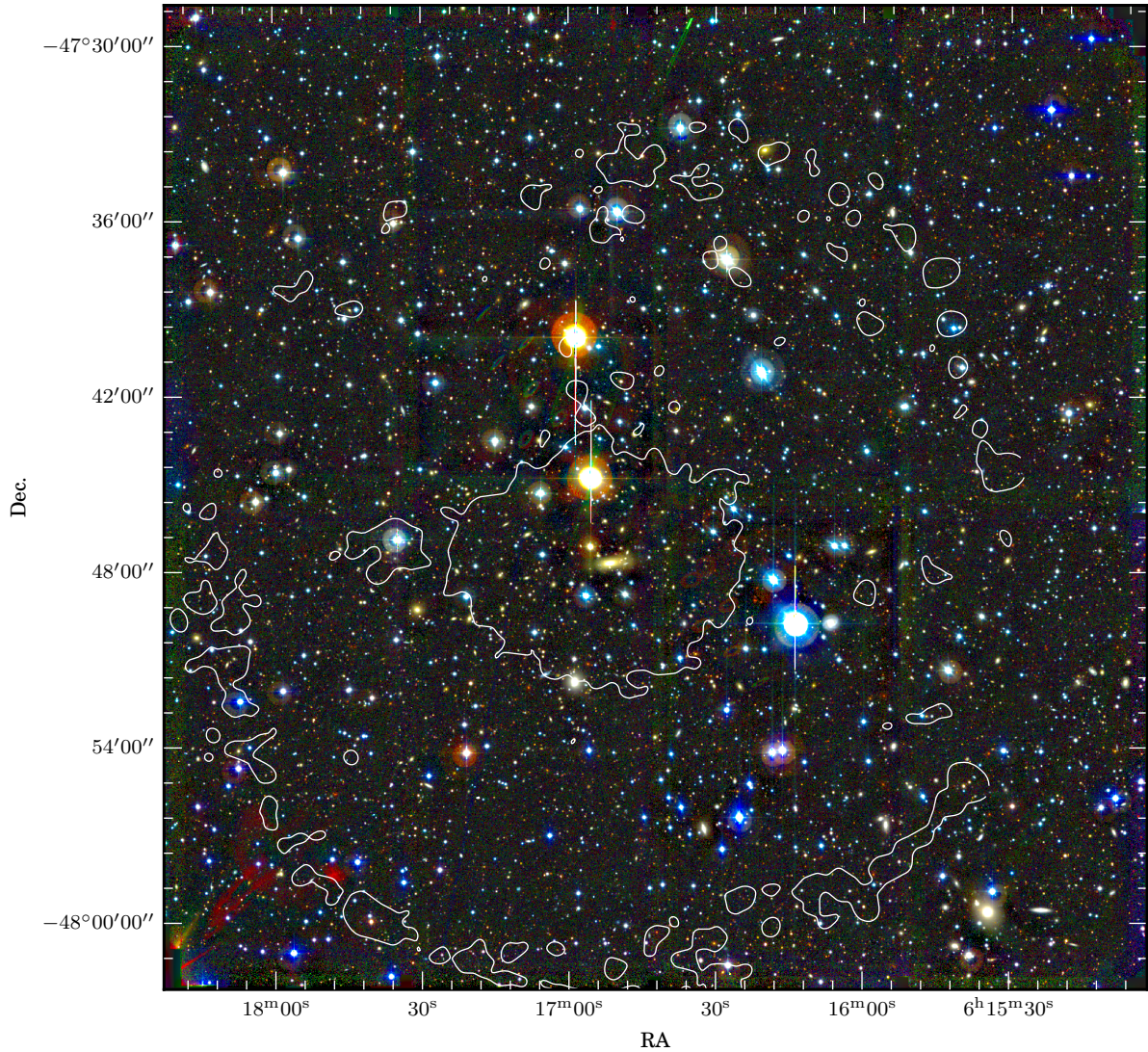


Figure A.12: Optical image of RXC J0616.8–4748 where the WFI@2.2m R_c , V and B bands are mapped to the red, green and blue channels respectively. The $3 \times 10^{-5} \text{ s}^{-1} \text{ pixel}^{-1}$ flux density contour from the (0.5–2) keV X-ray band image (on the facing page) is also shown.

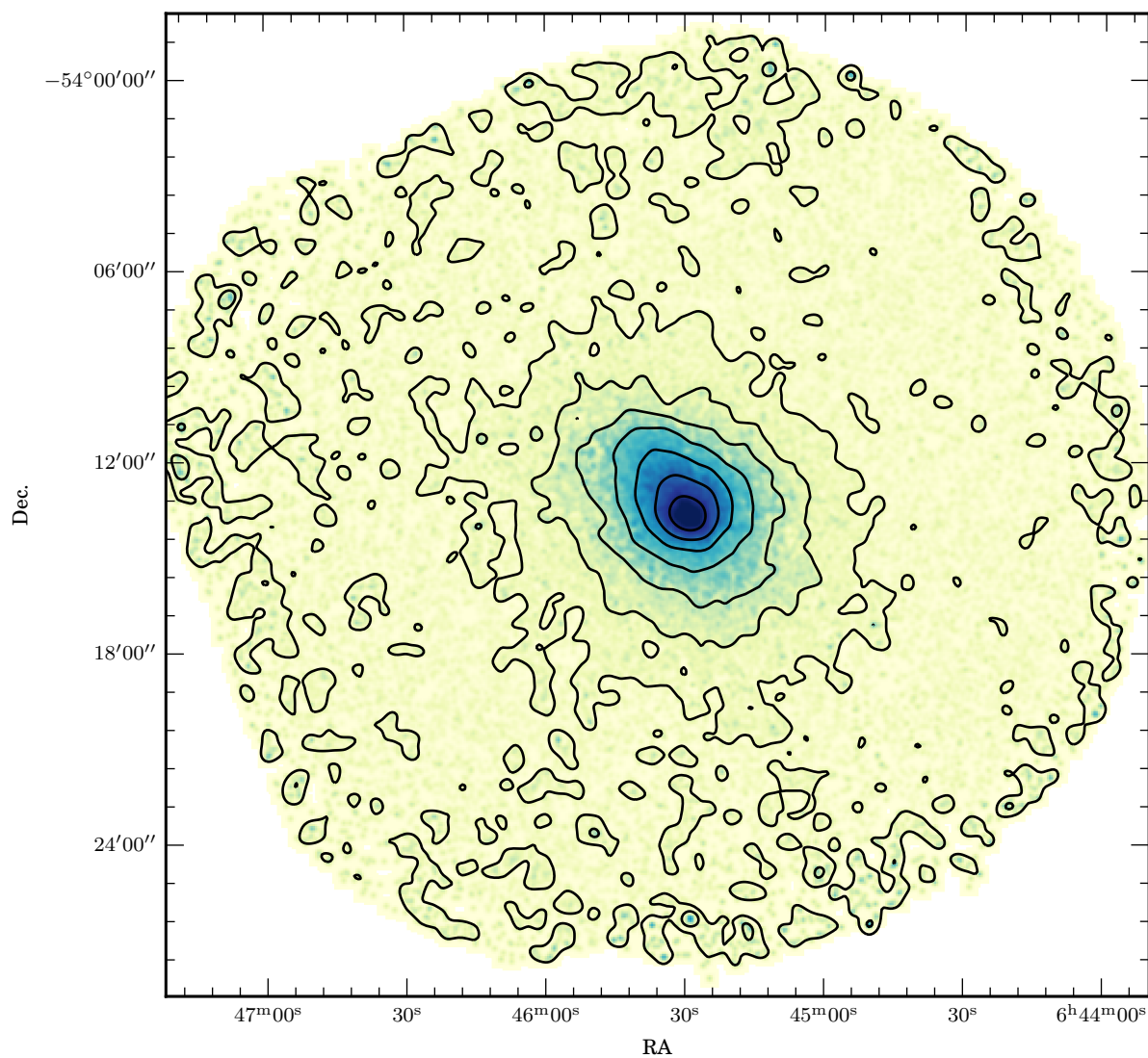


Figure A.13: X-ray flux density map of RXC J0645.4-5413 in the (0.5–2) keV band. The lowest contour is at $3 \times 10^{-5} \text{ s}^{-1} \text{ pixel}^{-1}$ and subsequent contours represent a $2\times$ increase in flux density. The pixel size is $4'' \times 4''$.

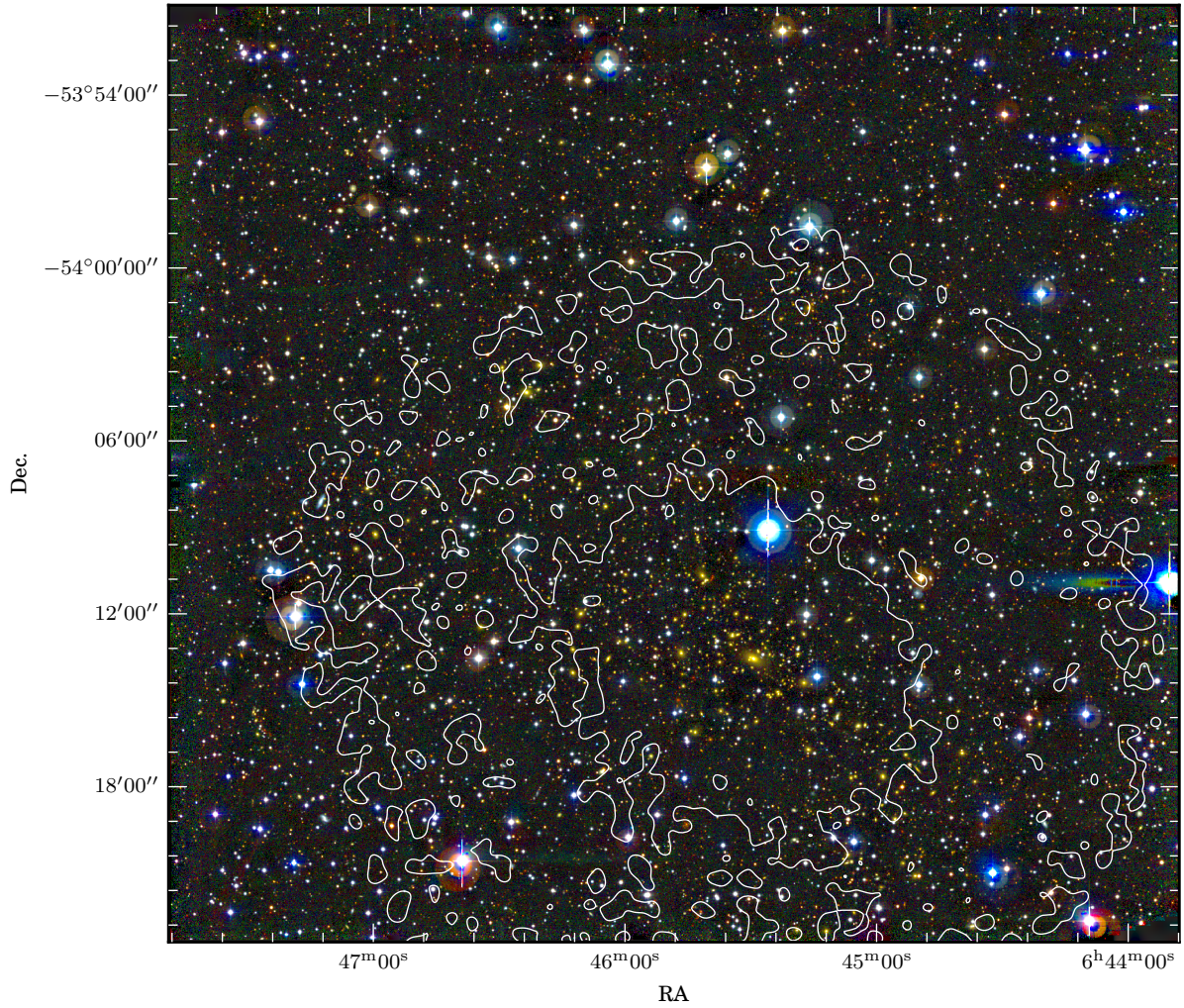


Figure A.14: Optical image of RXC J0645.4–5413 where the WFI@2.2m R_c , V and B bands are mapped to the red, green and blue channels respectively. The $3 \times 10^{-5} \text{ s}^{-1} \text{ pixel}^{-1}$ flux density contour from the (0.5–2) keV X-ray band image (on the facing page) is also shown.

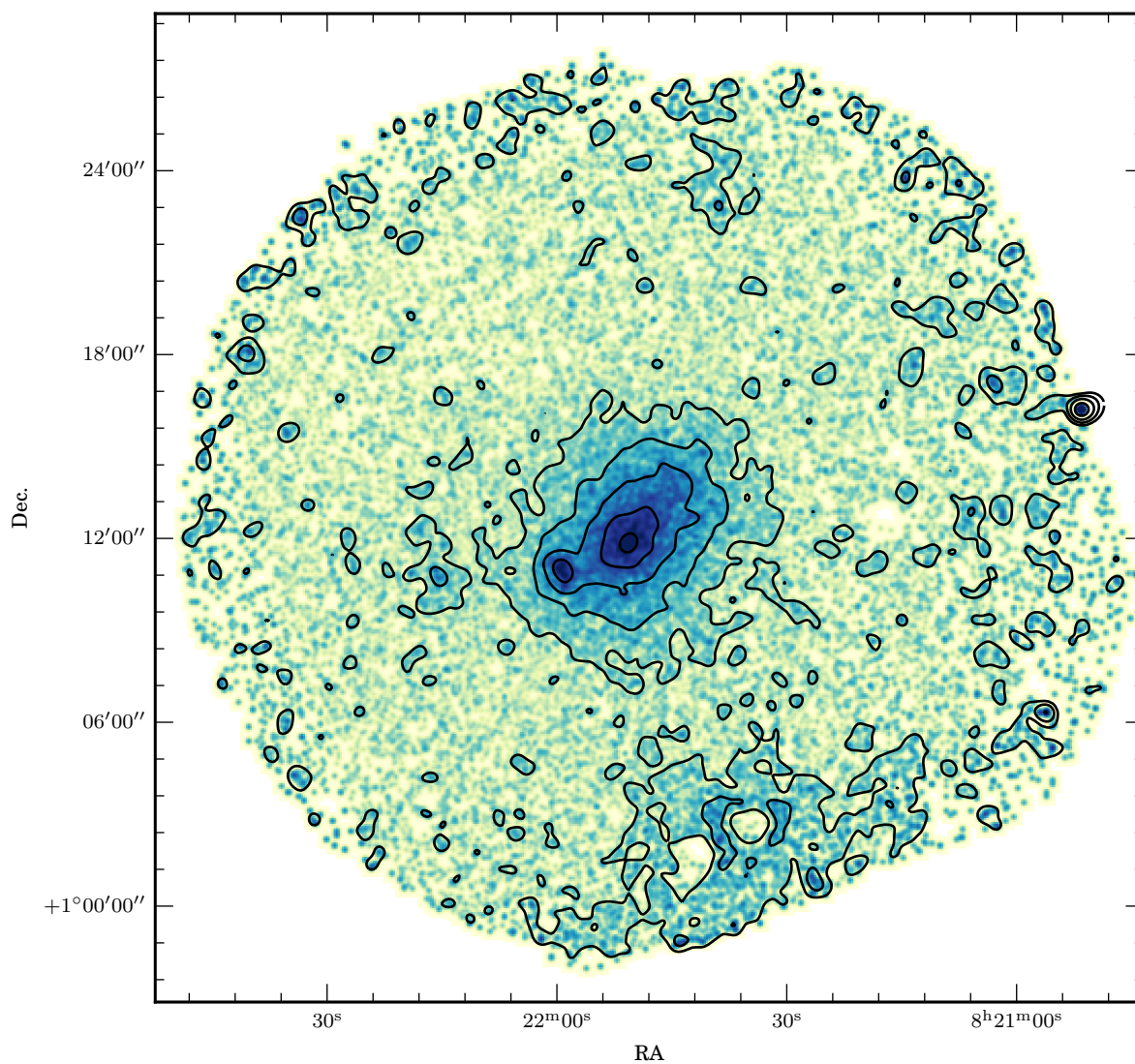


Figure A.15: X-ray flux density map of RXC J0821.8+0112 in the (0.5–2) keV band. The lowest contour is at $3 \times 10^{-5} \text{ s}^{-1} \text{ pixel}^{-1}$ and subsequent contours represent a $2\times$ increase in flux density. The pixel size is $4'' \times 4''$.

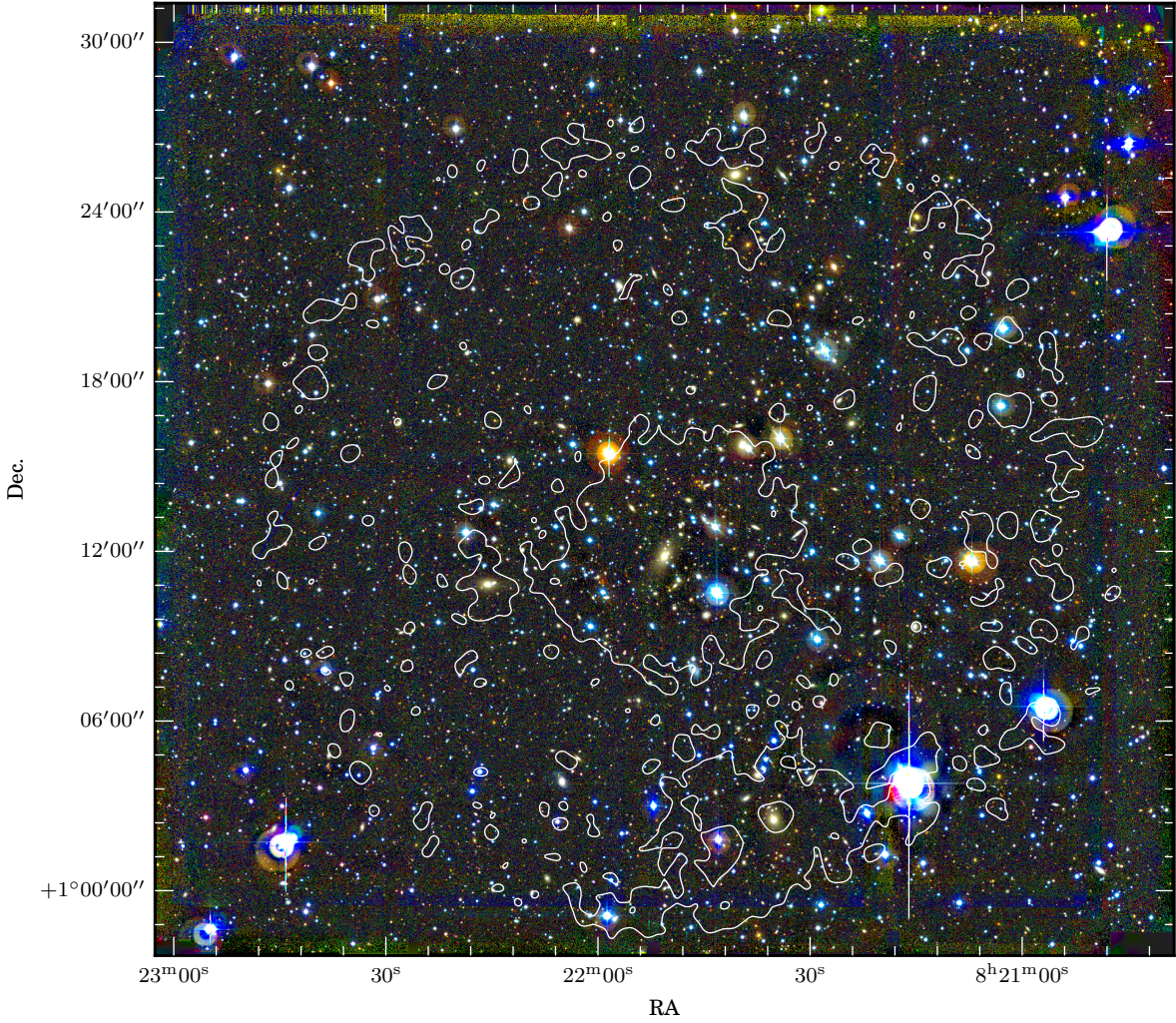


Figure A.16: Optical image of RXC J0821.8+0112 where the WFI@2.2m R_c , V and B bands are mapped to the red, green and blue channels respectively. The $3 \times 10^{-5} \text{ s}^{-1} \text{ pixel}^{-1}$ flux density contour from the (0.5–2) keV X-ray band image (on the facing page) is also shown.

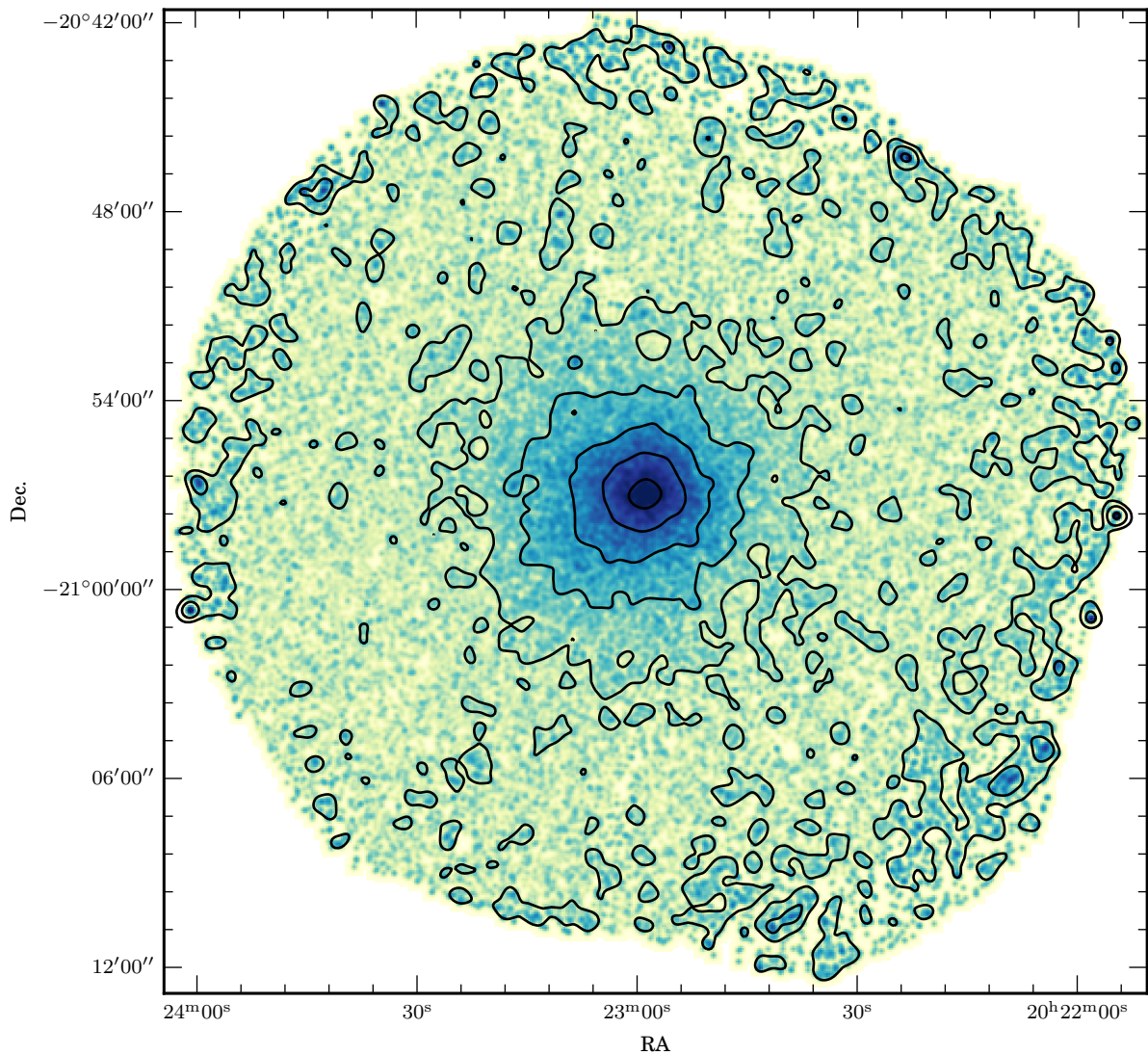


Figure A.17: X-ray flux density map of RXC J2023.0-2056 in the (0.5–2) keV band. The lowest contour is at $3 \times 10^{-5} \text{ s}^{-1} \text{ pixel}^{-1}$ and subsequent contours represent a $2\times$ increase in flux density. The pixel size is $4'' \times 4''$.

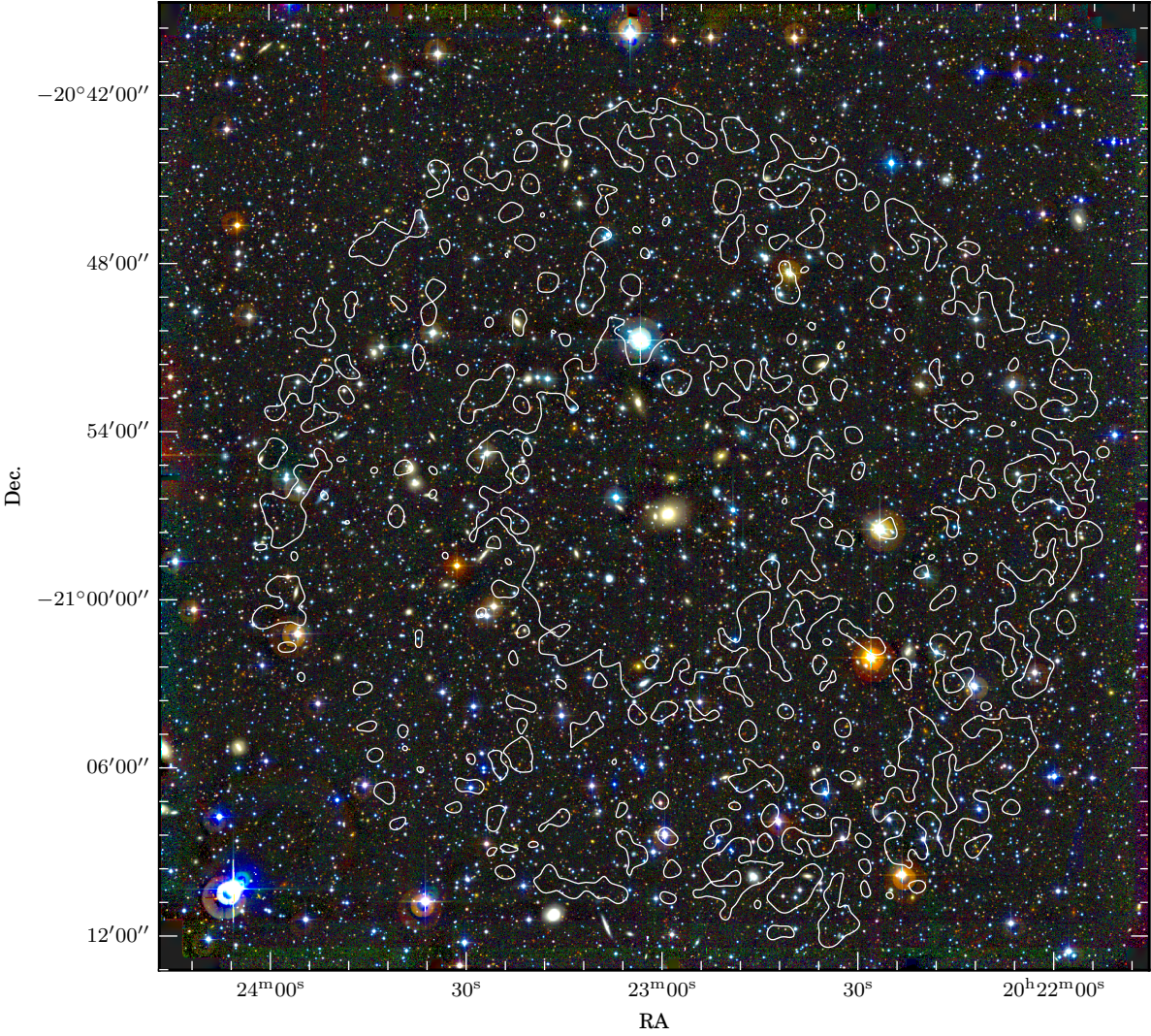


Figure A.18: Optical image of RXC J2023.0–2056 where the WFI@2.2m R_c , V and B bands are mapped to the red, green and blue channels respectively. The $3 \times 10^{-5} \text{ s}^{-1} \text{ pixel}^{-1}$ flux density contour from the (0.5–2) keV X-ray band image (on the facing page) is also shown.

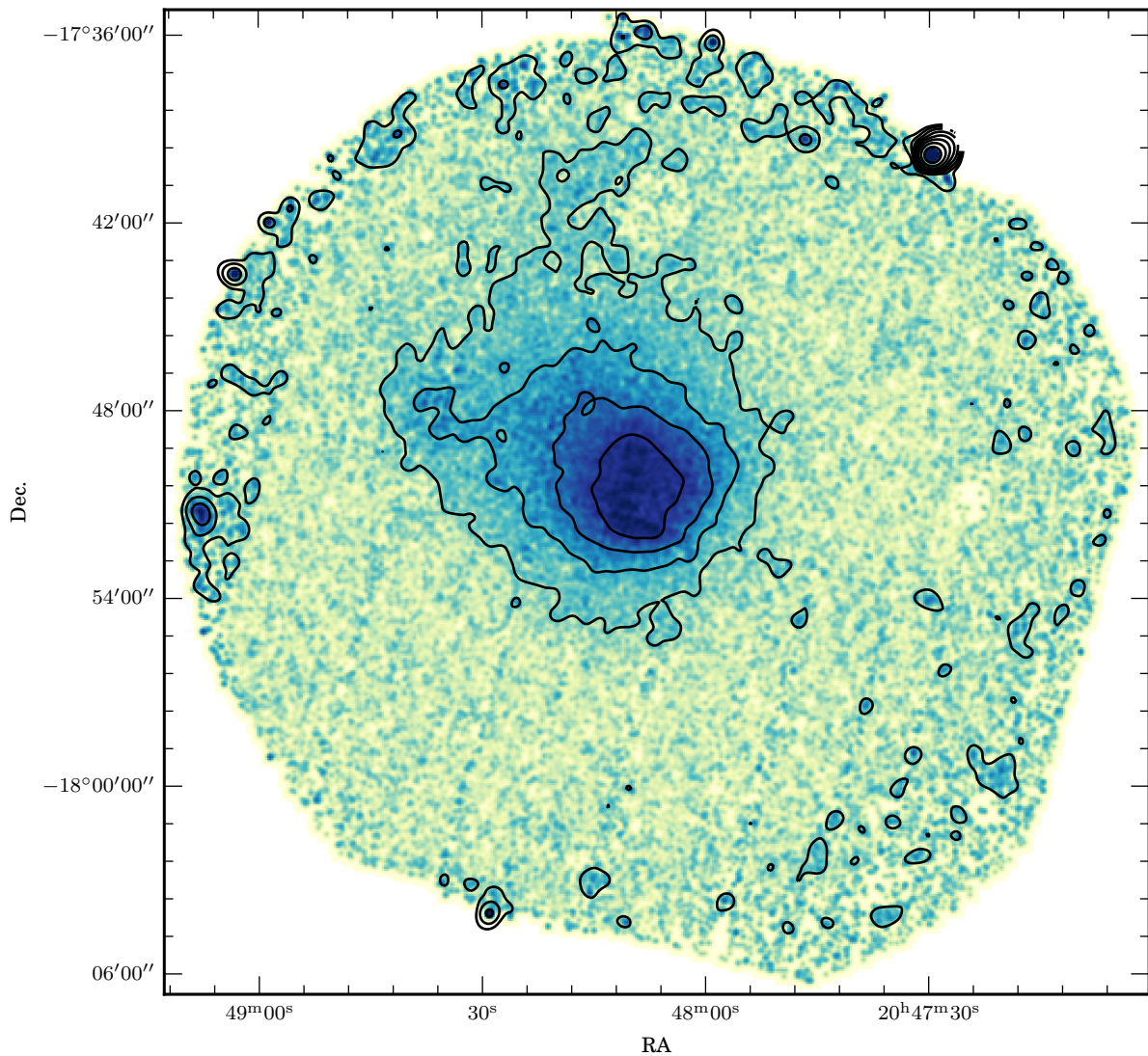


Figure A.19: X-ray flux density map of RXC J2048.1-1750 in the (0.5–2) keV band. The lowest contour is at $3 \times 10^{-5} \text{ s}^{-1} \text{ pixel}^{-1}$ and subsequent contours represent a $2\times$ increase in flux density. The pixel size is $4'' \times 4''$.

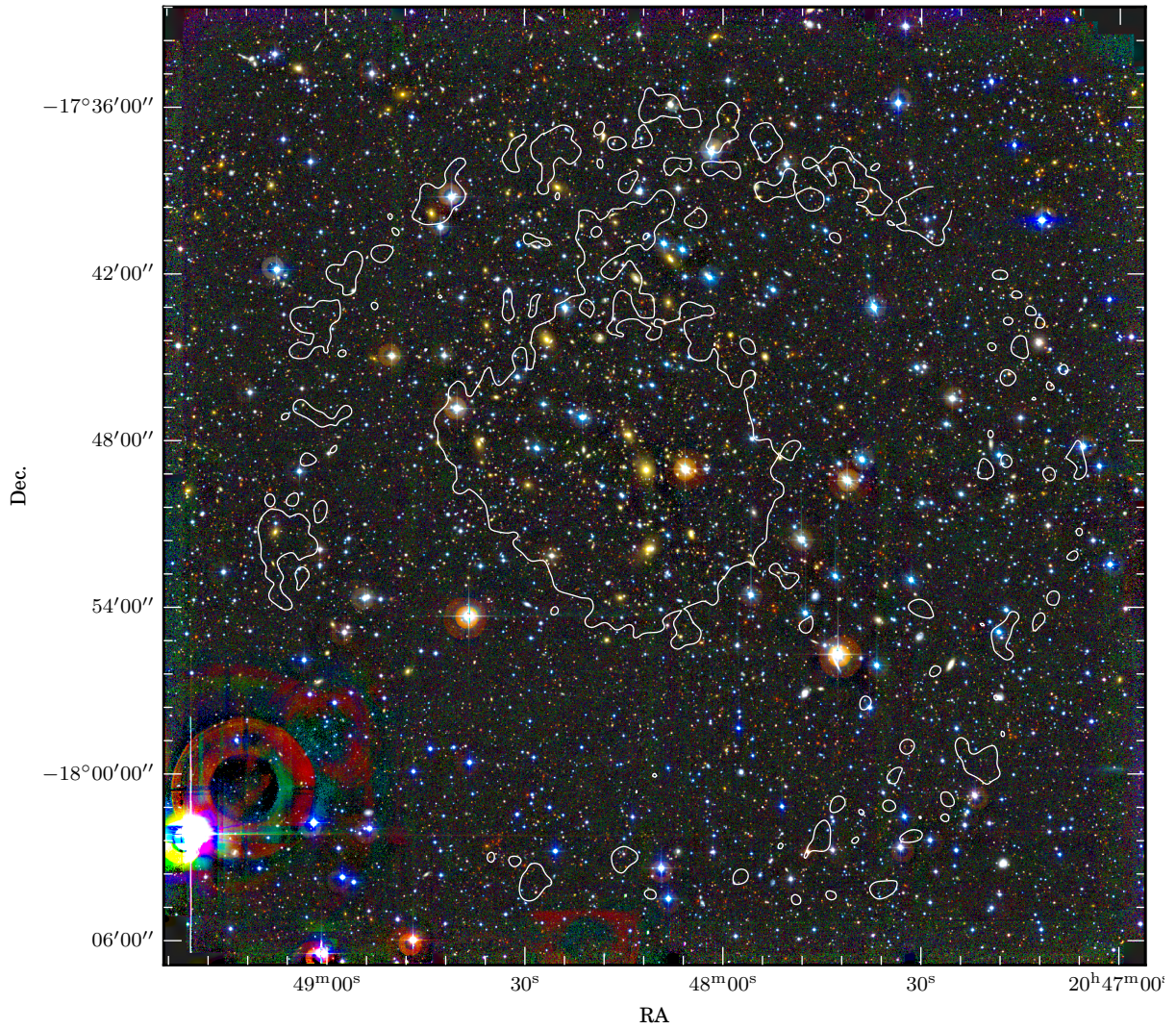


Figure A.20: Optical image of RXC J2048.1–1750 where the WFI@2.2m R_c , V and B bands are mapped to the red, green and blue channels respectively. The $3 \times 10^{-5} \text{ s}^{-1} \text{ pixel}^{-1}$ flux density contour from the (0.5–2) keV X-ray band image (on the facing page) is also shown.

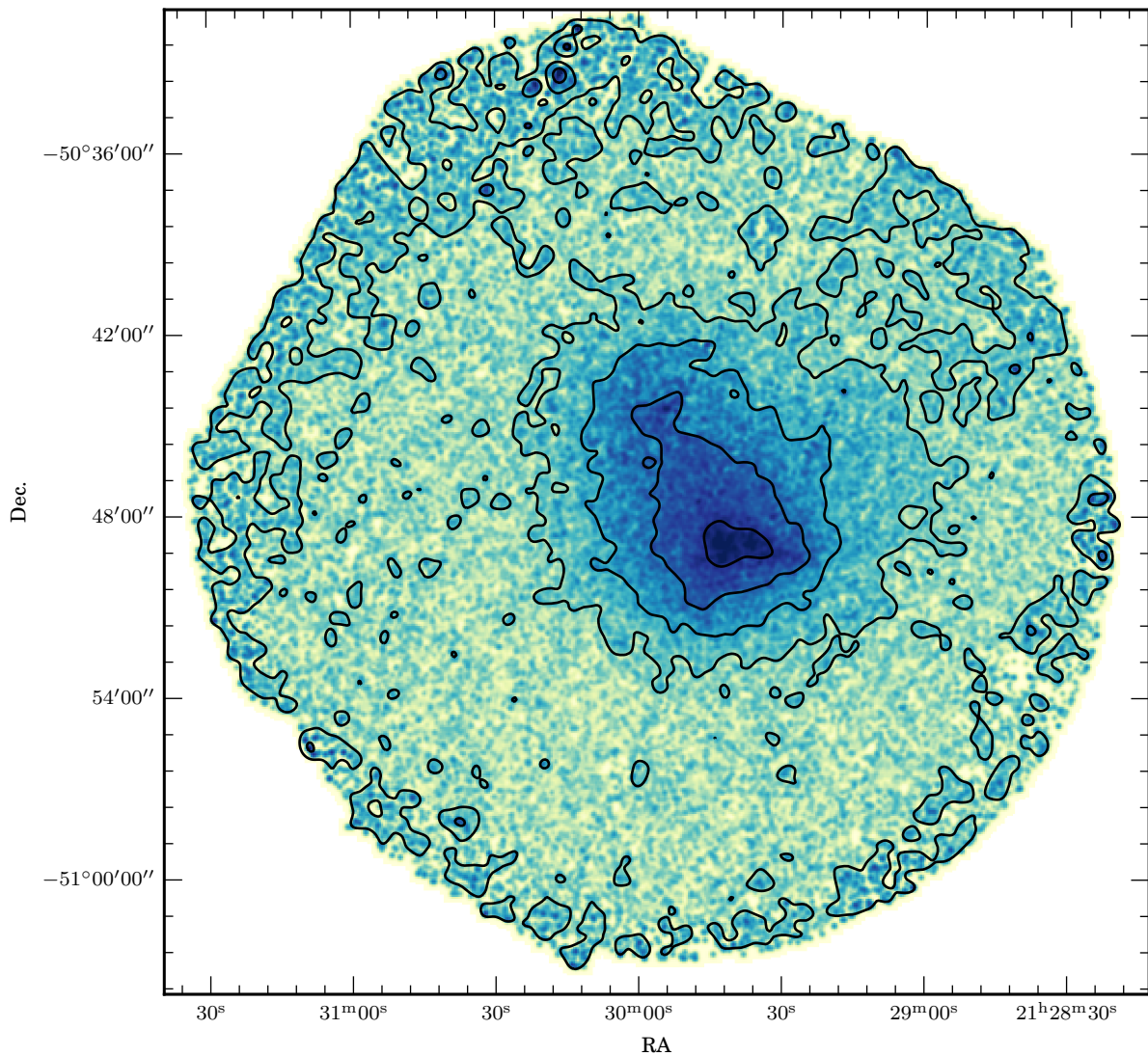


Figure A.21: X-ray flux density map of RXC J2129.8-5048 in the (0.5–2) keV band. The lowest contour is at $3 \times 10^{-5} \text{ s}^{-1} \text{ pixel}^{-1}$ and subsequent contours represent a $2\times$ increase in flux density. The pixel size is $4'' \times 4''$.

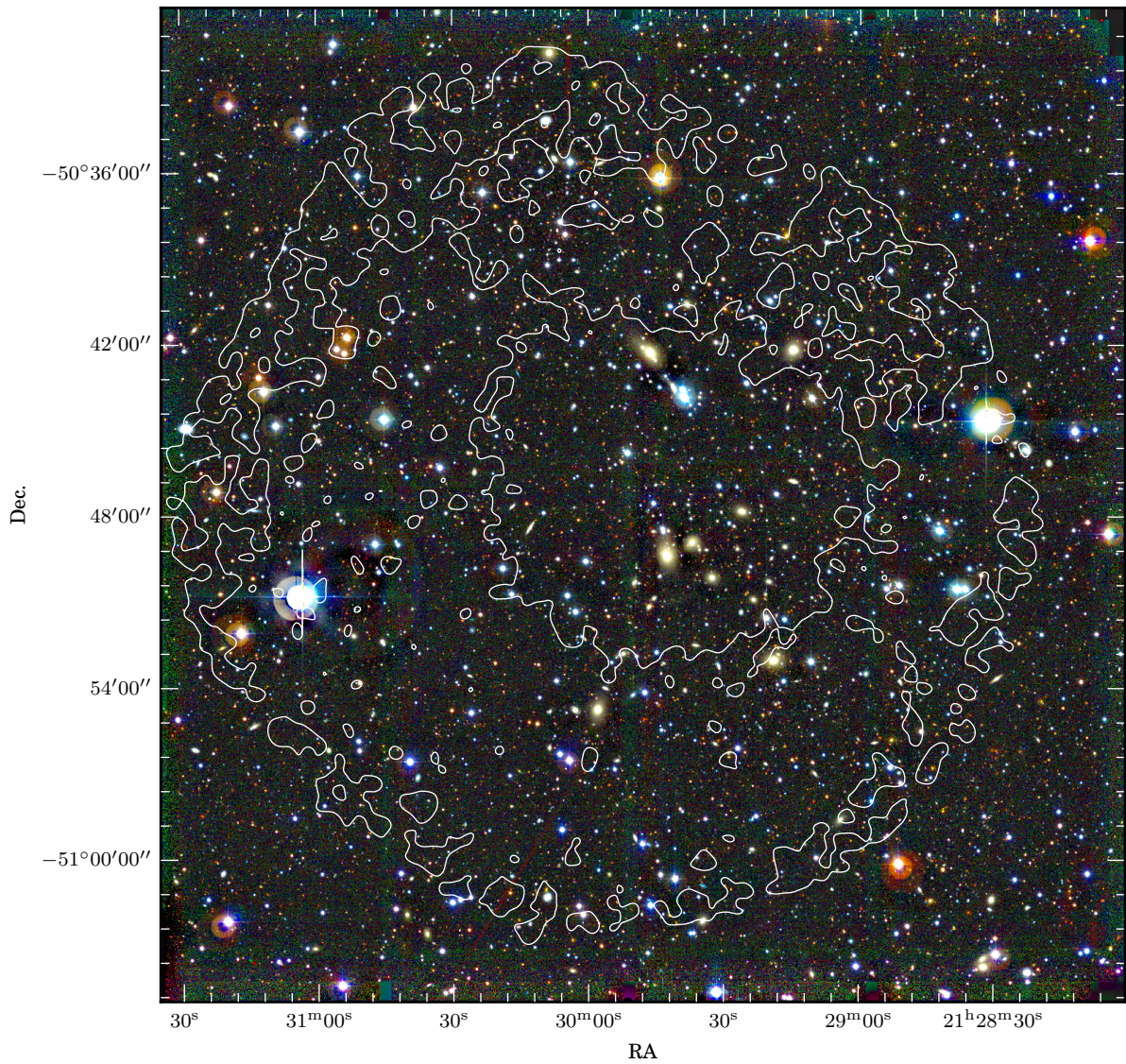


Figure A.22: Optical image of RXC J2129.8-5048 where the WFI@2.2m R_c , V and B bands are mapped to the red, green and blue channels respectively. The $3 \times 10^{-5} \text{ s}^{-1} \text{ pixel}^{-1}$ flux density contour from the (0.5-2) keV X-ray band image (on the facing page) is also shown.

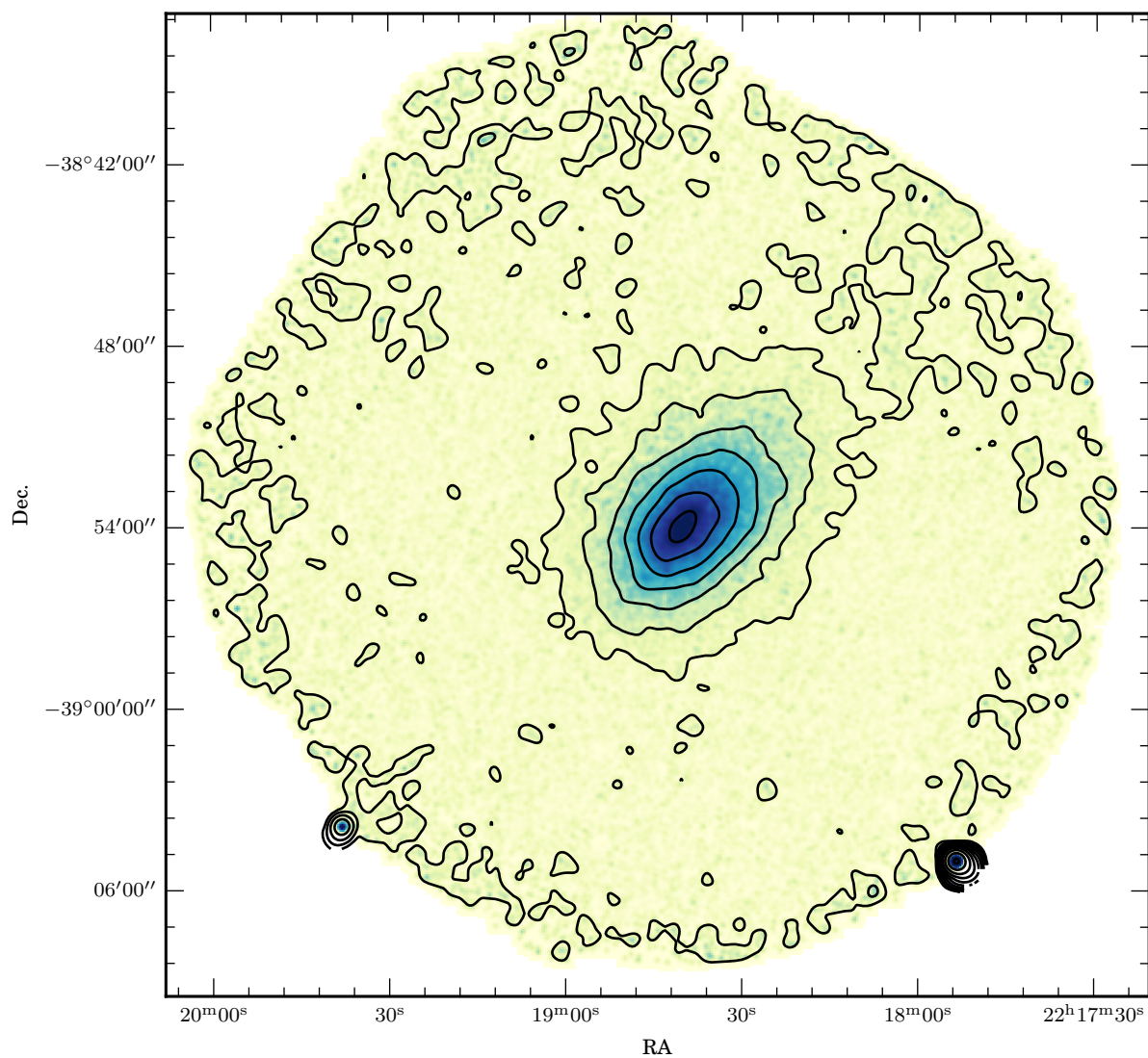


Figure A.23: X-ray flux density map of RXC J2218.6–3853 in the (0.5–2) keV band. The lowest contour is at $3 \times 10^{-5} \text{ s}^{-1} \text{ pixel}^{-1}$ and subsequent contours represent a $2\times$ increase in flux density. The pixel size is $4'' \times 4''$.

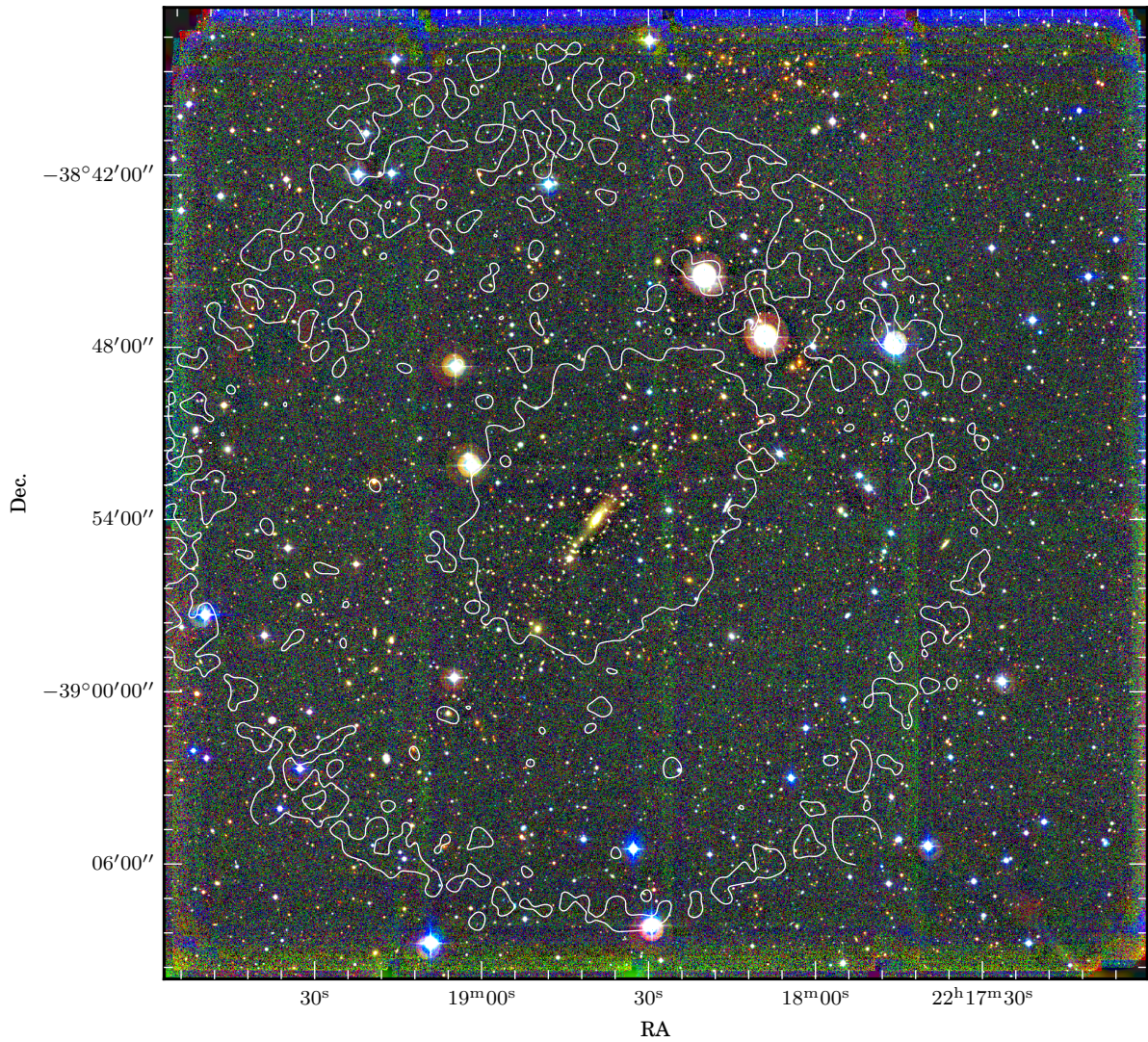


Figure A.24: Optical image of RXC J2218.6–3853 where the WFI@2.2m R_c , V and B bands are mapped to the red, green and blue channels respectively. The $3 \times 10^{-5} \text{ s}^{-1} \text{ pixel}^{-1}$ flux density contour from the (0.5–2) keV X-ray band image (on the facing page) is also shown.

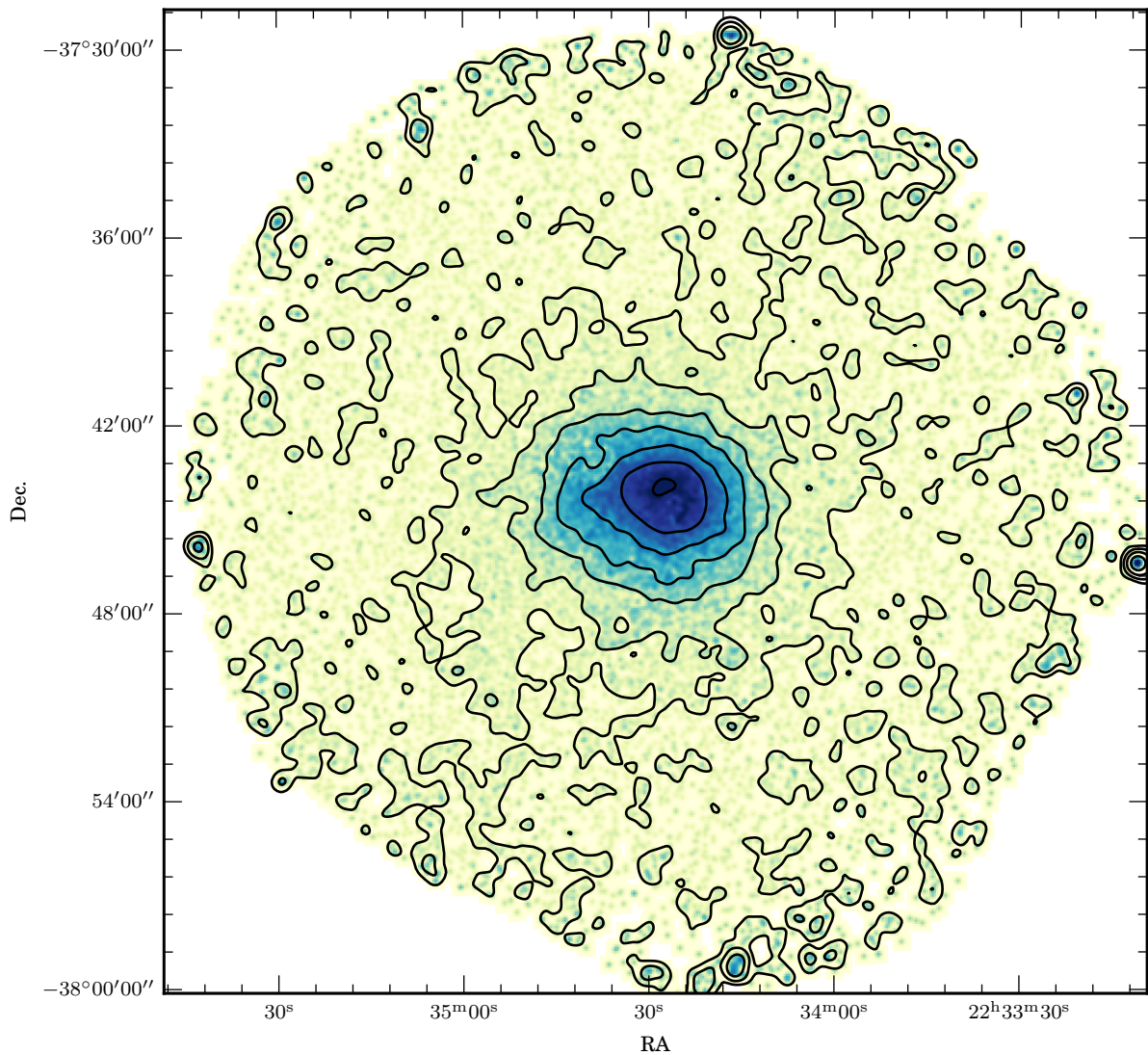


Figure A.25: X-ray flux density map of RXC J2234.5–3744 in the (0.5–2) keV band. The lowest contour is at $3 \times 10^{-5} \text{ s}^{-1} \text{ pixel}^{-1}$ and subsequent contours represent a $2\times$ increase in flux density. The pixel size is $4'' \times 4''$.

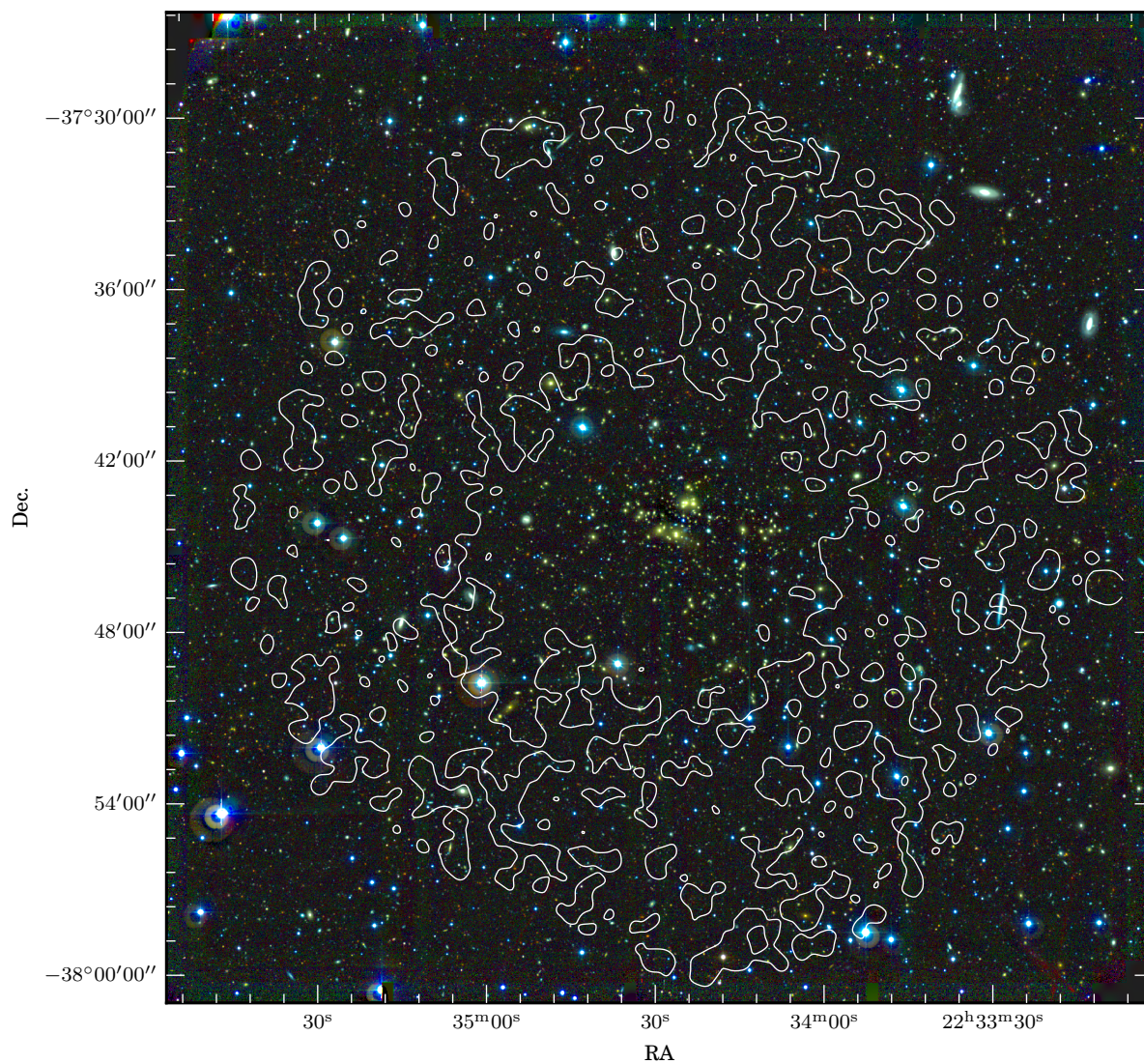


Figure A.26: Optical image of RXC J2234.5–3744 where the WFI@2.2m R_c , V and B bands are mapped to the red, green and blue channels respectively. The $3 \times 10^{-5} \text{ s}^{-1} \text{ pixel}^{-1}$ flux density contour from the (0.5–2) keV X-ray band image (on the facing page) is also shown.

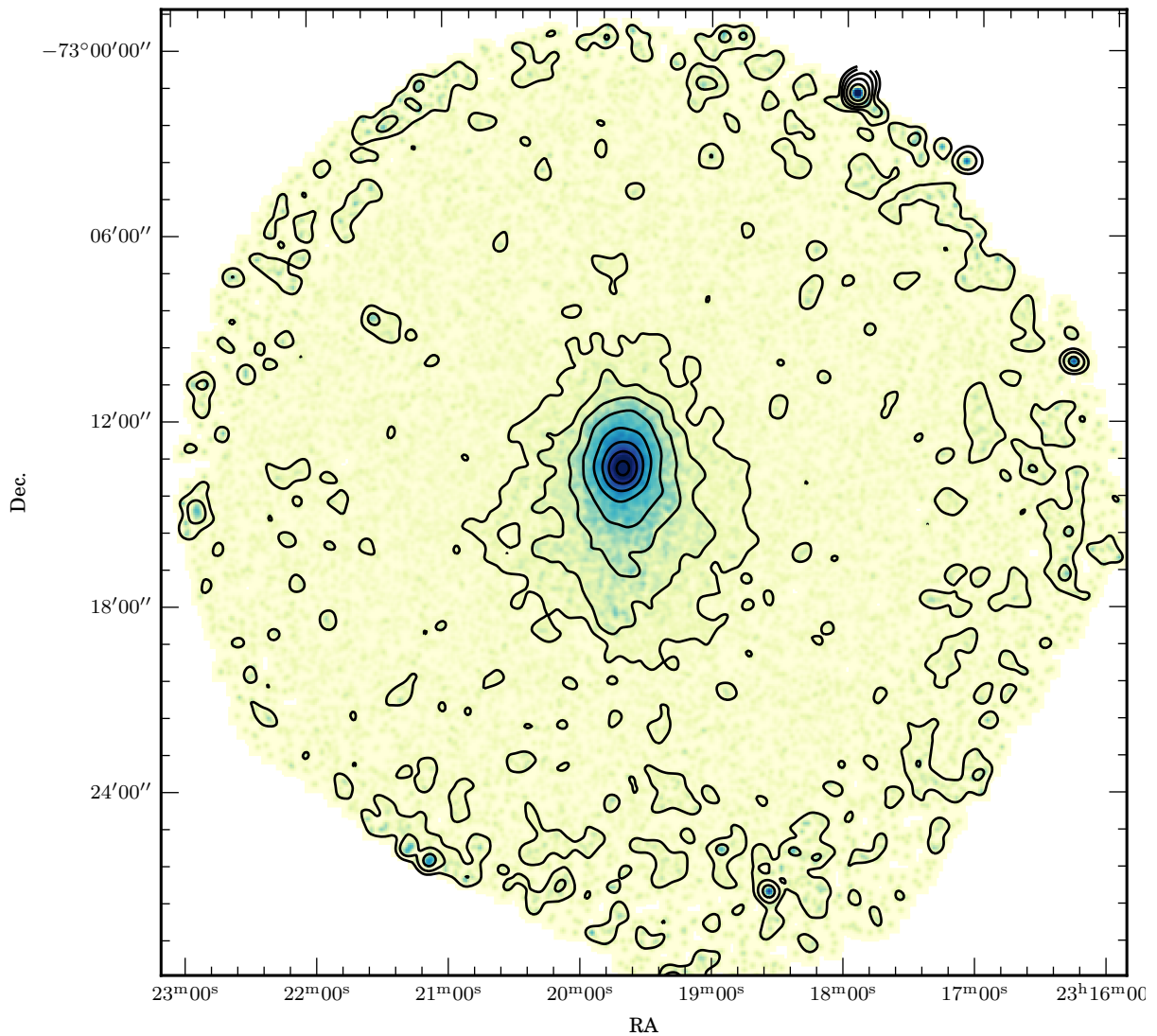


Figure A.27: X-ray flux density map of RXC J2319.6-7313 in the (0.5–2) keV band. The lowest contour is at $3 \times 10^{-5} \text{ s}^{-1} \text{ pixel}^{-1}$ and subsequent contours represent a $2\times$ increase in flux density. The pixel size is $4'' \times 4''$.

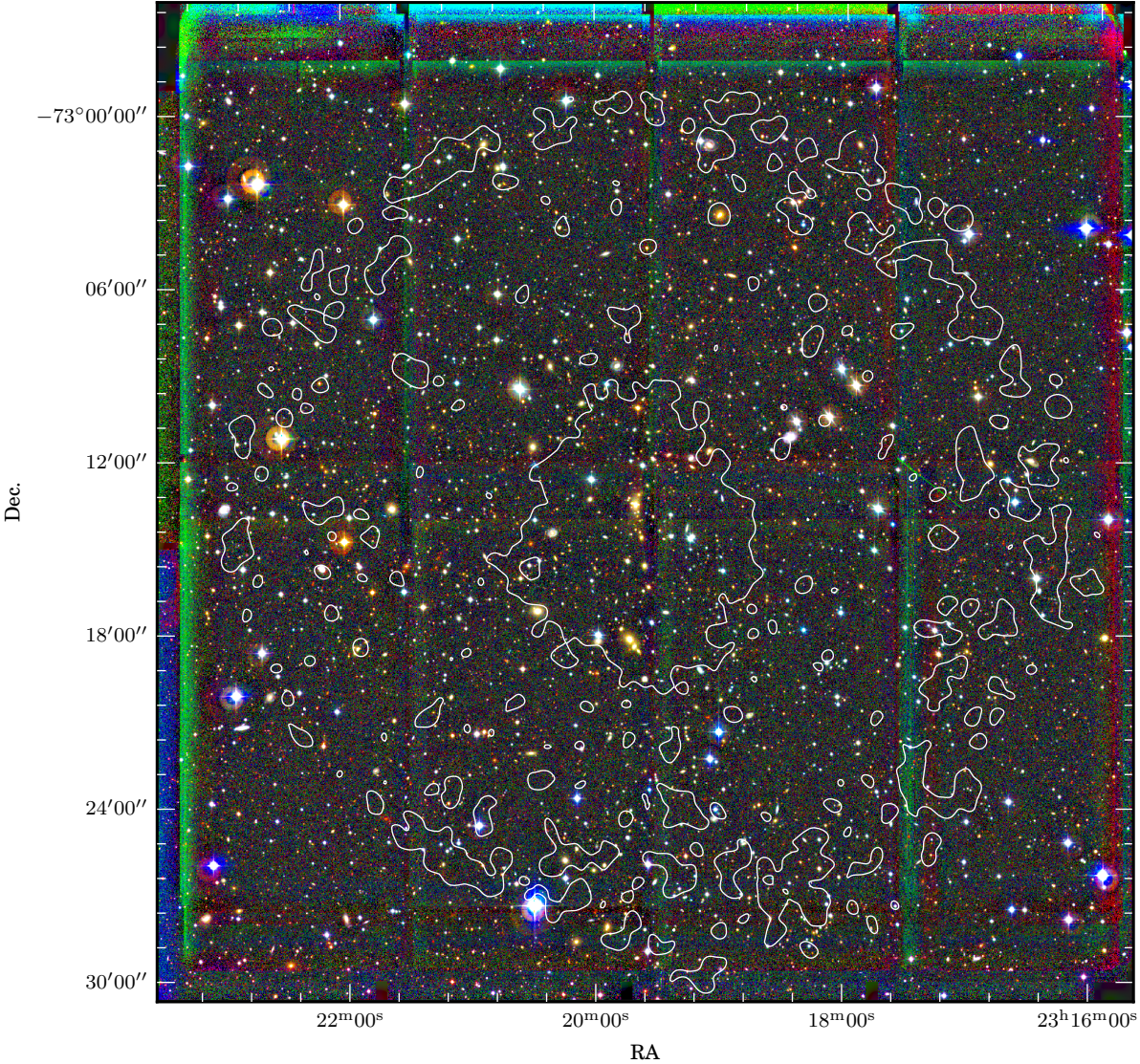


Figure A.28: Optical image of RXC J2319.6-7313 where the WFI@2.2m R_c , V and B bands are mapped to the red, green and blue channels respectively. The $3 \times 10^{-5} \text{ s}^{-1} \text{ pixel}^{-1}$ flux density contour from the (0.5-2) keV X-ray band image (on the facing page) is also shown.

Appendix B

SEXTRACTOR parameters

The parameters used in the SEXTRACTOR analysis of the cluster images are listed here.

```
# Configuration file for SExtractor 2.8.6

# We found that many SExtractor parameters were best set on an
# image-by-image basis, and are marked [image].
# The recipes used to calculate these are described in the
# following sections. These parameters were passed
# as command line arguments.
# Other parameters could be set globally. These are described below.
# For parameters not listed here, the defaults were used.

# The best approach by far is to simulate images of galaxies, and then try to
# run your analysis pipeline on those, checking that the results are as
# expected.
# Only then should you try to run the analysis on anything real. Real data
# has features you will not be able to simulate, and it's best to deal with
# those features independently, as far as possible.
# Simulations could be done using the Astromatic 'Skymaker' software package.
# I cannot stress this point enough.

#----- Catalog -----
CATALOG_TYPE      FITS_LDAC      # We found that FITS formats were the
# the easiest to deal with. They encapsulate
# all of the necessary metadata, and handle
# multi-exposure fits inputs (consecutive single
# frames of the same target, or multi chip data,
# e.g. from WFI@2.2)
# The only viable alternative is VOTABLE.

#----- Extraction -----
DETECT_TYPE       CCD           # CCD (linear) or PHOTO (with gamma correction)
DETECT_MINAREA    5             # minimum number of pixels above threshold
THRESH_TYPE       RELATIVE      # threshold type: RELATIVE (in sigmas)
# or ABSOLUTE (in ADUs)

DETECT_THRESH     2.0           # <sigmas> or <threshold>,<ZP> in mag.arcsec-2
# This threshold is active on the
# detection image.

ANALYSIS_THRESH   1.0           # <sigmas> or <threshold>,<ZP> in mag.arcsec-2
# This threshold is active on the
# measurement image, and is therefore necessarily
# lower than the more sensitive detection image.
```

```

# If this parameter set higher, then most
# objects aren't assigned FWHMs or
# stellarity classes.

FILTER          Y          # apply filter for detection (Y or N)?

FILTER_NAME     [image]   # Individual filters were generated
# for each detection image. These are the
# same shape as the point spread function.
# This suppresses background noise, because
# the noise varies on scales shorter than the PSF.
# This PSF filter effectively increases the signal
# from point sources.

DEBLEND_NTHRESH 32       # Number of deblending sub-thresholds
DEBLEND_MINCONT 0.00005  # Minimum contrast parameter for deblending
# We found that some objects were missed when
# the de-blending contrast threshold
# was the default of 0.005.

CLEAN          Y          # Clean spurious detections? (Y or N)?
CLEAN_PARAM    2.0       # Cleaning efficiency
# We increased this from the default value of 1.0.

MASK_TYPE      CORRECT   # type of detection MASKing: can be one of
# NONE, BLANK or CORRECT

#----- WEIGHTing -----

# Each WFI image was accompanied by an exposure map, showing the
# total exposure time in seconds at each image pixel.
# These are effectively gain maps. They were used for both
# detection and measurement images in double image mode;
# in single image mode (for example when measuring PSF)
# WEIGHT_TYPE=MAP_WEIGHT and WEIGHT_GAIN=Y were set on the command line.

WEIGHT_TYPE     MAP_WEIGHT,MAP_WEIGHT
# type of WEIGHTing: NONE, BACKGROUND,
# MAP_RMS, MAP_VAR or MAP_WEIGHT

WEIGHT_GAIN     Y,Y      # modulate gain (E/ADU) with weights? (Y/N)
# This effectively changes weight maps to
# gain maps; given that weight maps are
# exposure maps (well approximated by flat
# fields) this is correct.
# This should be set to Y,Y for double image
# mode, and to Y for single image mode.

WEIGHT_THRESH  # weight threshold[s] for bad pixels

#----- FLAGging -----

FLAG_IMAGE      flag.fits # filename for an input FLAG-image
FLAG_TYPE       OR        # flag pixel combination: OR, AND, MIN, MAX
# or MOST

#----- Photometry -----

# The photometry parameters for MAG_AUTO were
# left as their default values.
PHOT_AUTOPARAMS 2.5, 3.5 # MAG_AUTO parameters: <Kron_fact>,<min_radius>

PHOT_AUTOAPERS  0.0,0.0  # <estimation>,<measurement> minimum apertures
# for MAG_AUTO and MAG_PETRO

SATUR_LEVEL     0.0      # level (in ADUs) at which saturation arises

```

```

SATUR_KEY          SATURATE      # keyword for saturation level (in ADUs)
                               # The value of this parameter gives the SATUR_LEVEL.
                               # This is not equal to the absolute WFI saturation
                               # value due to the full well capacity (>200k e-) and
                               # the analogue-digital conversion (2.0 e-/ADU)
                               # because the images are short exposures which are
                               # stacked, increasing the maximum value
                               # before saturation.

MAG_ZEROPPOINT     0.0           # magnitude zero-point
                               # We handled the zero point in post-measurement
                               # analysis of the catalogues, rather than here, as the
                               # zero point is dependent on the calibration,
                               # and no calibration data were available for the
                               # REXCESS WFI data. We bootstrapped the zero point
                               # from the data themselves.

GAIN                [image]      # detector gain in e-/ADU
                               # 0.0 = infinite gain
                               # This is set in conjunction with the
                               # normalisation of the weight maps.
                               # Although the detector has a known gain of
                               # 2.0 e-/ADU, stacking, flat fielding etc. modifies
                               # the relationship between the final value in the image
                               # (ADU) and the number of electrons which needed to be
                               # liberated to reach it.

GAIN_KEY           GAIN          # keyword for detector gain in e-/ADU
PIXEL_SCALE        0            # size of pixel in arcsec (0=use FITS WCS info)
                               # For WFI images, the pixel scale is constant,
                               # set by the f/5.9 focal reducer of the WFI camera.
                               # Because this parameter is set in the image headers,
                               # there's no need to set it here.

#----- Star/Galaxy Separation -----#

SEEING_FWHM        [image]      # stellar FWHM in arcsec
                               # We measured the FWHM automatically for each
                               # image, and set it in the command line.
                               # On WFI images under good conditions,
                               # you can just take a histogram in FWHM space.
                               # The largest peak in the 0.4-3.0 arcsecond region
                               # is almost always the correct value.
                               # A more robust method is to:
                               # find the point source saturation limit Mlim
                               # by inspecting the FWHM-magnitude diagram,
                               # select all objects with magnitudes between that and
                               # Mlim + [a few --- could use 4]
                               # and then find the largest peak in that histogram.
                               # The saturation limit goes to brighter magnitudes
                               # with worsening seeing, so calibrating the
                               # limit under conditions of good seeing gives a
                               # reasonable global value.

#----- Background -----#

BACK_TYPE          AUTO         # AUTO or MANUAL
BACK_SIZE          32          # Background mesh: <size> or <width>,<height>
BACK_FILTERSIZE    3           # Background filter: <size> or <width>,<height>
                               # The value BACK_SIZE * BACK_FILTERSIZE gives the
                               # scale on which the background is sampled
                               # and must be half the scale of the smallest
                               # feature the background map has to characterise.
                               # We investigated much larger background sizes
                               # (BACK_SIZE~128, BACK_FILTERSIZE~5) which subtracted

```

```
# less of the intracluster light, but found that this
# would also allow fairly well defined, compact
# galaxies to extend to very large sizes, because the
# background level remained quite high.
# A double-pass approach is better — handle the obvious
# objects first, with a small filter size,
# remove those objects using an image mask,
# and then characterise the larger scale features
# using a larger filter scale.

BACKPHOTO_TYPE    LOCAL    # can be GLOBAL or LOCAL
                  # On wide field images, the background level can exhibit
                  # a lot of variability.
BACKPHOTO_THICK   24       # thickness of the background LOCAL annulus
BACK_FILTTHRESH   0.0     # Threshold above which the background-
                  # map filter operates

#----- Check Image -----
# Check images should always be inspected.

#----- ASSOCIation -----
# All catalogue matching and mixing was done using other tools.
```

Appendix C

Additional galaxy distribution structural analysis examples

C.1 2D point distribution smoothing examples

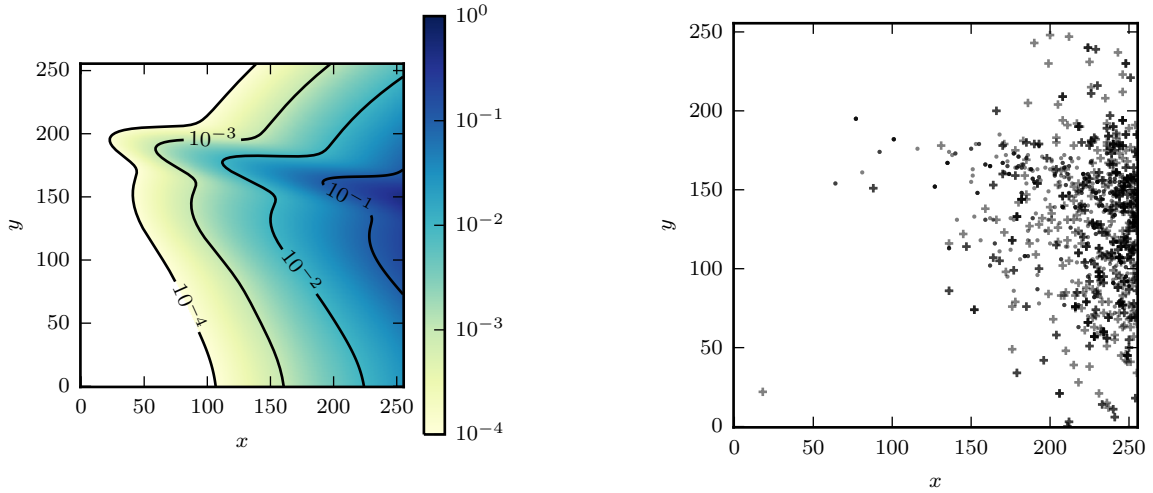
We ran additional tests of the smoothing analyses shown in Section §3.1 on a red sequence plus blue cloud model.

In Section §3.3.1.2, we outlined a red sequence detection method which disregards data about the magnitude of galaxies during the critical clipping stage. By re-introducing the magnitude information – the luminosity function of galaxies – we can make a full 2D model of the red sequence and blue cloud of clusters. After transforming the Schechter function Φ into magnitude space the density of galaxies in colour–magnitude space is given by $\Psi(C_{\text{residual}})\Phi(M)$. A simplified field galaxy distribution can be generated using the interpolated number counts function ξ_{Metcalfe} described in Section §4.3.3.1, multiplied by a broad Gaussian. The model was used to generate the colour–magnitude density diagram shown in Figure C.1b. It has an identical total expectation value $n_t = 2^{10}$ to the distribution used in Section §3.1, but has no compact component and has a much stronger background level variation due to the galaxy number counts distribution discussed in Section §1.3.2.3. This was used to generate the point catalogue shown in Figure C.1b. These points are smoothed by the algorithms described in Section §3.1. Comparable difference maps Σ and Υ as defined in Equations 3.1 and 3.2 are shown in Figure C.2a and Figure C.2b.

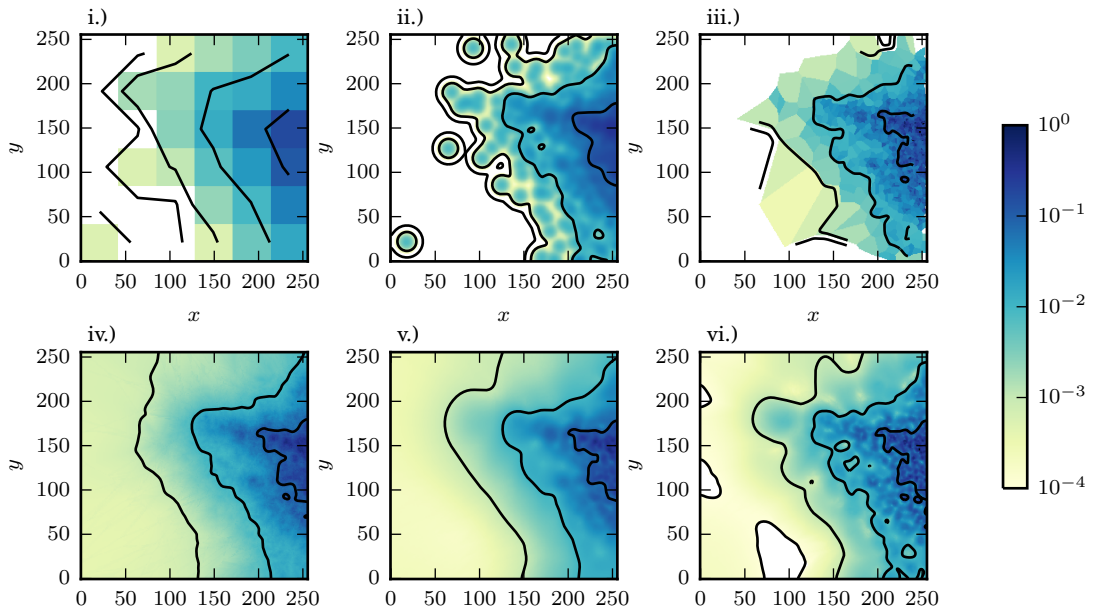
C.2 Additional background subtraction examples

We ran additional tests of background subtraction methods discussed in Sections 3.1 and 3.2 on the blue cloud model described in Section §C.1.

The results of running the stochastic point removal algorithm described in Section §3.2.1 with a perfect background model are shown in Figure C.3. Several background points in the regions $x < 50$, $y < 50$ and $y > 200$ are missed by the algorithm. The num-

(a) Input density distribution ω .

(b) Simulated point distribution based on Figure C.1a.



(c) Smoothed versions of Figure C.1b using different algorithms: i.) fixed bin histogram; ii.) fixed aperture smoothing; iii.) Voronoi tessellation; iv.) adaptive top-hat filter with $\text{SNR}_t = 5$; v.) adaptive Gaussian with $\text{SNR}_t = 5$; vi.) adaptive Gaussian with $\text{SNR}_t = \sqrt{8}$. The contour levels correspond with the levels shown in Figure C.1a.

Figure C.1: Point distribution and smoothing results for a simulated colour–magnitude diagram.

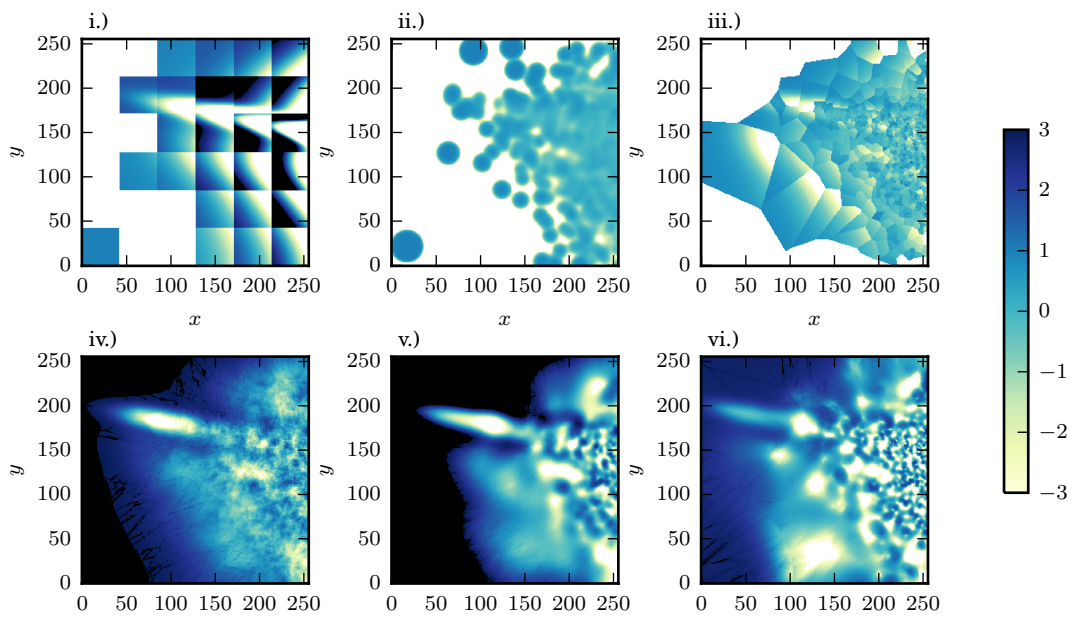
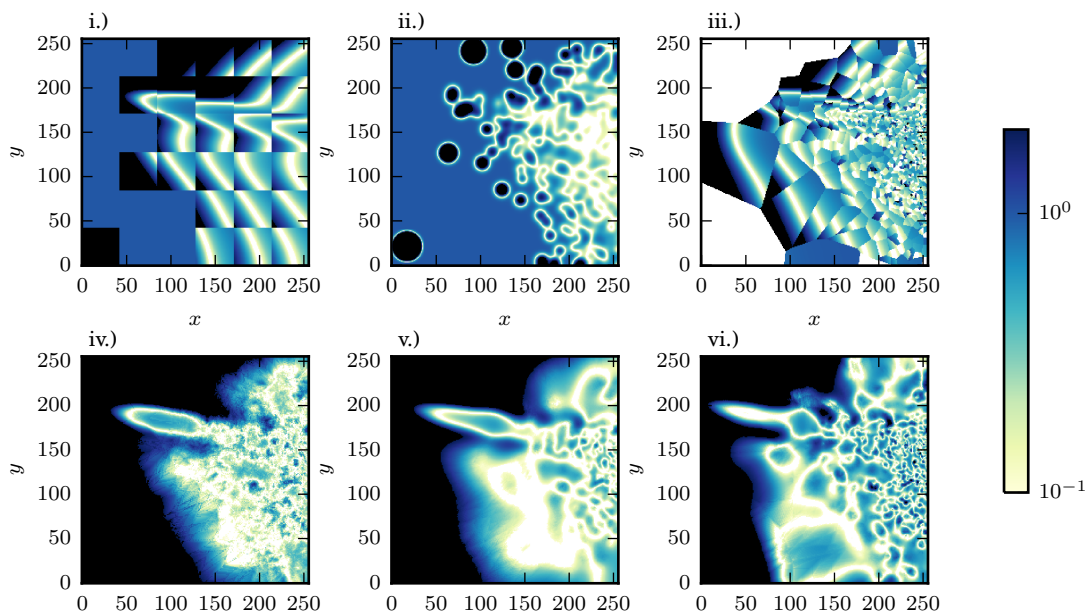
(a) Σ difference maps in units of the smoothed density map uncertainty [defined in Equation (3.1)].(b) Υ absolute difference maps in units of the original density map value [defined in Equation (3.2)].

Figure C.2: Differences between original input density from Figure C.1a and the smoothed density map results from Figure C.1c. Values above and below the colour range shown in the colour bar are shown as black and white respectively.

ber counts function component of the background distribution which was introduced in Section §1.3.2.3 leads to a much stronger background variation in the colour–magnitude diagram than when looking at the galaxy spatial distribution. The stronger variation in background level in this case leads to the complete removal of all points $x < 225$ if the background is modelled incorrectly as a uniform distribution.

The results of running the target probability estimation algorithm described in Section §3.2.2 under ideal conditions with perfect target and background density maps are shown in Figure C.4. The results highlight the issue noted in Section §3.2.2 – P_t for individual points is not a particularly valuable parameter; it is the overall distribution of P_t across points in high and low density regions of the field which reveals the density structure of the target object.

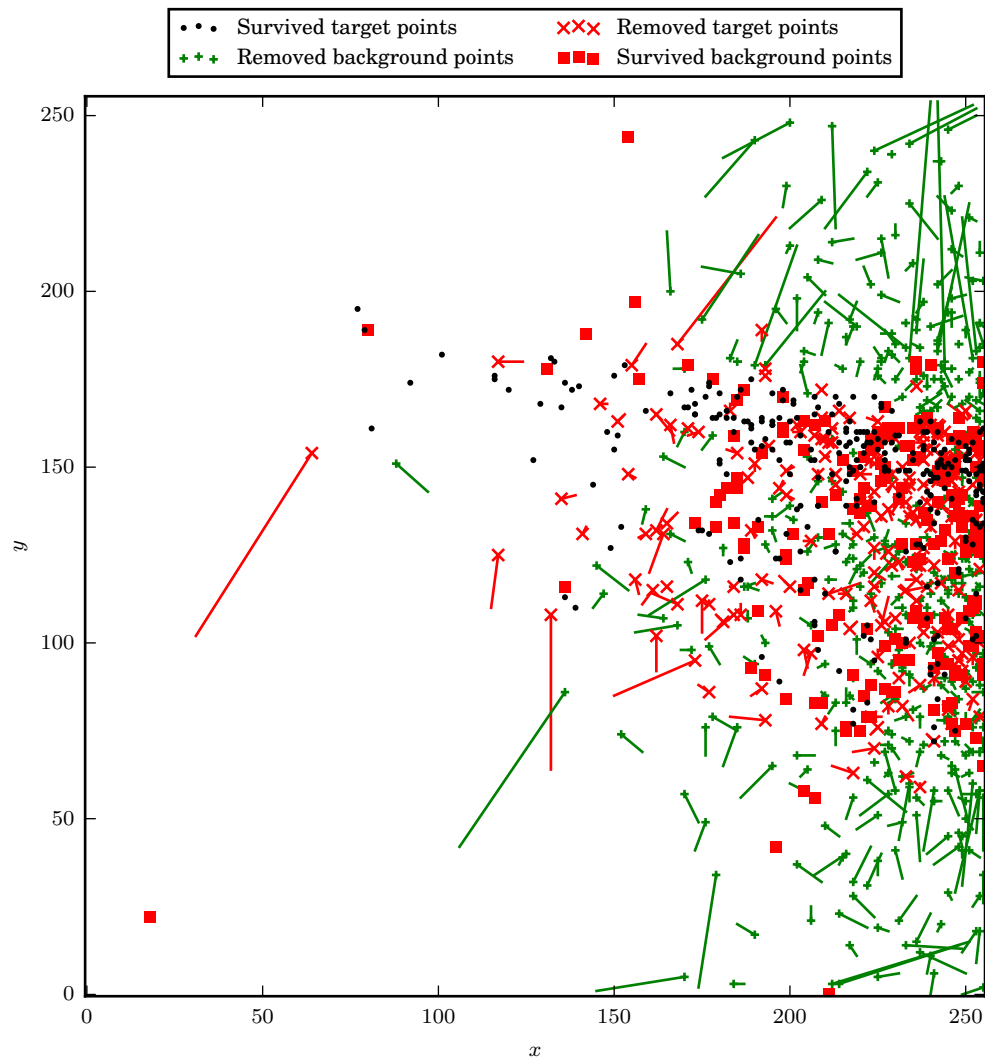


Figure C.3: Stochastic point removal applied to the point distribution shown in Figure C.1b, using background points derived from a perfect background map. The details are as in Figure 3.4.

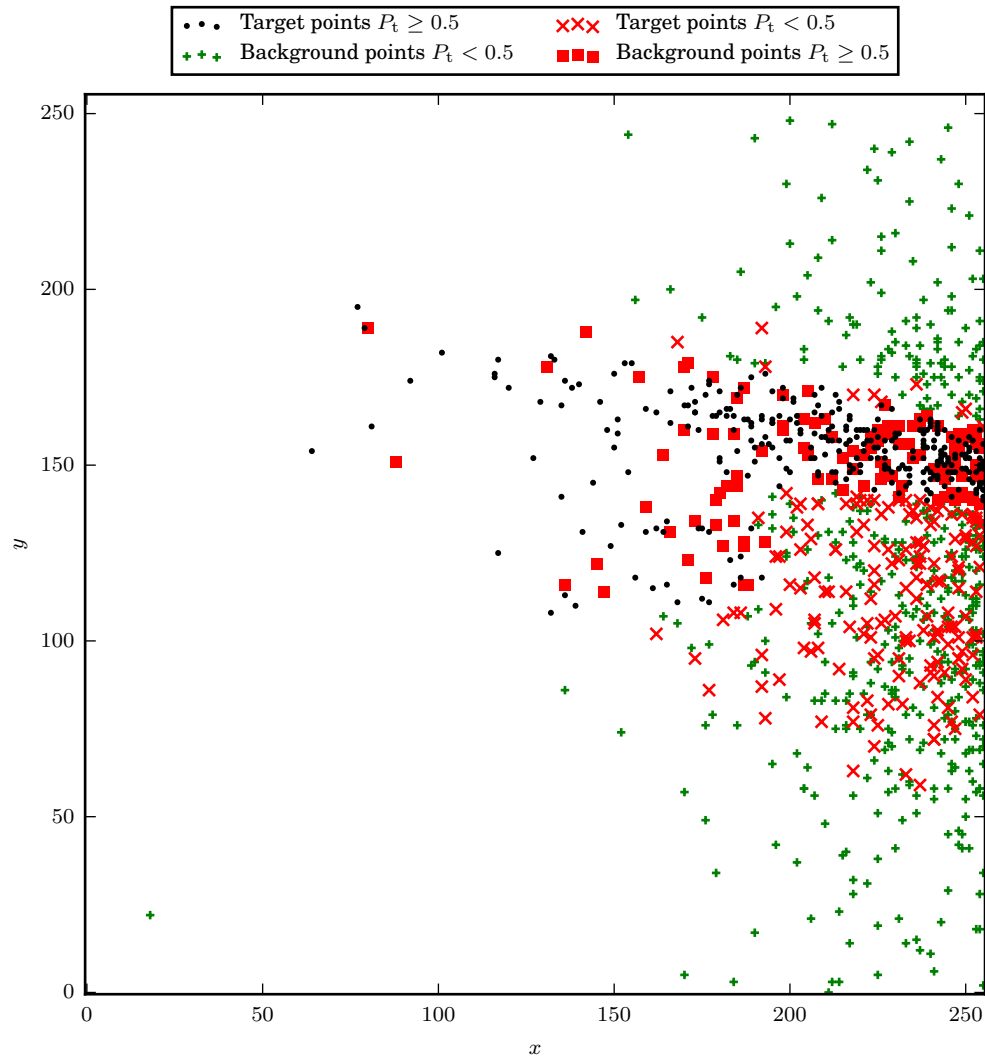


Figure C.4: Membership probability estimates for the point distribution shown in Figure C.1b. Probabilities are calculated using Equation (3.5), and the target and background densities used are identical to those used to generate the point data.

Appendix D

Additional plots and tables for Chapter 4

D.1 Additional figures

Figure D.1, Figure D.2, Figure D.3 and Figure D.4 show R_c band images of a selection of our targets, where the stars have been excised from the images.

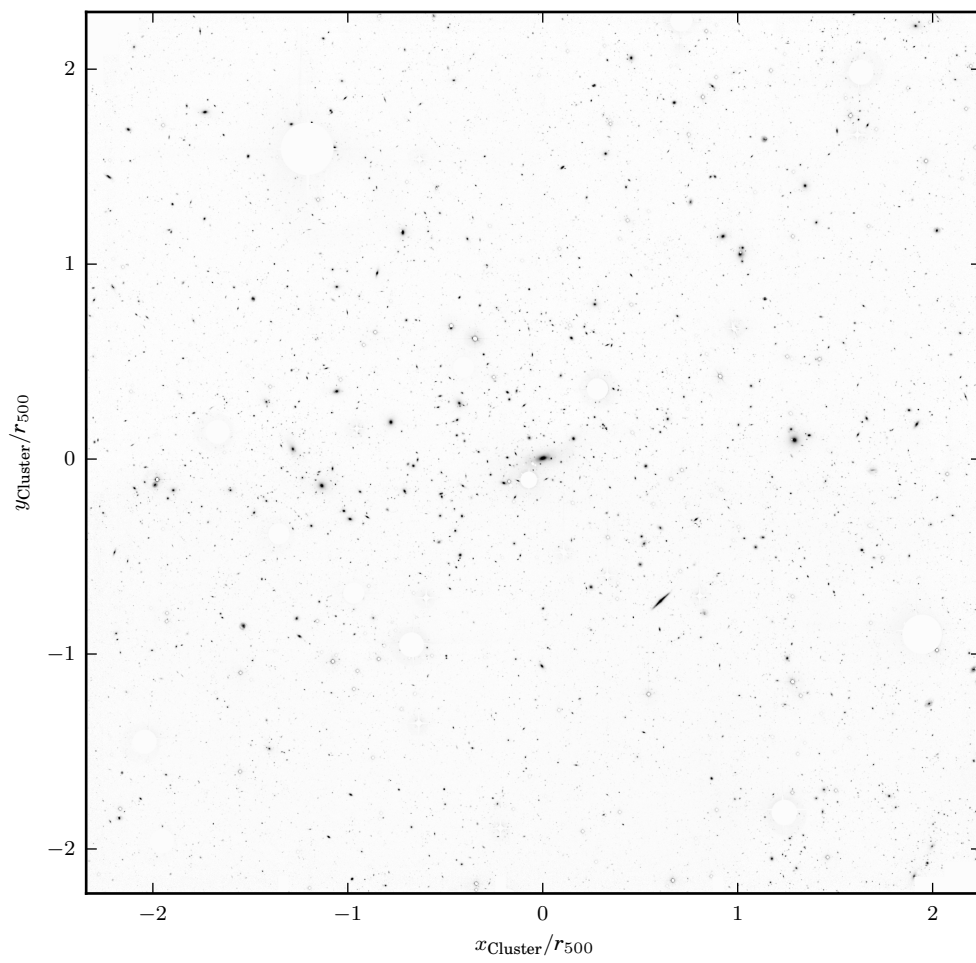


Figure D.1: RXC J0006.0–3443 in the R_c band. Stars have been excised from this image.

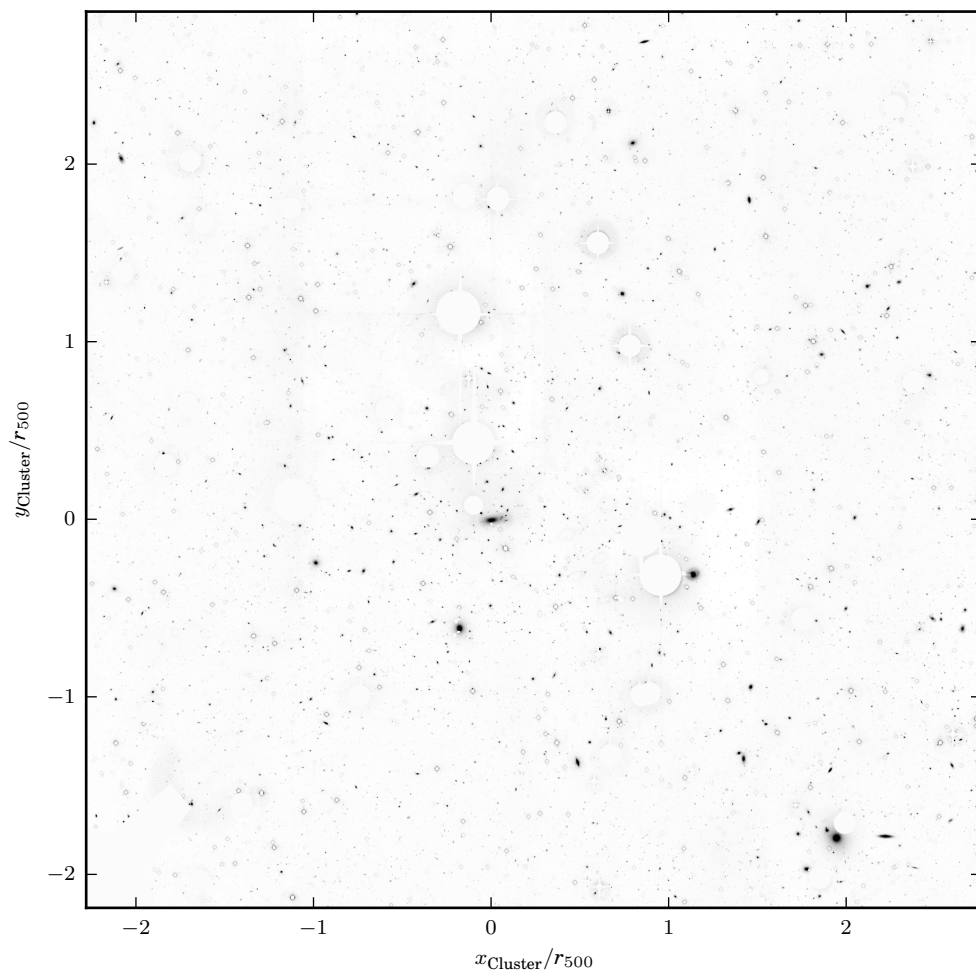


Figure D.2: RXC J0616.8–4748 in the R_c band. Stars have been excised from this image.

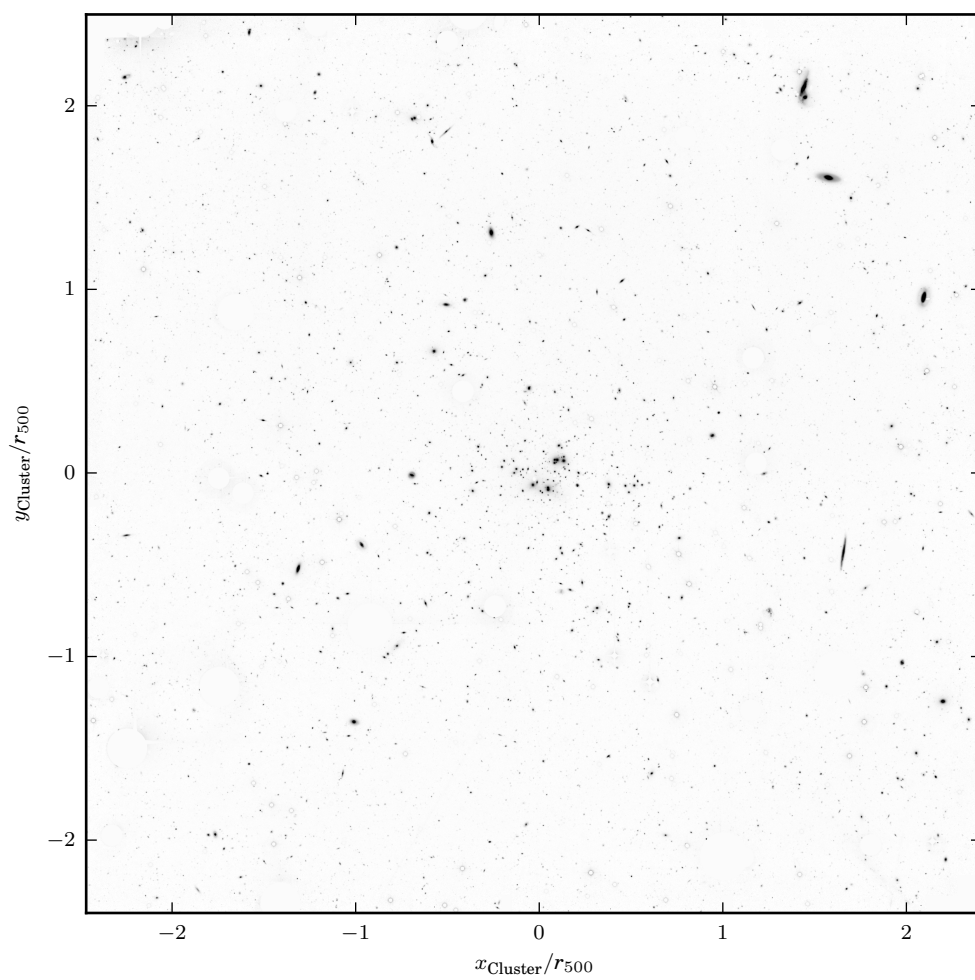


Figure D.3: RXC J2234.5–3744 in the R_c band. Stars have been excised from this image.

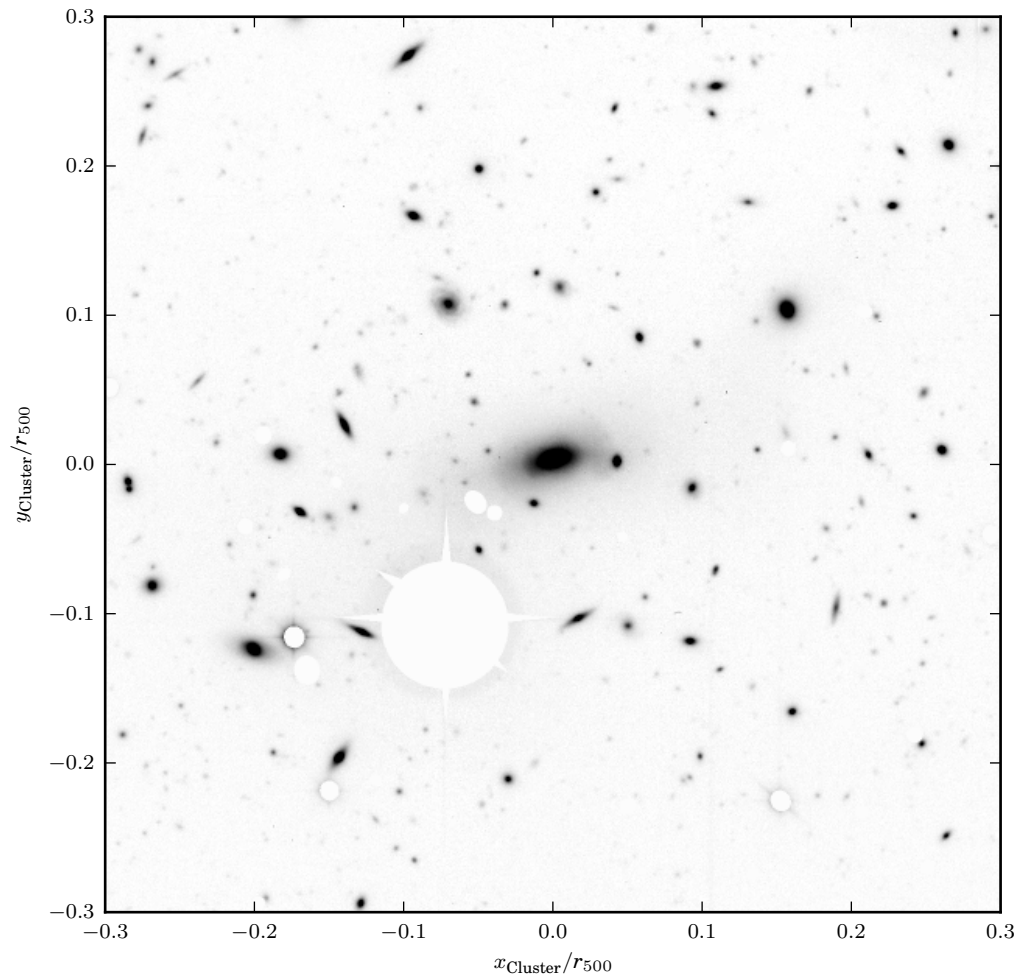
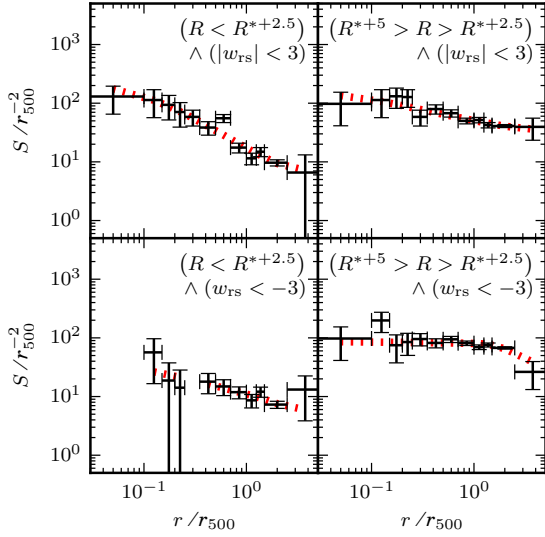


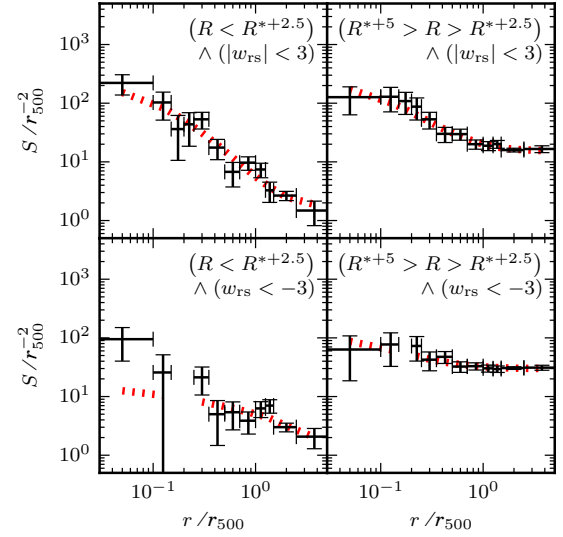
Figure D.4: The centre of RXC J0006.0-3443 in the R_c band. Stars have been excised from this image.

D.2 Individual cluster radial profiles

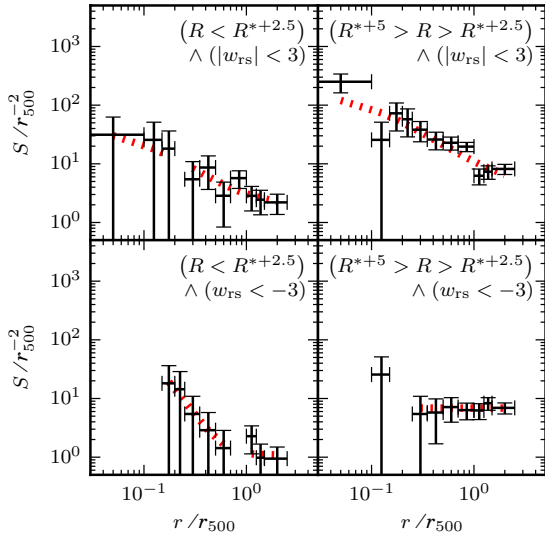
Figures D.5 to D.8 show radial count density profiles and best fitting models, before background subtraction, of individual clusters in the REXCESS sample. The best fitting radial profile parameters for each galaxy population in individual clusters in the REXCESS sample are given in Table D.1.



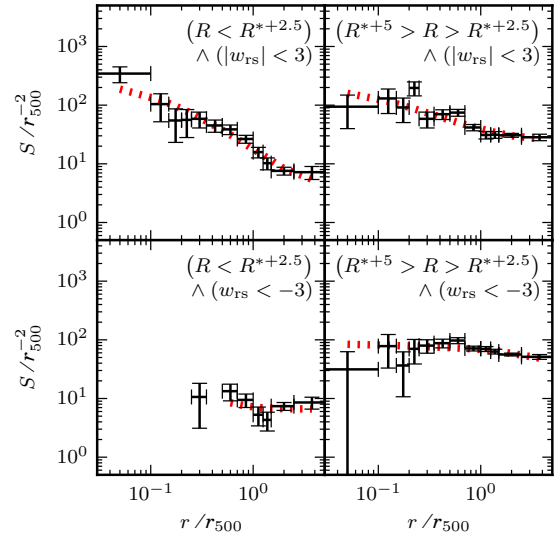
(a) Radial density profiles for RXC J0006.0-3443.



(b) Radial density profiles for RXC J0049.4-2931.

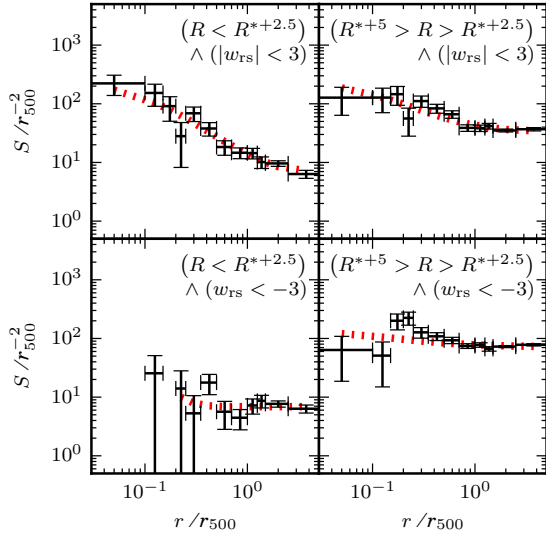


(c) Radial density profiles for RXC J0345.7-4112.

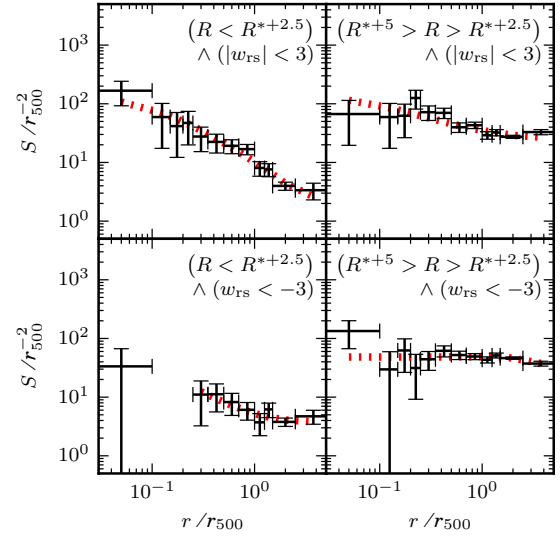


(d) Radial density profiles for RXC J0547.6-3152.

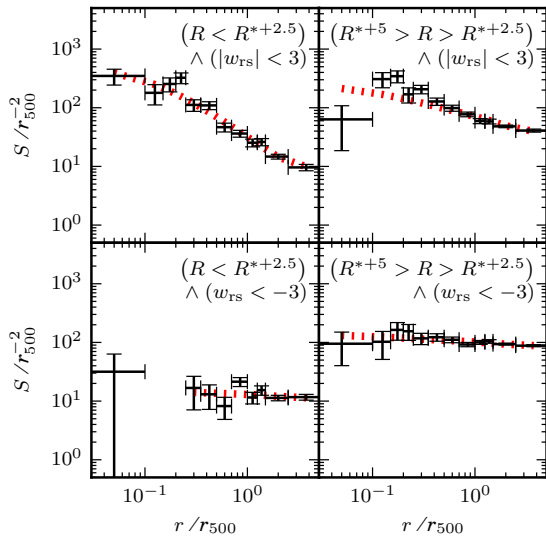
Figure D.5: Individual radial density profiles. The points with uncertainties represent the galaxy count density profile, normalised by r_{500}^2 , and the red dashed line is the best fitting model with parameters given in Table D.1.



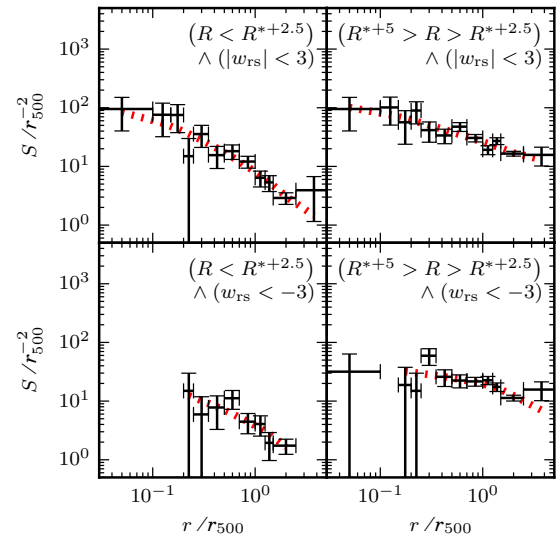
(a) Radial density profiles for RXC J0605.8–3518.



(b) Radial density profiles for RXC J0616.8–4748.

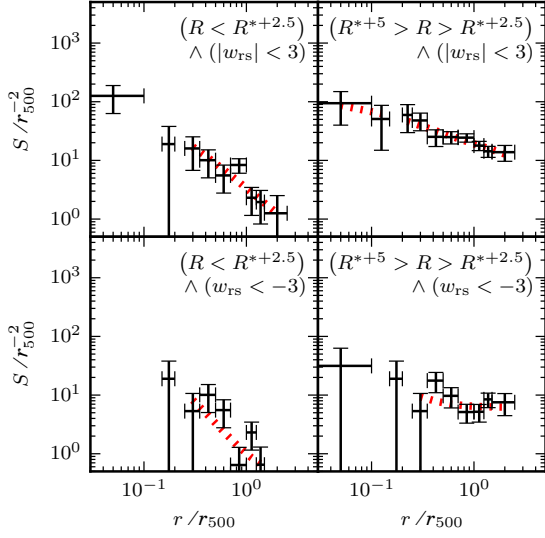


(c) Radial density profiles for RXC J0645.4–5413.

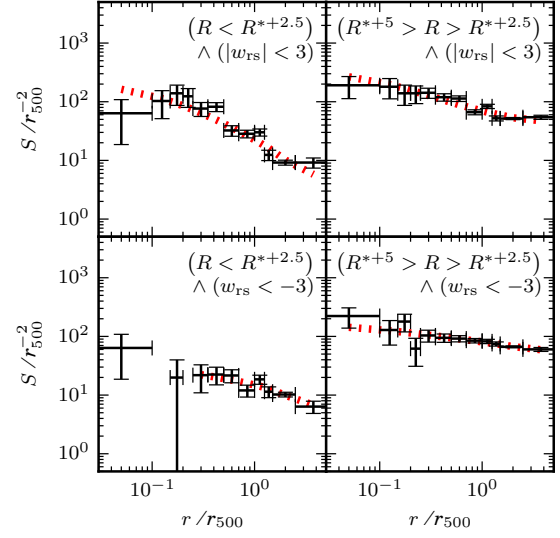


(d) Radial density profiles for RXC J0821.8+0112.

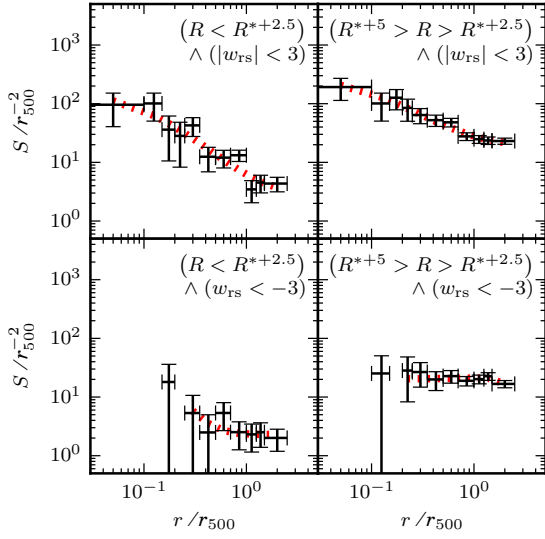
Figure D.6: Individual radial density profiles. The lines are as described in Figure D.5.



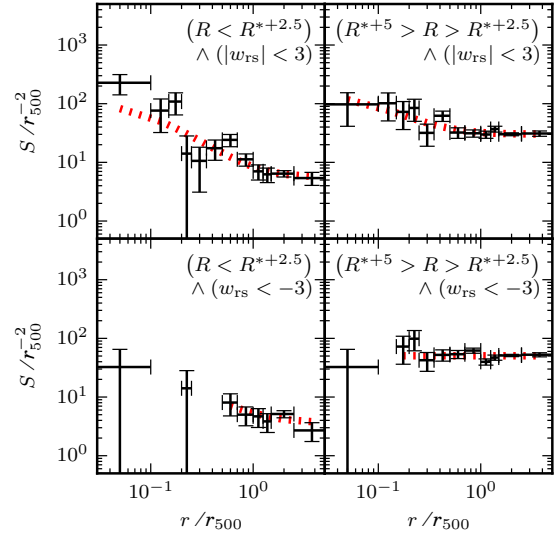
(a) Radial density profiles for RXC J2023.0–2056.



(b) Radial density profiles for RXC J2048.1–1750.

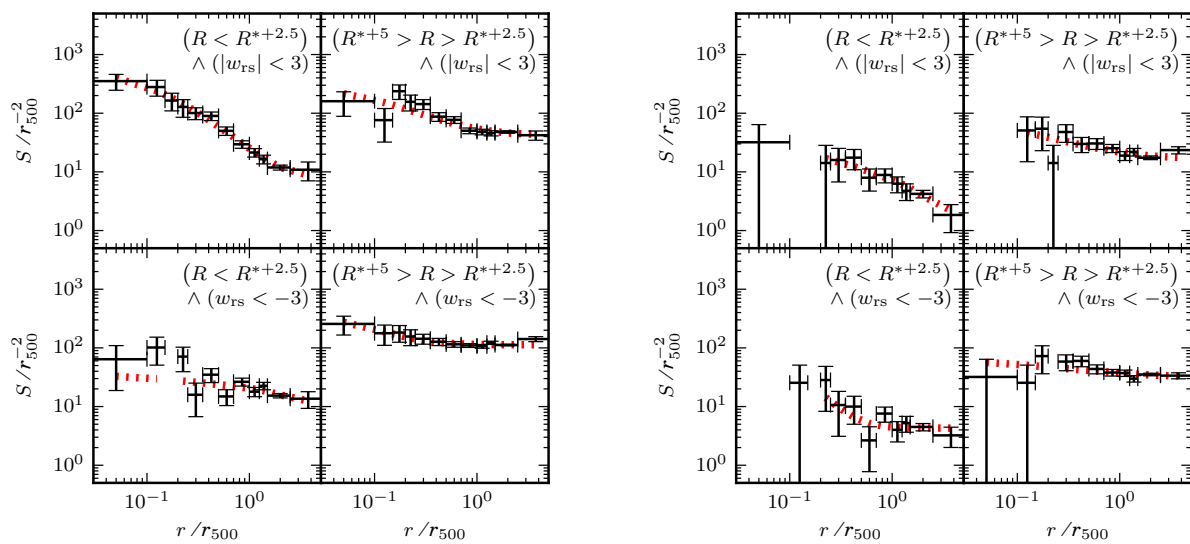


(c) Radial density profiles for RXC J2129.8–5048.



(d) Radial density profiles for RXC J2218.6–3853.

Figure D.7: Individual radial density profiles. The lines are as described in Figure D.5.



(a) Radial density profiles for RXC J2234.5–3744.

(b) Radial density profiles for RXC J2319.6–7313.

Figure D.8: Individual radial density profiles. The lines are as described in Figure D.5.

Table D.1: NFW fitting results for individual clusters.

Object	Galaxy filter	β	S_0 r_{500}^{-3}	S_{bgNFW} r_{500}^{-2}
RXC J0006.0–3443	Bright, red	2.7 ± 0.5	49.7 ± 9.0	7.2 ± 2.1
RXC J0049.4–2931	Bright, red	3.4 ± 0.4	60.2 ± 10.7	1.9 ± 0.5
RXC J0345.7–4112	Bright, red	3.0 ± 0.9	10.5 ± 3.3	2.1 ± 0.6
RXC J0547.6–3152	Bright, red	2.65 ± 0.34	50.7 ± 6.7	5.5 ± 1.4
RXC J0605.8–3518	Bright, red	3.1 ± 0.4	54.9 ± 8.8	7.2 ± 0.8
RXC J0616.8–4748	Bright, red	2.54 ± 0.28	29.2 ± 3.5	2.6 ± 0.6
RXC J0645.4–5413	Bright, red	2.87 ± 0.26	112.3 ± 12.9	9.9 ± 1.3
RXC J0821.8+0112	Bright, red	2.4 ± 0.4	22.5 ± 3.4	1.4 ± 0.9
RXC J2023.0–2056	Bright, red	3.0 ± 0.8	26.6 ± 6.6	0.8 ± 1.2
RXC J2048.1–1750	Bright, red	2.2 ± 0.4	37.0 ± 7.6	5.8 ± 2.2
RXC J2129.8–5048	Bright, red	3.3 ± 0.7	41.8 ± 10.3	3.2 ± 1.4
RXC J2218.6–3853	Bright, red	3.3 ± 1.1	26.7 ± 8.9	5.8 ± 1.1
RXC J2234.5–3744	Bright, red	3.13 ± 0.15	125.8 ± 6.7	8.8 ± 0.9
RXC J2319.6–7313	Bright, red	1.6 ± 0.4	4.5 ± 0.9	2.2 ± 0.5
RXC J0006.0–3443	Faint, red	1.9 ± 0.5	20.1 ± 3.4	36.2 ± 3.4
RXC J0049.4–2931	Faint, red	3.24 ± 0.33	59.7 ± 7.5	15.5 ± 0.8
RXC J0345.7–4112	Faint, red	2.7 ± 0.8	38.6 ± 11.4	5.4 ± 2.9
RXC J0547.6–3152	Faint, red	2.3 ± 0.6	32.5 ± 7.5	26.7 ± 3.4
RXC J0605.8–3518	Faint, red	2.8 ± 0.6	45.6 ± 10.4	34.6 ± 2.1
RXC J0616.8–4748	Faint, red	2.3 ± 0.7	22.0 ± 6.4	26.9 ± 2.5
RXC J0645.4–5413	Faint, red	1.8 ± 0.5	31.3 ± 7.2	39.4 ± 4.1
RXC J0821.8+0112	Faint, red	1.8 ± 0.5	18.1 ± 3.6	13.1 ± 2.9
RXC J2023.0–2056	Faint, red	2.1 ± 0.5	18.0 ± 3.1	10.5 ± 3.2
RXC J2048.1–1750	Faint, red	2.3 ± 0.5	52.2 ± 10.4	47.4 ± 4.3
RXC J2129.8–5048	Faint, red	2.93 ± 0.34	62.7 ± 7.7	20.1 ± 2.0
RXC J2218.6–3853	Faint, red	3.6 ± 1.2	34.0 ± 13.8	30.4 ± 1.6
RXC J2234.5–3744	Faint, red	2.8 ± 0.7	49.0 ± 12.5	43.6 ± 3.9
RXC J2319.6–7313	Faint, red	2.3 ± 1.3	11.2 ± 4.8	17.6 ± 2.1
RXC J0006.0–3443	Bright, blue	1.7 ± 0.9	4.9 ± 1.4	5.9 ± 1.7
RXC J0049.4–2931	Bright, blue	1.2 ± 1.2	1.4 ± 0.9	2.0 ± 0.8
RXC J0345.7–4112	Bright, blue	5.9 ± 1.7	$(1.1 \pm 0.5) \times 10^2$	1.09 ± 0.20
RXC J0547.6–3152	Bright, blue	4.2 ± 6.4	22.0 ± 34.6	6.6 ± 1.4
RXC J0605.8–3518	Bright, blue	9.6 ± 14.3	$(1.5 \pm 3.0) \times 10^2$	6.9 ± 0.6
RXC J0616.8–4748	Bright, blue	3.0 ± 0.8	11.8 ± 3.6	3.8 ± 0.5
RXC J0645.4–5413	Bright, blue	0.9 ± 4.7	0.4 ± 1.0	11.4 ± 1.6
RXC J0821.8+0112	Bright, blue	2.0 ± 0.9	5.2 ± 1.7	0.8 ± 1.0
RXC J2023.0–2056	Bright, blue	4.1 ± 2.5	33.9 ± 21.7	0.4 ± 1.2
RXC J2048.1–1750	Bright, blue	1.1 ± 0.6	3.2 ± 1.0	6.8 ± 1.2
RXC J2129.8–5048	Bright, blue	6.2 ± 2.9	$(7.2 \pm 5.3) \times 10^1$	2.29 ± 0.29
RXC J2218.6–3853	Bright, blue	2.7 ± 1.2	7.1 ± 4.1	3.8 ± 0.6
RXC J2234.5–3744	Bright, blue	0.9 ± 1.6	2.1 ± 1.2	12.4 ± 4.3
RXC J2319.6–7313	Bright, blue	5.2 ± 2.5	53.4 ± 32.3	4.3 ± 0.5
RXC J0006.0–3443	Faint, blue	-0.5 ± 0.6	1.02 ± 0.30	38.7 ± 10.8
RXC J0049.4–2931	Faint, blue	3.0 ± 0.7	20.0 ± 5.5	30.0 ± 0.9
RXC J0345.7–4112	Faint, blue	20.0 ± 12.8	$(0.0 \pm 1.7) \times 10^6$	6.86 ± 0.35
RXC J0547.6–3152	Faint, blue	0.3 ± 0.8	2.3 ± 1.0	48.7 ± 5.3
RXC J0605.8–3518	Faint, blue	2.3 ± 1.9	11.5 ± 9.4	73.4 ± 4.3
RXC J0616.8–4748	Faint, blue	-1.2 ± 1.1	0.08 ± 0.06	37.5 ± 2.7

Table D.1: (continued)

Object	Galaxy filter	β	S_0 r_{500}^{-3}	S_{bgNFW} r_{500}^{-2}
RXC J0645.4-5413	Faint, blue	1.2 ± 0.7	5.5 ± 1.8	88.3 ± 2.6
RXC J0821.8+0112	Faint, blue	0.9 ± 0.7	3.2 ± 0.9	7.0 ± 3.7
RXC J2023.0-2056	Faint, blue	4.1 ± 3.2	13.8 ± 17.0	6.2 ± 1.4
RXC J2048.1-1750	Faint, blue	1.4 ± 0.4	12.2 ± 2.1	59.3 ± 2.8
RXC J2129.8-5048	Faint, blue	-1.0 ± 0.7	0.14 ± 0.04	5.6 ± 8.0
RXC J2218.6-3853	Faint, blue	3.00^1	0.00^1	50.5 ± 1.7
RXC J2234.5-3744	Faint, blue	4.6 ± 1.7	$(8.0 \pm 4.3) \times 10^1$	113.2 ± 2.8
RXC J2319.6-7313	Faint, blue	1.6 ± 1.3	4.2 ± 2.5	33.1 ± 2.7

D.3 Background count density analysis

The background count densities for all of the objects, using the four main galaxy population filters are shown in Table D.2.

Table D.2: Background count density measurements. In the case of the RXC J2023.0–2056 bright blue filter, no objects are detected in the region used for measuring S_{bgsimple} .

Object	Galaxy filter	S_{bgsimple}	$\alpha_{S_{\text{bgsector}}}$	S_{bgNFW}	$\frac{S_{\text{bgsimple}}}{S_{\text{bgNFW}}}$
		arcmin ⁻²	arcmin ⁻²	arcmin ⁻²	
RXC J0006.0–3443	Bright, red	0.166 ± 0.020	0.02	0.12 ± 0.04	1.34
RXC J0006.0–3443	Faint, red	0.70 ± 0.04	0.04	0.62 ± 0.06	1.13
RXC J0006.0–3443	Bright, blue	0.128 ± 0.017	0.02	0.102 ± 0.029	1.25
RXC J0006.0–3443	Faint, blue	1.15 ± 0.05	0.07	0.67 ± 0.19	1.72
RXC J0049.4–2931	Bright, red	0.064 ± 0.011	0.01	0.050 ± 0.013	1.27
RXC J0049.4–2931	Faint, red	0.427 ± 0.027	0.03	0.413 ± 0.020	1.03
RXC J0049.4–2931	Bright, blue	0.074 ± 0.011	0.01	0.054 ± 0.022	1.38
RXC J0049.4–2931	Faint, blue	0.82 ± 0.04	0.04	0.797 ± 0.023	1.02
RXC J0345.7–4112	Bright, red	0.026 ± 0.010	0.01	0.024 ± 0.007	1.05
RXC J0345.7–4112	Faint, red	0.095 ± 0.019	0.02	0.063 ± 0.034	1.52
RXC J0345.7–4112	Bright, blue	0.011 ± 0.006	0.00	0.0126 ± 0.0024	0.87
RXC J0345.7–4112	Faint, blue	0.080 ± 0.017	0.02	0.079 ± 0.004	1.01
RXC J0547.6–3152	Bright, red	0.185 ± 0.024	0.05	0.135 ± 0.034	1.37
RXC J0547.6–3152	Faint, red	0.74 ± 0.05	0.07	0.66 ± 0.08	1.12
RXC J0547.6–3152	Bright, blue	0.191 ± 0.025	0.05	0.164 ± 0.035	1.16
RXC J0547.6–3152	Faint, blue	1.36 ± 0.07	0.21	1.21 ± 0.13	1.13
RXC J0605.8–3518	Bright, red	0.212 ± 0.019	0.03	0.186 ± 0.021	1.14
RXC J0605.8–3518	Faint, red	0.92 ± 0.04	0.06	0.89 ± 0.06	1.03
RXC J0605.8–3518	Bright, blue	0.183 ± 0.018	0.02	0.177 ± 0.015	1.03
RXC J0605.8–3518	Faint, blue	1.93 ± 0.06	0.06	1.89 ± 0.11	1.02
RXC J0616.8–4748	Bright, red	0.087 ± 0.012	0.01	0.059 ± 0.013	1.46
RXC J0616.8–4748	Faint, red	0.647 ± 0.034	0.04	0.61 ± 0.06	1.06
RXC J0616.8–4748	Bright, blue	0.090 ± 0.013	0.03	0.086 ± 0.010	1.05
RXC J0616.8–4748	Faint, blue	1.00 ± 0.04	0.05	0.85 ± 0.06	1.18
RXC J0645.4–5413	Bright, red	0.292 ± 0.022	0.08	0.234 ± 0.031	1.25
RXC J0645.4–5413	Faint, red	1.06 ± 0.04	0.06	0.93 ± 0.10	1.13
RXC J0645.4–5413	Bright, blue	0.272 ± 0.021	0.07	0.27 ± 0.04	1.01
RXC J0645.4–5413	Faint, blue	2.16 ± 0.06	0.08	2.09 ± 0.06	1.03
RXC J0821.8+0112	Bright, red	0.052 ± 0.011	0.02	0.026 ± 0.016	2.05
RXC J0821.8+0112	Faint, red	0.291 ± 0.026	0.04	0.23 ± 0.05	1.26
RXC J0821.8+0112	Bright, blue	0.029 ± 0.008	0.01	0.013 ± 0.017	2.13
RXC J0821.8+0112	Faint, blue	0.205 ± 0.022	0.02	0.12 ± 0.07	1.66
RXC J2023.0–2056	Bright, red	0.011 ± 0.011	0.01	0.007 ± 0.011	1.66
RXC J2023.0–2056	Faint, red	0.12 ± 0.04	0.04	0.092 ± 0.028	1.32
RXC J2023.0–2056	Bright, blue	0.0 ± 0	0.00	0.004 ± 0.010	0.00
RXC J2023.0–2056	Faint, blue	0.066 ± 0.027	0.02	0.055 ± 0.012	1.21
RXC J2048.1–1750	Bright, red	0.249 ± 0.022	0.05	0.16 ± 0.06	1.59
RXC J2048.1–1750	Faint, red	1.42 ± 0.05	0.08	1.29 ± 0.12	1.10
RXC J2048.1–1750	Bright, blue	0.257 ± 0.022	0.03	0.183 ± 0.033	1.40
RXC J2048.1–1750	Faint, blue	1.77 ± 0.06	0.06	1.61 ± 0.08	1.10

Table D.2: (continued)

Object	Galaxy filter	S_{bgsimple} arcmin ⁻²	$\alpha_{S_{\text{bgsector}}}$ arcmin ⁻²	S_{bgNFW} arcmin ⁻²	$\frac{S_{\text{bgsimple}}}{S_{\text{bgNFW}}}$
RXC J2129.8–5048	Bright, red	0.051 ± 0.014	0.01	0.037 ± 0.017	1.37
RXC J2129.8–5048	Faint, red	0.270 ± 0.033	0.07	0.235 ± 0.023	1.15
RXC J2129.8–5048	Bright, blue	0.023 ± 0.010	0.01	0.0268 ± 0.0034	0.88
RXC J2129.8–5048	Faint, blue	0.196 ± 0.028	0.04	0.07 ± 0.09	3.00
RXC J2218.6–3853	Bright, red	0.140 ± 0.016	0.02	0.131 ± 0.025	1.07
RXC J2218.6–3853	Faint, red	0.687 ± 0.034	0.06	0.688 ± 0.035	1.00
RXC J2218.6–3853	Bright, blue	0.104 ± 0.013	0.02	0.086 ± 0.015	1.21
RXC J2218.6–3853	Faint, blue	1.17 ± 0.04	0.04	1.14 ± 0.04	1.02
RXC J2234.5–3744	Bright, red	0.236 ± 0.022	0.02	0.177 ± 0.017	1.34
RXC J2234.5–3744	Faint, red	0.95 ± 0.04	0.05	0.87 ± 0.08	1.09
RXC J2234.5–3744	Bright, blue	0.305 ± 0.025	0.02	0.25 ± 0.09	1.22
RXC J2234.5–3744	Faint, blue	2.29 ± 0.07	0.06	2.27 ± 0.06	1.01
RXC J2319.6–7313	Bright, red	0.088 ± 0.012	0.01	0.051 ± 0.010	1.74
RXC J2319.6–7313	Faint, red	0.426 ± 0.027	0.02	0.41 ± 0.05	1.05
RXC J2319.6–7313	Bright, blue	0.099 ± 0.013	0.01	0.099 ± 0.011	1.00
RXC J2319.6–7313	Faint, blue	0.81 ± 0.04	0.06	0.76 ± 0.06	1.06

Appendix E

Additional plots and tables for Chapter 5

E.1 Smoothed density maps

Figures E.1 to E.14 red and blue count overdensity contour maps (described in Section §5.3.2.3) and the X-ray surface brightness maps. Sub-clump positions identified by inspection of the red galaxy contour map are also marked; those which failed to satisfy the significance threshold defined in Section §5.4.3.1 are shown with dashed lines. The clumps are listed in Table E.1.

Figures E.15 to E.28 show smoothed density maps for the clusters in X-ray, red sequence galaxies and blue cloud galaxies, overlaid with apertures placed at the most stable centres.

Table E.1: Significance measures and background subtracted object count for all the clumps found by inspection. Significant clumps with probability $P_x < 0.05$ are marked \mathcal{S}_x . Subscript r represents red galaxies, subscript b represents blue galaxies and subscript X represents the X-ray surface brightness. Clumps with red or blue counts significantly above the expected value from C0 and the global background are also given object counts c .

Object	Region	r r_{500}	P_r	c_r	P_b	c_b	P_X	\mathcal{S}_X
RXC J0006.0–3443	C0	0.00	0.000	150.9 ± 18.6	0.000	71.1 ± 19.4	0.000	\mathcal{S}_X
RXC J0006.0–3443	C1	0.57	0.000	19.2 ± 7.1	0.793	–	0.000	\mathcal{S}_X
RXC J0006.0–3443	C2	1.15	0.000	17.5 ± 6.6	0.005	15.0 ± 7.1	0.012	\mathcal{S}_X
RXC J0006.0–3443	C3	1.34	0.052	–	0.807	–	0.807	
RXC J0006.0–3443	C4	1.41	0.876	–	0.780	–	0.452	
RXC J0006.0–3443	C5	1.79	0.006	37.5 ± 18.8	0.123	–	0.437	
RXC J0006.0–3443	C6	1.93	0.022	16.0 ± 10.2	0.166	–	0.439	
RXC J0049.4–2931	C0	0.00	0.000	91.8 ± 12.5	0.000	26.0 ± 11.1	0.000	\mathcal{S}_X
RXC J0049.4–2931	C1	1.39	0.003	14.8 ± 6.7	0.643	–	0.319	
RXC J0049.4–2931	C2	1.44	0.062	–	0.344	–	0.791	
RXC J0049.4–2931	C3	1.77	0.034	8.7 ± 6.1	0.143	–	0.614	

Table E.1: (continued)

Object	Region	r r_{500}	P_r	c_r	P_b	c_b	P_X	\mathcal{S}_X
RXC J0049.4–2931	C4	2.77	0.007	20.9 ± 12.6	0.275	–	0.399	
RXC J0345.7–4112	C0	0.00	0.000	66.6 ± 11.4	0.000	2.1 ± 6.9	0.000	\mathcal{S}_X
RXC J0547.6–3152	C0	0.01	0.000	164.1 ± 16.6	0.000	70.4 ± 16.6	0.000	\mathcal{S}_X
RXC J0547.6–3152	C1	0.88	0.000	22.7 ± 8.4	0.142	–	0.570	
RXC J0547.6–3152	C2	1.64	0.060	–	0.609	–	0.492	
RXC J0547.6–3152	C3	1.81	0.345	–	0.278	–	0.445	
RXC J0605.8–3518	C0	0.00	0.000	134.7 ± 16.5	0.000	56.2 ± 19.0	0.000	\mathcal{S}_X
RXC J0605.8–3518	C1	1.37	0.033	13.8 ± 8.4	0.754	–	0.190	
RXC J0605.8–3518	C2	2.04	0.024	20.3 ± 13.3	0.056	–	0.445	
RXC J0605.8–3518	C3	2.67	0.000	45.6 ± 12.3	0.001	40.0 ± 15.5	0.423	
RXC J0605.8–3518	C4	3.05	0.315	–	0.290	–	0.783	
RXC J0605.8–3518	C5	1.23	0.014	12.4 ± 6.9	0.941	–	0.688	
RXC J0605.8–3518	C6	2.19	0.386	–	0.076	–	0.383	
RXC J0616.8–4748	C0	0.00	0.000	117.4 ± 15.9	0.000	36.2 ± 14.6	0.000	\mathcal{S}_X
RXC J0616.8–4748	C1	0.64	0.024	9.1 ± 5.7	0.884	–	0.920	
RXC J0616.8–4748	C2	2.15	0.030	6.2 ± 4.3	0.314	–	0.555	
RXC J0616.8–4748	C3	2.51	0.003	13.5 ± 6.3	0.054	–	0.574	
RXC J0616.8–4748	C4	2.75	0.373	–	0.707	–	–	
RXC J0616.8–4748	C5	1.16	0.047	7.1 ± 5.4	0.074	–	0.016	\mathcal{S}_X
RXC J0645.4–5413	C0	0.00	0.000	336.2 ± 23.5	0.000	53.2 ± 20.5	0.000	\mathcal{S}_X
RXC J0645.4–5413	C1	1.87	0.010	9.4 ± 5.1	0.340	–	0.450	
RXC J0645.4–5413	C2	2.19	0.000	18.3 ± 6.0	0.134	–	0.465	
RXC J0645.4–5413	C3	2.06	0.004	12.3 ± 5.8	0.910	–	0.536	
RXC J0645.4–5413	C4	1.82	0.000	22.9 ± 7.1	0.387	–	0.218	
RXC J0645.4–5413	C5	1.59	0.082	–	0.077	–	0.739	
RXC J0645.4–5413	C6	1.10	0.321	–	0.337	–	0.563	
RXC J0821.8+0112	C0	0.02	0.000	113.3 ± 14.0	0.000	52.5 ± 10.3	0.000	\mathcal{S}_X
RXC J0821.8+0112	C1	1.44	0.000	25.5 ± 9.0	0.005	13.2 ± 7.3	0.008	\mathcal{S}_X
RXC J0821.8+0112	C2	0.60	0.133	–	0.111	–	0.257	
RXC J2023.0–2056	C0	0.00	0.000	71.4 ± 13.3	0.000	9.9 ± 10.0	0.000	\mathcal{S}_X
RXC J2023.0–2056	C1	0.78	0.000	22.7 ± 7.4	0.168	–	0.441	
RXC J2048.1–1750	C0	0.00	0.000	246.7 ± 21.9	0.000	101.3 ± 19.4	0.000	\mathcal{S}_X
RXC J2048.1–1750	C1	1.11	0.006	16.3 ± 8.0	0.239	–	0.157	
RXC J2048.1–1750	C2	1.76	0.000	28.0 ± 8.4	0.051	–	0.003	\mathcal{S}_X
RXC J2048.1–1750	C3	1.88	0.008	16.8 ± 8.2	0.135	–	0.532	
RXC J2048.1–1750	C4	2.61	0.019	54.1 ± 26.0	0.554	–	0.527	
RXC J2048.1–1750	C5	2.65	0.252	–	0.159	–	0.507	
RXC J2129.8–5048	C0	0.00	0.000	104.2 ± 15.5	0.000	12.8 ± 11.2	0.000	\mathcal{S}_X
RXC J2129.8–5048	C1	1.33	0.007	10.3 ± 5.5	0.165	–	0.470	
RXC J2218.6–3853	C0	0.00	0.000	66.5 ± 13.0	0.000	17.2 ± 13.9	0.000	\mathcal{S}_X
RXC J2218.6–3853	C1	1.37	0.001	25.5 ± 9.3	0.009	17.2 ± 10.0	0.001	\mathcal{S}_X
RXC J2218.6–3853	C2	2.55	0.000	61.2 ± 17.0	0.007	38.4 ± 18.3	0.518	
RXC J2218.6–3853	C3	1.28	0.012	10.0 ± 5.6	0.781	–	0.539	
RXC J2234.5–3744	C0	0.00	0.000	224.4 ± 21.5	0.000	58.4 ± 23.3	0.000	\mathcal{S}_X
RXC J2234.5–3744	C1	1.02	0.009	17.1 ± 8.7	0.671	–	0.223	
RXC J2234.5–3744	C2	1.31	0.004	16.6 ± 7.7	0.353	–	0.532	
RXC J2234.5–3744	C3	2.17	0.005	22.7 ± 10.5	0.050	–	0.623	
RXC J2234.5–3744	C4	1.73	0.005	14.9 ± 6.9	0.585	–	0.565	

Table E.1: (continued)

Object	Region	r r_{500}	P_r	c_r	P_b	c_b	P_X	\mathcal{S}_X
RXC J2234.5-3744	C5	2.24	0.032	15.6 ± 10.4	0.826	–	0.501	
RXC J2234.5-3744	C6	1.83	0.077	–	0.504	–	0.426	
RXC J2234.5-3744	C7	0.78	0.059	–	0.741	–	0.846	
RXC J2319.6-7313	C0	0.00	0.000	47.7 ± 11.2	0.000	38.4 ± 13.6	0.000	\mathcal{S}_X
RXC J2319.6-7313	C1	0.95	0.006	13.2 ± 6.8	0.006	16.1 ± 7.8	0.008	\mathcal{S}_X
RXC J2319.6-7313	C2	1.42	0.049	8.4 ± 6.2	0.218	–	0.447	
RXC J2319.6-7313	C3	1.26	0.497	–	0.016	7.6 ± 4.6	0.647	
RXC J2319.6-7313	C4	1.64	0.102	–	0.254	–	0.349	

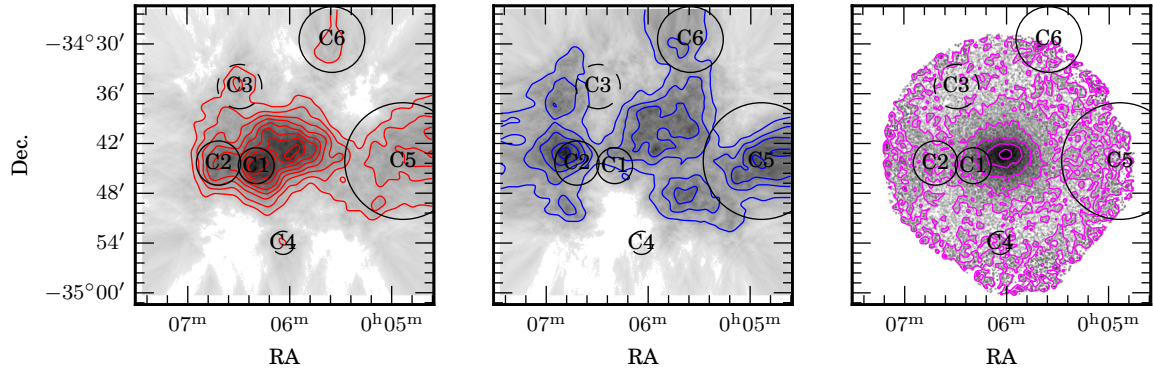


Figure E.1: Clump maps for RXC J0006.0–3443. The left and centre panels show the overdensity contours calculated with the method described in Section §5.3.2.3 for the red and blue galaxies respectively, where the lowest contour is 2σ above the background level and subsequent contours are spaced 1σ apart. The right panel shows the X-ray surface brightness map in the $(0.5–2.0)$ keV band, where the pixel size is $4'' \times 4''$, the lowest contour is at a brightness of $3 \times 10^{-5} \text{ s}^{-1} \text{ pixel}^{-1}$, and contours are spaced by a factor $2\times$. Each image is centred at the coordinates of the X-ray peak as listed in Table 5.2.

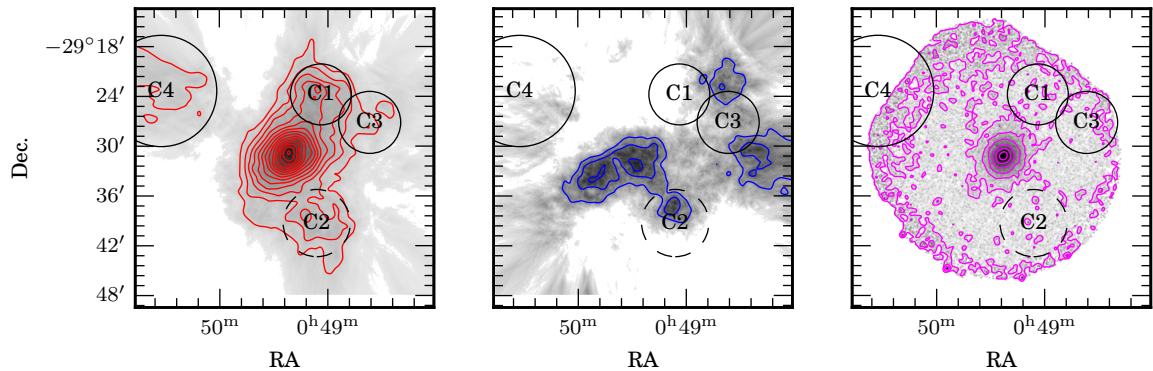


Figure E.2: Clump maps for RXC J0049.4–2931. The details are the same as described in Figure E.1.

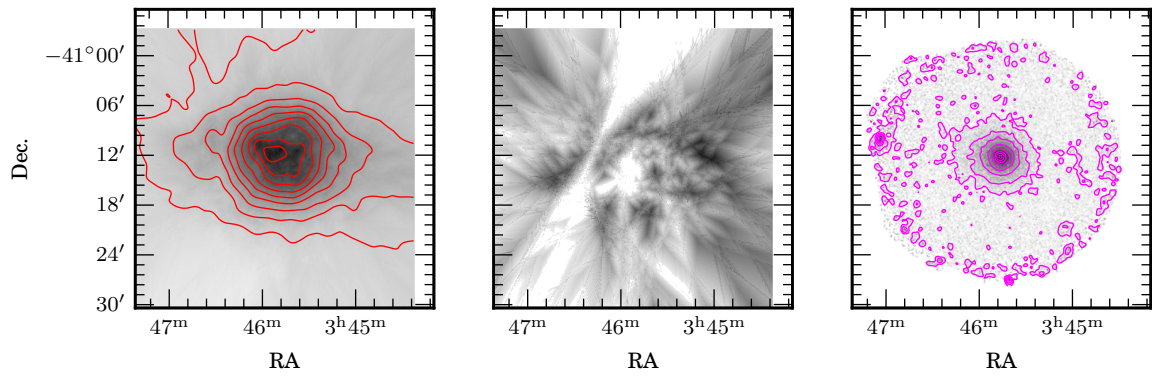


Figure E.3: Clump maps for RXC J0345.7-4112. The details are the same as described in Figure E.1.

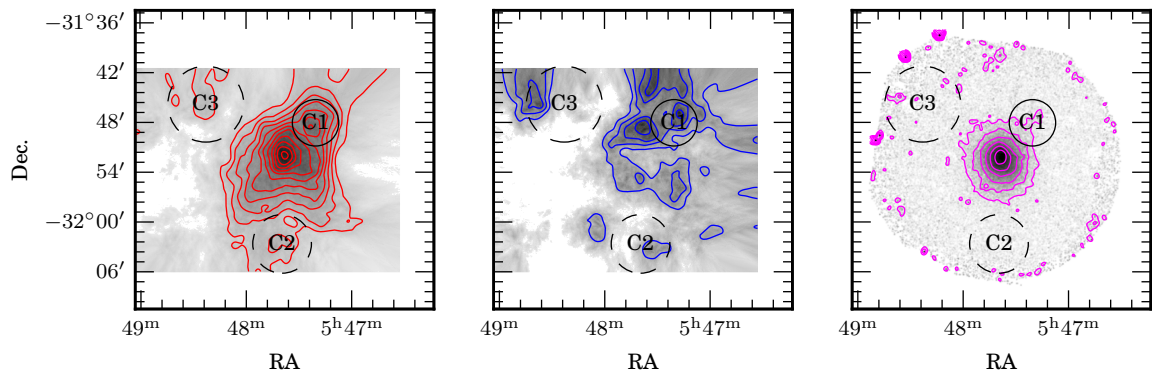


Figure E.4: Clump maps for RXC J0547.6-3152. The details are the same as described in Figure E.1.

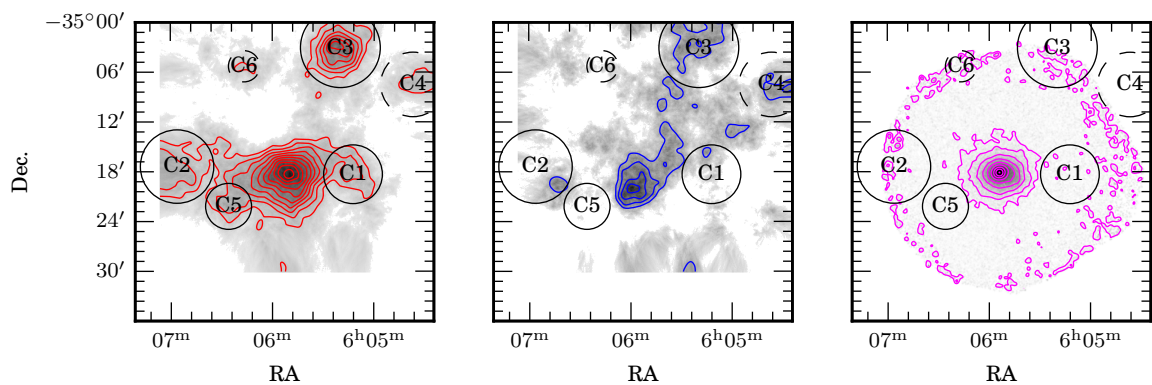


Figure E.5: Clump maps for RXC J0605.8-3518. The details are the same as described in Figure E.1.

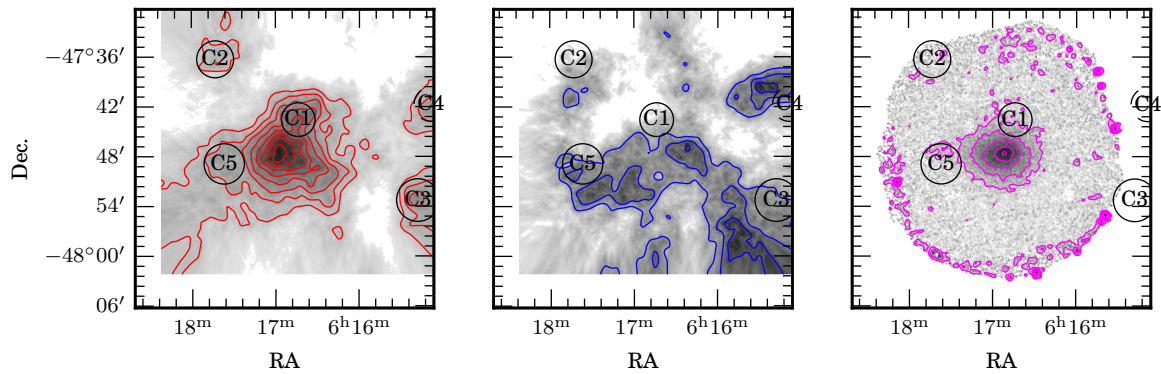


Figure E.6: Clump maps for RXC J0616.8–4748. The details are the same as described in Figure E.1.

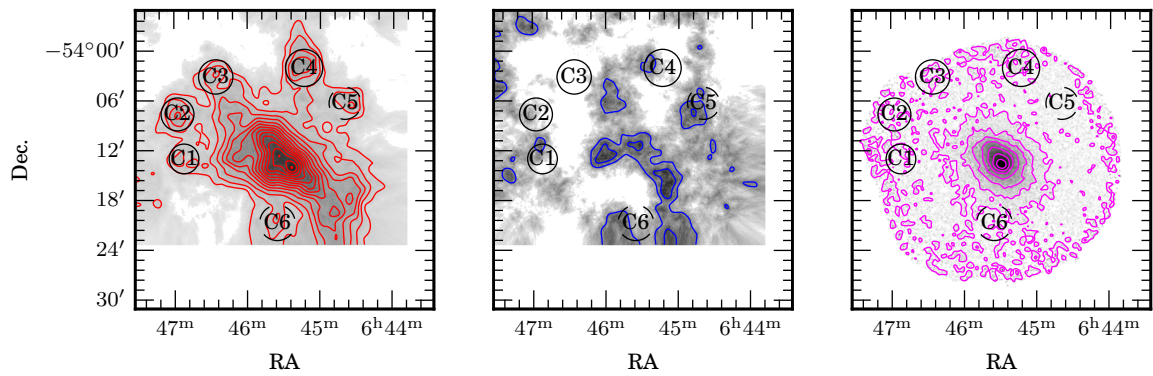


Figure E.7: Clump maps for RXC J0645.4–5413. The details are the same as described in Figure E.1.

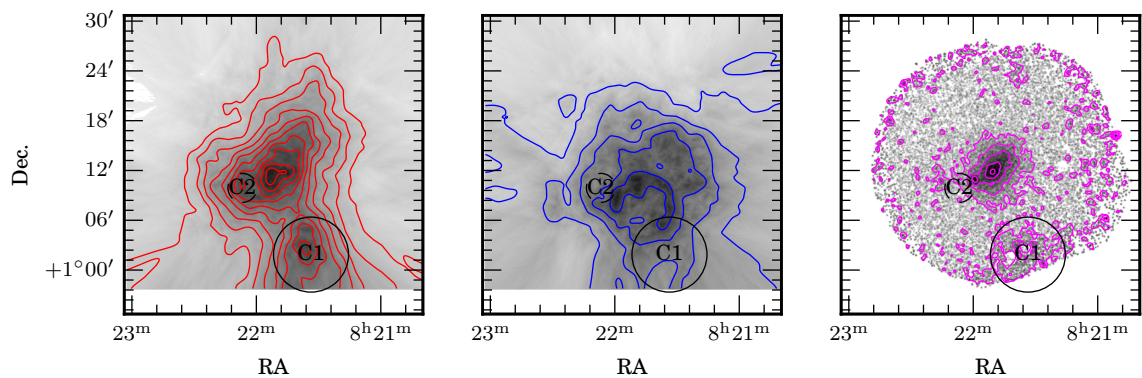


Figure E.8: Clump maps for RXC J0821.8+0112. The details are the same as described in Figure E.1.

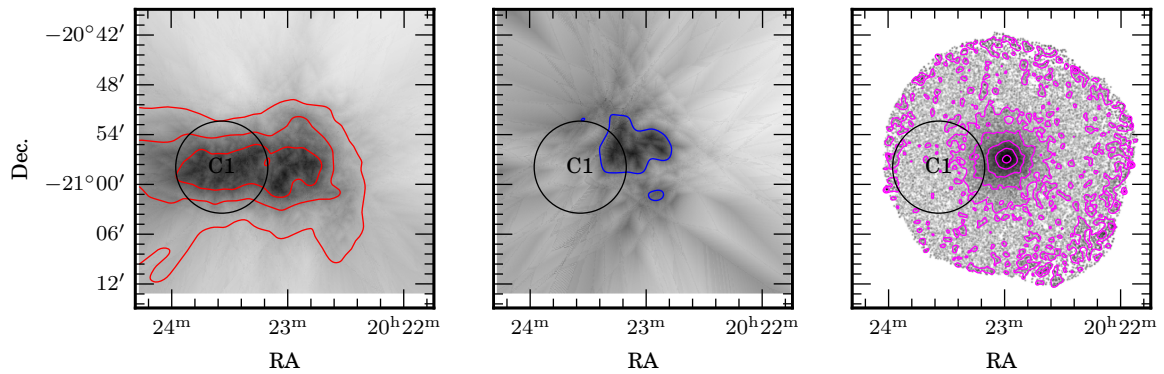


Figure E.9: Clump maps for RXC J2023.0–2056. The details are the same as described in Figure E.1.

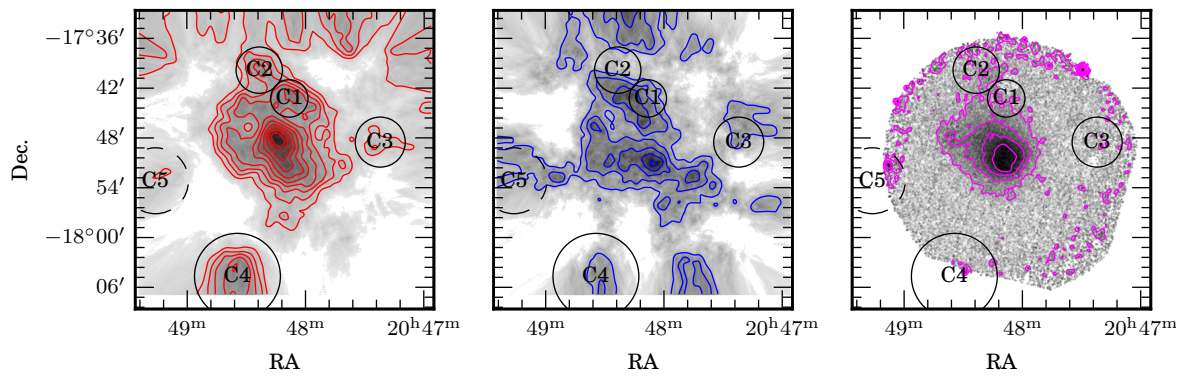


Figure E.10: Clump maps for RXC J2048.1–1750. The details are the same as described in Figure E.1.

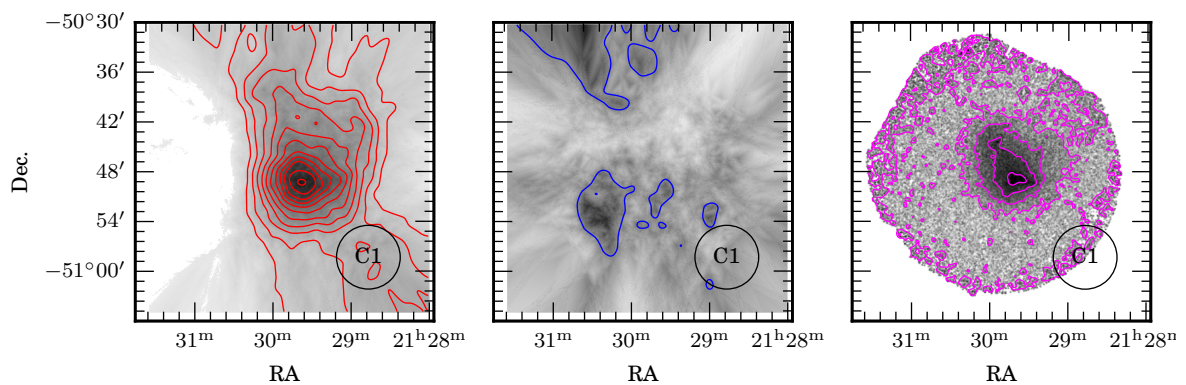


Figure E.11: Clump maps for RXC J2129.8–5048. The details are the same as described in Figure E.1.

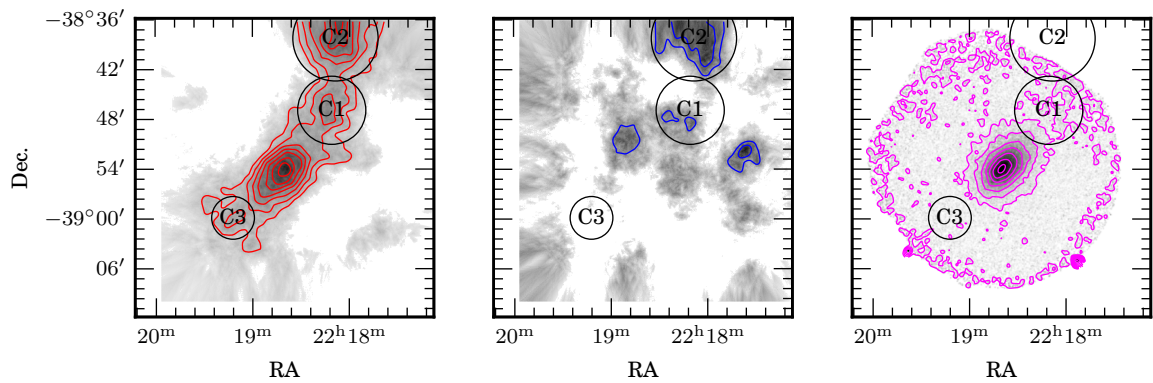


Figure E.12: Clump maps for RXC J2218.6–3853. The details are the same as described in Figure E.1.

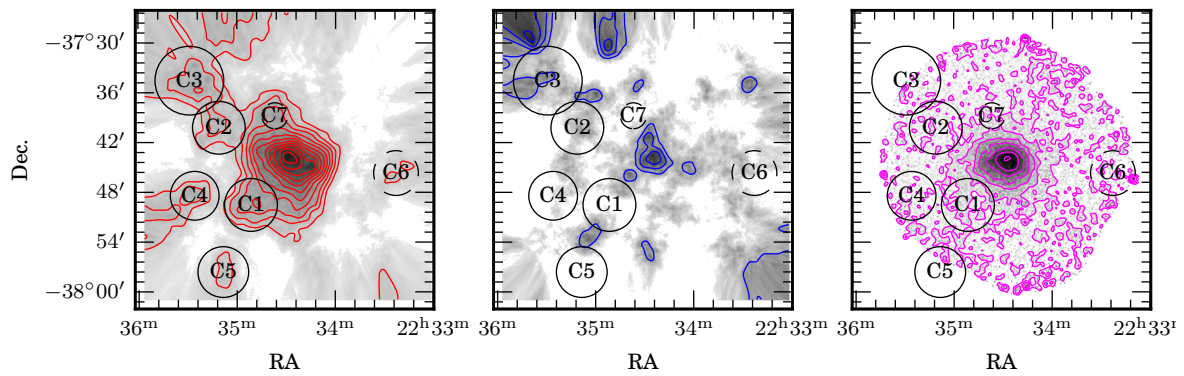


Figure E.13: Clump maps for RXC J2234.5–3744. The details are the same as described in Figure E.1.

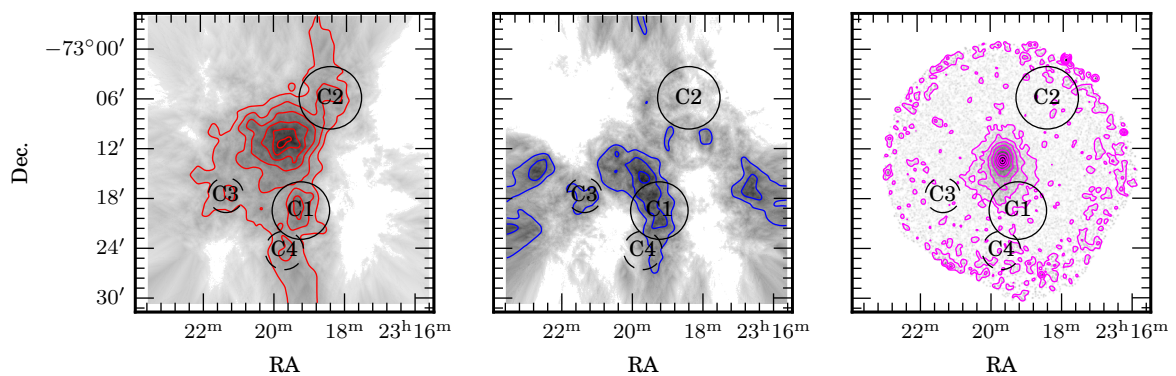


Figure E.14: Clump maps for RXC J2319.6–7313. The details are the same as described in Figure E.1.

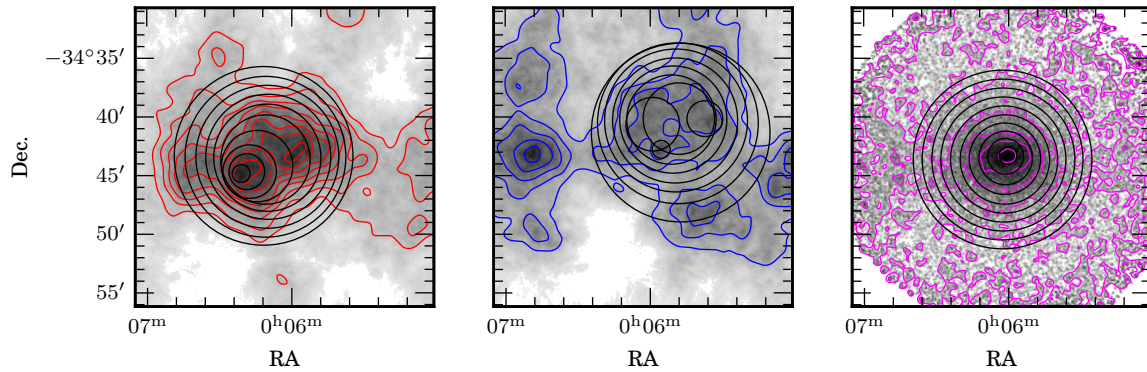


Figure E.15: Centre shift maps for RXC J0006.0–3443. The left and centre panels show the overdensity contours calculated with the method described in Section §5.3.2.3 for the red and blue galaxies respectively, where the lowest contour is 2σ above the background level and subsequent contours are spaced 1σ apart. The right panel shows the X-ray surface brightness map in the $(0.5-2.0)$ keV band, where the pixel size is $4'' \times 4''$, the lowest contour is at a brightness of $3 \times 10^{-5} \text{ s}^{-1} \text{ pixel}^{-1}$, and contours are spaced by a factor $2\times$.

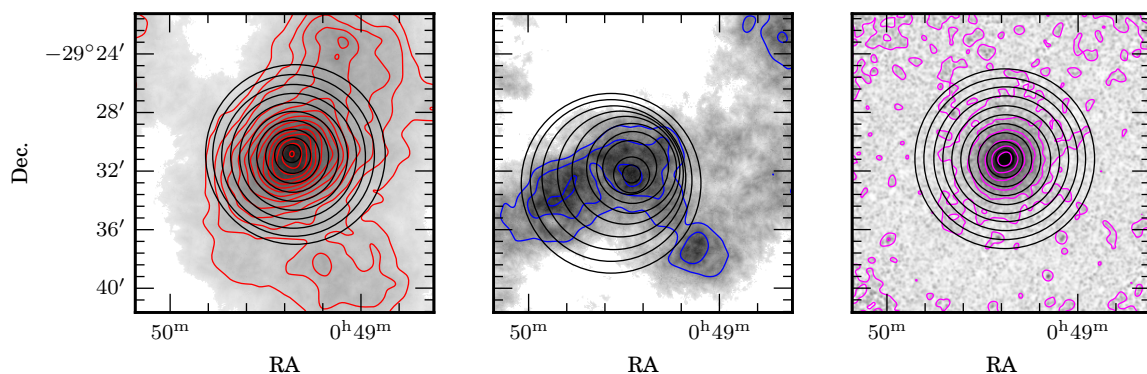


Figure E.16: Centre shift maps for RXC J0049.4–2931. The details are the same as described in Figure E.15.

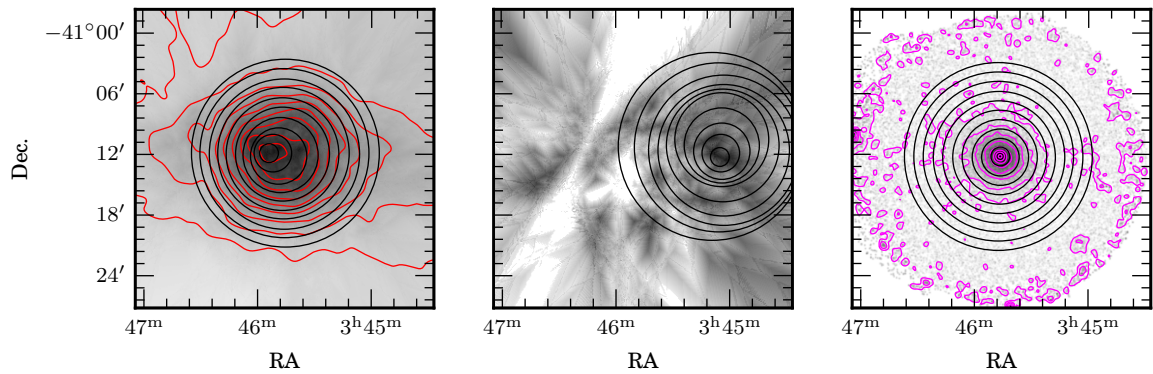


Figure E.17: Centre shift maps for RXC J0345.7–4112. The details are the same as described in Figure E.15.

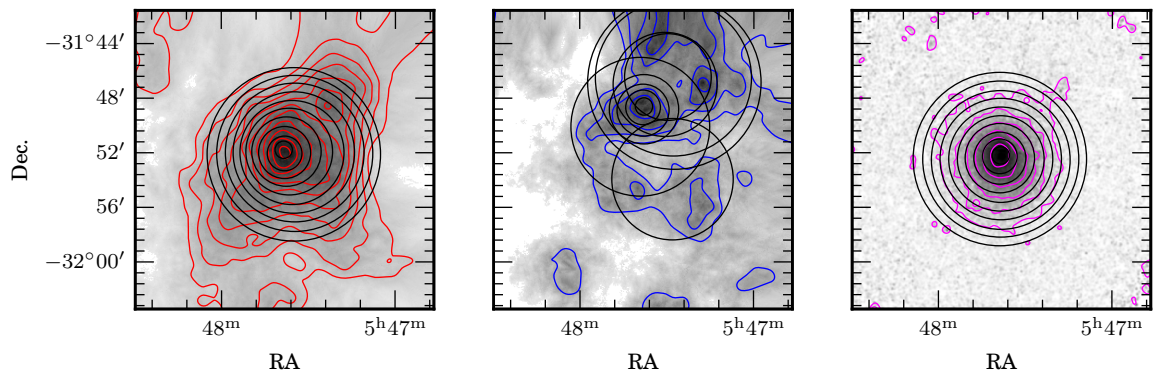


Figure E.18: Centre shift maps for RXC J0547.6–3152. The details are the same as described in Figure E.15.

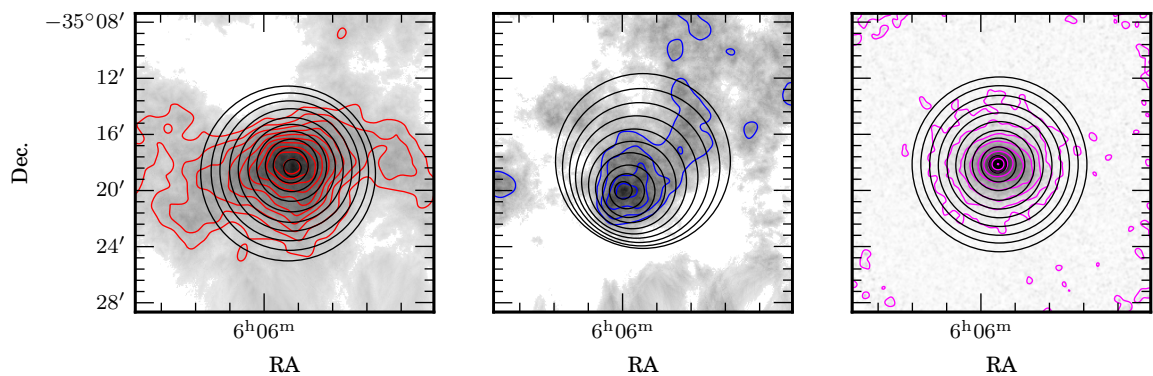


Figure E.19: Centre shift maps for RXC J0605.8–3518. The details are the same as described in Figure E.15.

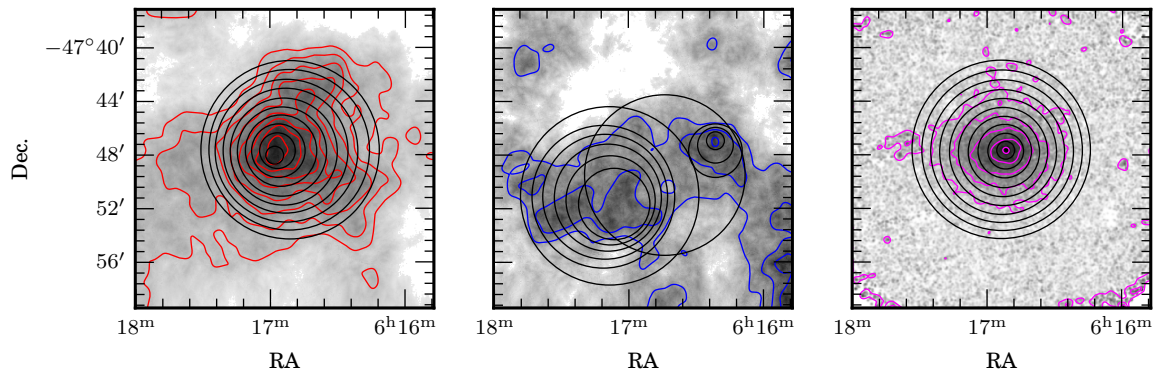


Figure E.20: Centre shift maps for RXC J0616.8–4748. The details are the same as described in Figure E.15.

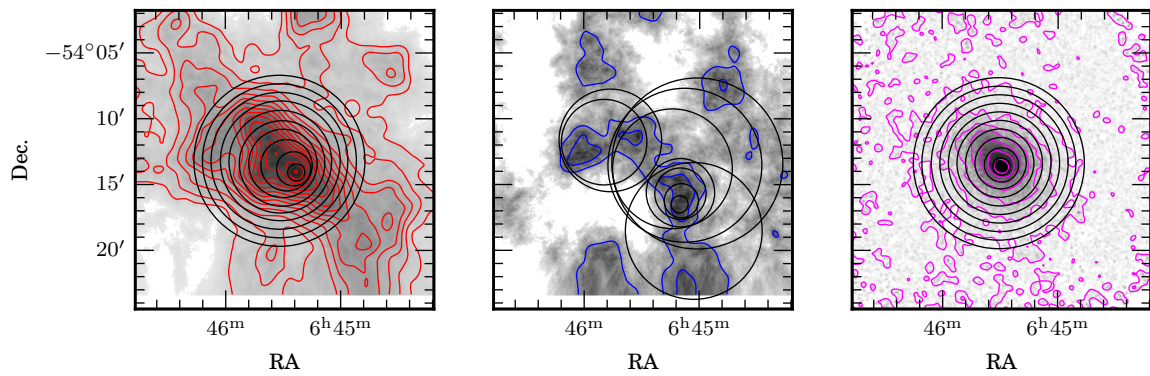


Figure E.21: Centre shift maps for RXC J0645.4–5413. The details are the same as described in Figure E.15.

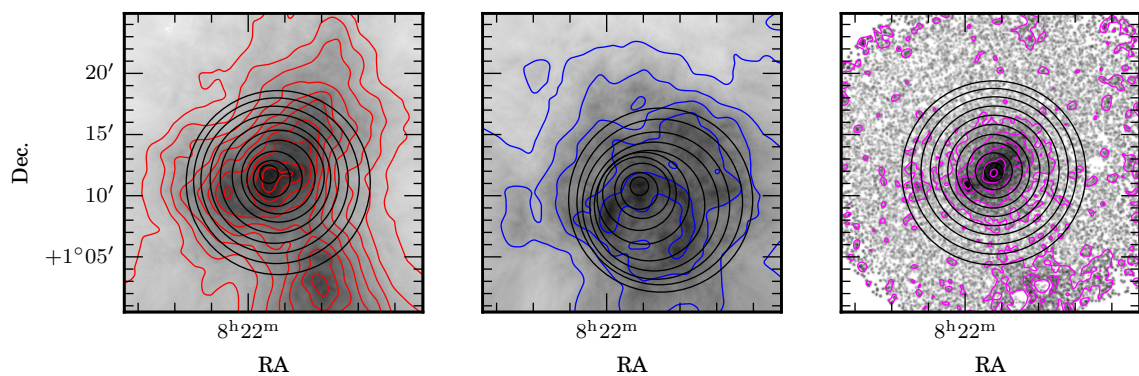


Figure E.22: Centre shift maps for RXC J0821.8+0112. The details are the same as described in Figure E.15.

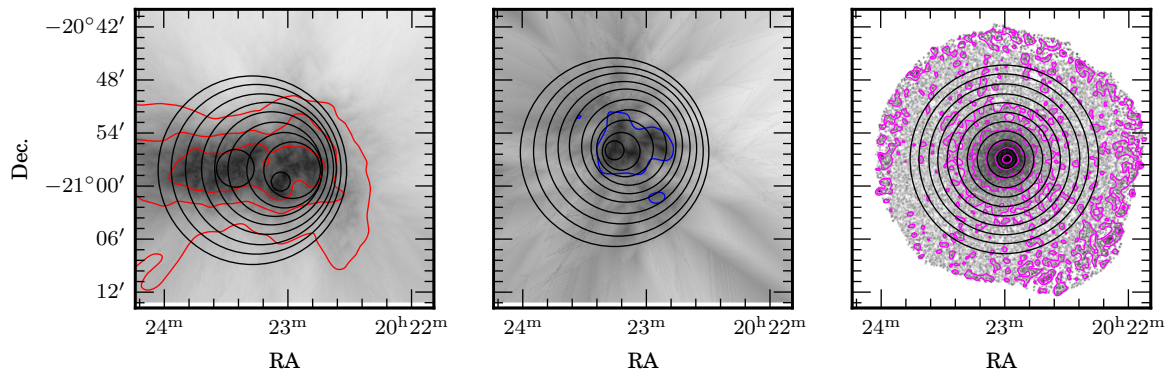


Figure E.23: Centre shift maps for RXC J2023.0–2056. The details are the same as described in Figure E.15.

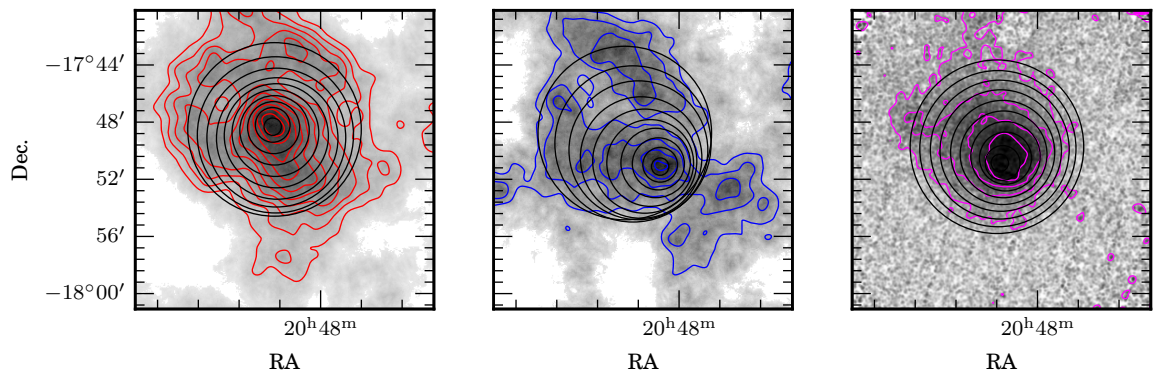


Figure E.24: Centre shift maps for RXC J2048.1–1750. The details are the same as described in Figure E.15.

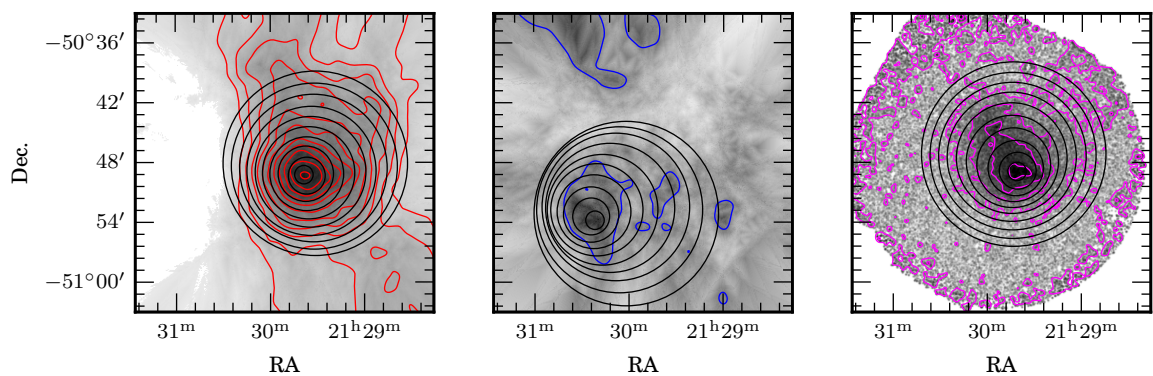


Figure E.25: Centre shift maps for RXC J2129.8–5048. The details are the same as described in Figure E.15.

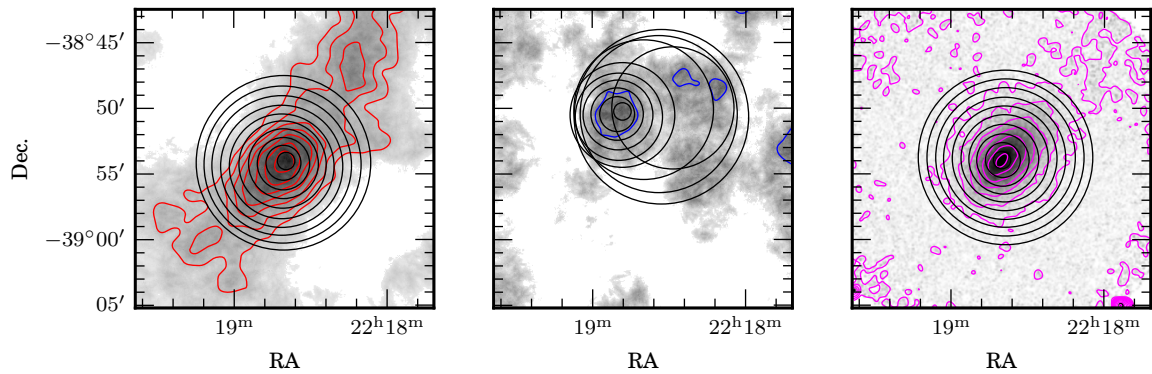


Figure E.26: Centre shift maps for RXC J2218.6–3853. The details are the same as described in Figure E.15.

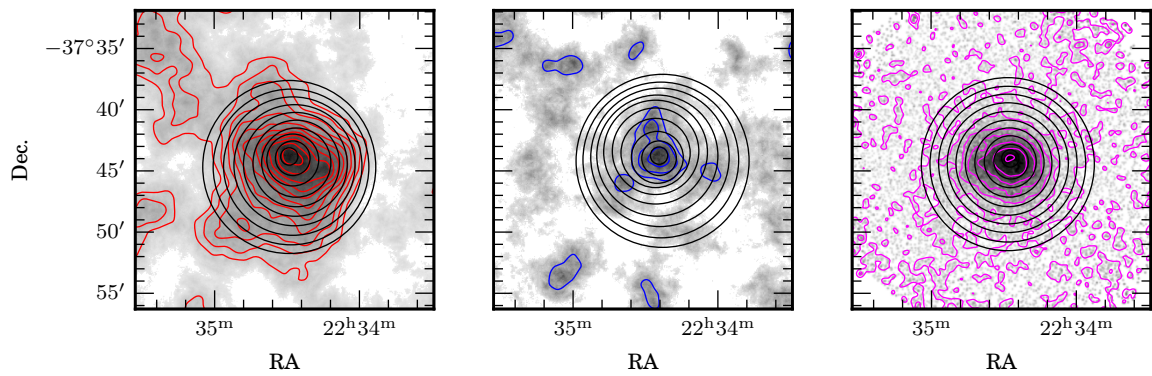


Figure E.27: Centre shift maps for RXC J2234.5–3744. The details are the same as described in Figure E.15.

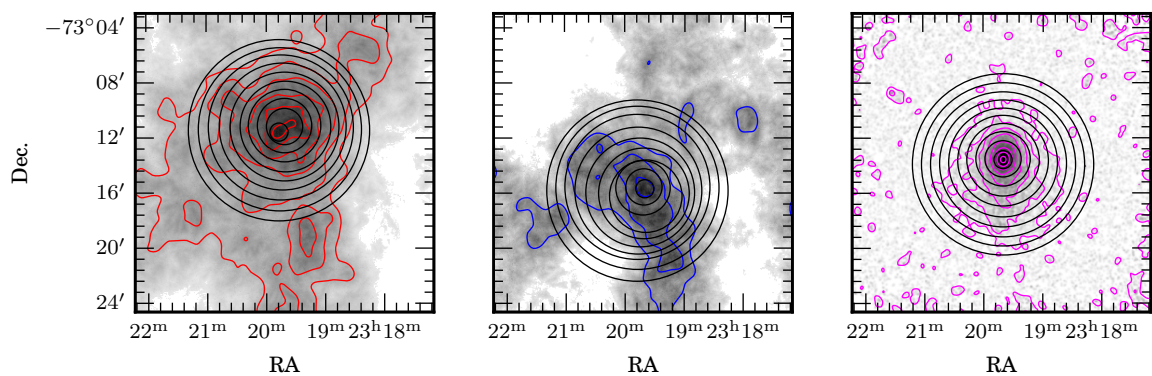


Figure E.28: Centre shift maps for RXC J2319.6–7313. The details are the same as described in Figure E.15.

Bibliography

- G. O. Abell. The Distribution of Rich Clusters of Galaxies. *ApJS*, 3:211, May 1958. doi:10.1086/190036.
- Douglas Adams. *The Hitchhiker's Guide to the Galaxy*. Pan Books, 1979.
- H. Akamatsu, M. Takizawa, K. Nakazawa, Y. Fukazawa, Y. Ishisaki, and T. Ohashi. X-Ray View of the Shock Front in the Merging Cluster Abell 3376 with Suzaku. *PASJ*, 64:67, August 2012. doi:10.1093/pasj/64.4.67.
- S. W. Allen, R. J. H. Dunn, A. C. Fabian, G. B. Taylor, and C. S. Reynolds. The relation between accretion rate and jet power in X-ray luminous elliptical galaxies. *MNRAS*, 372:21–30, October 2006. doi:10.1111/j.1365-2966.2006.10778.x.
- S. W. Allen, A. E. Evrard, and A. B. Mantz. Cosmological Parameters from Observations of Galaxy Clusters. *ARA&A*, 49:409–470, September 2011. doi:10.1146/annurev-astro-081710-102514.
- L. Anderson, E. Aubourg, S. Bailey, D. Bizyaev, M. Blanton, A. S. Bolton, J. Brinkmann, J. R. Brownstein, A. Burden, A. J. Cuesta, L. A. N. da Costa, K. S. Dawson, R. de Putter, D. J. Eisenstein, J. E. Gunn, H. Guo, J.-C. Hamilton, P. Harding, S. Ho, K. Honscheid, E. Kazin, D. Kirkby, J.-P. Kneib, A. Labatie, C. Loomis, R. H. Lupton, E. Malanushenko, V. Malanushenko, R. Mandelbaum, M. Manera, C. Maraston, C. K. McBride, K. T. Mehta, O. Mena, F. Montesano, D. Muna, R. C. Nichol, S. E. Nuza, M. D. Olmstead, D. Oravetz, N. Padmanabhan, N. Palanque-Delabrouille, K. Pan, J. Parejko, I. Pâris, W. J. Percival, P. Petitjean, F. Prada, B. Reid, N. A. Roe, A. J. Ross, N. P. Ross, L. Samushia, A. G. Sánchez, D. J. Schlegel, D. P. Schneider, C. G. Scóccola, H.-J. Seo, E. S. Sheldon, A. Simmons, R. A. Skibba, M. A. Strauss, M. E. C. Swanson, D. Thomas, J. L. Tinker, R. Tojeiro, M. V. Magaña, L. Verde, C. Wagner, D. A. Wake, B. A. Weaver, D. H. Weinberg, M. White, X. Xu, C. Yèche, I. Zehavi, and G.-B. Zhao. The clustering of galaxies in the SDSS-III Baryon Oscillation Spectroscopic Survey: baryon acoustic oscillations in the Data Release 9 spectroscopic galaxy sample. *MNRAS*, 427:3435–3467, December 2012. doi:10.1111/j.1365-2966.2012.22066.x.
- N. Arimoto and Y. Yoshii. Chemical and photometric properties of a galactic wind model for elliptical galaxies. *A&A*, 173:23–38, February 1987.

- M. Arnaud, E. Pointecouteau, and G. W. Pratt. Calibration of the galaxy cluster $M_{500}-Y_X$ relation with XMM-Newton. *A&A*, 474:L37–L40, November 2007. doi:10.1051/0004-6361:20078541.
- S. Arnouts, B. Vandame, C. Benoist, M. A. T. Groenewegen, L. da Costa, M. Schirmer, R. P. Mignani, R. Slijkhuis, E. Hatziminaoglou, R. Hook, R. Madejsky, C. Rit e, and A. Wicenec. ESO imaging survey. Deep public survey: Multi-color optical data for the Chandra Deep Field South. *A&A*, 379:740–754, November 2001. doi:10.1051/0004-6361:20011341.
- Astropy Collaboration, T. P. Robitaille, E. J. Tollerud, P. Greenfield, M. Droettboom, E. Bray, T. Aldcroft, M. Davis, A. Ginsburg, A. M. Price-Whelan, W. E. Kerzendorf, A. Conley, N. Crighton, K. Barbary, D. Muna, H. Ferguson, F. Grollier, M. M. Parikh, P. H. Nair, H. M. Unther, C. Deil, J. Woillez, S. Conseil, R. Kramer, J. E. H. Turner, L. Singer, R. Fox, B. A. Weaver, V. Zabalza, Z. I. Edwards, K. Azalee Bostroem, D. J. Burke, A. R. Casey, S. M. Crawford, N. Dencheva, J. Ely, T. Jenness, K. Labrie, P. L. Lim, F. Pierfederici, A. Pontzen, A. Ptak, B. Refsdal, M. Servillat, and O. Streicher. Astropy: A community Python package for astronomy. *A&A*, 558:A33, October 2013. doi:10.1051/0004-6361/201322068.
- J. Bagchi, F. Durret, G. B. L. Neto, and S. Paul. Giant Ringlike Radio Structures Around Galaxy Cluster Abell 3376. *Science*, 314:791–794, November 2006. doi:10.1126/science.1131189.
- J. S. Bagla, T. Padmanabhan, and J. V. Narlikar. Crisis in Cosmology: Observational Constraints on ω and H_0 . *Comments on Astrophysics*, 18:275, 1996.
- N. A. Bahcall and R. Cen. The mass function of clusters of galaxies. *ApJ*, 407:L49–L52, April 1993. doi:10.1086/186803.
- M. L. Balogh, J. F. Navarro, and S. L. Morris. The Origin of Star Formation Gradients in Rich Galaxy Clusters. *ApJ*, 540:113–121, September 2000. doi:10.1086/309323.
- P. Barai, H. Martel, and J. Germain. Anisotropic Active Galactic Nucleus Outflows and Enrichment of the Intergalactic Medium. II. Metallicity. *ApJ*, 727:54, January 2011. doi:10.1088/0004-637X/727/1/54.
- J. E. Barnes. Evolution of compact groups and the formation of elliptical galaxies. *Nature*, 338:123–126, March 1989. doi:10.1038/338123a0.
- J. E. Barnes and L. Hernquist. Transformations of Galaxies. II. Gasdynamics in Merging Disk Galaxies: Addendum. *ApJ*, 495:187–188, March 1998. doi:10.1086/305294.
- L. P. Bautz and W. W. Morgan. On the Classification of the Forms of Clusters of Galaxies. *ApJ*, 162:L149, December 1970. doi:10.1086/180643.

-
- M. C. Begelman, R. D. Blandford, and M. J. Rees. Theory of extragalactic radio sources. *Reviews of Modern Physics*, 56:255–351, April 1984. doi:10.1103/RevModPhys.56.255.
- A. J. Benson, R. G. Bower, C. S. Frenk, C. G. Lacey, C. M. Baugh, and S. Cole. What Shapes the Luminosity Function of Galaxies? *ApJ*, 599:38–49, December 2003.
- E. Bertin. *SExtractor User's Manual*. Institut d'Astrophysique and Observatoire de Paris, 2.13 edition, October 2010.
- E. Bertin. Displaying Digital Deep Sky Images. In P. Ballester, D. Egret, and N. P. F. Lorente, editors, *Astronomical Data Analysis Software and Systems XXI*, volume 461 of *Astronomical Society of the Pacific Conference Series*, page 263, September 2012.
- E. Bertin and S. Arnouts. SExtractor: Software for source extraction. *A&AS*, 117:393–404, June 1996.
- M. Birkinshaw, S. F. Gull, and H. Hardebeck. The Sunyaev-Zeldovich effect towards three clusters of galaxies. *Nature*, 309:34, May 1984. doi:10.1038/309034a0.
- H. Böhringer. X-ray observations of the chemical abundances in the Intra-Cluster Medium . *Mem. Soc. Astron. Italiana*, 85:396, 2014.
- H. Böhringer, W. Voges, J. P. Huchra, B. McLean, R. Giacconi, P. Rosati, R. Burg, J. Mader, P. Schuecker, D. Simić, S. Komossa, T. H. Reiprich, J. Retzlaff, and J. Trümper. The Northern ROSAT All-Sky (NORAS) Galaxy Cluster Survey. I. X-Ray Properties of Clusters Detected as Extended X-Ray Sources. *ApJS*, 129:435–474, August 2000. doi:10.1086/313427.
- H. Böhringer, P. Schuecker, L. Guzzo, C. A. Collins, W. Voges, S. Schindler, D. M. Neumann, R. G. Cruddace, S. De Grandi, G. Chincarini, A. C. Edge, H. T. MacGillivray, and P. Shaver. The ROSAT-ESO flux limited X-ray (REFLEX) galaxy cluster survey. I. The construction of the cluster sample. *A&A*, 369:826–850, April 2001a. doi:10.1051/0004-6361:20010240.
- H. Böhringer, P. Schuecker, P. Lynam, T. Reiprich, C. A. Collins, L. Guzzo, Y. Ikebe, E. Molinari, L. Barone, and C. Ambros. Harvesting the results from the REFLEX cluster survey: following-up on an ESO Key programme. *The Messenger*, 106:24–31, December 2001b.
- H. Böhringer, K. Matsushita, E. Churazov, Y. Ikebe, and Y. Chen. The new emerging model for the structure of cooling cores in clusters of galaxies. *A&A*, 382:804–820, February 2002. doi:10.1051/0004-6361:20011708.
- H. Böhringer, K. Matsushita, E. Churazov, A. Finoguenov, and Y. Ikebe. Implications of the central metal abundance peak in cooling core clusters of galaxies. *A&A*, 416:L21–L25, March 2004. doi:10.1051/0004-6361:20040047.

- H. Böhringer, P. Schuecker, G. W. Pratt, M. Arnaud, T. J. Ponman, J. H. Croston, S. Borgani, R. G. Bower, U. G. Briel, C. A. Collins, M. Donahue, W. R. Forman, A. Finoguenov, M. J. Geller, L. Guzzo, J. P. Henry, R. Kneissl, J. J. Mohr, K. Matsushita, C. R. Mullis, T. Ohashi, K. Pedersen, D. Pierini, H. Quintana, S. Raychaudhury, T. H. Reiprich, A. K. Romer, P. Rosati, K. Sabirli, R. F. Temple, P. T. P. Viana, A. Vikhlinin, G. M. Voit, and Y.-Y. Zhang. The representative XMM-Newton cluster structure survey (REXCESS) of an X-ray luminosity selected galaxy cluster sample. *A&A*, 469:363–377, July 2007. doi:10.1051/0004-6361:20066740.
- H. Böhringer, G. W. Pratt, M. Arnaud, S. Borgani, J. H. Croston, T. J. Ponman, S. Ameglio, R. F. Temple, and K. Dolag. Substructure of the galaxy clusters in the REXCESS sample: observed statistics and comparison to numerical simulations. *A&A*, 514:A32, May 2010. doi:10.1051/0004-6361/200913911.
- H. Böhringer, G. Chon, C. A. Collins, L. Guzzo, N. Nowak, and S. Bobrovskiy. The extended ROSAT-ESO flux limited X-ray galaxy cluster survey (REFLEX II) II. Construction and properties of the survey. *A&A*, 555:A30, July 2013. doi:10.1051/0004-6361/201220722.
- A. Boselli and G. Gavazzi. Environmental Effects on Late-Type Galaxies in Nearby Clusters. *PASP*, 118:517–559, April 2006. doi:10.1086/500691.
- R. G. Bower, J. R. Lucey, and R. S. Ellis. Precision Photometry of Early Type Galaxies in the Coma and Virgo Clusters - a Test of the Universality of the Colour / Magnitude Relation - Part Two - Analysis. *MNRAS*, 254:601, February 1992.
- R. G. Bower, A. J. Benson, R. Malbon, J. C. Helly, C. S. Frenk, C. M. Baugh, S. Cole, and C. G. Lacey. Breaking the hierarchy of galaxy formation. *MNRAS*, 370:645–655, August 2006.
- F. G. Braglia, D. Pierini, A. Biviano, and H. Böhringer. Multi-wavelength study of X-ray luminous clusters at $z \sim 0.3$. I. Star-formation activity of cluster galaxies. *A&A*, 500:947–963, June 2009. doi:10.1051/0004-6361/200811589.
- J. O. Burns, E. J. Hallman, B. Gantner, P. M. Motl, and M. L. Norman. Why Do Only Some Galaxy Clusters Have Cool Cores? *ApJ*, 675:1125–1140, March 2008. doi:10.1086/526514.
- G. S. Buswell, T. Shanks, W. J. Frith, P. J. Outram, N. Metcalfe, and R. Fong. The local hole in the galaxy distribution: new optical evidence. *MNRAS*, 354:991–1004, November 2004. doi:10.1111/j.1365-2966.2004.08217.x.
- H. Butcher and A. Oemler, Jr. The evolution of galaxies in clusters. I - ISIT photometry of C1 0024+1654 and 3C 295. *ApJ*, 219:18–30, January 1978a. doi:10.1086/155751.

-
- H. Butcher and A. Oemler, Jr. The evolution of galaxies in clusters. II - The galaxy content of nearby clusters. *ApJ*, 226:559–565, December 1978b. doi:10.1086/156640.
- H. Butcher and A. Oemler, Jr. The evolution of galaxies in clusters. V - A study of populations since Z approximately equal to 0.5. *ApJ*, 285:426–438, October 1984. doi:10.1086/162519.
- G. Byrd and M. Valtonen. Tidal generation of active spirals and S0 galaxies by rich clusters. *ApJ*, 350:89–94, February 1990. doi:10.1086/168362.
- P. Capak, L. L. Cowie, E. M. Hu, A. J. Barger, M. Dickinson, E. Fernandez, M. Giavalisco, Y. Komiyama, C. Kretchmer, C. McNally, S. Miyazaki, S. Okamura, and D. Stern. A Deep Wide-Field, Optical, and Near-Infrared Catalog of a Large Area around the Hubble Deep Field North. *AJ*, 127:180–198, January 2004. doi:10.1086/380611.
- R. G. Carlberg, H. K. C. Yee, and E. Ellingson. The Average Mass and Light Profiles of Galaxy Clusters. *ApJ*, 478:462, March 1997. doi:10.1086/303805.
- A. Cattaneo, S. M. Faber, J. Binney, A. Dekel, J. Kormendy, R. Mushotzky, A. Babul, P. N. Best, M. Brüggen, A. C. Fabian, C. S. Frenk, A. Khalatyan, H. Netzer, A. Mahdavi, J. Silk, M. Steinmetz, and L. Wisotzki. The role of black holes in galaxy formation and evolution. *Nature*, 460:213–219, July 2009. doi:10.1038/nature08135.
- A. G. Cavaliere, H. Gursky, and W. H. Tucker. Extragalactic X-ray Sources and Associations of Galaxies. *Nature*, 231:437–438, June 1971. doi:10.1038/231437a0.
- S. Chandrasekhar. Dynamical Friction. I. General Considerations: the Coefficient of Dynamical Friction. *ApJ*, 97:255, March 1943a. doi:10.1086/144517.
- S. Chandrasekhar. Dynamical Friction. II. The Rate of Escape of Stars from Clusters and the Evidence for the Operation of Dynamical Friction. *ApJ*, 97:263, March 1943b. doi:10.1086/144518.
- S. Chandrasekhar. Dynamical Friction. III. a More Exact Theory of the Rate of Escape of Stars from Clusters. *ApJ*, 98:54, July 1943c. doi:10.1086/144544.
- Y. Chen, T. H. Reiprich, H. Böhringer, Y. Ikebe, and Y.-Y. Zhang. Statistics of X-ray observables for the cooling-core and non-cooling core galaxy clusters. *A&A*, 466: 805–812, May 2007. doi:10.1051/0004-6361:20066471.
- G. Chon, H. Böhringer, and N. Nowak. The extended ROSAT-ESO Flux-Limited X-ray Galaxy Cluster Survey (REFLEX II) - III. Construction of the first flux-limited supercluster sample. *MNRAS*, 429:3272–3287, March 2013. doi:10.1093/mnras/sts584.
- D. Clowe, M. Bradač, A. H. Gonzalez, M. Markevitch, S. W. Randall, C. Jones, and D. Zaritsky. A Direct Empirical Proof of the Existence of Dark Matter. *ApJ*, 648: L109–L113, September 2006. doi:10.1086/508162.

- Ronald Harry Coase. Warren Nutter Lecture, 1981.
- S. Cole, A. Aragon-Salamanca, C. S. Frenk, J. F. Navarro, and S. E. Zepf. A Recipe for Galaxy Formation. *MNRAS*, 271:781, December 1994.
- S. Cole, W. J. Percival, J. A. Peacock, P. Norberg, C. M. Baugh, C. S. Frenk, I. Baldry, J. Bland-Hawthorn, T. Bridges, R. Cannon, M. Colless, C. Collins, W. Couch, N. J. G. Cross, G. Dalton, V. R. Eke, R. De Propris, S. P. Driver, G. Efstathiou, R. S. Ellis, K. Glazebrook, C. Jackson, A. Jenkins, O. Lahav, I. Lewis, S. Lumsden, S. Maddox, D. Madgwick, B. A. Peterson, W. Sutherland, and K. Taylor. The 2dF Galaxy Redshift Survey: power-spectrum analysis of the final data set and cosmological implications. *MNRAS*, 362:505–534, September 2005. doi:10.1111/j.1365-2966.2005.09318.x.
- M. Colless, G. Dalton, S. Maddox, W. Sutherland, P. Norberg, S. Cole, J. Bland-Hawthorn, T. Bridges, R. Cannon, C. Collins, W. Couch, N. Cross, K. Deeley, R. De Propris, S. P. Driver, G. Efstathiou, R. S. Ellis, C. S. Frenk, K. Glazebrook, C. Jackson, O. Lahav, I. Lewis, S. Lumsden, D. Madgwick, J. A. Peacock, B. A. Peterson, I. Price, M. Seaborne, and K. Taylor. The 2dF Galaxy Redshift Survey: spectra and redshifts. *MNRAS*, 328:1039–1063, December 2001. doi:10.1046/j.1365-8711.2001.04902.x.
- A. P. Cooper, L. Gao, Q. Guo, C. S. Frenk, A. Jenkins, V. Springel, and S. D. M. White. Surface photometry of BCGs and intracluster stars in Lambda-CDM. *ArXiv e-prints*, July 2014.
- L. Cortese, D. Marcillac, J. Richard, H. Bravo-Alfaro, J.-P. Kneib, G. Rieke, G. Covone, E. Egami, J. Rigby, O. Czoske, and J. Davies. The strong transformation of spiral galaxies infalling into massive clusters at $z \sim 0.2$. *MNRAS*, 376:157–172, March 2007. doi:10.1111/j.1365-2966.2006.11369.x.
- K. R. Covey, Ž. Ivezić, D. Schlegel, D. Finkbeiner, N. Padmanabhan, R. H. Lupton, M. A. Agüeros, J. J. Bochanski, S. L. Hawley, A. A. West, A. Seth, A. Kimball, S. M. Gogarten, M. Claire, D. Haggard, N. Kaib, D. P. Schneider, and B. Sesar. Stellar SEDs from 0.3 to 2.5 μm : Tracing the Stellar Locus and Searching for Color Outliers in the SDSS and 2MASS. *AJ*, 134:2398–2417, December 2007. doi:10.1086/522052.
- L. L. Cowie, A. Songaila, E. M. Hu, and J. G. Cohen. New Insight on Galaxy Formation and Evolution From Keck Spectroscopy of the Hawaii Deep Fields. *AJ*, 112:839, September 1996. doi:10.1086/118058.
- J. H. Croston, M. Arnaud, E. Pointecouteau, and G. W. Pratt. An improved deprojection and PSF-deconvolution technique for galaxy-cluster X-ray surface-brightness profiles. *A&A*, 459:1007–1019, December 2006. doi:10.1051/0004-6361:20065795.
- J. H. Croston, G. W. Pratt, H. Böhringer, M. Arnaud, E. Pointecouteau, T. J. Ponman, A. J. R. Sanderson, R. F. Temple, R. G. Bower, and M. Donahue. Galaxy-cluster

- gas-density distributions of the representative XMM-Newton cluster structure survey (REXCESS). *A&A*, 487:431–443, August 2008. doi:10.1051/0004-6361:20079154.
- D. J. Croton, V. Springel, S. D. M. White, G. De Lucia, C. S. Frenk, L. Gao, A. Jenkins, G. Kauffmann, J. F. Navarro, and N. Yoshida. The many lives of active galactic nuclei: cooling flows, black holes and the luminosities and colours of galaxies. *MNRAS*, 365: 11–28, January 2006. doi:10.1111/j.1365-2966.2005.09675.x.
- R. Cruddace, W. Voges, H. Böhringer, C. A. Collins, A. K. Romer, H. MacGillivray, D. Yentis, P. Schuecker, H. Ebeling, and S. De Grandi. The ROSAT All-Sky Survey: a Catalog of Clusters of Galaxies in a Region of 1 steradian around the South Galactic Pole. *ApJS*, 140:239–264, June 2002. doi:10.1086/324519.
- M. Davis, J. Huchra, D. W. Latham, and J. Tonry. A survey of galaxy redshifts. II - The large scale space distribution. *ApJ*, 253:423–445, February 1982. doi:10.1086/159646.
- M. Davis, G. Efstathiou, C. S. Frenk, and S. D. M. White. The evolution of large-scale structure in a universe dominated by cold dark matter. *ApJ*, 292:371–394, May 1985.
- J. de Plaa. The origin of the chemical elements in cluster cores. *Astronomische Nachrichten*, 334:416, April 2013. doi:10.1002/asna.201211870.
- R. De Propris, S. Phillipps, and M. N. Bremer. Deep luminosity functions and colour-magnitude relations for cluster galaxies at $0.2 < z < 0.6$. *MNRAS*, 434:3469–3486, October 2013. doi:10.1093/mnras/stt1262.
- J. W. den Herder, A. C. Brinkman, S. M. Kahn, G. Branduardi-Raymont, K. Thomsen, H. Aarts, M. Audard, J. V. Bixler, A. J. den Boggende, J. Cottam, T. Decker, L. Dubbeldam, C. Erd, H. Goulooze, M. Güdel, P. Guttridge, C. J. Hailey, K. A. Janabi, J. S. Kaastra, P. A. J. de Korte, B. J. van Leeuwen, C. Mauche, A. J. McCalden, R. Mewe, A. Naber, F. B. Paerels, J. R. Peterson, A. P. Rasmussen, K. Rees, I. Sakelliou, M. Sako, J. Spodek, M. Stern, T. Tamura, J. Tandy, C. P. de Vries, S. Welch, and A. Zehnder. The Reflection Grating Spectrometer on board XMM-Newton. *A&A*, 365:L7–L17, January 2001. doi:10.1051/0004-6361:20000058.
- K. Dolag, M. Bartelmann, F. Perrotta, C. Baccigalupi, L. Moscardini, M. Meneghetti, and G. Tormen. Numerical study of halo concentrations in dark-energy cosmologies. *A&A*, 416:853–864, March 2004. doi:10.1051/0004-6361:20031757.
- Arthur Conan Doyle. *The Adventures of Sherlock Holmes*. George Newnes, 1892.
- A. Dressler. Galaxy morphology in rich clusters - Implications for the formation and evolution of galaxies. *ApJ*, 236:351–365, March 1980. doi:10.1086/157753.
- A. Dressler. The Evolution of Galaxies in Clusters. *ARA&A*, 22:185–222, 1984. doi:10.1146/annurev.aa.22.090184.001153.

- A. Dressler, A. Oemler, Jr., H. R. Butcher, and J. E. Gunn. The morphology of distant cluster galaxies. 1: HST observations of CL 0939+4713. *ApJ*, 430:107–120, July 1994. doi:10.1086/174386.
- J. Dubinski. The Origin of the Brightest Cluster Galaxies. *ApJ*, 502:141–149, July 1998. doi:10.1086/305901.
- P.-A. Duc, E. Brinks, J. E. Wink, and I. F. Mirabel. Gas segregation in the interacting system ARP 105. *A&A*, 326:537–553, October 1997.
- R. J. H. Dunn and A. C. Fabian. Investigating heating and cooling in the BCS and B55 cluster samples. *MNRAS*, 385:757–768, April 2008. doi:10.1111/j.1365-2966.2008.12898.x.
- H. Ebeling, A. C. Edge, H. Bohringer, S. W. Allen, C. S. Crawford, A. C. Fabian, W. Voges, and J. P. Huchra. The ROSAT Brightest Cluster Sample - I. The compilation of the sample and the cluster log N-log S distribution. *MNRAS*, 301:881–914, December 1998. doi:10.1046/j.1365-8711.1998.01949.x.
- J. Einasto, G. Hütsi, M. Einasto, E. Saar, D. L. Tucker, V. Müller, P. Heinämäki, and S. S. Allam. Clusters and superclusters in the Sloan Digital Sky Survey. *A&A*, 405:425–443, July 2003. doi:10.1051/0004-6361:20030419.
- D. J. Eisenstein, D. H. Weinberg, E. Agol, H. Aihara, C. Allende Prieto, S. F. Anderson, J. A. Arns, É. Aubourg, S. Bailey, E. Balbinot, and et al. SDSS-III: Massive Spectroscopic Surveys of the Distant Universe, the Milky Way, and Extra-Solar Planetary Systems. *AJ*, 142:72, September 2011. doi:10.1088/0004-6256/142/3/72.
- T. Erben, M. Schirmer, J. P. Dietrich, O. Cordes, L. Habertzettl, M. Hetterscheidt, H. Hildebrandt, O. Schmithuesen, P. Schneider, P. Simon, E. Deul, R. N. Hook, N. Kaiser, M. Radovich, C. Benoist, M. Nonino, L. F. Olsen, I. Prandoni, R. Wichmann, S. Zaggia, D. Bomans, R. J. Dettmar, and J. M. Miralles. GaBoDS: The Garching-Bonn Deep Survey. IV. Methods for the image reduction of multi-chip cameras demonstrated on data from the ESO Wide-Field Imager. *Astronomische Nachrichten*, 326:432–464, July 2005. doi:10.1002/asna.200510396.
- ESO. Wfi zeropoints. <https://www.eso.org/sci/facilities/lasilla/instruments/wfi/inst/zeropoints.html> [Accessed: 2013-07-24], March 2003.
- A. E. Evrard. The intracluster gas fraction in X-ray clusters - Constraints on the clustered mass density. *MNRAS*, 292:289, December 1997.
- A. E. Evrard, C. A. Metzler, and J. F. Navarro. Mass Estimates of X-Ray Clusters. *ApJ*, 469:494, October 1996. doi:10.1086/177798.
- A. C. Fabian. Cooling Flows in Clusters of Galaxies. *ARA&A*, 32:277–318, 1994. doi:10.1146/annurev.aa.32.090194.001425.

-
- A. C. Fabian. Observational Evidence of Active Galactic Nuclei Feedback. *ARA&A*, 50: 455–489, September 2012. doi:10.1146/annurev-astro-081811-125521.
- D. Fabjan, S. Borgani, L. Tornatore, A. Saro, G. Murante, and K. Dolag. Simulating the effect of active galactic nuclei feedback on the metal enrichment of galaxy clusters. *MNRAS*, 401:1670–1690, January 2010. doi:10.1111/j.1365-2966.2009.15794.x.
- D. Fadda, A. Biviano, F. R. Marleau, L. J. Storrie-Lombardi, and F. Durret. Starburst Galaxies in Cluster-feeding Filaments Unveiled by Spitzer. *ApJ*, 672:L9–L12, January 2008. doi:10.1086/526457.
- R. Farouki and S. L. Shapiro. Computer simulations of environmental influences on galaxy evolution in dense clusters. II - Rapid tidal encounters. *ApJ*, 243:32–41, January 1981. doi:10.1086/158563.
- L. Feretti and G. Giovannini. Clusters of Galaxies in the Radio: Relativistic Plasma and ICM/Radio Galaxy Interaction Processes. In M. Plionis, O. López-Cruz, and D. Hughes, editors, *A Pan-Chromatic View of Clusters of Galaxies and the Large-Scale Structure*, volume 740 of *Lecture Notes in Physics*, Berlin Springer Verlag, page 143, 2008. doi:10.1007/978-1-4020-6941-3_5.
- L. Feretti, G. Giovannini, F. Govoni, and M. Murgia. Clusters of galaxies: observational properties of the diffuse radio emission. *A&A Rev.*, 20:54, May 2012. doi:10.1007/s00159-012-0054-z.
- W. L. Freedman, B. F. Madore, V. Scowcroft, C. Burns, A. Monson, S. E. Persson, M. Seibert, and J. Rigby. Carnegie Hubble Program: A Mid-infrared Calibration of the Hubble Constant. *ApJ*, 758:24, October 2012. doi:10.1088/0004-637X/758/1/24.
- W. J. Frith, G. S. Buswell, R. Fong, N. Metcalfe, and T. Shanks. The local hole in the galaxy distribution: evidence from 2MASS. *MNRAS*, 345:1049–1056, November 2003. doi:10.1046/j.1365-8711.2003.07027.x.
- C. Fritsch, H. Böhringer, W. Voges, and H. MacGillivray. The fundamental properties of clusters of galaxies. *Astrophysical Letters and Communications*, 36:167–171, December 1997.
- G. Fritz, A. Davidsen, J. F. Meekins, and H. Friedman. Discovery of an X-Ray Source in Perseus. *ApJ*, 164:L81, March 1971. doi:10.1086/180697.
- M. J. Geller and T. C. Beers. Substructure within clusters of galaxies. *PASP*, 94:421–439, June 1982. doi:10.1086/131003.
- M. J. Geller and J. P. Huchra. Mapping the universe. *Science*, 246:897–903, November 1989. doi:10.1126/science.246.4932.897.

- R. Giacconi, S. Murray, H. Gursky, E. Kellogg, E. Schreier, and H. Tananbaum. The Uhuru catalog of X-ray sources. *ApJ*, 178:281–308, December 1972. doi:10.1086/151790.
- S. Giodini, D. Pierini, A. Finoguenov, G. W. Pratt, H. Boehringer, A. Leauthaud, L. Guzzo, H. Aussel, M. Bolzonella, P. Capak, M. Elvis, G. Hasinger, O. Ilbert, J. S. Kartaltepe, A. M. Koekemoer, S. J. Lilly, R. Massey, H. J. McCracken, J. Rhodes, M. Salvato, D. B. Sanders, N. Z. Scoville, S. Sasaki, V. Smolcic, Y. Taniguchi, D. Thompson, and COSMOS Collaboration. Stellar and Total Baryon Mass Fractions in Groups and Clusters Since Redshift 1. *ApJ*, 703:982–993, September 2009. doi:10.1088/0004-637X/703/1/982.
- G. R. Gisler. The fate of gas in elliptical galaxies and the density evolution of radio sources. *A&A*, 51:137–150, August 1976.
- M. D. Gladders and H. K. C. Yee. A New Method For Galaxy Cluster Detection. I. The Algorithm. *AJ*, 120:2148–2162, October 2000. doi:10.1086/301557.
- M. D. Gladders and H. K. C. Yee. The Red-Sequence Cluster Survey. I. The Survey and Cluster Catalogs for Patches RCS 0926+37 and RCS 1327+29. *ApJS*, 157:1–29, March 2005. doi:10.1086/427327.
- T. Goerdt, O. Y. Gnedin, B. Moore, J. Diemand, and J. Stadel. The survival and disruption of cold dark matter microhaloes: implications for direct and indirect detection experiments. *MNRAS*, 375:191–198, February 2007. doi:10.1111/j.1365-2966.2006.11281.x.
- A. H. Gonzalez, D. Zaritsky, and A. I. Zabludoff. A Census of Baryons in Galaxy Clusters and Groups. *ApJ*, 666:147–155, September 2007. doi:10.1086/519729.
- A. H. Gonzalez, S. Sivanandam, A. I. Zabludoff, and D. Zaritsky. Galaxy Cluster Baryon Fractions Revisited. *ApJ*, 778:14, November 2013. doi:10.1088/0004-637X/778/1/14.
- J. R. Gott, III, M. Jurić, D. Schlegel, F. Hoyle, M. Vogeley, M. Tegmark, N. Bahcall, and J. Brinkmann. A Map of the Universe. *ApJ*, 624:463–484, May 2005. doi:10.1086/428890.
- G. L. Granato, G. De Zotti, L. Silva, A. Bressan, and L. Danese. A Physical Model for the Coevolution of QSOs and Their Spheroidal Hosts. *ApJ*, 600:580–594, January 2004. doi:10.1086/379875.
- J. E. Gunn and J. R. Gott, III. On the Infall of Matter Into Clusters of Galaxies and Some Effects on Their Evolution. *ApJ*, 176:1, August 1972. doi:10.1086/151605.
- J. E. Gunn and B. M. Tinsley. An accelerating Universe. *Nature*, 257:454–457, October 1975. doi:10.1038/257454a0.

-
- H. Gursky, E. Kellogg, S. Murray, C. Leong, H. Tananbaum, and R. Giacconi. A Strong X-Ray Source in the Coma Cluster Observed by UHURU. *ApJ*, 167:L81, August 1971. doi:10.1086/180765.
- D. B. Haarsma, L. Leisman, M. Donahue, S. Bruch, H. Böhringer, J. H. Croston, G. W. Pratt, G. M. Voit, M. Arnaud, and D. Pierini. Brightest Cluster Galaxies and Core Gas Density in REXCESS Clusters. *ApJ*, 713:1037–1047, April 2010. doi:10.1088/0004-637X/713/2/1037.
- N. Häring and H.-W. Rix. On the Black Hole Mass-Bulge Mass Relation. *ApJ*, 604:L89–L92, April 2004. doi:10.1086/383567.
- Y. Hashimoto, J. P. Henry, H. Böhringer, and G. Hasinger. Comparison between X-ray morphology and optical characteristics of clusters of galaxies. *A&A*, 468:25–31, June 2007. doi:10.1051/0004-6361:20066833.
- N. Hasler, E. Bulbul, M. Bonamente, J. E. Carlstrom, T. L. Culverhouse, M. Gralla, C. Greer, D. Hawkins, R. Hennessy, M. Joy, J. Kolodziejczak, J. W. Lamb, D. Landry, E. M. Leitch, A. Mantz, D. P. Marrone, A. Miller, T. Mroczkowski, S. Muchovej, T. Plagge, C. Pryke, and D. Woody. Joint Analysis of X-Ray and Sunyaev-Zel’dovich Observations of Galaxy Clusters Using an Analytic Model of the Intracluster Medium. *ApJ*, 748:113, April 2012. doi:10.1088/0004-637X/748/2/113.
- W. Herschel. On the Construction of the Heavens. *Royal Society of London Philosophical Transactions Series I*, 75:213–266, 1785.
- F. W. High, C. W. Stubbs, A. Rest, B. Stalder, and P. Challis. Stellar Locus Regression: Accurate Color Calibration and the Real-Time Determination of Galaxy Cluster Photometric Redshifts. *AJ*, 138:110–129, July 2009. doi:10.1088/0004-6256/138/1/110.
- J. Hlavacek-Larrondo, S. W. Allen, G. B. Taylor, A. C. Fabian, R. E. A. Canning, N. Werner, J. S. Sanders, C. K. Grimes, S. Ehlert, and A. von der Linden. Probing the extreme realm of AGN feedback in the massive galaxy cluster, RX J1532.9+3021. June 2013. URL <http://de.arxiv.org/abs/1306.0907>.
- H. Hoekstra and B. Jain. Weak Gravitational Lensing and Its Cosmological Applications. *Annual Review of Nuclear and Particle Science*, 58:99–123, November 2008. doi:10.1146/annurev.nucl.58.110707.171151.
- D. W. Hogg. Distance measures in cosmology. *ArXiv Astrophysics e-prints*, May 1999.
- J. G. Holland, H. Böhringer, G. Chon, and D. Pierini. Optical and X-ray profiles in the REXCESS sample of galaxy clusters*. *MNRAS*, 448:2644–2664, April 2015. doi:10.1093/mnras/stv097.
- I. Horváth, J. Hakkila, and Z. Bagoly. Possible structure in the GRB sky distribution at redshift two. *A&A*, 561:L12, January 2014. doi:10.1051/0004-6361/201323020.

- J.-S. Huang, D. Thompson, M. W. Kümmel, K. Meisenheimer, C. Wolf, S. V. W. Beckwith, R. Fockenbrock, J. W. Fried, H. Hippelein, B. von Kuhlmann, S. Phleps, H.-J. Röser, and E. Thommes. The Calar Alto Deep Imaging Survey: K-band Galaxy number counts. *A&A*, 368:787–796, March 2001. doi:10.1051/0004-6361:20010057.
- E. Hubble. A Relation between Distance and Radial Velocity among Extra-Galactic Nebulae. *Proceedings of the National Academy of Science*, 15:168–173, March 1929. doi:10.1073/pnas.15.3.168.
- J. Huchra, M. Davis, D. Latham, and J. Tonry. A survey of galaxy redshifts. IV - The data. *ApJS*, 52:89–119, June 1983. doi:10.1086/190860.
- D. S. Hudson, R. Mittal, T. H. Reiprich, P. E. J. Nulsen, H. Andernach, and C. L. Sarazin. What is a cool-core cluster? a detailed analysis of the cores of the X-ray flux-limited HIFLUGCS cluster sample. *A&A*, 513:A37, April 2010. doi:10.1051/0004-6361/200912377.
- J. D. Hunter. Matplotlib: A 2d graphics environment. *Computing In Science & Engineering*, 9(3):90–95, 2007.
- F. Jansen, D. Lumb, B. Altieri, J. Clavel, M. Ehle, C. Erd, C. Gabriel, M. Guainazzi, P. Gondoin, R. Much, R. Munoz, M. Santos, N. Schartel, D. Texier, and G. Vacanti. XMM-Newton observatory. I. The spacecraft and operations. *A&A*, 365:L1–L6, January 2001. doi:10.1051/0004-6361:20000036.
- D. H. Jones, M. A. Read, W. Saunders, M. Colless, T. Jarrett, Q. A. Parker, A. P. Fairall, T. Mauch, E. M. Sadler, F. G. Watson, D. Burton, L. A. Campbell, P. Cass, S. M. Croom, J. Dawe, K. Fiegert, L. Frankcombe, M. Hartley, J. Huchra, D. James, E. Kirby, O. Lahav, J. Lucey, G. A. Mamon, L. Moore, B. A. Peterson, S. Prior, D. Proust, K. Russell, V. Safouris, K.-I. Wakamatsu, E. Westra, and M. Williams. The 6dF Galaxy Survey: final redshift release (DR3) and southern large-scale structures. *MNRAS*, 399:683–698, October 2009. doi:10.1111/j.1365-2966.2009.15338.x.
- L. R. Jones, R. Fong, T. Shanks, R. S. Ellis, and B. A. Peterson. Galaxy number counts. I - Photographic observations to $B = 23.5$ mag. *MNRAS*, 249:481–497, April 1991.
- S. Juneau, K. Glazebrook, D. Crampton, P. J. McCarthy, S. Savaglio, R. Abraham, R. G. Carlberg, H.-W. Chen, D. Le Borgne, R. O. Marzke, K. Roth, I. Jørgensen, I. Hook, and R. Murowinski. Cosmic Star Formation History and Its Dependence on Galaxy Stellar Mass. *ApJ*, 619:L135–L138, February 2005. doi:10.1086/427937.
- N. Kashikawa, K. Shimasaku, N. Yasuda, M. Ajiki, M. Akiyama, H. Ando, K. Aoki, M. Doi, S. S. Fujita, H. Furusawa, T. Hayashino, F. Iwamuro, M. Iye, H. Karoji, N. Kobayashi, K. Kodaira, T. Kodama, Y. Komiyama, Y. Matsuda, S. Miyazaki, Y. Mizumoto, T. Morokuma, K. Motohara, T. Murayama, T. Nagao, K. Nariai, K. Ohta, S. Okamura, M. Ouchi, T. Sasaki, Y. Sato, K. Sekiguchi, Y. Shioya,

-
- H. Tamura, Y. Taniguchi, M. Umemura, T. Yamada, and M. Yoshida. The Subaru Deep Field: The Optical Imaging Data. *PASJ*, 56:1011–1023, December 2004. doi:10.1093/pasj/56.6.1011.
- G. Kauffmann, S. D. M. White, and B. Guiderdoni. The Formation and Evolution of Galaxies Within Merging Dark Matter Haloes. *MNRAS*, 264:201, September 1993.
- G. Kauffmann, T. M. Heckman, S. D. M. White, S. Charlot, C. Tremonti, J. Brinchmann, G. Bruzual, E. W. Peng, M. Seibert, M. Bernardi, M. Blanton, J. Brinkmann, F. Castander, I. Csábai, M. Fukugita, Z. Ivezic, J. A. Munn, R. C. Nichol, N. Padmanabhan, A. R. Thakar, D. H. Weinberg, and D. York. Stellar masses and star formation histories for 10^5 galaxies from the Sloan Digital Sky Survey. *MNRAS*, 341:33–53, May 2003. doi:10.1046/j.1365-8711.2003.06291.x.
- F. Köhlinger and R. W. Schmidt. Strong lensing in RX J1347.5-1145 revisited. *MNRAS*, 437:1858–1871, January 2014. doi:10.1093/mnras/stt2017.
- V. Kolokotronis, S. Basilakos, M. Plionis, and I. Georgantopoulos. Searching for cluster substructure using APM and ROSAT data. *MNRAS*, 320:49–60, January 2001. doi:10.1046/j.1365-8711.2001.03924.x.
- Andrey V. Kravtsov and Stefano Borgani. Formation of galaxy clusters. *Annual Review of Astronomy and Astrophysics*, 50(1):353–409, 2012. doi:10.1146/annurev-astro-081811-125502. URL <http://www.annualreviews.org/doi/abs/10.1146/annurev-astro-081811-125502>.
- La Scilla SciOps. *The Wide-field Imager Handbook*. La Scilla SciOps, 2.0 edition, May 2005.
- R. B. Larson, B. M. Tinsley, and C. N. Caldwell. The evolution of disk galaxies and the origin of S0 galaxies. *ApJ*, 237:692–707, May 1980. doi:10.1086/157917.
- S. M. Lea, J. Silk, E. Kellogg, and S. Murray. Thermal-Bremsstrahlung Interpretation of Cluster X-Ray Sources. *ApJ*, 184:L105, September 1973. doi:10.1086/181300.
- Y.-T. Lin, J. J. Mohr, and S. A. Stanford. Near-Infrared Properties of Galaxy Clusters: Luminosity as a Binding Mass Predictor and the State of Cluster Baryons. *ApJ*, 591:749–763, July 2003. doi:10.1086/375513.
- M. Loewenstein. Chemical Composition of the Intracluster Medium. *Origin and Evolution of the Elements*, page 422, 2004.
- Y.-S. Loh, E. Ellingson, H. K. C. Yee, D. G. Gilbank, M. D. Gladders, and L. F. Barrientos. The Color Bimodality in Galaxy Clusters since $z \sim 0.9$. *ApJ*, 680:214–223, June 2008. doi:10.1086/587830.

- J. Loveday. The APM Bright Galaxy Catalogue. *MNRAS*, 278:1025–1048, February 1996.
- D. Lynden-Bell. Statistical mechanics of violent relaxation in stellar systems. *MNRAS*, 136:101, 1967.
- C.-J. Ma, H. Ebeling, P. Marshall, and T. Schrabback. The impact of a major cluster merger on galaxy evolution in MACSJ0025.4-1225. *MNRAS*, 406:121–136, July 2010. doi:10.1111/j.1365-2966.2010.16673.x.
- A. Mahdavi, H. Hoekstra, A. Babul, C. Bildfell, T. Jeltema, and J. P. Henry. Joint Analysis of Cluster Observations. II. Chandra/XMM-Newton X-Ray and Weak Lensing Scaling Relations for a Sample of 50 Rich Clusters of Galaxies. *ApJ*, 767:116, April 2013. doi:10.1088/0004-637X/767/2/116.
- M. Markevitch and A. Vikhlinin. Shocks and cold fronts in galaxy clusters. *Phys. Rep.*, 443:1–53, May 2007. doi:10.1016/j.physrep.2007.01.001.
- T. A. Matthews, W. W. Morgan, and M. Schmidt. A Discussion of Galaxies Identified with Radio Sources. *ApJ*, 140:35, July 1964. doi:10.1086/147890.
- I. G. McCarthy, C. S. Frenk, A. S. Font, C. G. Lacey, R. G. Bower, N. L. Mitchell, M. L. Balogh, and T. Theuns. Ram pressure stripping the hot gaseous haloes of galaxies in groups and clusters. *MNRAS*, 383:593–605, January 2008. doi:10.1111/j.1365-2966.2007.12577.x.
- H. J. McCracken, N. Metcalfe, T. Shanks, A. Campos, J. P. Gardner, and R. Fong. Galaxy number counts - IV. Surveying the Herschel Deep Field in the near-infrared. *MNRAS*, 311:707–718, February 2000. doi:10.1046/j.1365-8711.2000.03096.x.
- H. J. McCracken, M. Radovich, E. Bertin, Y. Mellier, M. Dantel-Fort, O. Le Fèvre, J. C. Cuillandre, S. Gwyn, S. Foucaud, and G. Zamorani. The VIRMOS deep imaging survey. II: CFH12K BVRI optical data for the 0226-04 deep field. *A&A*, 410:17–32, October 2003. doi:10.1051/0004-6361:20031081.
- M. McDonald, M. Bayliss, B. A. Benson, R. J. Foley, J. Ruel, P. Sullivan, S. Veilleux, K. A. Aird, M. L. N. Ashby, M. Bautz, G. Bazin, L. E. Bleem, M. Brodwin, J. E. Carlstrom, C. L. Chang, H. M. Cho, A. Clocchiatti, T. M. Crawford, A. T. Crites, T. de Haan, S. Desai, M. A. Dobbs, J. P. Dudley, E. Egami, W. R. Forman, G. P. Garmire, E. M. George, M. D. Gladders, A. H. Gonzalez, N. W. Halverson, N. L. Harrington, F. W. High, G. P. Holder, W. L. Holzzapfel, S. Hoover, J. D. Hrubes, C. Jones, M. Joy, R. Keisler, L. Knox, A. T. Lee, E. M. Leitch, J. Liu, M. Lueker, D. Luongvan, A. Mantz, D. P. Marrone, J. J. McMahan, J. Mehl, S. S. Meyer, E. D. Miller, L. Mocanu, J. J. Mohr, T. E. Montroy, S. S. Murray, T. Natoli, S. Padin, T. Plagge, C. Pryke, T. D. Rawle, C. L. Reichardt, A. Rest, M. Rex, J. E. Ruhl, B. R. Saliwanchik, A. Saro, J. T. Sayre, K. K. Schaffer, L. Shaw, E. Shirokoff, R. Simcoe, J. Song, H. G.

- Spieler, B. Stalder, Z. Staniszewski, A. A. Stark, K. Story, C. W. Stubbs, R. Šuhada, A. van Engelen, K. Vanderlinde, J. D. Vieira, A. Vikhlinin, R. Williamson, O. Zahn, and A. Zenteno. A massive, cooling-flow-induced starburst in the core of a luminous cluster of galaxies. *Nature*, 488:349–352, August 2012. doi:10.1038/nature11379.
- C. F. McKee. X-Ray Emission from an Inward-Propagating Shock in Young Supernova Remnants. *ApJ*, 188:335–340, March 1974. doi:10.1086/152721.
- B. R. McNamara and P. E. J. Nulsen. Heating Hot Atmospheres with Active Galactic Nuclei. *ARA&A*, 45:117–175, September 2007. doi:10.1146/annurev.astro.45.051806.110625.
- J. F. Meekins, G. Fritz, T. A. Chubb, and H. Friedman. Physical Sciences: X-rays from the Coma Cluster of Galaxies. *Nature*, 231:107–108, May 1971. doi:10.1038/231107a0.
- D. Merritt. Relaxation and tidal stripping in rich clusters of galaxies. I. Evolution of the mass distribution. *ApJ*, 264:24–48, January 1983. doi:10.1086/160571.
- C. Messier. Catalogue des Nébuleuses & des amas d'Étoiles (Catalog of Nebulae and Star Clusters). Technical report, 1781.
- N. Metcalfe. The galaxy number-counts page, January 2010. URL <http://astro.dur.ac.uk/~nm/pubhtml/counts/counts.html>. accessed: 13-05-2013.
- N. Metcalfe, T. Shanks, R. Fong, and L. R. Jones. Galaxy number counts. II - CCD observations to $B = 25$ mag. *MNRAS*, 249:498–522, April 1991.
- N. Metcalfe, T. Shanks, R. Fong, and N. Roche. Galaxy number counts - III. Deep CCD observations to $B=27.5$ mag. *MNRAS*, 273:257–276, March 1995.
- N. Metcalfe, T. Shanks, A. Campos, R. Fong, and J. P. Gardner. Galaxy formation at high redshifts. *Nature*, 383:236–239, September 1996. doi:10.1038/383236a0.
- N. Metcalfe, T. Shanks, A. Campos, H. J. McCracken, and R. Fong. Galaxy number counts - V. Ultradeep counts: the Herschel and Hubble Deep Fields. *MNRAS*, 323: 795–830, May 2001. doi:10.1046/j.1365-8711.2001.04168.x.
- N. Metcalfe, T. Shanks, P. M. Weilbacher, H. J. McCracken, R. Fong, and D. Thompson. Galaxy number counts - VI. An H-band survey of the Herschel Deep Field. *MNRAS*, 370:1257–1273, August 2006. doi:10.1111/j.1365-2966.2006.10534.x.
- R. Mittal, D. S. Hudson, T. H. Reiprich, and T. Clarke. AGN heating and ICM cooling in the HIFLUGCS sample of galaxy clusters. *A&A*, 501:835–850, July 2009. doi:10.1051/0004-6361/200810836.
- H. Mo, F. Van den Bosch, and S. White. *Galaxy formation and evolution*. Cambridge University Press, 2010.

- J. J. Mohr, D. G. Fabricant, and M. J. Geller. An X-ray method for detecting substructure in galaxy clusters - Application to Perseus, A2256, Centaurus, Coma, and Sersic 40/6. *ApJ*, 413:492–505, August 1993. doi:10.1086/173019.
- J. J. Mohr, A. E. Evrard, D. G. Fabricant, and M. J. Geller. Cosmological Constraints from Observed Cluster X-Ray Morphologies. *ApJ*, 447:8, July 1995. doi:10.1086/175852.
- B. Moore, N. Katz, G. Lake, A. Dressler, and A. Oemler. Galaxy harassment and the evolution of clusters of galaxies. *Nature*, 379:613–616, February 1996. doi:10.1038/379613a0.
- B. Moore, G. Lake, and N. Katz. Morphological Transformation from Galaxy Harassment. *ApJ*, 495:139, March 1998. doi:10.1086/305264.
- B. Moore, J. Diemand, and J. Stadel. On the age-radius relation and orbital history of cluster galaxies. In A. Diaferio, editor, *IAU Colloq. 195: Outskirts of Galaxy Clusters: Intense Life in the Suburbs*, pages 513–518, July 2004. doi:10.1017/S1743921304001127.
- W. W. Morgan, S. Kayser, and R. A. White. cD galaxies in poor clusters. *ApJ*, 199: 545–548, August 1975. doi:10.1086/153721.
- J. E. Morrison, S. Röser, B. McLean, B. Bucciarelli, and B. Lasker. The Guide Star Catalog, Version 1.2: An Astrometric Recalibration and Other Refinements. *AJ*, 121: 1752–1763, March 2001. doi:10.1086/319383.
- J. F. Navarro, C. S. Frenk, and S. D. M. White. Simulations of X-ray clusters. *MNRAS*, 275:720–740, August 1995.
- J. F. Navarro, C. S. Frenk, and S. D. M. White. The Structure of Cold Dark Matter Halos. *ApJ*, 462:563–+, May 1996.
- J. F. Navarro, C. S. Frenk, and S. D. M. White. A Universal Density Profile from Hierarchical Clustering. *ApJ*, 490:493, December 1997. doi:10.1086/304888.
- D.O. North. An analysis of the factors which determine signal/noise discrimination in pulsed-carrier systems. *Proceedings of the IEEE*, 51(7):1016–1027, July 1963. ISSN 0018-9219. doi:10.1109/PROC.1963.2383.
- P. E. J. Nulsen and B. R. McNamara. AGN feedback in clusters: Shock and sound heating. *Astronomische Nachrichten*, 334:386, April 2013. doi:10.1002/asna.201211863.
- Harry Nyquist. Certain topics in telegraph transmission theory. *American Institute of Electrical Engineers, Transactions of the*, 47(2):617–644, 1928.
- A. Oemler, Jr. The Systematic Properties of Clusters of Galaxies. Photometry of 15 Clusters. *ApJ*, 194:1–20, November 1974. doi:10.1086/153216.

-
- A. Oemler, Jr. The structure of elliptical and cD galaxies. *ApJ*, 209:693–709, November 1976. doi:10.1086/154769.
- A. Oemler, Jr., A. Dressler, and H. R. Butcher. The Morphology of Distant Cluster Galaxies. II. HST Observations of Four Rich Clusters at $Z \approx 0.4$. *ApJ*, 474:561, January 1997. doi:10.1086/303472.
- G. A. Ogrean, N. A. Hatch, A. Simionescu, H. Böhringer, M. Brüggen, A. C. Fabian, and N. Werner. Central galaxy growth and feedback in the most massive nearby cool core cluster. *MNRAS*, 406:354–367, July 2010. doi:10.1111/j.1365-2966.2010.16718.x.
- T. B. O’Hara, J. J. Mohr, J. J. Bialek, and A. E. Evrard. Effects of Mergers and Core Structure on the Bulk Properties of Nearby Galaxy Clusters. *ApJ*, 639:64–80, March 2006. doi:10.1086/499327.
- J. B. Oke and J. E. Gunn. Secondary standard stars for absolute spectrophotometry. *ApJ*, 266:713–717, March 1983. doi:10.1086/160817.
- J. P. Ostriker and M. A. Hausman. Cannibalism among the galaxies - Dynamically produced evolution of cluster luminosity functions. *ApJ*, 217:L125–L129, November 1977. doi:10.1086/182554.
- P. Patel, S. Maddox, F. R. Pearce, A. Aragón-Salamanca, and E. Conway. An imaging survey of a uniform sample of brightest cluster galaxies and intracluster light. *MNRAS*, 370:851–883, August 2006. doi:10.1111/j.1365-2966.2006.10510.x.
- J. A. Peacock. Studying Large-scale Structure with the 2dF Galaxy Redshift Survey. In N. Metcalfe and T. Shanks, editors, *A New Era in Cosmology*, volume 283 of *Astronomical Society of the Pacific Conference Series*, page 19, 2002.
- A. A. Penzias and R. W. Wilson. A Measurement of Excess Antenna Temperature at 4080 Mc/s. *ApJ*, 142:419–421, July 1965. doi:10.1086/148307.
- S. Perlmutter, G. Aldering, G. Goldhaber, R. A. Knop, P. Nugent, P. G. Castro, S. Deustua, S. Fabbro, A. Goobar, D. E. Groom, I. M. Hook, A. G. Kim, M. Y. Kim, J. C. Lee, N. J. Nunes, R. Pain, C. R. Pennypacker, R. Quimby, C. Lidman, R. S. Ellis, M. Irwin, R. G. McMahon, P. Ruiz-Lapuente, N. Walton, B. Schaefer, B. J. Boyle, A. V. Filippenko, T. Matheson, A. S. Fruchter, N. Panagia, H. J. M. Newberg, W. J. Couch, and Supernova Cosmology Project. Measurements of Omega and Lambda from 42 High-Redshift Supernovae. *ApJ*, 517:565–586, June 1999. doi:10.1086/307221.
- J. R. Peterson and A. C. Fabian. X-ray spectroscopy of cooling clusters. *Phys. Rep.*, 427: 1–39, April 2006. doi:10.1016/j.physrep.2005.12.007.

- J. R. Peterson, S. M. Kahn, F. B. S. Paerels, J. S. Kaastra, T. Tamura, J. A. M. Bleeker, C. Ferrigno, and J. G. Jernigan. High-Resolution X-Ray Spectroscopic Constraints on Cooling-Flow Models for Clusters of Galaxies. *ApJ*, 590:207–224, June 2003. doi:10.1086/374830.
- A. Pillepich, C. Porciani, and T. H. Reiprich. The X-ray cluster survey with eRosita: forecasts for cosmology, cluster physics and primordial non-Gaussianity. *MNRAS*, 422: 44–69, May 2012. doi:10.1111/j.1365-2966.2012.20443.x.
- Planck Collaboration. Planck 2015 results. XIII. Cosmological parameters. *ArXiv e-prints*, February 2015.
- Planck Collaboration, P. A. R. Ade, N. Aghanim, M. I. R. Alves, C. Armitage-Caplan, M. Arnaud, M. Ashdown, F. Atrio-Barandela, J. Aumont, H. Aussel, and et al. Planck 2013 results. I. Overview of products and scientific results. *A&A*, 571:A1, November 2014a. doi:10.1051/0004-6361/201321529.
- Planck Collaboration, P. A. R. Ade, N. Aghanim, C. Armitage-Caplan, M. Arnaud, M. Ashdown, F. Atrio-Barandela, J. Aumont, H. Aussel, C. Baccigalupi, and et al. Planck 2013 results. XXIX. The Planck catalogue of Sunyaev-Zeldovich sources. *A&A*, 571:A29, November 2014b. doi:10.1051/0004-6361/201321523.
- B. M. Poggianti. K and evolutionary corrections from UV to IR. *A&AS*, 122:399–407, May 1997. doi:10.1051/aas:1997142.
- B. M. Poggianti, A. Aragón-Salamanca, D. Zaritsky, G. De Lucia, B. Milvang-Jensen, V. Desai, P. Jablonka, C. Halliday, G. Rudnick, J. Varela, S. Bamford, P. Best, D. Clowe, S. Noll, R. Saglia, R. Pelló, L. Simard, A. von der Linden, and S. White. The Environments of Starburst and Post-Starburst Galaxies at $z = 0.4-0.8$. *ApJ*, 693: 112–131, March 2009. doi:10.1088/0004-637X/693/1/112.
- O. R. Pols, K.-P. Schröder, J. R. Hurley, C. A. Tout, and P. P. Eggleton. Stellar evolution models for $Z = 0.0001$ to 0.03 . *MNRAS*, 298:525–536, August 1998. doi:10.1046/j.1365-8711.1998.01658.x.
- G. B. Poole, M. A. Fardal, A. Babul, I. G. McCarthy, T. Quinn, and J. Wadsley. The impact of mergers on relaxed X-ray clusters - I. Dynamical evolution and emergent transient structures. *MNRAS*, 373:881–905, December 2006. doi:10.1111/j.1365-2966.2006.10916.x.
- P. Popesso, H. Böhringer, J. Brinkmann, W. Voges, and D. G. York. RASS-SDSS Galaxy clusters survey. I. The catalog and the correlation of X-ray and optical properties. *A&A*, 423:449–467, August 2004. doi:10.1051/0004-6361:20035818.
- P. Popesso, A. Biviano, H. Böhringer, and M. Romaniello. RASS-SDSS Galaxy cluster survey. IV. A ubiquitous dwarf galaxy population in clusters. *A&A*, 445:29–42, January 2006. doi:10.1051/0004-6361:20052954.

-
- P. Popesso, A. Biviano, H. Böhringer, and M. Romaniello. RASS-SDSS galaxy cluster survey. VII. On the cluster mass-to-light ratio and the halo occupation distribution. *A&A*, 464:451–464, March 2007. doi:10.1051/0004-6361:20054708.
- Terry Pratchett. *The Last Hero*. Victor Gollancz, 2001.
- G. W. Pratt, J. H. Croston, M. Arnaud, and H. Böhringer. Galaxy cluster X-ray luminosity scaling relations from a representative local sample (REXCESS). *A&A*, 498:361–378, May 2009. doi:10.1051/0004-6361/200810994.
- W. H. Press and P. Schechter. Formation of Galaxies and Clusters of Galaxies by Self-Similar Gravitational Condensation. *ApJ*, 187:425–438, February 1974. doi:10.1086/152650.
- M. Ramella, A. Biviano, A. Pisani, J. Varela, D. Bettoni, W. J. Couch, M. D’Onofrio, A. Dressler, G. Fasano, P. Kjörgaard, M. Moles, E. Pignatelli, and B. M. Poggianti. Substructures in WINGS clusters. *A&A*, 470:39–51, July 2007. doi:10.1051/0004-6361:20077245.
- M. J. Rees and J. P. Ostriker. Cooling, dynamics and fragmentation of massive gas clouds - Clues to the masses and radii of galaxies and clusters. *MNRAS*, 179:541–559, June 1977.
- T. H. Reiprich and H. Böhringer. The Mass Function of an X-Ray Flux-limited Sample of Galaxy Clusters. *ApJ*, 567:716–740, March 2002. doi:10.1086/338753.
- T. H. Reiprich, K. Basu, S. Ettori, H. Israel, L. Lovisari, S. Molendi, E. Pointecouteau, and M. Roncarelli. Outskirts of Galaxy Clusters. *Space Sci. Rev.*, 177:195–245, August 2013. doi:10.1007/s11214-013-9983-8.
- D. O. Richstone. Collisions of galaxies in dense clusters. II - Dynamical evolution of cluster galaxies. *ApJ*, 204:642–648, March 1976. doi:10.1086/154213.
- A. G. Riess, A. V. Filippenko, P. Challis, A. Clocchiatti, A. Diercks, P. M. Garnavich, R. L. Gilliland, C. J. Hogan, S. Jha, R. P. Kirshner, B. Leibundgut, M. M. Phillips, D. Reiss, B. P. Schmidt, R. A. Schommer, R. C. Smith, J. Spyromilio, C. Stubbs, N. B. Suntzeff, and J. Tonry. Observational Evidence from Supernovae for an Accelerating Universe and a Cosmological Constant. *AJ*, 116:1009–1038, September 1998. doi:10.1086/300499.
- A. G. Riess, L. Macri, S. Casertano, H. Lampeitl, H. C. Ferguson, A. V. Filippenko, S. W. Jha, W. Li, and R. Chornock. A 3% Solution: Determination of the Hubble Constant with the Hubble Space Telescope and Wide Field Camera 3. *ApJ*, 730:119, April 2011. doi:10.1088/0004-637X/730/2/119.

- E. Rizza, J. O. Burns, M. J. Ledlow, F. N. Owen, W. Voges, and M. Bliton. X-ray observations of distant Abell clusters. *MNRAS*, 301:328–342, December 1998. doi:10.1046/j.1365-8711.1998.01972.x.
- P. Rosati, R. Della Ceca, C. Norman, and R. Giacconi. The ROSAT Deep Cluster Survey: The X-Ray Luminosity Function out to $z = 0.8$. *ApJ*, 492:L21–L24, January 1998. doi:10.1086/311085.
- H. R. Russell, J. S. Sanders, A. C. Fabian, S. A. Baum, M. Donahue, A. C. Edge, B. R. McNamara, and C. P. O’Dea. Chandra observation of two shock fronts in the merging galaxy cluster Abell 2146. *MNRAS*, 406:1721–1733, August 2010. doi:10.1111/j.1365-2966.2010.16822.x.
- J. S. Santos, P. Tozzi, P. Rosati, and H. Böhringer. The evolution of cool-core clusters. *A&A*, 521:A64, October 2010. doi:10.1051/0004-6361/201015208.
- C. L. Sarazin. Galactic coronae, quasar absorption lines, and the origin of the intracluster medium. *Astrophys. Lett.*, 20:93–99, 1979.
- C. L. Sarazin. X-ray emission from clusters of galaxies. *Reviews of Modern Physics*, 58:1–115, January 1986. doi:10.1103/RevModPhys.58.1.
- CL Sarazin. Gas dynamics in clusters of galaxies. In *A Pan-Chromatic View of Clusters of Galaxies and the Large-Scale Structure*, pages 1–30. Springer, 2008.
- M. Sarazin and F. Roddier. The ESO differential image motion monitor. *A&A*, 227:294–300, January 1990.
- P. Schechter. An analytic expression for the luminosity function for galaxies. *ApJ*, 203:297–306, January 1976. doi:10.1086/154079.
- J. M. Schombert. The structure of brightest cluster members. I - Surface photometry. *ApJS*, 60:603–693, March 1986. doi:10.1086/191100.
- J. M. Schombert. The structure of brightest cluster members. III - cD envelopes. *ApJ*, 328:475–488, May 1988. doi:10.1086/166306.
- E. S. Sheldon, D. E. Johnston, M. Masjedi, T. A. McKay, M. R. Blanton, R. Scranton, R. H. Wechsler, B. P. Koester, S. M. Hansen, J. A. Frieman, and J. Annis. Cross-correlation Weak Lensing of SDSS Galaxy Clusters. III. Mass-to-Light Ratios. *ApJ*, 703:2232–2248, October 2009a. doi:10.1088/0004-637X/703/2/2232.
- E. S. Sheldon, D. E. Johnston, R. Scranton, B. P. Koester, T. A. McKay, H. Oyaizu, C. Cunha, M. Lima, H. Lin, J. A. Frieman, R. H. Wechsler, J. Annis, R. Mandelbaum, N. A. Bahcall, and M. Fukugita. Cross-correlation Weak Lensing of SDSS Galaxy Clusters. I. Measurements. *ApJ*, 703:2217–2231, October 2009b. doi:10.1088/0004-637X/703/2/2217.

-
- J. Silk. On the fragmentation of cosmic gas clouds. I - The formation of galaxies and the first generation of stars. *ApJ*, 211:638–648, February 1977. doi:10.1086/154972.
- S. Smith. The Mass of the Virgo Cluster. *ApJ*, 83:23, January 1936. doi:10.1086/143697.
- V. Springel, S. D. M. White, A. Jenkins, C. S. Frenk, N. Yoshida, L. Gao, J. Navarro, R. Thacker, D. Croton, J. Helly, J. A. Peacock, S. Cole, P. Thomas, H. Couchman, A. Evrard, J. Colberg, and F. Pearce. Simulations of the formation, evolution and clustering of galaxies and quasars. *Nature*, 435:629–636, June 2005. doi:10.1038/nature03597.
- C. Stoughton, R. H. Lupton, M. Bernardi, M. R. Blanton, S. Burles, F. J. Castander, A. J. Connolly, D. J. Eisenstein, J. A. Frieman, G. S. Hennessey, R. B. Hindsley, Ž. Ivezić, S. Kent, P. Z. Kunszt, B. C. Lee, A. Meiksin, J. A. Munn, H. J. Newberg, R. C. Nichol, T. Nicinski, J. R. Pier, G. T. Richards, M. W. Richmond, D. J. Schlegel, J. A. Smith, M. A. Strauss, M. SubbaRao, A. S. Szalay, A. R. Thakar, D. L. Tucker, D. E. Vanden Berk, B. Yanny, J. K. Adelman, J. E. Anderson, Jr., S. F. Anderson, J. Annis, N. A. Bahcall, J. A. Bakken, M. Bartelmann, S. Bastian, A. Bauer, E. Berman, H. Böhringer, W. N. Boroski, S. Bracker, C. Briegel, J. W. Briggs, J. Brinkmann, R. Brunner, L. Carey, M. A. Carr, B. Chen, D. Christian, P. L. Colestock, J. H. Crocker, I. Csabai, P. C. Czarapata, J. Dalcanton, A. F. Davidsen, J. E. Davis, W. Dehnen, S. Dodelson, M. Doi, T. Dombeck, M. Donahue, N. Ellman, B. R. Elms, M. L. Evans, L. Eyer, X. Fan, G. R. Federwitz, S. Friedman, M. Fukugita, R. Gal, B. Gillespie, K. Glazebrook, J. Gray, E. K. Grebel, B. Greenawalt, G. Greene, J. E. Gunn, E. de Haas, Z. Haiman, M. Haldeman, P. B. Hall, M. Hamabe, B. Hansen, F. H. Harris, H. Harris, M. Harvanek, S. L. Hawley, J. J. E. Hayes, T. M. Heckman, A. Helmi, A. Henden, C. J. Hogan, D. W. Hogg, D. J. Holmgren, J. Holtzman, C.-H. Huang, C. Hull, S.-I. Ichikawa, T. Ichikawa, D. E. Johnston, G. Kauffmann, R. S. J. Kim, T. Kimball, E. Kinney, M. Klaene, S. J. Kleinman, A. Klypin, G. R. Knapp, J. Korienek, J. Krolik, R. G. Kron, J. Krziesiński, D. Q. Lamb, R. F. Leger, S. Limmon-gkol, C. Lindenmeyer, D. C. Long, C. Loomis, J. Loveday, B. MacKinnon, E. J. Manners, P. M. Mantsch, B. Margon, P. McGehee, T. A. McKay, B. McLean, K. Menou, A. Merelli, H. J. Mo, D. G. Monet, O. Nakamura, V. K. Narayanan, T. Nash, E. H. Neilsen, Jr., P. R. Newman, A. Nitta, M. Odenkirchen, N. Okada, S. Okamura, J. P. Ostriker, R. Owen, A. G. Pauls, J. Peoples, R. S. Peterson, D. Petravick, A. Pope, R. Pordes, M. Postman, A. Prosapio, T. R. Quinn, R. Rechenmacher, C. H. Rivetta, H.-W. Rix, C. M. Rockosi, R. Rosner, K. Ruthmansdorfer, D. Sandford, D. P. Schneider, R. Scranton, M. Sekiguchi, G. Sergey, R. Sheth, K. Shimasaku, S. Smee, S. A. Snedden, A. Stebbins, C. Stubbs, I. Szapudi, P. Szkody, G. P. Szokoly, S. Tabachnik, Z. Tsvetanov, A. Uomoto, M. S. Vogeley, W. Voges, P. Waddell, R. Walterbos, S.-i. Wang, M. Watanabe, D. H. Weinberg, R. L. White, S. D. M. White, B. Wilhite, D. Wolfe, N. Yasuda, D. G. York, I. Zehavi, and W. Zheng. Sloan Digital Sky Survey: Early Data Release. *AJ*, 123:485–548, January 2002. doi:10.1086/324741.

- L. Strüder, U. Briel, K. Dennerl, R. Hartmann, E. Kendziorra, N. Meidinger, E. Pfeffermann, C. Reppin, B. Aschenbach, W. Bornemann, H. Bräuninger, W. Burkert, M. Elender, M. Freyberg, F. Haberl, G. Hartner, F. Heuschmann, H. Hippmann, E. Kastelic, S. Kemmer, G. Kettenring, W. Kink, N. Krause, S. Müller, A. Oppitz, W. Pietsch, M. Popp, P. Predehl, A. Read, K. H. Stephan, D. Stötter, J. Trümper, P. Holl, J. Kemmer, H. Soltau, R. Stötter, U. Weber, U. Weichert, C. von Zanthier, D. Carathanassis, G. Lutz, R. H. Richter, P. Solc, H. Böttcher, M. Kuster, R. Staubert, A. Abbey, A. Holland, M. Turner, M. Balasini, G. F. Bignami, N. La Palombara, G. Villa, W. Buttler, F. Gianini, R. Lainé, D. Lumb, and P. Dhez. The European Photon Imaging Camera on XMM-Newton: The pn-CCD camera. *A&A*, 365:L18–L26, January 2001. doi:10.1051/0004-6361:20000066.
- R. A. Sunyaev and Y. B. Zeldovich. The Observations of Relic Radiation as a Test of the Nature of X-Ray Radiation from the Clusters of Galaxies. *Comments on Astrophysics and Space Physics*, 4:173, November 1972.
- D. S. Taranu, J. Dubinski, and H. K. C. Yee. Mergers in Galaxy Groups. I. Structure and Properties of Elliptical Remnants. *ApJ*, 778:61, November 2013. doi:10.1088/0004-637X/778/1/61.
- P. F. Teague, D. Carter, and P. M. Gray. The dynamics and structure of rich clusters of galaxies. I - Velocity data. *ApJS*, 72:715–753, April 1990. doi:10.1086/191430.
- M. J. L. Turner, A. Abbey, M. Arnaud, M. Balasini, M. Barbera, E. Belsole, P. J. Ben-
nie, J. P. Bernard, G. F. Bignami, M. Boer, U. Briel, I. Butler, C. Cara, C. Chabaud,
R. Cole, A. Collura, M. Conte, A. Cros, M. Denby, P. Dhez, G. Di Coco, J. Dowson,
P. Ferrando, S. Ghizzardi, F. Gianotti, C. V. Goodall, L. Gretton, R. G. Griffiths,
O. Hainaut, J. F. Hochedez, A. D. Holland, E. Jourdain, E. Kendziorra, A. Lagostina,
R. Laine, N. La Palombara, M. Lortholary, D. Lumb, P. Marty, S. Molendi, C. Pigot,
E. Poindron, K. A. Pounds, J. N. Reeves, C. Reppin, R. Rothenflug, P. Salvétat, J. L.
Sauvageot, D. Schmitt, S. Sembay, A. D. T. Short, J. Spragg, J. Stephen, L. Strüder,
A. Tiengo, M. Trifoglio, J. Trümper, S. Vercellone, L. Vigroux, G. Villa, M. J. Ward,
S. Whitehead, and E. Zonca. The European Photon Imaging Camera on XMM-
Newton: The MOS cameras. *A&A*, 365:L27–L35, January 2001. doi:10.1051/0004-
6361:20000087.
- T. Valentinuzzi, B. M. Poggianti, G. Fasano, M. D’Onofrio, A. Moretti, M. Ramella,
A. Biviano, J. Fritz, J. Varela, D. Bettoni, B. Vulcani, M. Moles, W. J. Couch,
A. Dressler, P. Kjærgaard, A. Omizzolo, and A. Cava. The red-sequence of 72
WINGS local galaxy clusters. *A&A*, 536:A34, December 2011. doi:10.1051/0004-
6361/201117522.
- M. Valluri. Compressive tidal heating of a disk galaxy in a rich cluster. *ApJ*, 408:57–70,
May 1993. doi:10.1086/172569.

-
- F. van de Voort, J. Schaye, C. M. Booth, M. R. Haas, and C. Dalla Vecchia. The rates and modes of gas accretion on to galaxies and their gaseous haloes. *MNRAS*, 414: 2458–2478, July 2011. doi:10.1111/j.1365-2966.2011.18565.x.
- S. van den Bergh. A Preliminary Luminosity Classification for Galaxies of Type Sb. *ApJ*, 131:558, May 1960. doi:10.1086/146869.
- S. Veilleux, G. Cecil, and J. Bland-Hawthorn. Galactic Winds. *ARA&A*, 43:769–826, September 2005. doi:10.1146/annurev.astro.43.072103.150610.
- M. Verdugo, M. Lerchster, H. Böhringer, H. Hildebrandt, B. L. Ziegler, T. Erben, A. Finoguenov, and G. Chon. The Cosmic Web and galaxy evolution around the most luminous X-ray cluster: RX J1347.5-1145. *MNRAS*, 421:1949–1968, April 2012. doi:10.1111/j.1365-2966.2012.20396.x.
- A. Vikhlinin, B. R. McNamara, W. Forman, C. Jones, H. Quintana, and A. Hornstrup. A Catalog of 200 Galaxy Clusters Serendipitously Detected in the ROSAT PSPC Pointed Observations. *ApJ*, 502:558–581, August 1998a. doi:10.1086/305951.
- A. Vikhlinin, B. R. McNamara, W. Forman, C. Jones, H. Quintana, and A. Hornstrup. Evolution of Cluster X-Ray Luminosities and Radii: Results from the 160 Square Degree ROSAT Survey. *ApJ*, 498:L21–L25, May 1998b. doi:10.1086/311305.
- M. Vogelsberger, S. Genel, V. Springel, P. Torrey, D. Sijacki, D. Xu, G. Snyder, S. Bird, D. Nelson, and L. Hernquist. Properties of galaxies reproduced by a hydrodynamic simulation. *Nature*, 509:177–182, May 2014a. doi:10.1038/nature13316.
- M. Vogelsberger, S. Genel, V. Springel, P. Torrey, D. Sijacki, D. Xu, G. Snyder, D. Nelson, and L. Hernquist. Introducing the Illustris Project: simulating the coevolution of dark and visible matter in the Universe. *MNRAS*, 444:1518–1547, October 2014b. doi:10.1093/mnras/stu1536.
- W. Voges, B. Aschenbach, T. Boller, H. Bräuninger, U. Briel, W. Burkert, K. Dennerl, J. Englhauser, R. Gruber, F. Haberl, G. Hartner, G. Hasinger, M. Kürster, E. Pfeffermann, W. Pietsch, P. Predehl, C. Rosso, J. H. M. M. Schmitt, J. Trümper, and H. U. Zimmermann. The ROSAT all-sky survey bright source catalogue. *A&A*, 349:389–405, September 1999.
- S. D. M. White. Violent Relaxation in Hierarchical Clustering. In O. Lahav, E. Terlevich, and R. J. Terlevich, editors, *Gravitational dynamics*, page 121, 1996.
- S. D. M. White and C. S. Frenk. Galaxy formation through hierarchical clustering. *ApJ*, 379:52–79, September 1991. doi:10.1086/170483.
- S. D. M. White and M. J. Rees. Core condensation in heavy halos - A two-stage theory for galaxy formation and clustering. *MNRAS*, 183:341–358, May 1978.

- M. Wolf. Über einen Nebelfleck-Haufen im Perseus. *Astronomische Nachrichten*, 170: 211, January 1906.
- G. Worthey. Comprehensive stellar population models and the disentanglement of age and metallicity effects. *ApJS*, 95:107–149, November 1994. doi:10.1086/192096.
- N. Yasuda, M. Fukugita, V. K. Narayanan, R. H. Lupton, I. Strateva, M. A. Strauss, Ž. Ivezić, R. S. J. Kim, D. W. Hogg, D. H. Weinberg, K. Shimasaku, J. Loveday, J. Annis, N. A. Bahcall, M. Blanton, J. Brinkmann, R. J. Brunner, A. J. Connolly, I. Csabai, M. Doi, M. Hamabe, S.-I. Ichikawa, T. Ichikawa, D. E. Johnston, G. R. Knapp, P. Z. Kunszt, D. Q. Lamb, T. A. McKay, J. A. Munn, R. C. Nichol, S. Okamura, D. P. Schneider, G. P. Szokoly, M. S. Vogeley, M. Watanabe, and D. G. York. Galaxy Number Counts from the Sloan Digital Sky Survey Commissioning Data. *AJ*, 122: 1104–1124, September 2001. doi:10.1086/322093.
- D. G. York, J. Adelman, J. E. Anderson, Jr., S. F. Anderson, J. Annis, N. A. Bahcall, J. A. Bakken, R. Barkhouser, S. Bastian, E. Berman, W. N. Boroski, S. Bracker, C. Briegel, J. W. Briggs, J. Brinkmann, R. Brunner, S. Burles, L. Carey, M. A. Carr, F. J. Castander, B. Chen, P. L. Colestock, A. J. Connolly, J. H. Crocker, I. Csabai, P. C. Czarapata, J. E. Davis, M. Doi, T. Dombeck, D. Eisenstein, N. Ellman, B. R. Elms, M. L. Evans, X. Fan, G. R. Federwitz, L. Fiscelli, S. Friedman, J. A. Frieman, M. Fukugita, B. Gillespie, J. E. Gunn, V. K. Gurbani, E. de Haas, M. Haldeman, F. H. Harris, J. Hayes, T. M. Heckman, G. S. Hennessey, R. B. Hindsley, S. Holm, D. J. Holmgren, C.-h. Huang, C. Hull, D. Husby, S.-I. Ichikawa, T. Ichikawa, Ž. Ivezić, S. Kent, R. S. J. Kim, E. Kinney, M. Klaene, A. N. Kleinman, S. Kleinman, G. R. Knapp, J. Korienek, R. G. Kron, P. Z. Kunszt, D. Q. Lamb, B. Lee, R. F. Leger, S. Limmongkol, C. Lindemeyer, D. C. Long, C. Loomis, J. Loveday, R. Lucinio, R. H. Lupton, B. MacKinnon, E. J. Mannery, P. M. Mantsch, B. Margon, P. McGehee, T. A. McKay, A. Meiksin, A. Merelli, D. G. Monet, J. A. Munn, V. K. Narayanan, T. Nash, E. Neilsen, R. Neswold, H. J. Newberg, R. C. Nichol, T. Nicinski, M. Nonino, N. Okada, S. Okamura, J. P. Ostriker, R. Owen, A. G. Pauls, J. Peoples, R. L. Peterson, D. Petravick, J. R. Pier, A. Pope, R. Pordes, A. Prosapio, R. Rechenmacher, T. R. Quinn, G. T. Richards, M. W. Richmond, C. H. Rivetta, C. M. Rockosi, K. Ruthmansdorfer, D. Sandford, D. J. Schlegel, D. P. Schneider, M. Sekiguchi, G. Sergey, K. Shimasaku, W. A. Siegmund, S. Smee, J. A. Smith, S. Snedden, R. Stone, C. Stoughton, M. A. Strauss, C. Stubbs, M. SubbaRao, A. S. Szalay, I. Szapudi, G. P. Szokoly, A. R. Thakar, C. Tremonti, D. L. Tucker, A. Uomoto, D. Vanden Berk, M. S. Vogeley, P. Waddell, S.-i. Wang, M. Watanabe, D. H. Weinberg, B. Yanny, N. Yasuda, and SDSS Collaboration. The Sloan Digital Sky Survey: Technical Summary. *AJ*, 120:1579–1587, September 2000. doi:10.1086/301513.
- J. S. Young, J. E. Baldwin, R. C. Boyesen, C. A. Haniff, P. R. Lawson, C. D. Mackay, D. Pearson, J. Rogers, D. St.-Jacques, P. J. Warner, D. M. A. Wilson, and R. W. Wilson. New views of Betelgeuse: multi-wavelength surface imaging and implications

-
- for models of hotspot generation. *MNRAS*, 315:635–645, July 2000. doi:10.1046/j.1365-8711.2000.03438.x.
- A. I. Zabludoff and D. Zaritsky. A Collision of Subclusters in Abell 754. *ApJ*, 447:L21, July 1995. doi:10.1086/309552.
- I. Zehavi, Z. Zheng, D. H. Weinberg, M. R. Blanton, N. A. Bahcall, A. A. Berlind, J. Brinkmann, J. A. Frieman, J. E. Gunn, R. H. Lupton, R. C. Nichol, W. J. Percival, D. P. Schneider, R. A. Skibba, M. A. Strauss, M. Tegmark, and D. G. York. Galaxy Clustering in the Completed SDSS Redshift Survey: The Dependence on Color and Luminosity. *ApJ*, 736:59, July 2011. doi:10.1088/0004-637X/736/1/59.
- Y.-Y. Zhang, H. Böhringer, A. Finoguenov, Y. Ikebe, K. Matsushita, P. Schuecker, L. Guzzo, and C. A. Collins. X-ray properties in massive galaxy clusters: XMM-Newton observations of the REFLEX-DXL sample. *A&A*, 456:55–74, September 2006. doi:10.1051/0004-6361:20053650.
- S. Zibetti, S. D. M. White, D. P. Schneider, and J. Brinkmann. Intergalactic stars in $z \sim 0.25$ galaxy clusters: systematic properties from stacking of Sloan Digital Sky Survey imaging data. *MNRAS*, 358:949–967, April 2005. doi:10.1111/j.1365-2966.2005.08817.x.
- F. Ziparo, F. G. Braglia, D. Pierini, A. Finoguenov, H. Böhringer, and A. Bongiorno. In the whirlpool’s coils: tracing substructure from combined optical/X-ray data in the galaxy cluster A1300. *MNRAS*, 420:2480–2496, March 2012. doi:10.1111/j.1365-2966.2011.20212.x.
- F. Zwicky. Die Rotverschiebung von extragalaktischen Nebeln. *Helvetica Physica Acta*, 6:110–127, 1933.

Acknowledgments

I wish to thank friends, family, clubs and others who have supported this work in so many ways. In no particular order: Katharina ‘Schlippsi’ Büchl, Andrea Kim (née Müller), Julian Lloyd, Vitus Reiter, Kristin Palfreyman, Benedikt Reiter, Sofia Rieger, Janina Dörr, Denis Tümen, Sarah Fischer, Brigitte and Thorsten Gundel, Claudia Zinsmeister and all the rest at Fly ‘n’ Dance Freising e.V. Other friends who’ve supported me a great deal deserve a mention: Stephanie Braun, Noëmi Ortmann, Jeremy Dykes, Rebecca Devine, Aisha Mohammad, Katharina Lang, Andrew Chung, Addressa Jendreieck and the young musicians of Musikverein St. Andreas Eching e.V. Many thanks to Hans Böhringer, Gayoung Chon and Ortwin Gerhard for guidance, support, patience and proof-reading.

This work is dedicated to Michael, Yvonne, Andrew, Enid, and John (Snr.) Holland. Without your support, encouragement and love over so many years, nothing would have been written at all.